MAGNETIC RESONANCE STUDIES OF CHEMICAL REACTIONS IN MICROEMULSIONS

by

DANIEL ANTHONY BINKS

A thesis submitted to
The University of Birmingham
for the degree of
DOCTOR OF PHILOSOPHY

School of Chemistry
College of Engineering and Physical Sciences
The University of Birmingham
October 2009

Abstract

The Belousov-Zhabotinsky (BZ) reaction is the preeminent oscillating chemical reaction for the study of pattern formation in reaction-diffusion systems. The dispersal of the reaction in a water-in-oil AOT microemulsion (BZ-AOT reaction) gives rise to an extended range of patterns, including dash waves, segmented spirals and, most notably, stationary Turing patterns that are thought to be significant to an understanding of the biological process of morphogenesis. To date, these patterns have only been observed in two-dimensions using optical microscopy.

In this project, nuclear magnetic resonance (NMR) spectroscopy and imaging (MRI) techniques were used along with existing optical methods in order to identify redox indicators suitable for the visualisation of pattern formation in the BZ-AOT reaction using MRI. The location of the redox indicator in the microemulsion was found to be important with respect to its application as an indicator. Thus, the use of Ru(II)(bpy)$_3$ as an MR contrast agent was ruled out as it was found to reside within the micellar interface. Manganese, however, proved to be a viable MR indicator. Oscillations were observed in the manganese-catalysed BZ-AOT reaction through changes in the NMR relaxation times of solvent water molecules. The ability of manganese to act as an MR contrast indicator has enabled pattern formation in the BZ-AOT reaction to be visualised using MRI for the first time. Further development of the technique may allow pattern formation to be visualised in three-dimensions.

Dedicated in memory of Peter Frederick Birks

Acknowledgments

First and foremost I would like to express my sincerest gratitude to my supervisor, Dr. Melanie Britton, for her advice, support and encouragement during the last four years, without which, the production of this thesis would have been impossible.

I would also like to offer my thanks to our collaborators at Brandeis University, in particular Dr. Vladimir Vanag for his advice regarding the BZ-AOT reaction. My sincerest thanks also go to Dr. Neil Spencer, not least for his wealth of NMR knowledge, and to Tony Rothin and Steve Williams for deciphering my technical drawings and building various contraptions.

I am indebted to members of the Britton group, past and present; in particular to Dr Andrei Nossov and Jan Novak for their practical nous, and to Nicola Cowell for invaluable discussion during countless coffee and lunch breaks! My thanks also go to my colleagues, friends and staff at the School of Chemistry, University of Birmingham: Andy, Oliver, Emma, Adam, Tom, Jon, Lasse, Johanna, Kousik, Christina, Roy, Maryjane, Graham, Sarah, Bhav, Benedicte, Scott, Claire, Laura, Lynne, Helen and Pam.

To my friends: Luke, Paul, Matt, Gavin, and their families and to my girlfriend Nikki, I continue to be grateful for your friendship and support.

Finally, I would like to thank my family, and especially my parents, for their continued support throughout the last twenty-seven years.

This thesis and the work described in it are entirely the work of the author. Exceptions to this are where the help of another person is acknowledged or a reference is given to a published source, and these are clearly noted in the text.

Table of Contents

List of abbreviations

AOT – aerosol OT (sodium bis(2-ethylhexyl) sulfosuccinate)

bpy - 2,2'-bipyridine

BZ-AOT reaction – the BZ reaction dispersed in an AOT microemulsion

BZ reaction – Belousov Zhabotinsky reaction

CHESS – CHEmical Shift Selective – MR imaging sequence in which only signal from one component of a multi-component system is imaged.

FOV – field-of-view

MA – malonic acid

ME – microemulsion

MR(I) – Magnetic Resonance (Imaging)

NMR – Nuclear Magnetic Resonance

NOE – Nuclear Overhauser effect

phen - 1,10-phenanthroline

r.f. – radiofrequency

$Ru(bpy)_3$ – $Ru(II)(bpy)_3$ or $[Ru(bpy)_3]^{2+}$

Chapter 1. Introduction

1.1. Synopsis

This work is an experimental study of pattern formation in the BZ-AOT reaction-diffusion system using nuclear magnetic resonance (NMR) and magnetic resonance imaging (MRI). The BZ-AOT reaction displays many features exemplary of a reaction-diffusion system, and is only the second chemical system in which stationary Turing type patterns have been observed. To date, pattern formation in the BZ-AOT reaction has only been studied in two-dimensions using optical imaging techniques. Through the use of MRI, it is hoped to develop imaging methods that will enable pattern formation in the BZ-AOT reaction to be observed in three-dimensions for the first time. This will present an opportunity to observe the first example of 3-D Turing patterns in a chemical system. The use of magnetic resonance is not limited to the visualisation of patterns and will also be used to probe the physical structure of the microemulsion structure in order to understand how the microemulsion structure influences the development and formation of the extended range of patterns observed in the BZ-AOT system.

1.1.1. Thesis outline

The work conducted and presented as part of this thesis draws upon previous research conducted across a broad range of scientific disciplines; from an

understanding of the nuclear physics fundamental to NMR and MRI; the non-linear reaction kinetics of the BZ reaction; through to the materials chemistry of surfactants relevant to microemulsion systems. These principles are introduced and reviewed in the remainder of Chapter 1.

One of the initial objectives of the project was to become familiar with the chemistry of the BZ-AOT system, with a particular interest in identifying the reaction parameters that control and affect the types of patterns that are formed. Pattern formation in the BZ-AOT system was studied for a variety of catalyst systems. This aspect of the project is covered in Chapter 2.

A major aim of this project was the characterisation of suitable catalyst systems for the visualisation of pattern formation using magnetic resonance imaging. The $[Ru(bpy)_3]^{2+}$ complex was identified as one potentially suitable catalyst system. The work presented in Chapter 3 deals with the characterisation process of the complex in terms of its NMR relaxivity in the aqueous BZ system and the BZ-AOT microemulsion system. The interaction of the $[Ru(bpy)_3]^{2+}$ complex with the microemulsion environment is also investigated and discussed in this chapter.

In Chapter 4, the manganese-catalysed BZ-AOT system is investigated and characterised with respect to its use as an MRI active contrast agent for the reaction. Results are presented that show that manganese is able to provide the necessary relaxation time contrast to observe changes in oxidation state

of the oscillatory BZ-AOT reaction. The use of phosphate compounds to improve the level of contrast available is also investigated.

Finally, in Chapter 5, the characterisation of the manganese catalyst is exploited in order to develop a method for the visualisation of pattern formation in the BZ-AOT reaction using MRI. This method is used to obtain the first 2-D images of chemical waves in the BZ-AOT reaction taken using MRI. The implications of these results are discussed with respect to future developments that could enable pattern formation to be visualised in three-dimensions.

1.2. Introduction to chemical patterns and waves

1.2.1. Patterns in nature

Pattern formation is a recurring theme throughout the natural world. Patterns of chemical, physical and biological origin are evident in a diverse range of phenomena[1,2]. From relatively small scale systems such as the growth of colonies of bacteria; animal markings such as a tiger's stripes; the electrical impulses that control the beating of the heart; through to larger scale systems including the propagation of cloud formations; plankton blooms observed in the ocean; networks of sand dunes; and even the organisation of collections of stars into galaxies.

Motivation for the study of pattern formation in chemical reactions, therefore, comes not only from a desire to comprehend the mechanism of the chemical

system in question, but also in applying this knowledge to an understanding of how chemical systems may be used to model pattern forming behaviour observed in nature. One simply has to compare spiral patterns observed in colonies of the slime mould *Dictyostelium discoideum* to spiral patterns observed in the Belousov-Zhabotinsky reaction (Figure 1.1) to appreciate how the two may be linked. However, similar looking patterns may not necessarily share the same underlying mechanism.

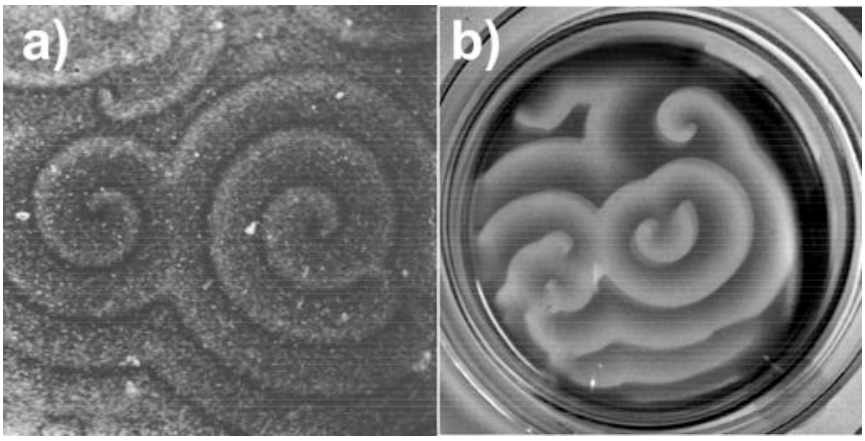

Figure 1.1 Spiral patterns seen in a) a colony of *Dictyostelium discoideum* undergoing chemotaxis[3] and b) the Belousov-Zhabotinsky reaction performed in a Petri dish.

1.2.2. Study of pattern formation in chemical systems

1.2.2.1. Excitable media

Many of the patterns found in nature share some commonality in that they are excitable. An excitable medium is one that possesses a rest state, which is stable to small perturbations. Larger perturbations, however, will cause the system to change its state. Typically, the system is then insensitive to further perturbations for a period of time – the refractory period – before recovering to its initial excitable state.

1.2.2.2. Autocatalysis and feedback

An autocatalytic reaction is one in which one of the products of the reaction is itself a catalyst for the reaction. The autocatalytic species is often referred to as the activator species. The example shown in Equation 1.1 is an overall second-order reaction and therefore describes quadratic autocatalysis.

$$X + Y \rightarrow 2Y \qquad \textbf{(1.1)}$$

Feedback is the process by which the products of a reaction step influence the kinetics of an earlier reaction step[4]. Feedback can be classed as either positive or negative. In Equation 1.1, the autocatalytic production of *Y* results in an acceleration of its own production. This is an example of positive feedback. The opposite case is negative feedback, in which the product of a reaction inhibits its own production.

1.2.2.3. Travelling waves in reaction-diffusion systems

Pattern formation in chemical reactions arises due to a coupling of autocatalytic reaction kinetics with diffusion of reactants through an excitable reaction medium. Patterns formed in this manner are known as reaction-diffusion phenomena. If a discrete point in the excitable medium is perturbed such that localised production of the autocatalyst results, then the autocatalyst will diffuse into neighbouring regions causing them to be excited. This results in a travelling front of excitation propagating outwards from the initial point of perturbation. The autocatalyst is, therefore, often called the “propagator” species[2]. In some cases the system may be returned to its initial state by another chemical species, dubbed the “controller” species. In this case a

wave is formed allowing another travelling front to be initiated by further perturbation, provided the system has recovered from its refractory state.

1.2.2.4. Stationary Turing structures

In a paper entitled *The Chemical Basis of Morphogensis*[5], mathematician Alan Turing described a hypothetical chemical system in which a coupling of autocatalysis and diffusion could generate stationary patterns in an initially homogeneous medium. Turing surmised that such a reaction could be used to rationalise the process of cell differentiation during embryonic development. The requirements for this *symmetry-breaking* process were based around the interplay of two chemical species: The *activator*, which catalyses its own production, and also promotes the formation of the second species, the *inhibitor*, which inhibits the formation of the activator[1]. The requirement for the formation of stationary patterns is that the inhibitor species is able to diffuse through the reaction medium much more quickly (by at least an order of magnitude). In this way, the influence of the inhibitor species is felt at a longer range than the activator species. The autocatalytic reaction and production of the inhibitor species are localised processes, whereas the inhibition of autocatalysis is long-ranged due to rapid diffusion of the inhibitor. This leads to spatial ordering of the reaction medium with distinct regions dominated by either activation or inhibition of the reaction.

1.3. Introduction to the BZ reaction

1.3.1. Discovery of the BZ reaction

The Belousov-Zhabotinsky (BZ) reaction is the most widely studied chemical reaction-diffusion system. The BZ reaction was discovered at some point during the early 1950s by Boris Belousov[6]. At the time Belousov was interested in modelling the Krebs cycle using an inorganic reaction to replicate the function of protein-bound metal ions found in such enzymatic systems. His investigations would lead him to the serendipitous discovery of what would later be accepted as the first example of a homogeneous oscillating chemical reaction[7]. Belousov noticed his solution of citric acid, acidified bromate and cerium ions periodically oscillated between colourless and yellow, as well as producing carbon dioxide. Initially, Belousov's discovery was met with scepticism, as the concept of an oscillating reaction was deemed to be in violation of the second law of thermodynamics; its detractors reasoned that the back and forth conversion of products to reactants would require the system to oscillate about its equilibrium point. This would in turn implicate an oscillation in the Gibbs free energy of the system, which is where the contradiction of the second law arises[8]. However, a chemical oscillator is not an equilibrium process; oscillations in the concentration of *intermediate* species are not disallowed by thermodynamics, as the system does not oscillate about its equilibrium free energy point, rather it oscillates *far-from-equilibrium.* The overall free energy of the system is always decreasing towards its equilibrium point, satisfying the requirement of the second law.

Anatol Zhabotinsky would later refine Belousov's original reaction, replacing citric acid with malonic acid, and substituting the cerium catalyst with ferroin, a redox indicator with superior colour contrast. The ferroin-catalysed reaction has since come to represent the BZ reaction in its most classical and most studied form[9]. It has been extensively investigated and has been shown to exhibit a number of phenomena exemplary of an oscillating chemical reaction, going on to become the archetypal reaction for the study of non-linear chemical kinetics.

1.3.2. Oscillatory behaviour in the BZ reaction

1.3.2.1. Optical observation of oscillations

In stirred reactors, the BZ reaction displays temporal oscillations in the chemical concentration of certain intermediate species. These oscillations can be observed as a colour change, as with Belousov's cerium-catalysed reaction that oscillated between colourless and yellow. Other indicators also exist where oscillations can be observed as a colour change, either directly[10,11] or via spectrophotometric measurements[12,13]. The ferroin-catalysed reaction would be the best example of oscillations directly observable as a colour change. In systems like the manganese-catalysed system and, to a lesser extent, the cerium-catalysed reaction, where the colour change is less distinct, oscillations can be observed using UV/visible spectrophotometry[14].

1.3.2.2. Potentiometric observation of oscillations

Oscillations are also commonly measured using potentiometry. The concentration of bromide ions in the reaction can be measured using a bromide ion sensitive electrode. A platinum electrode is sensitive to changes in the oxidation state of the metal-ion catalyst. With a suitable reference electrode, the measured electrode potential can be used to monitor oscillations in $[Br^-]$ and $[M_{ox}]/[M_{red}]$, Figure 1.2.

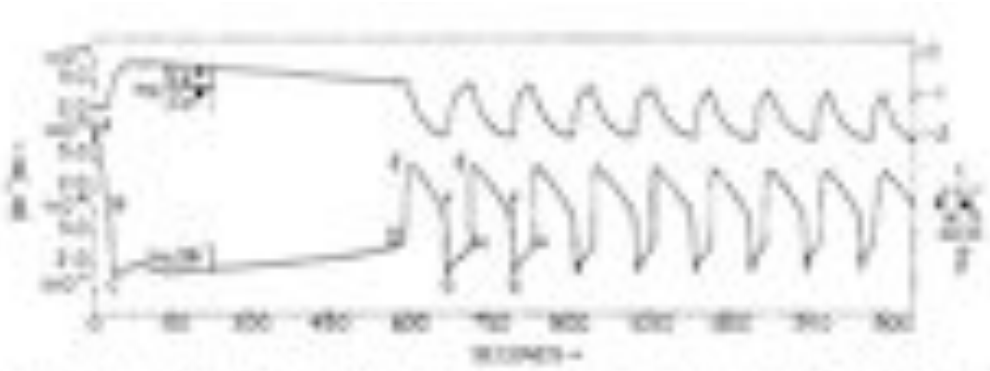

Figure 1.2 Oscillations in a cerium-catalysed BZ reaction measured using potentiometric methods. The lower trace shows oscillations in $[Br^-]$, and the upper trace shows oscillations in concentration of the oxidised form of the cerium catalyst[15].

1.3.2.3. Observation of oscillations using nuclear magnetic resonance

Hansen and Ruoff[16] have shown that oscillations in the manganese-catalysed BZ reaction can be observed via changes in the NMR parameters of the water protons of the system. The chemical shift, line width and spin-lattice relaxation time can all be used to monitor oscillations as the manganese ion oscillates between the reduced (Mn^{2+}) and oxidised (Mn^{3+}) states.

1.3.2.4. Oscillations observed using other techniques

Oscillations may also be seen from calorimetric measurements[17], since the rate of heat production during different phases of the oscillation varies. Similarly, the rate of production of CO_2 gas during the reaction has been used to observe oscillations. CO_2 pressure was measured as a function of time using a Warburg apparatus and related to different phases of the oscillation period[13].

1.3.3. Induction period of the BZ reaction

In the cerium- and manganese-catalysed BZ reactions, oscillations are not observed until a critical concentration of bromomalonic acid is reached[18]. Reactions catalysed by ferroin and $Ru(bpy)_3$ catalysts do not show this induction period[17]. The different behaviour of the ferroin- and $Ru(bpy)_3$-catalysed reactions, with respect to the cerium- and manganese-catalysed systems, may arise from the similarity of ferroin and $Ru(bpy)_3$ in terms of electron-transfer mechanisms, which occur via outer-sphere transfer processes. Electron transfer in the cerium and manganese systems occurs via an inner-sphere mechanism[19].

1.3.4. Effects of oxygen and stirring on the BZ reaction

The effect of molecular oxygen (O_2) on the oscillatory BZ reaction is complex and varies depending upon the exact reaction conditions. It is unsurprising then, that there have been (separate) reports of oxygen both increasing and decreasing the oscillation period, and also that oxygen inhibits and also

causes oscillations[20]. However, it is now accepted that oxygen has an inhibitory effect on oscillations[21,22]. Oxygen effects were thought to be related to stirring, with the rate of stirring affecting the uptake of O_2 from the atmosphere into the reaction[21,22]. However, stirring rate has also been shown to affect reactions performed under inert atmospheres[23], showing that the effects of stirring are not limited to the introduction of O_2 into the system. Stirring effects can be mediated through the use of sealed reaction vessels in which there is no gas/liquid interface *i.e.* the reaction vessel is filled completely with the reaction mixture and fitted with a stopper. This precludes the transfer of gases into the reaction mixture. The stirring rate itself can be controlled using a magnetic stirrer with a calibrated speed control[21].

1.3.5. Spatial pattern formation in the BZ reaction

1.3.5.1. Travelling waves

If the BZ reaction is performed in a shallow unstirred layer, *e.g.* a Petri dish filled with the reaction mixture, then the oscillatory behaviour seen in the stirred reaction can manifest itself in the formation of travelling chemical waves such as those shown in Figure 1.3 a). The diffusion of the autocatalyst, $HBrO_2$ causes a wave front of the oxidised state of the reaction to propagate through the reaction medium. Behind the wave front, the oxidised form of the metal ion catalyst reacts with malonic acid to restore the system back to its initial state. This phenomenon was first observed by Zhabotinsky,[9] in a 2 mm layer of the ferroin-catalysed BZ reaction. Patterns initially take the form of concentric travelling waves. As multiple waves fill the dish, their interaction

can bring about the formation of relatively complex structures. Perturbations of these so called “target waves” can be brought about either by the presence of air bubbles or dust particles, or by more deliberate methods such as tilting or blowing the reaction mixture. These perturbations can result in the formation of rotating spiral waves[26-29], (Figure 1.3 b)).

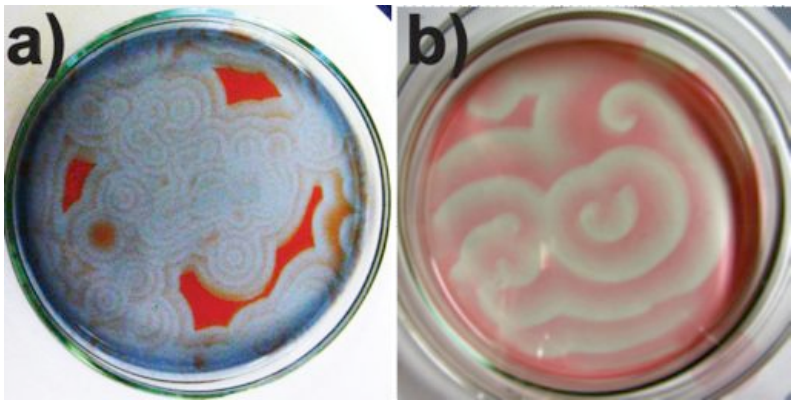

Figure 1.3 a) Target, and b) spiral pattern observed in the ferroin-catalysed BZ reaction. The light areas are where the ferroin catalyst is in its oxidised (blue) state (ferriin), and the darker areas are where the catalyst is in its reduced (red) oxidation state. In each case the patterns are formed in a shallow layer of the reaction in an 8 cm diameter Petri dish.

1.3.5.2. Wave velocity

The velocity at which chemical waves propagate in the BZ reaction has been the subject of several studies[24-26]. The velocity of a chemical wave through the reaction medium has been found to be constant and dependent upon the diffusion coefficient of the autocatalytic species, *D,* and the pseudo first order rate constant, k^1, that governs the autocatalytic step, Equation 1.2.

$$c \propto \sqrt{k^1 D} \qquad \textbf{(1.2)}$$

Given a diffusion coefficient of approximately 10^{-5} cm^2 s^{-1}, typical for a small molecule in aqueous solution, this equates to wave velocities of the order of 1 to 10 mm min^{-1} at the reagent concentrations normally used in the BZ reaction.

1.3.5.3. Three-dimensional patterns

If the BZ reaction medium is extended beyond a thin layer and into a third dimension, then it is possible to observe the three-dimensional manifestation of 2-D spiral waves in the form of a "scroll wave"[27]. The structure and evolution of such patterns has been the subject of much conjecture and discussion, a good deal of which has been communicated by Art Winfree[28-32]. In a novel experiment where a stack of filter papers was loaded with the BZ reaction, Winfree was able to show the existence of scroll waves by effectively showing several cross-sections through a 3-D reaction medium[33]. It is, however, difficult to observe 3-D structures directly due to such factors as convection and bubble formation. Gomatam and Welsh[34] alleviated these problems by performing the reaction in a small sealed vessel, and were able to photograph 2-D cross sections of various scroll waves. Another approach was taken by Winfree *et al*[35]; they performed a CHD (cyclohexanedione) reaction using an agarose gel medium to suppress bubble formation and convection effects. They were then able to reconstruct 3-D representations of scroll waves by combining 2-D projections taken as their reaction vessel was rotated. Optical imaging techniques are, however, unable to penetrate optically opaque systems. Magnetic resonance imaging (MRI) is not constrained in this way, and is able to visualise 3-D structures directly. Cross

et al[36] have been able to produce 3-D images of waves in the manganese-catalysed BZ reaction performed in an agarose gel.

1.3.6. Mechanism of the BZ reaction

The classic BZ reaction is based on the oxidation of malonic acid by acidified bromate, catalyzed by the presence of a one-electron metal-ion redox couple[19]. A mechanistic understanding of the reaction has been developed by Richard Field, Endre Körös and Richard Noyes[15,37]. Their extensive analysis of the reaction from a chemical kinetics point of view has been revised and modified since its publication in 1972, but has been shown to be able to account for many of the features and behaviour of the BZ reaction. The mechanism is now simply known by the initials of its discoverers - the FKN mechanism.

1.3.6.1. The FKN mechanism

In its original form, the FKN mechanism consists of 11 elementary reactions involving 15 different species[19]. These 11 elementary reactions can be further simplified down to three distinct processes, each concerned with a separate facet of the overall reaction[4].

Process A governs the removal of bromide ions from the system via their reaction with bromate ions. Molecular bromine is also produced during Process A, which reacts with malonic acid to produce bromomalonic acid. This species is fundamental to the oscillatory nature of the reaction as it subsequently reacts with the oxidised form of the metal ion catalyst to “reset

the clock". Process B involves the autocatalytic production of bromous acid ($HBrO_2$) and the oxidation of the metal ion catalyst.

Combined, Processes A and B form the basis of a simple clock reaction, much like the classic iodine clock (Landolt[38]) reaction; the concentration of bromide ion at a given time determines whether the reaction proceeds via Process A or B. At high bromide ion concentration, Process A dominates. The net effect of Process A is to remove bromide from the system. Process A thus continues until the bromide ion concentration falls below a critical value, at which point Process B takes over. Bromide ions play the role of the inhibitor species in the reaction, impeding the autocatalytic reaction until their concentration has fallen sufficiently. Process C involves the reduction of the metal ion catalyst by bromomalonic acid, whilst simultaneously liberating bromide ions. The increase in concentration of bromide switches the reaction pathway back to Process A. Process C is where the BZ reaction differs from an ordinary clock reaction. It is often described as "the resetting of the clock", and it is what allows multiple oscillations to be observed in the reaction by regenerating the reduced form of the metal ion catalyst and providing a means of inhibiting the autocatalytic reaction.

Process A

$$HOBr + Br^- + H^+ \rightleftarrows Br_2 + H_2O \qquad \textbf{(FKN1)}$$

$$BrO_3^- + Br^- + 2H^+ \rightleftarrows HBrO_2HOBr \qquad \textbf{(FKN3)}$$

$$HBrO_2 + Br^- + H^+ \rightleftarrows 2HOBr \qquad \textbf{(FKN2)}$$

Overall Process: $BrO_3^- + 2Br^- + 3H^+ \rightleftarrows 3HOBr$

Process B

$$2HBrO_2 \rightleftarrows BrO_3^- + HOBr + H^+ \qquad \textbf{(FKN4)}$$

$$BrO_3^- + HBrO_2 + H^+ \rightleftarrows 2BrO_2\bullet + H_2O \qquad \textbf{(FKN5)}$$

$$BrO_2\bullet + M_{red} + H^+ \rightleftarrows HBrO_2 + M_{ox} \qquad \textbf{(FKN6)}$$

Overall Process: $BrO_3^- + HBrO_2 + 2M_{red} + 3H^+ \rightleftarrows 2HBrO_2 + 2M_{ox} + H_2O$

Process C

Overall Process: $2M_{ox} + MA + BrMA \rightarrow 2M_{red} + Br^- + \text{other products}$

Figure 1.4 Reduced representation of the FKN mechanism[4], showing the important reactions in each of the three key processes. M_{red} and M_{ox} represent the reduced and oxidised forms of the metal ion catalyst respectively, MA is malonic acid, and BrMA represents bromomalonic acid. The equation numbering is consistent with the conventional FKN numbering[15,37].

1.3.7. Modifications of the BZ reaction

The most common modification to the BZ reaction is the substitution of the metal-ion catalyst. The cerium catalyst can be replaced with a variety of metal-ions or metal-ion complexes. Suitable metal-ion catalysts[19] possess two stable oxidation states that are separated by the transfer of one electron, with a standard electrode potential of 1-1.5 V, sufficient for the one electron reduction of $BrO_2\bullet$. Table 1.1 collates the standard electrode potentials of four

metal-ion or metal-ion complexes that are frequently used to catalyse the BZ reaction.

Catalyst system	Standard electrode potential / V
Ce^{3+}/Ce^{4+}	1.44
Mn^{2+}/Mn^{3+}	1.51
$[Fe(phen)_3]^{2+}$ / $[Fe(phen)_3]^{3+}$	1.06
$[Ru(bpy)_3]^{2+}$ / $[Ru(bpy)_3]^{3+}$	1.25

Table 1.1 Comparison of the standard electrode potentials of catalyst systems commonly employed in the BZ reaction.

1.3.7.1. Ferroin-catalysed BZ reaction

As has been mentioned, the ferroin ($[Fe(phen)_3]^{2+}$) catalysed system is now considered to be the classical form of the reaction. The $[Fe(phen)_3]^{2+}/[Fe(phen)_3]^{3+}$ redox couple has a standard electrode potential[39] of 1.06 V. The reduced and oxidised forms of the catalyst (ferroin and ferriin respectively) are also distinguished by different colours; red in the reduced state and blue in the oxidised state. The ferroin catalyst is therefore able to catalyse oscillations in the BZ reaction and also act as a visual indicator. Zhabotinsky *et al*[9] were the first to exploit the visual contrast available with the ferroin-catalysed reaction to observe two-dimensional spatial patterns in a Petri dish filled with a thin layer of the reaction. It should, however, be noted that the ferroin catalyst dissociates in the acidic conditions prevailing in the BZ reaction[40]. This results in degradation of visual contrast during the course of the reaction. The products of this dissociation are ferrous and ferric ions, which are not able to catalyse the BZ reaction. This precludes the use of ferroin as an MRI contrast indicator[41]. MRI contrast indicators of the BZ reaction are discussed in more detail in Section 1.8.6.

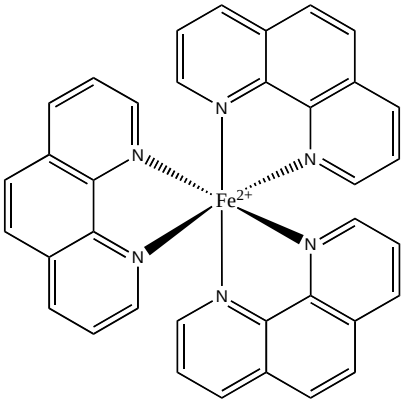

Figure 1.5 Structure of the ferroin catalyst showing the coordination of three bi-dentate 1,10-phenanthroline ligands to the Fe^{2+} metal-ion centre.

1.3.7.2. The $Ru(bpy)_3$-catalysed BZ reaction

The ruthenium complex with 2,2'-bipyridine, $[Ru(bpy)_3]^{2+}$, is another commonly used catalyst/indicator system. The $Ru(bpy)_3$ complex is octahedral and soluble in water[42]. The reduced form ($[Ru(bpy)_3]^{2+}$) can be oxidised to $[Ru(bpy)_3]^{3+}$. The standard redox potential for this reversible process[39] is 1.25 V. Aqueous solutions of $[Ru(bpy)_3]^{2+}$ are orange in colour, whereas the oxidised form, $[Ru(bpy)_3]^{3+}$ is green. The combination of a redox potential in the desired range and the ability to distinguish visually between the two involved oxidative states makes the $Ru(bpy)_3$ complex a suitable catalyst and contrast agent with which to study oscillations and pattern formation in the BZ reaction. $Ru(bpy)_3$ is also able to act as an MRI contrast indicator for the BZ reaction[41].

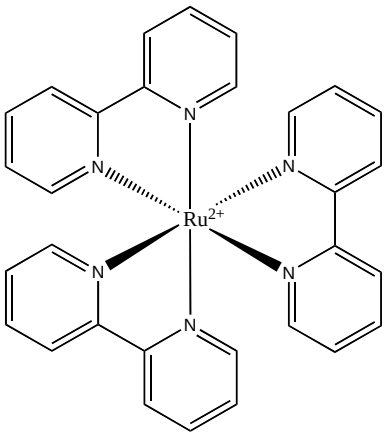

Figure 1.6 Structure of $[Ru(bpy)_3]^{2+}$, showing the coordination of three bi-dentate 2-2'-bipyridine (bpy) ligands to the Ru^{2+} metal-ion centre.

The $[Ru(bpy)_3]^{2+}$ complex is noteworthy due to its light sensitive nature. The complex absorbs light at 452nm to give an excited singlet electronic state. The excited state can be thought of as $[Ru(bpy)_2(bpy)^{-}]^{3+}$, which reacts with bromomalonic acid to produce bromide ions that inhibit the autocatalytic forward reaction[43]. The photochemistry of the $[Ru(bpy)_3]^{2+}$ complex therefore provides a method with which to control the excitability of the reaction medium. The luminescent properties of the $Ru(bpy)_3$ catalyst also make for a particularly striking variant of the BZ reaction, with the reduced form glowing bright orange when stimulated by UV light[10].

1.3.7.3. The manganese-catalysed BZ reaction

The use of manganese as the metal ion catalyst in the BZ reaction was first suggested in 1971[44]. Electron spin resonance (ESR) spectroscopy was used to observe oscillations in the concentration of Mn^{2+} during the oxidation of a malic acid substrate by acidified bromate. Oscillations were later observed, by Körös *et al*[17,45], in the manganese-catalysed BZ reaction using standard potentiometric methods.

The standard electrode potential[46] for the one electron redox process in the Mn^{2+}/Mn^{3+} couple is 1.51 V. In aqueous solutions of manganese there is a slight difference in colour for the two oxidation states, with Mn(II) being colourless whereas Mn(III) solutions are pink. In practice, the colour change observed during oscillations in the BZ reaction is not profound at the catalyst concentrations typically employed in the system, particularly when compared with the ferroin-catalysed system. Studies of pattern formation in the manganese-catalysed reaction have therefore been limited due to the lack of visual contrast.

1.3.7.4. Other catalysts of the BZ reaction

The catalysts discussed in the preceding sections account for the majority of BZ reactions, though a number of other single catalyst systems exist that catalyse BZ type oscillations[39]. Many of these are complexes of transition metal-ions with 1,10-phenanthroline or 2,2'-bipyridyl, *e.g.* $Os(bpy)_3^{2+}$, $Co(phen)_3^{2+}$ and $Ag(bpy)_2^{+}$, however, the range of reactant concentrations at which oscillations have been observed in some of these systems is limited[47,48].

1.3.8. Other pattern forming and oscillatory reactions

Although the BZ reaction is the preeminent oscillatory chemical reaction, other chemical systems also exist in which oscillations and pattern formation can be observed.

1.3.8.1. Bray reaction

The Bray reaction[49] is the earliest example of an oscillatory chemical reaction. During the reaction of iodate with iodine and hydrogen peroxide, oscillations in the concentration of iodine can be observed. As with the BZ reaction, the Bray reaction was initially dismissed, with oscillations in the system attributed to the presence of dust and bubbles[50]. The reaction has since been revisited and a mechanism elucidated[51].

1.3.8.2. Uncatalysed bromate oscillators

A class of reactions exists called uncatalysed bromate oscillators (UBOs) in which oscillations are observed in the absence of a metal-ion catalyst. The 1,4-cyclohexandione (CHD) reaction[52] is one such example. In UBO reactions, the one-electron reduction of BrO_2•, normally accomplished by the metal-ion catalyst (see Figure 1.4, (FKN6)), is instead mediated by the organic substrate[53]. Unlike the BZ reaction, the CHD reaction proceeds without significant evolution of gaseous products such as CO_2 and CO[54]. The CHD system, therefore, represents an appealing system to study when the study of oscillations or pattern formation may be hampered by the production of bubbles.

1.3.8.3. Observation of Turing patterns in the CIMA reaction

Turing patterns are not observed in the liquid phase BZ reaction, as the activator and inhibitor species diffuse at similar rates. However, since Turing suggested that stationary patterns could be formed in a chemical system through a reaction-diffusion mechanism, there has been considerable focus

within the non-linear science community on the design of chemical systems that can support Turing patterns.

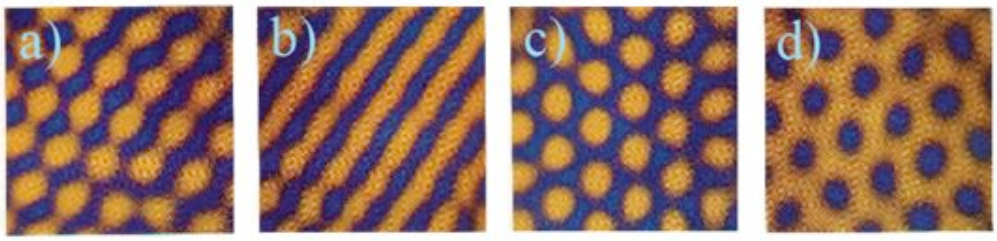

Figure 1.7 b) Striped, c) hexagonal spot and d) honeycomb Turing patterns observed in the CIMA system[55]. The image in a) shows a region where striped patterns are evolving into spots.

Turing patterns were first observed by Patrick De Kepper's group in the chlorite-iodide-malonic acid (CIMA) system[55], (Figure 1.7). Stationary structures were observed in a continuously fed unstirred reactor (CFUR). In a CFUR, the concentrations of reactants in an unstirred medium are controlled by a continuous flow of fresh reactants. The CFUR design consisted of a thin flat piece of polyacrylamide gel in contact, at opposite ends of the strip, with two separate reservoirs of chemical reactants. The reactants of the system are distributed between the two reservoirs in a way that ensures neither reservoir is independently reactive. The concentrations of reactants in each reservoir are maintained by continuous refreshment and stirring. Reactants diffuse from the reservoir into the gel. In this way, the system is maintained far-from-equilibrium. The other intended purpose of the reactor design was to suppress the effect of hydrodynamic instabilities. This ensures that the mobility of the reactants is only dependent upon their diffusivity and not on

convection. This is important as convection can also give rise to spatial patterns similar to Turing structures[56].

Patterns in the CIMA system are visualised through the presence of a starch indicator. Tri-iodide (I_3^-) ions (the activator species) bind to starch forming a blue coloured complex in the reduced state of the system. Oxidation of the tri-iodide results in a pale yellow colour. In De Kepper's experiment, starch was incorporated into the polyacrylamide gel, effectively making it immobile. The unintended consequence of this was to inhibit the diffusivity of the iodide ions as they became bound to the starch indicator. The diffusion of chlorite (ClO_2^-) (the inhibitor species) is not affected in this way, thus the inhibitor diffuses much faster than the activator, satisfying the requirement for Turing patterns. However, the design of the CFUR is limited to the production of Turing patterns in only two-dimensions as the reactant concentrations for Turing patterns are only maintained in a thin layer of the gel medium.

1.4. Microemulsions

1.4.1. Structure and composition of microemulsions

A microemulsion is a thermodynamically stable mixture of water, oil and a surfactant molecule. The surfactant molecule provides a stabilising interface between two otherwise immiscible phases[57]. It is the thermodynamic stability of microemulsions that distinguishes them from a normal emulsion[58]; mixtures of oil and water are possible (an emulsion), however, such mixtures are unstable and will gradually separate into two phases. Microemulsions, on the

other hand, represent an energetically favourable configuration of the water, oil and surfactant constituents. Another distinguishing feature is the transparency of microemulsions. Microemulsions consist of sub-microscopic structures, and as such do not significantly scatter light. Macroemulsions, on the other hand, are opaque, as they consist of larger particles that scatter light much more efficiently.

1.4.2. AOT/water/oil microemulsions

The water-in-oil bis(2-ethylhexyl) sulfosuccinate (AOT) microemulsion is one of the most-characterised microemulsion systems[59,60]. AOT forms microemulsions with a range of non-polar solvents including octane, decane and cyclohexane. The octane/AOT/water microemulsion was the system studied in this work. The AOT system is of particular interest due to its ability to solubilise large amounts of water without the need for a co-surfactant[59]. The surfactant molecule, AOT (Figure 1.8) has a polar, negatively charged head group, and two long, hydrophobic tails.

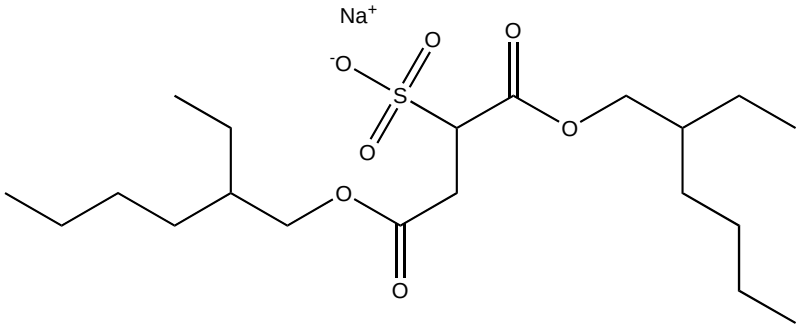

Figure 1.8 Structure of sodium bis(2-ethylhexyl) sulfosuccinate (AOT).

1.4.2.1. Composition of the AOT microemulsion

The parameters that define the relative amounts of water, oil and surfactant in a microemulsion are: the droplet volume fraction, ϕ_d, the water volume fraction, ϕ_w, and the water-to-surfactant molar ratio, ω, given by Equations 1.3, 1.4 and 1.5 respectively, where V_{AOT}, V_{water} and V_{oil} refer to the volumes of AOT, water and octane present in the microemulsion respectively. Using Equation 1.6, the droplet volume fraction of the AOT/octane/water microemulsion can be calculated[61] from the water volume fraction and the water-to-surfactant ratio, ω.

$$\phi_d = \frac{V_{AOT} + V_{water}}{V_{AOT} + V_{water} + V_{oil}} \quad \textbf{(1.3)}$$

$$\phi_w = \frac{V_{water}}{V_{AOT} + V_{water} + V_{oil}} \quad \textbf{(1.4)}$$

$$\omega = \frac{[H_2O]}{[AOT]} \quad \textbf{(1.5)}$$

$$\phi_d \approx \phi_w\left(1 + \frac{21.6}{\omega}\right) \quad \textbf{(1.6)}$$

1.4.2.2. Physical structure of the AOT microemulsion

A variety of structures are formed depending upon the composition of the microemulsion including: spherical oil droplets dispersed in bulk water (micelles), spherical water droplets dispersed in bulk oil (reverse micelles, Figure 1.9) and bicontinuous structures, Figure 1.10 c).

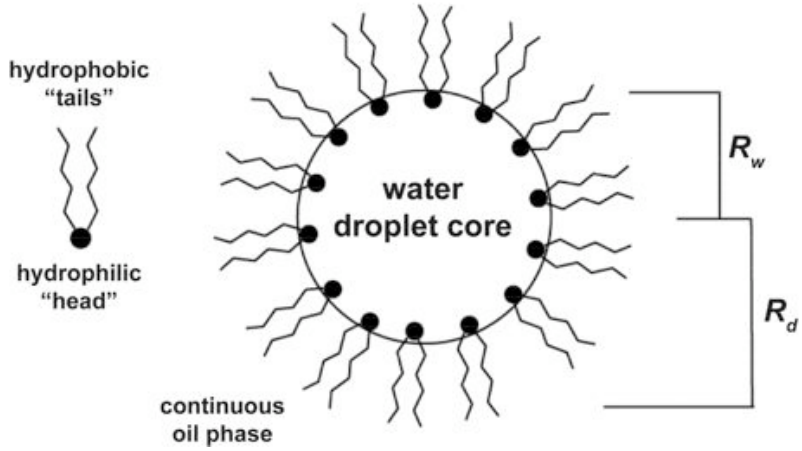

Figure 1.9 Schematic diagram of a reverse micelle formed in the AOT/water/octane microemulsion system. A monolayer of surfactant molecules is arranged around the water droplet core, with the polar head groups of the surfactant molecules adjacent to the droplet core, and the hydrophobic tail groups trailing in the octane continuous phase. R_w is the radius of the water droplet core, whilst R_d is the radius of the micelle as a whole.

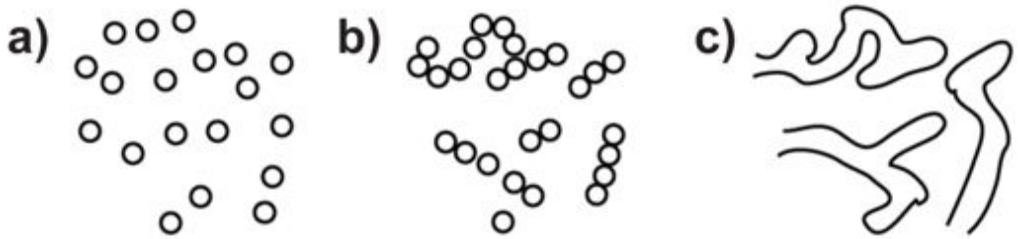

Figure 1.10 Schematic representation of the percolation of individual micelles in a) to form clusters of droplets, b). As the droplet volume fraction is increased, bicontinuous water channels are formed, c).

At values of ϕ_d below a critical value, the AOT system is one of a number of microemulsion systems able to stabilise the formation of water droplets in a continuous octane organic phase (reverse micelles), via formation of a cage-like monolayer of surfactant molecules around a spherical water droplet core, (Figure 1.9).

The ratio ω determines the approximate radius, R_w, of the water droplet core[61], (Equation 1.7), where R_w is in nanometres. The droplet radius can be measured experimentally using neutron or light scattering methods[62], as well as pulsed-gradient spin echo (PGSE) NMR experiment[63].

$$R_w \approx 0.17\omega \qquad \textbf{(1.7)}$$

AOT microemulsions are able to solubilise large amounts of water, through the formation of reverse micelles, with values of ω_{max} in excess of 70, depending upon the identity of the continuous oil phase[59]. Microemulsions with higher water solubilisation potential exist, such as the cetyltrimethylammonium bromide (CTAB) system, however, in this case, a co-surfactant is required[62].

1.4.2.3. Properties of the water pool within AOT reverse micelles

The properties of water molecules are altered by their location within the AOT microemulsion structure. IR spectroscopy has been used to observe differences in the OH stretching vibration at different droplet sizes and surfactant concentrations[64,65]. These were attributed to the presence of water molecules in one of three environments, namely; bound water, associated with the polar head group of the AOT molecule, free water that behaves more like the bulk solvent, and water trapped between the tails of the surfactant molecule. Calorimetric methods have also shown the existence of different water environments in the AOT microemulsion[66]. Levinger *et al*[67] have investigated the solvation dynamics using time resolved fluorescence spectroscopy. At low values of ω (ω < 5) they found that the water pool was

highly immobile, with a greater proportion of the water pool accounted for by the bound environments. As the droplet size was increased the mobility of the water pool becomes less restricted and its properties become more bulk-like. However, even at larger droplet sizes solvation dynamics were still slower than in bulk water, indicative of the influence of the micellar interface.

The properties of the water pool in AOT reverse micelles systems has also been studied through the use of molecular probes[68]. ^{23}Na- and ^{1}H-NMR measurements performed by Nowak *et al*[69] also show that the mobility of the water pool in small droplets is restricted. By relating the longitudinal relaxation time T_1 of the water droplet to its rotational correlation time *i.e.* the tumbling rate of the droplet, they were able to show that presence of sodium counter ions within the droplet also restrict the mobility of water molecules.

^{51}V-NMR studies have been used to monitor the coordination environment of a vanadium probe molecule ($[V_{10}O_{28}]^{6-}$) in AOT reverse micelles. The ^{51}V chemical shift was measured as a function of ω. For larger droplet sizes the chemical shift values observed were found to be closer to the values obtained for the complex in bulk solution. However, it was shown that even in large micelles (ω > 10), the properties of micellar water are still different to that of bulk water. This result was based on the hypothesis that the probe molecule resides within the water droplet core due to its hydrophilicity and Coulombic repulsion between the negative charge on the probe molecule and negatively charged surfactant headgroups. However, this is not always the case. The location within AOT reverse micelles of another vanadium probe molecule

([VO_2dipic]$^-$) was investigated using NOESY NMR experiments[70]. Counter-intuitively, NOE experiments were able to show that the negatively charged and polar complex resides within the hydrophobic part of the micellar interface. The ability of probe molecules to investigate the water environment of reverse micelles, then, depends upon the location of the probe molecule within the micelle. Rack *et al*[71] have used time resolved emission spectroscopy to probe the location of $[Ru(bpy)_3]^{2+}$ in AOT reverse micelle systems. A single emission maximum was observed for values of ω up to ω = 15, showing the water environment surrounding $[Ru(bpy)_3]^{2+}$ is unchanged with increasing water content. This was attributed to localisation of $[Ru(bpy)_3]^{2+}$ at the water-surfactant interface.

1.4.2.4. Percolation of water droplets

As the droplet volume fraction is increased, clusters of water droplets begin to aggregate. The percolation threshold is defined as the point where the first infinite cluster of droplets is formed[72]. The critical value (ϕ_{cr}) of ϕ_d at which percolation occurs, is dependent upon the exact composition of the microemulsion and also on temperature[73]. Values of ϕ_{cr} can range from around 0.1 to 0.7. When the volume fraction is much greater than the percolation threshold, bicontinuous structures are formed. Clusters of droplets amalgamate further to form water channels that span the entire microemulsion, Figure 1.10 c). The onset of percolation can be observed through changes of the conductivity[74] and viscosity[75] as the droplet volume fraction is increased beyond ϕ_{cr}. NMR self-diffusion measurements[60,76] have also been used to probe the structure of the microemulsion. These techniques

are all able to show that the mobility of the water phase is significantly increased above the droplet percolation threshold.

1.4.3. Uses of microemulsions

A wide variety of microemulsion systems exist, with neutral, anion, cationic and even zwitterionic surfactant molecules, with each system possessing unique properties and characteristics. Applications and uses are just as diverse. One potential application of microemulsion systems is in the field of enhanced oil recovery (EOR). Microemulsions could be used to break down the high interfacial tension between crude oil deposits in underground salt-water reservoirs, allowing the recovery of residual oil deposits[77]. Microemulsions are also used as lubricants during machining processes, where the increased thermal conductivity of the water pool allows greater heat transfer compared with purely oil based lubricants[78]. Another important application of microemulsion systems is that of drug delivery. Microemulsions are able to solubilise a wide variety of both hydrophilic and hydrophobic drugs. They are then also able to assist in targeted delivery of the pharmaceutical, *i.e.* to transfer the active component of the drug to the target area in the body. Other advantages can include reduced toxicity, enhanced uptake and the ability to control the rate of release of the drug into the blood[77].

1.4.3.1. Chemical reactions in microemulsions

Microemulsions provide a controllable microenvironment in which to perform chemical reactions[79,80]. Their ability to compartmentalise reactants within the polar water droplet core, and to have a degree of control over the size,

polarity, pH *etc* of the water pool, has spawned interest in the use of microemulsions as "nano-reactors". A review by Maitra[59] presents a table of twenty-eight reactions studied in reverse micelle systems, varying from polymerisation reactions to ester hydrolysis. Interest in microemulsions also arises due to their ability to model biological systems. The ability to solubilise both polar and non-polar species has been used to study enzymatic reactions[81]. Microemulsion and reverse micelle systems are also able to mimic and model biological membranes[82]. The presence of a polar water droplet core separated from a non-polar continuous oil phase by an ambiphillic interface makes micelle systems similar, in some respects, to cellular systems found in nature. The synthesis of nanoparticles inside reverse micelles is also a growing area, with the well-defined structure of the reverse micelle environment being exploited to template the formation of the nanoparticles. By controlling the size of the reverse micelles, the growth and size of nanoparticles can be confined to the interior of the reverse micelle[83]. Nanoparticles of Pt, Pd, Rh and Ir were prepared with high monodispersity by reduction of an appropriate metal salt in reversed micelle systems[84].

1.5. The BZ-AOT reaction

1.5.1. Introduction to the BZ-AOT reaction

The first instance of the incorporation of the BZ reaction into an AOT reverse micelle system was reported in 1988[85]. The motivation for this study was the coupling of an oscillating chemical reaction that displays spatial and temporal ordering relevant to biological systems with a reaction medium also

possessing biological relevance. Oscillatory behaviour was observed in this case in the manganese-catalysed reaction. Since then, the BZ-AOT reaction has been studied in great detail by Vanag *et al*[61], concentrating in particular on the formation of non-equilibrium chemical patterns.

1.5.2. Tunability of the BZ-AOT system

Encompassing the BZ reaction into the AOT microemulsion adds a further degree of complexity to the system. The aqueous reactants of the BZ reaction are now partitioned within the discontinuous pseudo-aqueous phase (discrete water droplets) of the microemulsion. As was seen in Section 1.4.2.2, the size and concentration of these droplets can be controlled and thus the structure of the reaction medium can be "tuned"[86]. The droplets themselves are dispersed in a sea of oil. Transport of species between droplets can occur via two mechanisms. Firstly, mass exchange can occur when droplets coalesce during droplet-droplet collisions[87]. Clearly, the frequency of collisions and, thus, the rate of mass exchange are then dependent upon the concentration of droplets. Secondly, transport of reactants between droplets may occur via diffusion of the reactants through the continuous oil phase. This process will depend upon the solubility of the reactant in the oil phase. Species that are charged or polar, *e.g.* bromate, malonic acid and metal ions, will reside predominantly inside the water droplets. As such, their mobility will largely depend upon the diffusivity of the droplets through the continuous phase. However, non-polar species such as molecular bromine and the BrO_2• radical will be soluble in the oil phase. The diffusivity of species soluble in the oil phase is significantly greater than that of water droplet; the diffusion

coefficient, *D*, of a small molecule through the continuous oil phase is of the order of 10^{-5} cm^2 s^{-1}, compared to around 10^{-7} cm^2 s^{-1} for the diffusivity of a droplet[60]. This is a key factor with respect to pattern formation in the BZ-AOT system, and specifically the formation of Turing patterns, which require the diffusivities of activating and inhibiting species to differ by at least an order of magnitude.

1.5.2.1. Turing patterns in the BZ-AOT reaction

The BZ-AOT system does not suffer from the same limitations as the CIMA/CDIMA system. The BZ-AOT system is a *closed* system in which the reactants are not continuously replenished, as is the case with the *open* CIMA/CDIMA reaction. Additionally, in the CIMA/CDIMA reaction the reactant concentrations required for the formation of Turing patterns are only maintained in a thin layer of the polyacrylamide gel. This is not the case in the BZ-AOT system, where the required concentrations, and thus the potential for Turing patterns, can exist throughout the entire reaction medium. However, as the reactants are not replenished, the patterns observed only have a finite lifetime, as the system eventually reaches equilibrium. Examples of Turing structures observed in the ferroin-catalysed BZ-AOT system[86] are shown in Figure 1.11. Structurally, these Turing patterns are similar to those seen in the CIMA reaction. The patterns in the BZ-AOT system were observed in a thin layer (approximately 90 μm) of the reaction sandwiched between two flat glass plates. The ferroin-catalysed reaction is illuminated through a 510 nm interference filter and visualised using a microscope. Turing patterns are also observed in the $Ru(bpy)_3$ catalysed reaction[88].

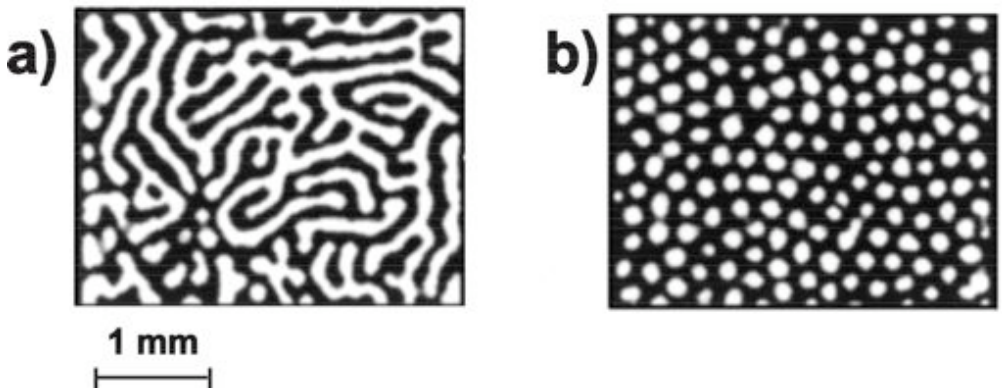

Figure 1.11 a) Labyrinth and b) hexagonal spot stationary Turing patterns observed in the ferroin-catalysed BZ-AOT system[86].

As was discussed in Section 1.5.2, it is the partitioning of water-soluble and oil-soluble reactants between the pseudo-aqueous phase and the continuous oil phase that accounts for the different diffusion rates of the activator and inhibitor species, and thus allows for the formation of Turing patterns in the BZ-AOT system. The water-soluble $HBrO_2$ (activator) diffuses around 100 times more slowly than the oil-soluble Br_2, which is readily converted to bromide ions that inhibit autocatalysis[60]. Therefore, Turing patterns in the BZ-AOT system are only observed in microemulsion samples below the droplet percolation threshold, $\phi_d < 0.5$. Above the percolation threshold, bicontinuous water channels begin to form and the diffusion coefficients of the activator and inhibitor species become comparable.

1.5.3. Pattern formation in the BZ-AOT reaction

As well as Turing patterns, the BZ-AOT reaction plays host to a whole range of patterns (Figure 1.12), including several that are unique to the system. The rich variety of non-equilibrium patterns observed in the BZ-AOT system

comes as a consequence of the tunability of the AOT microemulsion. The majority of the published literature on the BZ-AOT system comes from the Epstein group at Brandeis University, and a number of reviews exist that attempt to catalogue the wealth of different patterns observed in the system[61,89-91].

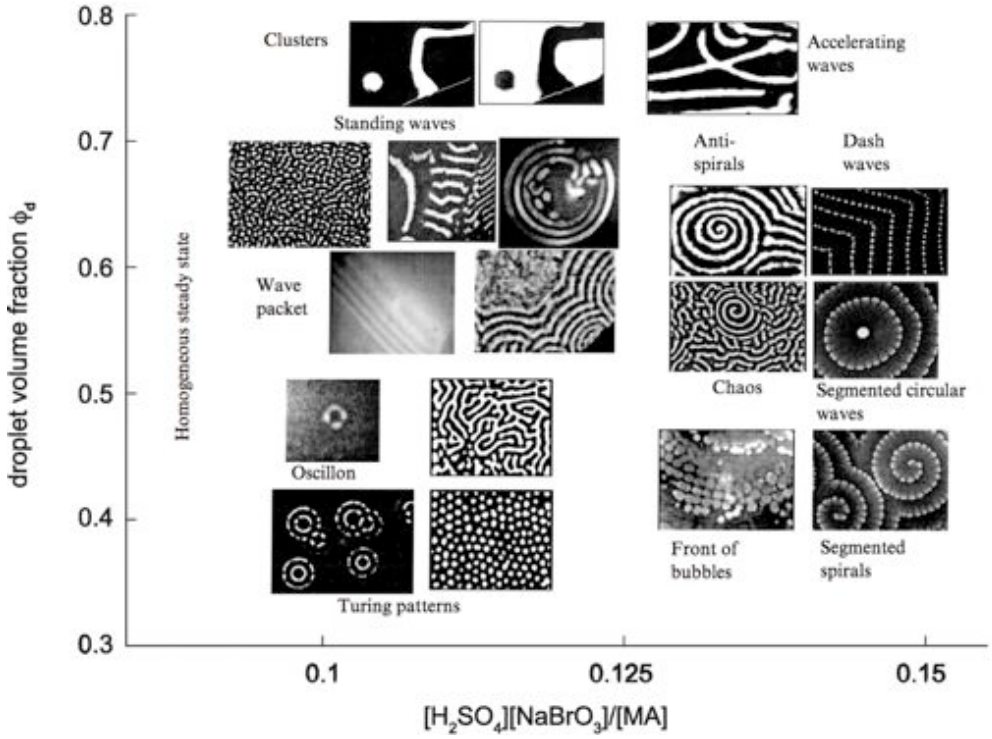

Figure 1.12 Overview of the range of patterns observed in the BZ-AOT system, showing how pattern selection is affected by the structure of the microemulsion and concentration of the BZ reactants.

1.5.3.1. Dash waves, segmented waves and segmented spirals

Segmented waves are also observed, where travelling wave fronts develop periodically spaced breaks. As the wave front breaks, the newly formed segments continue to propagate and grow, before segmenting again. This segmentation leads to propagating fronts of dash waves[92]. Dash waves have

been observed in the ferroin-catalysed system and the bathoferroin-catalysed system.

When dash waves interact with spiral travelling waves, the formation of segmented spirals can be observed[93]. Segmented spirals have been observed in the bathoferroin-catalysed reaction, and are only formed through the interaction of non-segmented spirals with dash waves. Interestingly, dash waves are only observed in reactions performed using freshly prepared microemulsions. This is believed to be due to a bimodal distribution of droplet sizes in freshly prepared microemulsion samples. Older samples contain a more monodisperse distribution of droplet sizes, and do not display the formation of dash waves. The formation of dash waves, therefore, depends on the interaction between two sub-systems of the reaction. The lifetime of dash wave patterns can be extended through the addition of polyethylene oxide (PEO) to the microemulsion[94]. Dynamic light scattering methods have shown that PEO stabilises the bimodal droplet size distribution. Dash waves in the bathoferroin-catalysed reaction were only observed for 2-3 hours in the unstabilised system, whereas they were still observable after 12 hours in the PEO stabilised microemulsion.

1.5.3.2. Inwardly rotating spiral waves

Target patterns and spiral waves are commonly observed in the aqueous BZ reaction. They are also observed in the BZ-AOT system. However, the BZ-AOT reaction is also able to support the formation of so-called anti-pacemaker and anti-spiral patterns. Anti-pacemakers are analogous to target patterns, but the waves move inwardly towards the pacemaker site. Likewise, anti-

spirals rotate inwardly towards their centre. Anti-pacemakers and anti-spirals have been found to coexist in the ferroin-catalysed BZ-AOT reaction[95]. Below the percolation threshold of the microemulsion, normal outwardly propagating patterns are seen, above the percolation threshold the inwardly propagating patterns are observed. The appearance of inwardly propagating waves is related to the appearance of accelerating wave fronts, which are also only observed above the percolation threshold.

1.5.3.3. The $Ru(bpy)_3$-catalysed BZ-AOT reaction

The BZ-AOT reaction catalysed by $Ru(bpy)_3$ plays host to another pattern type not seen with other catalyst systems. Black spot Turing patterns were observed in the $Ru(bpy)_3$ catalysed reaction performed in a surfactant rich (ω = 9) microemulsion, at high concentration of $[NaBrO_3]$[96]. Normal Turing patterns were observed at higher water-to-surfactant ratio (ω = 15) and at lower concentration of $NaBrO_3$ ($[NaBrO_3] \leq 0.24$). The "black spots" refer to regions with a high concentration of the reduced form of the catalyst, $[Ru(bpy)_3]^{2+}$. This is the inverse of normal Turing patterns, which consist of "white spots" of the oxidised form of the catalyst. The black spot patterns are thought to arise from the increased sensitivity of the system to dust particles at the high bromate concentration employed.

The effect of temperature on the $Ru(bpy)_3$-catalysed reaction has also been studied[97]. Transitions between pattern types were observed as the temperature was increased during the reaction. At lower temperatures (15 – 30 ºC), stationary spot Turing patterns were observed. As the temperature was increased these evolved into striped Turing patterns. At 35 ºC a transition

to oscillatory Turing patterns was seen, where the position of Turing spots is oscillatory with time. As the temperature was increased further (50 ºC), the $Ru(bpy)_3$ catalyst became predominantly oxidised, with stationary spots of the reduced state of the catalyst. At this point reduction waves were also seen *i.e.* propagating wave fronts of the reduced form of the catalyst (as opposed to oxidation fronts more typically seen). The transitional behaviour of the system with temperature was attributed to structural changes in the microemulsion, inferred through measurements of the conductivity of the system, rather than any change in the kinetics of the BZ chemistry.

1.5.3.4. Effect of catalyst choice on pattern selection in the BZ-AOT system

As shown in Figure 1.12, the BZ-AOT system supports a rich variety of pattern types, many unique to the BZ-AOT system. As well as this, a number of pattern types have only been observed when a particular catalyst is employed. Stationary Turing patterns, for instance, have been observed in both the ferroin- and $Ru(bpy)_3$-catalysed BZ-AOT reactions, however, they have not been observed in the bathoferroin-catalysed system. The bathoferroin-catalysed system itself has been shown to support the formation of jumping, bubble and rotating waves[98]. These discontinuously propagating waves have not been observed using other catalyst systems, or in any other experimental reaction-diffusion system.

1.6. Introduction to NMR

Nuclear magnetic resonance (NMR) is an incredibly powerful technique with a variety of uses across a range of scientific disciplines. In chemistry and

biology it is a useful tool for the determination of molecular structures, both in its own right and also as a compliment to other techniques. It is also possible to measure transport properties such as flow and diffusion using NMR. In this study, the application of NMR is focussed on two main aspects. Firstly, NMR is applied to characterise and probe the structure of the BZ-AOT microemulsion system. Secondly, the nuclear magnetic resonance imaging (MRI) technique is applied to visualise pattern formation in the BZ-AOT system. An introduction to magnetic resonance is presented here and the reader can find further details elsewhere[99-105].

1.6.1. Basic principles of NMR

1.6.1.1. Nuclear spin

The property of nuclear spin is the basis of nuclear magnetic resonance (NMR) and magnetic resonance imaging (MRI). To acquire an NMR signal, the nucleus being probed must have nuclear angular momentum and hence a non-zero net spin value. Unpaired nucleons (protons and neutrons) in a nucleus have a spin of ½. The total nuclear spin (I) is the sum of individual spin contributions from unpaired nucleons. In the hydrogen (^{1}H) nucleus, the single unpaired proton has a spin of ½ and the total nuclear spin is ½. The deuterium (^{2}H) nucleus has an unpaired proton and an unpaired neutron, each contributing ½ nuclear spin, for a total nuclear spin of 1. The most studied case is that of the hydrogen nucleus because it has a high natural abundance (99.985%). ^{1}H-NMR also has a high sensitivity due to the high gyromagnetic ratio of the ^{1}H nucleus (γ = 267.5 × 10^6 rad s^{-1} T^{-1}). Compare

this to the ^{13}C nucleus, which has a smaller gyromagnetic ratio ($\gamma = 67.3 \times 10^6$ rad s^{-1} T^{-1}) and a lower natural abundance (1.11%). ^{13}C-NMR is, therefore, less sensitive than ^{1}H-NMR.

A nucleus with angular momentum has a number of degenerate spin states equal to 2I + 1. The ^{1}H nucleus has I = ½, thus there are two states (±½). Nuclei possessing non-zero angular momentum have an associated magnetic moment, *μ.*

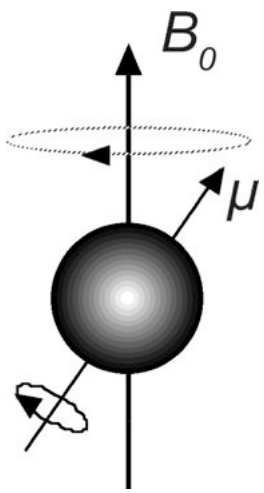

Figure 1.13 Schematic diagram of a precessing nucleus, showing the direction of the B_0 static magnetic field and the magnetic moment *μ*. In this case the nucleus is aligned with the static magnetic field (spin - up)

When a nucleus possessing nuclear spin is subject to a static magnetic field (B_0), the nuclear spin states lose their degeneracy. In the simplest case where I = ½, the two non-degenerate states are designated *spin up* (I = ½), where the spins are aligned parallel with the static magnetic field, and *spin down* (I = -½), where spins are aligned anti-parallel. The magnetic field also imposes a turning force (torque) on the magnetic moment of the nucleus, causing it to

precess (rotate), Figure 1.13. The nucleus will precess about the B_0 magnetic field at a rate determined by the strength of the magnetic field and the gyromagnetic ratio (γ) associated with the nucleus in question. The rate of precession is known as the *Larmor Frequency*, given the symbol ω in angular units of radians s^{-1} or ν in Hertz, Equations 1.8 and 1.9.

$$\omega = \gamma B_0 \qquad \textbf{(1.8)}$$

$$\nu = \frac{\gamma B_0}{2\pi} \qquad \textbf{(1.9)}$$

There is a Boltzmann distribution of nuclei between spin states given by Equation 1.10.

$$\frac{N_{1/2}}{N_{-1/2}} = e^{\Delta E / k_b T} \qquad \textbf{(1.10)}$$

$N_{1/2}$ and $N_{-1/2}$ are the populations of spin up and spin down states respectively, ΔE is the energy difference between the two states, k_b is the Boltzmann constant and T is the temperature. The spin up state is slightly lower in energy than the spin down state, thus there is a slightly larger population of spin up nuclei. The energy level diagram for a spin system with two possible states, spin up (α) and spin down (β), in a static magnetic field, B_0, is shown in Figure 1.14.

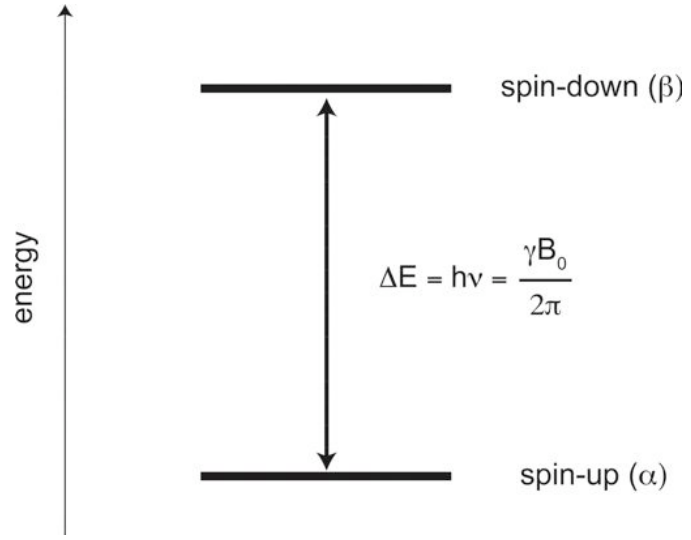

Figure 1.14 Energy level diagram for a nucleus with spin quantum number I = ½ in a static magnetic field. The spin-up state (α) is lower in energy than the spin-down state (β).

At thermal equilibrium, the spin-up state is slightly favoured; therefore, summing up the contribution of individual spins for an ensemble of spins gives an overall macroscopic magnetisation vector (M_0) that is aligned along the direction of the static magnetic field (B_0), (Figure 1.15 a)). Transitions between the spin up and spin down states can be brought about by applying a pulse of radiofrequency radiation with energy equal to ΔE, which corresponds to the Larmor frequency. The radiofrequency (r.f.) pulse also applies a torque on the magnetic moment and acts to redistribute the populations of the spin states and hence the direction of the macroscopic magnetisation vector. The duration, τ, and amplitude, B_1, of the r.f. pulse determines the tip angle, θ, Equation 1.11.

$$\theta = 2\pi\gamma\tau B_1 \qquad \textbf{(1.11)}$$

By convention, the direction of the static magnetic field is defined as the *z*-axis. A 90° pulse will equalise the population of spin up and spin down states and bring the magnetisation onto the *x/y* (transverse) plane with phase coherence *i.e.* spins precess with synchronisation, producing a net magnetisation in the transverse plane, (Figure 1.15 b)). A 180° pulse will put the magnetisation vector onto the –*z*–axis (Figure 1.15 c)). When there is a transverse component of the magnetisation vector, its precession induces an oscillating voltage in the same r.f. coils that provide the excitation pulse. This voltage is detected and forms the NMR signal. The amplitude of the induced voltage decays as this happens so the NMR signal is often described as a free induction decay or FID. Through relaxation processes, described below, the magnetisation vector eventually returns to its equilibrium position.

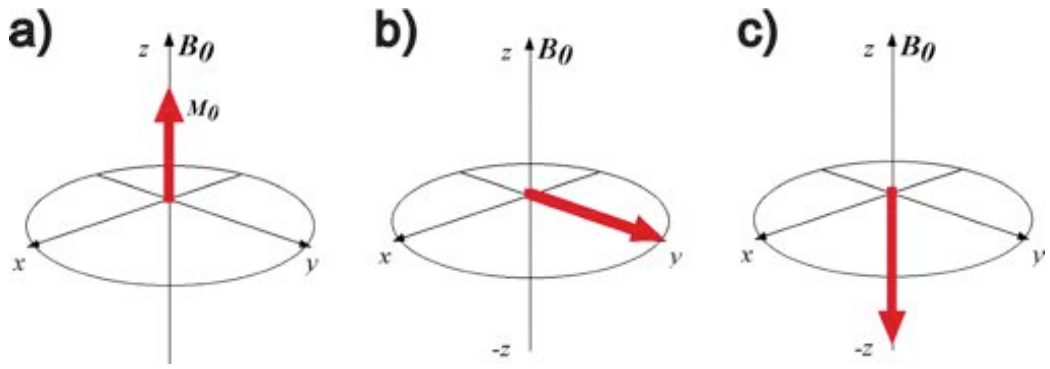

Figure 1.15 Diagram showing the position of the macroscopic magnetisation vector in a static magnetic field at equilibrium a), after a 90°x r.f. pulse b), and after a 180° r.f pulse c).

The vector model of NMR presented here serves as a convenient semi-classical description of the basic principles involved. However, it is limited in

its ability to describe more complex situations and pulse sequences. For example, the coupling of multiple spin systems (which forms the basis of 2-D correlation spectroscopy (COSY) experiments and J-coupling evolution in high resolution spectroscopy) is not adequately described by the vector model and requires a quantum mechanical treatment to be rationalised.

1.6.1.2. Relaxation

After an excitation pulse, the system will return to thermal equilibrium via two main relaxation processes, T_1 relaxation and T_2 relaxation. T_1 (spin-lattice) relaxation is the process by which the magnetisation vector returns to the equilibrium value (M_0), aligned along the B_0 axis. Neighbouring spins generate fluctuating weak local magnetic fields. Fluctuations at the Larmor frequency bring about transitions between spin states, eventually returning the system to equilibrium. The most important contribution to spin-lattice relaxation is dipolar coupling, *i.e.* a "through space" interaction between two nuclei. The magnitude of dipolar coupling is highly dependent upon the proximity of the two nuclei, and is proportional to $1/r^6$, where r is the distance between the two nuclei. It is also modulated by the rotational correlation time, τ_c, of the nuclei. The rotational correlation time is a measure of how fast a nucleus tumbles, shorter correlation times corresponding to rapid tumbling. The maximum relaxation rate occurs when the tumbling rate (τ_c^{-1}) matches the Larmor frequency of the nuclei, *i.e.* $\omega\tau_c = 1$.

At thermal equilibrium a 90° pulse will saturate the spin system equalising the population of spin-up and spin-down states. A net longitudinal magnetisation vector no longer exists, *i.e.* $M_Z = 0$. The recovery of longitudinal magnetisation

from M_Z = 0, with respect to time (t), is exponential in behaviour, (Equation 1.12), with T_1 being the time constant for this process.

$$M_z = M_0(1 - e^{-t/T_1}) \qquad \textbf{(1.12)}$$

As well as bringing the magnetisation vector into the transverse plane, a 90° excitation pulse also aligns individual spins along the *x* or *y* axes depending upon the direction of the pulse. Initially the spins will have phase coherence, *i.e.* all spins are aligned. This is maintained as long as each spin experiences the same magnetic field. However, molecular interactions will cause slight variations in the precessional rates of individual spins, leading to de-phasing of the macroscopic magnetic vector in the *x/y* plane. The magnetisation in the transverse plane, $M_{x/y}$, decays exponentially with time, *t,* according to Equation 1.13, where M_0 is the initial transverse magnetisation at $t = 0$.

$$M_{x/y} = M_0 e^{-t/T_2} \qquad \textbf{(1.13)}$$

T_2 is the time constant for transverse (spin-spin) relaxation, and is related to intrinsic properties of the spin system. Spin-spin relaxation is also affected by inhomogeneities in the static magnetic field and has the time constant $T_{2(\Delta B_0)}$ associated with it. The effects of magnetic field inhomogeneities can be minimised by shimming, a process where current is applied through a set of shim coils that make fine adjustments to the static B_0 magnetic field so making

it homogeneous. Both processes contribute to the observed decay of transverse magnetisation, T_2^*, Equation 1.14.

$$\frac{1}{T_2^*} = \frac{1}{T_2} + \frac{1}{T_{2(\Delta B_0)}} \qquad \textbf{(1.14)}$$

1.6.1.3. The Fourier transformation

The FID is acquired in the form of a time dependent oscillating voltage, induced in the r.f. receiver. The FID may contain a range of frequencies. In NMR spectroscopy these frequencies correspond to different chemical shifts of nuclei in different chemical environments. In MRI, as will be seen in Section 1.8, the spread of frequencies contains spatial information. In order to reconstruct a spectrum or an image, the time domain data (FID), is converted to the frequency domain representation through the Fourier transformation[106].

1.7. NMR pulse sequences

Pulse sequences are sets of instructions used to control and coordinate the various hardware components of the spectrometer (the r.f. amplifier and coils, gradient amplifiers, receiver coils etc). A pulse sequence is stored as a computer program file, and describes a sequence of r.f. and/or gradient pulses and the time delays between them required to acquire an NMR signal. Pulse sequences vary in complexity depending upon their application; a one-dimensional NMR spectrum may be acquired with a single r.f. pulse. A three-dimensional imaging pulse sequence will contain a whole series of r.f. pulses and gradient pulses with various delays between them.

1.7.1.1. Pulse-acquire

The pulse-acquire sequence is the simplest pulse sequence, consisting of a single, *e.g.* 90°, excitation, followed by acquisition of the NMR signal. A schematic diagram of the pulse sequence is shown in Figure 1.16. The pulse acquire sequence can be used to acquire one-dimensional NMR spectra. Typically, the pulse sequence is repeated multiple times with the phase of the excitation pulse cycled. Phase cycling allows for the removal of certain artefacts that may be present due to imperfections in the electronics of the spectrometer hardware. Multiple signal acquisitions also improve the signal-to-noise ratio. Signal adds coherently, so a second repetition doubles the signal, whereas random noise is only increased by a factor of √2. Acquiring a total of four signal acquisitions can therefore, double the signal-to-noise ratio of a single acquisition. The time between successive excitations is the repetition time, T_R. After excitation, magnetisation will return to its equilibrium value by relaxation processes discussed in Section 1.6.1.2. By setting the repetition time to at least 5 × T_1, the system is fully relaxed between successive repetitions. Shorter repetition times result in incomplete relaxation; thus, the steady state magnetisation is reduced, leading to reduced signal intensity. Therefore, for a given number of signal acquisitions, the maximum signal-to-noise ratio can be achieved by having a repetition time of at least 5 × T_1. However, for a given acquisition time, the maximum signal-to-noise ratio may be achieved by performing more signal acquisitions with a shorter repetition time *i.e.* less than 5 × T_1. This is an important consideration when a time-series of experiments is envisaged, as it allows signal-to-noise ratio to be maximised whilst maintaining a sufficiently short acquisition time.

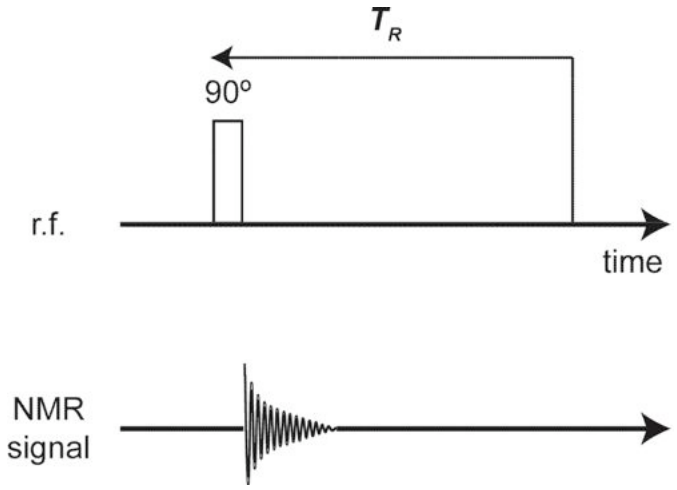

Figure 1.16 Schematic diagram of a pulse acquire pulse sequence. The time between successive 90º pulses is the repetition time T_R. Fourier transformation of the acquired FID results in a one-dimensional NMR spectrum.

1.7.1.2. Inversion recovery

A schematic diagram of the inversion recovery pulse sequence is shown in Figure 1.17. The initial 180° inversion pulse flips the magnetisation vector onto the -*z* axis, (the spin population is inverted). Magnetisation will then return to its equilibrium position via T_1 relaxation processes. After a delay time, τ, a 90° pulse is applied that transfers the magnetisation vector on to the transverse plane and the FID is acquired. The signal intensity depends upon the length of the delay time τ.

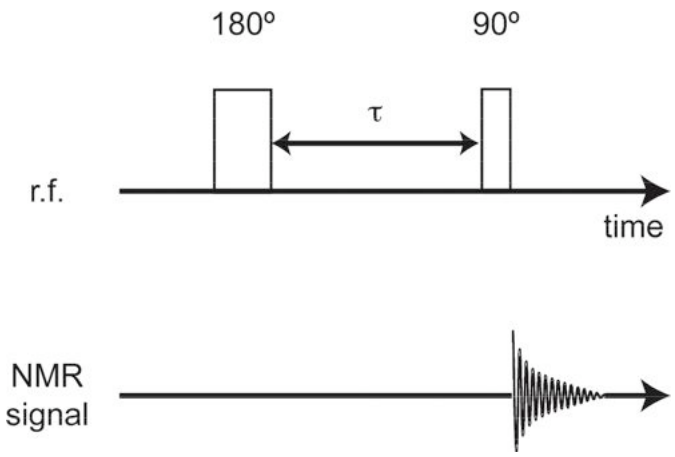

Figure 1.17 Schematic diagram of an inversion recovery pulse sequence, used to measure T_1 relaxation times.

The magnetisation vector goes through a null point at a value of τ given by Equation 1.15.

$$\tau_{null} = \ln 2(T_1) \qquad \textbf{(1.15)}$$

An inversion recovery sequence can be used to determine the T_1 relaxation time of a sample. The pulse sequence is repeated for multiple values of τ. A sequence of one-dimensional NMR spectra is acquired. The peak amplitudes of the resonance of interest are then fitted to Equation 1.16. This is similar to Equation 1.12, however, Equation 1.16 describes the recovery of magnetisation after population inversion. Equation 1.12 describes the recovery of magnetisation after saturation.

$$M_z = M_0(1 - 2e^{-t/T_1}) \qquad \textbf{(1.16)}$$

A typical example of an inversion recovery curve is shown in Figure 1.18. The T_1 relaxation time can also be found by finding the value of τ_{null} and solving Equation 1.15. Inversion recovery can also be used to remove signal contributions from nuclei with a particular value of T_1, by setting τ according to Equation 1.15.

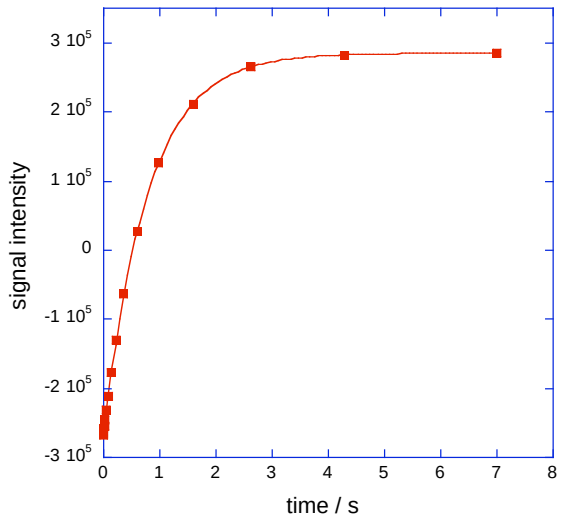

Figure 1.18 Example of an inversion recovery curve fitted to Equation 1.16. The signal intensity goes from its most negative value at *t* = 0 s, through its null point at approximately 0.5 s before becoming fully relaxed after approximately 5 s. The T_1 in this case is approximately 0.8 s.

1.7.1.3. Spin-echo

Figure 1.19 shows a schematic representation of a spin-echo pulse sequence, (sometimes referred to as a Hahn-echo[107]). The pulse sequence starts with a 90° excitation pulse that brings the magnetisation down onto the transverse plane. Initially, all the precessing nuclei have phase coherence, however, T_2

relaxation acts to dephase the spins, with some spins precessing faster and some precessing slower. After a delay, τ, a 180° pulse flips the spins about the transverse plane. The spins now begin to rephase, and after a further delay of τ, phase coherence is fully restored and a spin-echo – or Hahn-echo - is formed. The time between the initial 90° and the top of the echo is called the echo time. A spin-echo pulse sequence can be used to measure the T_2 relaxation time constant of a sample. The pulse sequence is repeated for a series of τ values and the amplitude of the spin-echo is fitted to Equation 1.12 to obtain T_2.

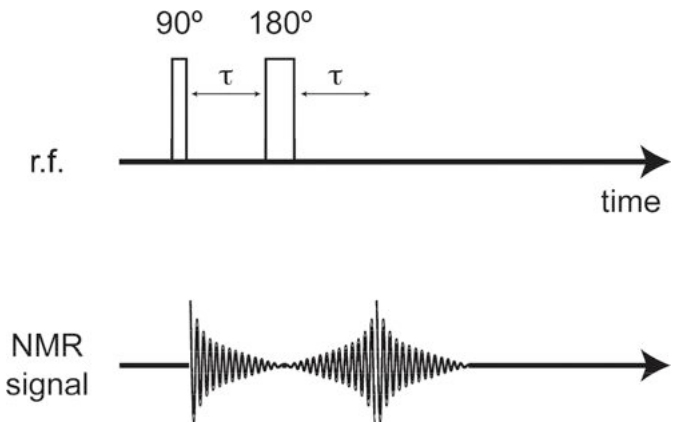

Figure 1.19 Schematic diagram of a Hahn-echo pulse sequence.

1.7.1.4. CPMG

The Hahn-echo pulse sequence is sensitive to inhomogeneities in the magnetic field, whereby if spins diffuse to a region where the B_0 field is different, the 180° pulse does not fully refocus them. In this case it is T_2* that is being measured rather than T_2, *i.e.* the combined intrinsic spin-spin relaxation of the sample and relaxation due to inhomogeneity in the B_0 field (see Equation 1.13). The CPMG (Carr-Purcell-Meiboom-Gill) pulse sequence

(Figure 1.20) is a modification of the Hahn-echo pulse sequence in which multiple refocusing 180° pulses are applied. The refocusing pulses are applied on a timescale where diffusion is limited, which enables the intrinsic T_2 of the sample to be measured as opposed to T_2^*. In a CPMG experiment, the delay time, τ, is held constant (typically 100 ms or less to limit diffusion effects), and the number of echoes, n, before acquisition is varied. The peak amplitude of the echo is plotted and fitted to an exponential decay function (Equation 1.13) to give T_2.

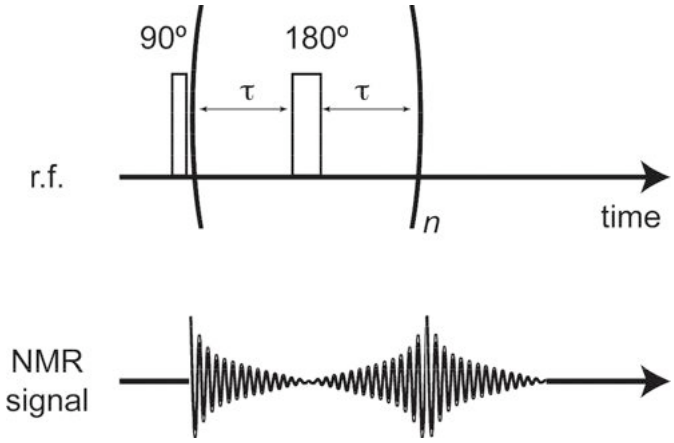

Figure 1.20 Schematic diagram of a CPMG pulse sequence.

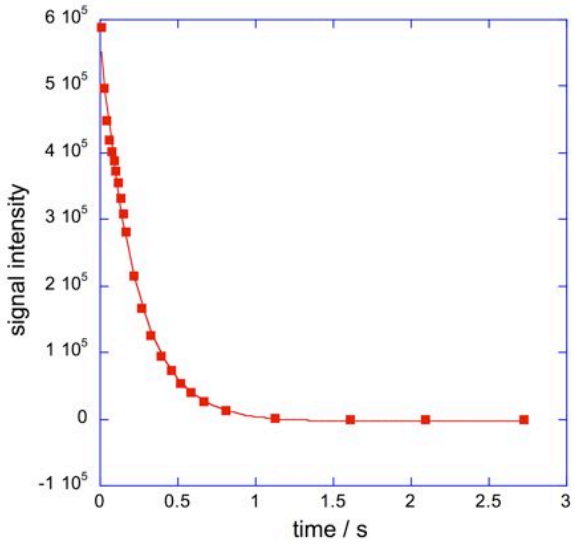

Figure 1.21 Typical example of a T_2 exponential decay curve. The signal intensity has its maximum value at t = 0 where no dephasing has occurred. After approximately 1.5 s, significant dephasing of the transverse magnetisation has occurred resulting in very low signal intensity. The T_2 relaxation time in this case is approximately 250 ms.

1.7.2. The nuclear Overhauser effect.

The nuclear Overhauser effect or NOE is a phenomenon brought about by dipolar coupling between spins in close proximity[108]. This effect can be exploited to acquire information concerning the spatial and conformational arrangement of nuclei within a molecule, and also *between* molecules, *i.e.* intermolecular arrangements. Quantitative analysis of NOE interactions allows inter-nuclear distances to be measured.

1.7.2.1. Principles of the NOE

Longitudinal relaxation was discussed in Section 1.6.1.2, and it has been shown how a 180° pulse can bring about population inversion of a spin system. T_1 relaxation processes then act to restore the system to thermal

equilibrium *i.e.* spins in the slightly higher energy spin-down state relax to the lower energy spin-up state.

In the NOE, magnetisation can be transferred between nuclei through a splitting of energy levels caused by dipole-dipole coupling. The local magnetic field experienced by a nucleus is modulated by the fluctuating magnetic field due to the presence of neighbouring nuclei. Dipole-dipole interactions may arise between nuclei in molecules due to the tumbling of the molecules as a whole, *i.e.* molecular rotation. Intermolecular dipole-dipole interactions can also arise from the translational and rotational motion of molecules.

Coupling between two spins through dipole-dipole interactions results in a more complex energy level diagram. An energy level diagram for two coupled spins, I and S is shown in Figure 1.22. Each spin has two possible states, α and β, which corresponds to spin-up and spin-down respectively for the hydrogen nucleus. The W_1 transitions, of which there are four, correspond to spin-flip of a single nucleus, I or S, which may be brought about, as before, by a suitable r.f. pulse or T_1 relaxation. However, there are also two transitions, W_0 and W_2, that involve simultaneous flip of both spin systems. These are known as cross-relaxation pathways. These cross-relaxation pathways provide a mechanism by which the signal intensity of the I resonance can be enhanced (W_2) or attenuated (W_0) through transfer of magnetisation from spin S.

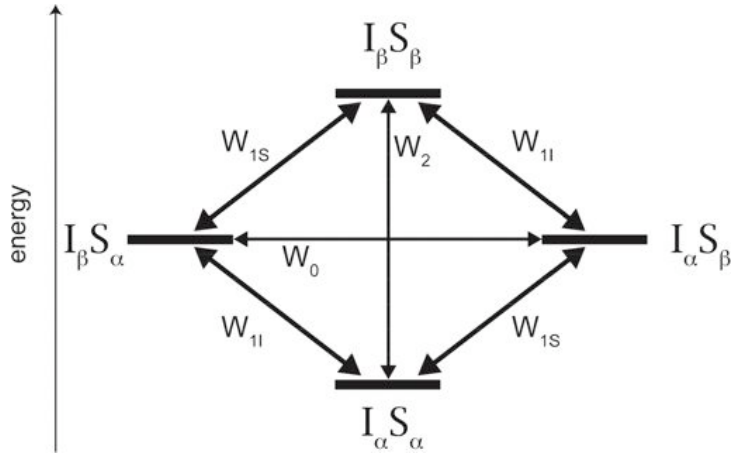

Figure 1.22 Energy level diagram for two coupled spin systems, I and S, each with two possible states, α and β.

The sign of the NOE enhancement is dependent upon which cross-relaxation process dominates. If after saturation of spin S, the W_2 cross-relaxation pathway dominates, magnetisation is transferred from the saturated spin system S to spin system I. This results in an enhancement of the NMR signal from spin I. On the other hand, if the W_0 cross-relaxation pathway dominates after saturation of S, then the equilibrium populations of states $I_\beta S_\alpha$ and $I_\alpha S_\beta$ are restored, and the NMR signal from spin I is attenuated. For rapidly tumbling (short rotational correlation time) molecules, W_2 dominates and positive NOE enhancements are observed. For slowly tumbling (long rotational correlation time) molecules, W_1 dominates and negative NOE enhancements are observed.

1.7.2.2. Measuring inter-nuclear distances using the NOE

NOE enhancements are dependent on dipolar coupling of nuclei and are, therefore, inversely proportional to r^6, where r is the distance between the two nuclei that are coupled. This strong spatial dependence means that

enhancements are only observed when the inter-nuclear distance is around 5 Å or less. NOE spectroscopy (NOESY) can therefore be used to provide qualitative structural information, *i.e.* two nuclei are within 5 Å of each other. However, under certain conditions, it is possible to further quantify the inter-nuclear distance by measuring the initial cross-relaxation rate, σ_{IS}. Typically, the cross-relaxation rate between two nuclei is measured and compared to a reference cross-relaxation rate of known distance. The unknown inter-nuclear, r_{IS}, distance can then be found using Equation 1.17.

$$\sigma_{IS} = \sigma_{ref} \sqrt[6]{\frac{r_{ref}}{r_{IS}}} \qquad \textbf{(1.17)}$$

The measurement of NOE cross-relaxation rates is typically done by measuring the intensity of NOEs as a function of mixing time, τ_m. The mixing time is the time between saturation of the S signal and subsequent sampling of the I NMR signal. The data points are fitted to an exponential function and the initial build up rate is found by extrapolating the plot down to $\tau_m = 0$. Alternatively, the NOE can be measured for a short value of τ_m. The assumption is then made that the build up rate is linear for short mixing times. At longer mixing times, indirect NOE enhancements, *i.e.* magnetisation transferred from S to I via a third spin system X, will affect the intensity of the direct NOE enhancements.

1.8. Magnetic Resonance Imaging

1.8.1. Introduction to MRI

Magnetic resonance imaging (MRI) enables the position of nuclei to be spatially located using magnetic field gradients. It is thus possible to non-invasively acquire one-, two-, or three-dimensional images of optically opaque systems *e.g.* the human body, as well as non-opaque systems. The MRI technique is extremely versatile and has many applications.

1.8.2. Basic principles of MRI

1.8.2.1. Magnetic field gradients

In magnetic resonance imaging, the magnetic field in the direction of the B_0 field, B_z, is varied by the application of magnetic field gradients. Magnetic field gradients can be applied in the *x, y* and *z* directions. The magnetic field gradient strengths in the *x, y* and *z* directions are given by Equations 1.18 – 1.20.

$$G_x = \frac{dB_z}{dx} \qquad \textbf{(1.18)}$$

$$G_y = \frac{dB_z}{dy} \qquad \textbf{(1.19)}$$

$$G_z = \frac{dB_z}{dz} \qquad \textbf{(1.20)}$$

The precessional frequencies of nuclei are then dependent upon their position along the direction of the magnetic field gradient. Equation 1.8 is thus modified to include the contribution from the magnetic field gradient. Equation

1.21 gives the Larmor frequency of a nucleus at a position, **r**, along a linear magnetic field of strength **G**.

$$\omega(\mathbf{r}) = \gamma(B_0 + \mathbf{Gr}) \qquad \textbf{(1.21)}$$

Figure 1.23 shows the effect of applying a magnetic field gradient along the *x*-direction. In the absence of a magnetic field gradient, the B_z magnetic field is unaffected. With the gradient applied, the B_z field is no longer homogeneous and varies with position along the *x*-axis. At the isocentre of the magnet, *i.e.* where (*x,y,z*) = (*0,0,0*), $B_z = B_0$.

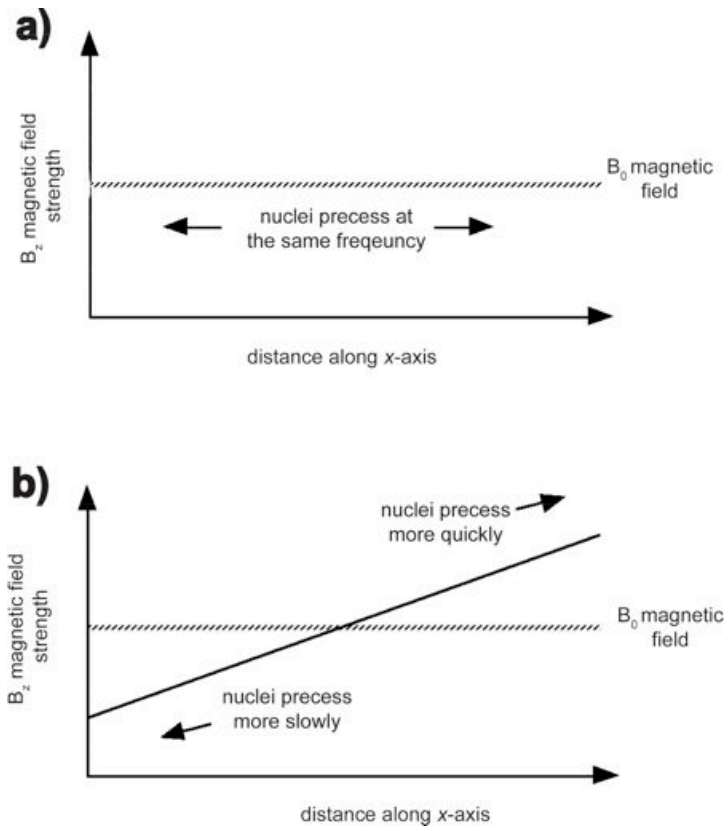

Figure 1.23 a) Variation of the B_z magnetic field with position along the *x*-axis. b) Variation of the B_z magnetic field when a linear magnetic field gradient is applied in the *x*-direction.

1.8.2.2. Frequency encoding

By applying a magnetic field gradient, the precessional frequency of a nucleus becomes dependent upon its position along the applied gradient. This premise, then, forms the basis of a frequency encoding gradient. A constant magnetic field gradient is applied during the course of signal acquisition. The acquired signal is then Fourier transformed, resulting in a frequency domain spectrum. Equation 1.21 relates the position of spins to the frequency. The signal intensity is then proportional to the number of nuclei with a particular frequency, *i.e.* the number of nuclei with a particular position along the frequency encoded gradient. For a one-dimensional imaging experiment where a single frequency encoding gradient is applied along the *x*-axis, the resultant spectrum is a one-dimensional profile of all the spins in the *z*- and *y*-axes projected onto the *x*-axis, Figure 1.24.

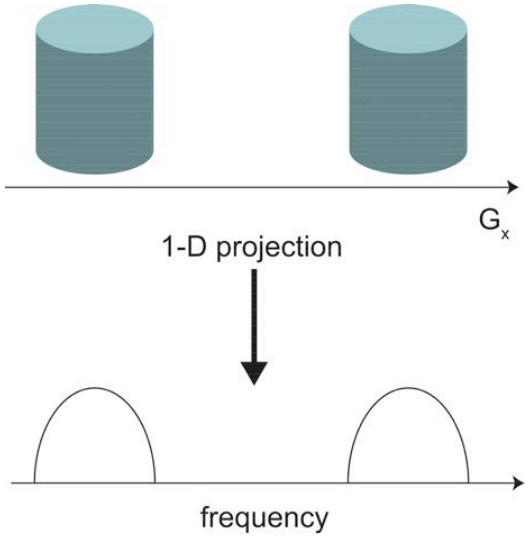

Figure 1.24 Schematic representation of the resultant frequency domain spectrum from a one-dimensional frequency encoded image of two tubes of water. A frequency encoding gradient is applied along the *x*-axis. The spectrum is a projection of all spins in the *z*- and *y*- axes onto the *x*-axis.

1.8.2.3. Phase encoding

In phase encoding a magnetic field gradient is applied for a fixed time interval but switched off prior to signal acquisition. Again, the precessional frequency of nuclei is dependent on their position. When the gradient is switched off, nuclei will again precess at identical frequencies, however their *phase* will now be dependent upon their position. A helix of phase is wound by the application of a phase encoding gradient, Figure 1.25. The pitch of the helix is determined by the strength of the gradient applied and the duration that it is applied for. The wavelength of the helix, λ, is the distance over which a 360° phase shift occurs. This is related to the spatial resolution and field-of-view, (refer to Section 1.8.2.5). Unlike frequency encoding, where a single excitation can produce a 1-D profile, phase encoding requires multiple excitations where the strength of the phase encoding gradient is incremented

for each excitation. Spatial information in the phase encoding direction is encoded in the value of the phase shift.

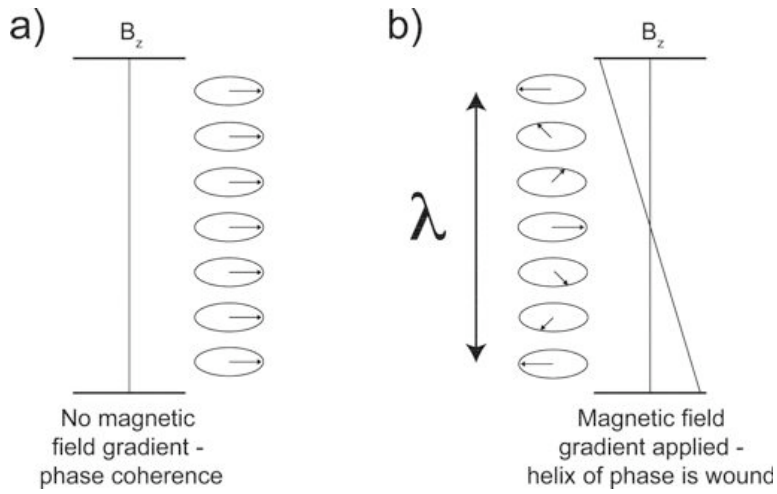

Figure 1.25 Effect of a phase encoding gradient upon the phase of nuclei. In the absence of the phase encoding gradient, a), nuclei precess with phase coherence. The application of a magnetic field gradient, b), winds a helix of phase with a wavelength, λ. When the gradient is switched off, nuclei will precess with the same frequency but with a phase shift dependent upon their position.

1.8.2.4. k-space

In the previous section two methods of spatially encoding the NMR signal were discussed, frequency and phase encoding. In an imaging experiment, a combination of frequency and phase encoding gradients is used to build up an array of NMR data over reciprocal space, or *k*-space. *k*-space is defined by the *k*-space vectors k_x, k_y and (for 3-D images) k_z. Figure 1.26 shows a two-dimensional *k*-space raster with a frequency encoded *x*-direction and a phase encoded *y*-direction. The NMR signal is sampled for each point in the *k*-space raster. Subsequent 2-D Fourier transformation of the data stored in the raster results in reconstruction of an MR image.

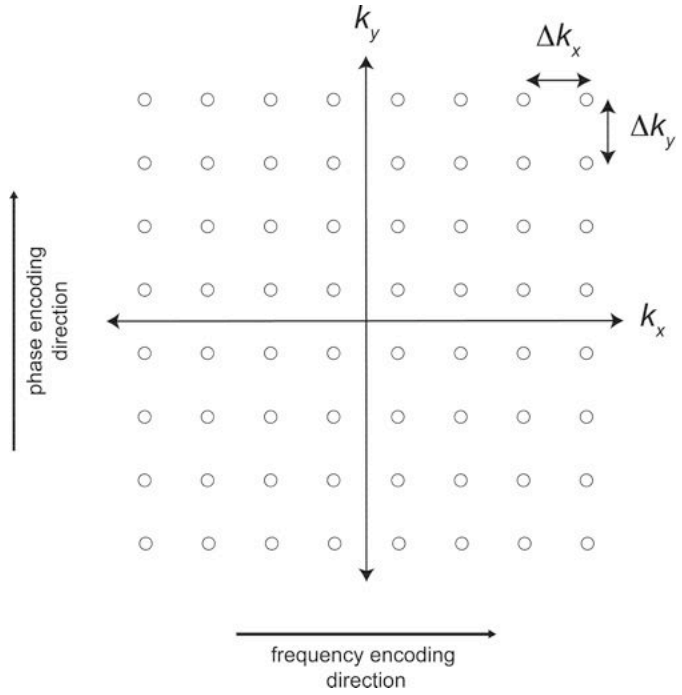

Figure 1.26 A two-dimensional k-space raster, with a frequency encoded *x*-direction and phase encoded *y*-direction. There are 8 pixels in both the frequency and phase encoded directions.

k_x is traversed in time through the application of a frequency encoding gradient. The *k*-space sampling interval in the *x*-direction, Δk_x, is given by Equation 1.22, where Δt is the sampling interval of the FID. Negative values of k_x are accessed by applying a negative read precursor gradient prior to the positive read gradient. The negative precursor gradient winds a helix of phase that is then unwound by the positive read gradient during signal acquisition. In this way, a whole line of k_x data is acquired in one go, both negative and positive values.

$$\Delta k_x = \frac{\gamma G_x \Delta t}{2\pi} \qquad \textbf{(1.22)}$$

k_y is traversed through the application of a succession of phase encoding gradients of varying strength. The *k*-space sampling interval in the *y*-direction, Δk_y, is given by Equation 1.23. ΔG_y is the phase encoding gradient step size and *t* is the duration of the phase encoding gradient.

$$\Delta k_y = \frac{\gamma \Delta G_y t}{2\pi} \qquad \textbf{(1.23)}$$

Negative values of k_y require negative phase encoding gradients, positive k_y is accessed using positive gradients. Typically, each horizontal line in the raster is acquired with a single excitation and "read out" during signal acquisition. The frequency encoded direction is, therefore, often referred to as the read direction. As the frequency encoding gradient is on during acquisition, only one direction can be frequency encoded. Spatial encoding in the second (and third) dimension is achieved using phase encoding gradients. Each horizontal line in the raster requires a different value of the phase encoding gradient and, therefore, each point in the phase encoding direction requires a separate excitation.

1.8.2.5. Image resolution and field-of-view (FOV)

The image resolution (or spatial resolution) determines the size of spatial features that can be resolved in an image. A higher resolution allows smaller features to be distinguished. The field-of-view (FOV) is the size of the spatially encoded area that is imaged. If the field-of-view is set incorrectly, or if the sample being imaged extends outside the FOV, image aliasing can occur. The positions of spins outside the FOV are incorrectly located, resulting in

image foldover. Spatial resolution in imaging experiments is determined by the *k*-space sampling intervals given by Equations 1.22 and 1.23, and how far out into *k*-space the data are sampled, *i.e.* the number of points in the raster. The spatial resolution in the frequency (*x*) and phase encoded (*y*) directions is given by Equations 1.24 and 1.25 respectively, where n_x and n_y refer to the number of data points in the k_x and k_y directions respectively.

$$\frac{1}{\Delta x} = n_x \Delta k_x \qquad \textbf{(1.24)}$$

$$\frac{1}{\Delta y} = n_y \Delta k_y \qquad \textbf{(1.25)}$$

Additionally, in the frequency encoding direction, the spatial resolution available, is limited by the line width, $\Delta\nu$, of the NMR signal in question, (Equation 1.26). It can be seen from Equation 1.26 that spatial resolution is increased for narrower linewidths. The spatial resolution can also be increased by using a stronger frequency encoding gradient. This, however, leads to a reduction in signal-to-noise ratio, as there will be fewer spins contributing to each frequency band.

$$\left|\frac{1}{\Delta x}\right| = \left|\frac{\gamma G_x}{2\pi\Delta\nu}\right| \qquad \textbf{(1.26)}$$

The field-of-view, in both the frequency and phase encoding directions is inversely related to the respective k-space sampling intervals, Equations 1.27 and 1.28.

$$x_{\max} = \left| \frac{1}{\Delta k_x} \right| \qquad \textbf{(1.27)}$$

$$y_{\max} = \left| \frac{1}{\Delta k_y} \right| \qquad \textbf{(1.28)}$$

1.8.3. Contrast in MR imaging

In the previous section, it was shown how spatial information can be encoded in the NMR signal using frequency and phase encoding gradients. However, it is also important for images to have contrast between regions of differing chemical composition and/or physical environment. This can be achieved by making the signal intensity of the pixels within an image dependent upon the NMR parameters of the nuclei contributing to them.

1.8.3.1. Spin density

In spin density imaging, the signal intensity of a given pixel is determined solely by the number of nuclei in that pixel. The signal intensity at a point **r** in an image acquired using a spin-echo imaging sequence is given by Equation 1.29.

$$S_{(\mathbf{r},\, T_R,\, T_E)} = M_0(\mathbf{r})\left(1 - \exp\left(-\frac{T_R}{T_1(\mathbf{r})}\right)\right)\exp\left(-\frac{T_E}{T_2(\mathbf{r})}\right) \qquad \textbf{(1.29)}$$

Pure spin density contrast is achieved by having a repetition time, T_R, much greater than the longest T_1 present in the sample ($T_R > 5 \times T_1$) and as short an echo time, T_E, as possible ($T_E \ll T_2$).

1.8.3.2. T_1 and T_2 relaxation time contrast

Weighting the signal according to the T_1 and T_2 relaxation times of the system can produce greater contrast. Signal intensity is still determined in part by the spin density, however the T_1 or T_2 relaxation times of the nuclei will also affect the signal intensity. Cleary, this is useful if a sample contains components with different T_1 and/or T_2 relaxation times. If the repetition time is reduced so that it is now comparable with the longest T_1 present in the sample then T_1-weighted images can be produced. The signal intensity of regions with shorter T_1 relaxation times will be greatest as T_1 relaxation effects are still minor, however, regions with longer T_1 relaxation times will have reduced signal intensity due to incomplete relaxation between repetitions. Conversely, if the repetition time is kept much longer than the longest T_1 and the echo time is increased, it is possible to obtain T_2-weighted images. The signal intensity of regions containing nuclei with shorter T_2 relaxation times will be reduced more due to dephasing, than regions with longer T_2 relaxation times.

1.8.3.3. Chemical shift contrast

Nuclei that are in different chemical environments have slightly different chemical shifts and, therefore, they will precess at slightly different Larmor frequencies to each other. In imaging, this difference can bring about mis-registration of nuclei at the same spatial location, as their precessional frequency is now dependent upon their chemical environment as well as their position. In this case, the chemical shift difference brings about unwanted artefacts in the acquired image. However, it is also possible to exploit the chemical shift difference to obtain image contrast. A short, square-shaped, hard r.f. pulse excites the whole range of frequencies within a sample.

However, by applying a chemically selective soft r.f. pulse, it is possible to excite a narrow band of resonance frequencies. Thus, it is possible to use a chemically selective soft r.f. pulse to selectively excite nuclei with a particular Larmor frequency. This, then, forms the basis of the CHESS (CHEmical Shift Selective) imaging sequence, where the spin density of nuclei with a specific chemical shift determines the signal intensity of the NMR signal.

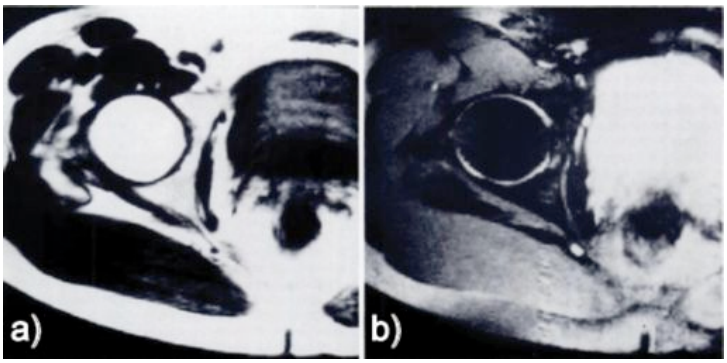

Figure 1.27 CHESS images of a hipbone. In a) the fat signal has been selectively excited and in b) the water signal has been selectively excited. Tissues containing mostly fat appear bright in image a), tissues containing mostly water appear bright in image b). Tissues containing a mixture of fat and water components appear bright in both images *e.g.* the layers of skin spanning the bottom of both images.

1.8.4. MRI contrast agents

Paramagnetic contrast agents are commonly used to increase relaxation time contrast in MR images[109-111]. Unpaired electrons in paramagnetic species cause localised magnetic field fluctuations that enhance the relaxation rate of solvent nuclei (most often water molecules) in their vicinity[110]. The magnitude of the enhancement is determined by the relaxivity of the contrast agent, usually expressed in units of $mM^{-1}\ s^{-1}$, *i.e.* the increase in the relaxation rate per millimole of the contrast agent. Typically, the effect on T_1 is more

pronounced than on T_2. A shorter T_1 relaxation time leads to increased signal intensity because solvent nuclei relax more quickly and hence, the steady-state magnetisation is greater. This allows imaging sequences to be performed with faster repetition times, which in turn allows for increased sensitivity and resolution in MR images.

1.8.5. Relaxivity theory

Interactions by which the relaxivities of solvent water molecules are affected can be broadly grouped into two mechanisms. Inner-sphere relaxation mechanisms are concerned with the relaxation of solvent molecules bound directly to the paramagnetic metal-ion centre. Conversely, outer-sphere mechanisms account for the enhancement of relaxation processes where there are no water molecules bound directly to the contrast agent[109].

1.8.5.1. Inner-sphere relaxation

For inner-sphere relaxation mechanisms the T_1 Equation 1.30 governs relaxivity. P_M is the mole fraction of metal ion, q is the number of coordinated solvent water molecules, τ_M is the residence time of the coordinated water and T_{1M} is the relaxation time of the bound water.

$$\frac{1}{T_1} = \frac{P_M q}{T_{1M} + \tau_m} \qquad \textbf{(1.30)}$$

If bound water molecules are in fast exchange with the bulk solvent (short residence time, τ_M) and multiple coordination sites are available (high number of bound water molecules, q), then the influence of the contrast agent will be

greater, (higher relaxivity). T_{1M} itself is given by the Solomon-Bloembergen equation[112], and has contributions from the total electronic spin, *S*, of the metal-ion, the proton-metal ion distance, *r*, and the rotational correlation time τ_c. Metal-ions with higher paramagnetism (higher *S*) will have a greater influence, as will metal-ions that are able to coordinate water molecules closer to the paramagnetic centre. However, these contributions are modulated by the rotational correlation time τ_c, whereby slowly tumbling contrast agents are able to exert a greater influence on relaxation of bound water molecules. The complexation of metal-ions with large chelates or macro-molecules can greatly reduce their mobility, increasing their rotational correlation time and leading to enhanced relaxivity. Indeed, many clinical contrast agents are based around complexes of manganese and gadolinium with bulky chelates such as DOTA and DTPA. The rotational correlation time is also affected by the micro-viscosity of the medium. Equation 1.31 relates the correlation time of a spherical molecule of radius *a*, in a medium with viscosity η. This is of particular importance with respect to microemulsion systems, where the micro-viscosity of the water pool can be altered by the microemulsion structure[59].

$$\tau_c = \frac{4\pi a^3 \eta}{3k_b T} \qquad \textbf{(1.31)}$$

1.8.5.2. Outer-sphere relaxation

Outer-sphere relaxation processes can be further classified into second-sphere and true outer-sphere mechanisms. Second-sphere coordination

involves the hydrogen bonding of water molecules into the second coordination sphere. The mechanism of second-sphere relaxation is similar to that of inner-sphere relaxation, and is governed by analogous parameters, the limiting factors being the residence lifetime of water in the second coordination shell, τ_M' and the coordination distance r' (where prime denotes a second-sphere interaction).

True outer-sphere relaxation arises from translational diffusion of solvent water molecules past the paramagnetic metal-ion. The relaxivity is still dependent upon the concentration and total nuclear spin of the paramagnetic metal-ions, however, the relaxivity is modulated by the translational diffusion time, $\tau_{D,}$ (Equation 1.32), where d is the distance of closest approach of the water molecule to the metal-ion and D_S and D_I are the diffusion coefficients of the metal-ion and water molecules respectively.

$$\tau_D = \frac{d^2}{3(D_I + D_S)} \qquad \textbf{(1.32)}$$

1.8.6. Contrast agents for the BZ reaction

Typically, the catalysts employed in the BZ reaction are either transition metal-ions or complexes of transition metal-ions. During the course of the reaction the metal-ion oscillates between two oxidative states. The two oxidative states have different *d*-electron configurations and therefore the paramagnetism of the metal-ion changes. The relaxation times of solvent water molecules should, therefore, be sensitive to changes in the oxidative

state of the metal-ion, allowing the metal-ion to be used as an MRI contrast indicator for the BZ reaction.

1.8.6.1. Ferroin

Ferroin, and its oxidised form ferriin, are both low spin octahedral complexes of Fe^{2+} and Fe^{3+} respectively[42]. Ferriin, therefore, has one unpaired electron, whilst ferroin is diamagnetic. Relaxation times of solvent water molecules surrounding ferriin should, therefore, be shorter than those surrounding ferroin, and the ferroin/ferriin redox pair should be usable as an MRI contrast agent for the BZ reaction. However, in the acidic reaction conditions prevailing in the BZ reaction, ferroin and ferriin are unstable and dissociate to free, uncomplexed ferrous and ferric ions[40]. In contrast to the complexed metal-ions, ferrous and ferric ions are both high-spin, possessing four and five unpaired electrons respectively.

The suitability of the ferroin catalyst as an MRI contrast indicator has been investigated previously by Gao *et al*[41]. They found the ferroin catalyst/indicator was not a suitable MRI contrast indicator for the BZ reaction, due to its dissociation in the acidic reaction conditions. As the ferroin complex degrades, the relaxation times of solvent water molecules are dominated by the presence of the more paramagnetic Fe^{2+} and Fe^{3+} ions. The local proton relaxation times are not, therefore, indicative of the oxidation state of the ferroin catalyst and cannot be used to image chemical waves.

1.8.6.2. Cerium, $Ru(bpy)_3$ and manganese

Although the ferroin-catalysed reaction cannot be imaged using MRI, the cerium, manganese and $Ru(bpy)_3$ catalysts have all been shown to be capable of providing sufficient relaxation time contrast to observe chemical waves in the liquid phase BZ reaction[41,113]. In the case of the cerium- and $Ru(bpy)_3$-catalysed reactions, the water proton relaxation times measured were not significantly different to those measured for pure water, and, as such, the image contrast was relatively poor in comparison to the manganese-catalysed system. The manganese catalyst is particularly suitable as an MRI contrast agent due to a large number of unpaired electrons that significantly reduce the relaxation time of solvent water molecules. Manganese is also able to coordinate a large number of solvent water molecules that are in exchange with bulk water. Cross *et al*[113] have used phosphate stabilisers to further enhance the available relaxation time contrast. However, increasing concentrations of phosphates have been shown to suppress oscillations, with the amplitude of oscillations decreasing and the period between them increasing, as the phosphate concentration is increased[114]. This behaviour was also apparent for one- and two-dimensional travelling waves, with the time between wave fronts increasing with higher phosphate concentrations.

1.9. MRI pulse sequences

1.9.1. Spin-echo imaging sequence

The spin-echo imaging sequence is based on the spin-echo pulse sequence discussed in Section 1.7.1.3, with the addition of slice selection, frequency and phase encoding gradients to spatially encode the NMR signal.

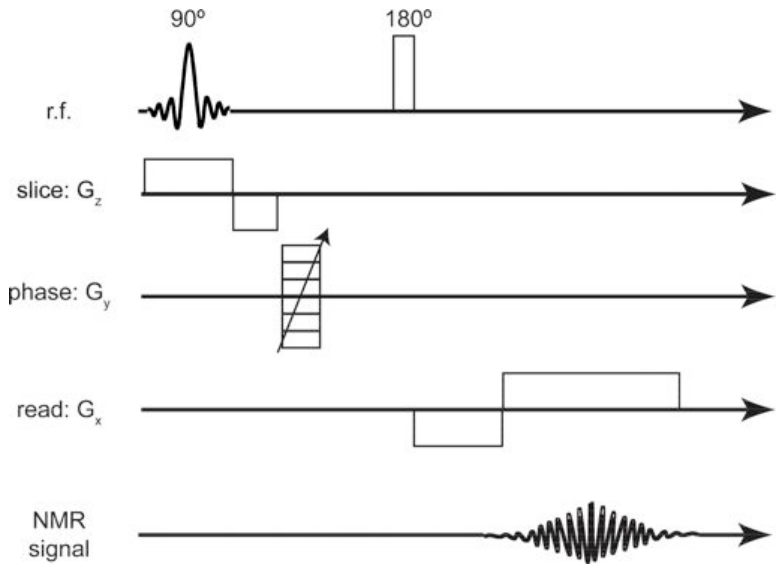

Figure 1.28 Schematic diagram of a 2-D spin-echo imaging pulse sequence.

Figure 1.28 shows the spin-echo imaging pulse sequence. The first stage is slice selection. A slice selection gradient is applied in the *z*-direction. This makes the frequency of spins in the *z*-direction spatially dependent. The initial 90º excitation pulse is a "soft" frequency selective pulse, and excites only a range of frequencies, corresponding to a slice of the sample in the *z*-direction. A negative slice gradient pulse then refocuses the magnetisation. A phase encoding gradient is then applied that spatially encodes the spins in the *y*-direction. A non-selective "hard" 180º r.f. pulse is then applied that produces a spin-echo. A negative read precursor gradient is applied in order to dephase

the magnetisation and access negative values of k_x. A positive refocussing read gradient is then applied, forming the spin-echo. The signal is acquired during the application of the positive read gradient, and a whole line of k_x data is collected. The sequence is then repeated with the strength of the phase encoding gradient varied to acquire data for different values of k_y. The sequence can also be repeated to obtain multiple signal acquisitions in order to the increase signal-to-noise ratio.

The 2-D spin echo produces a 2-D array of data that is subsequently Fourier transformed in the *x* and *y* directions to obtain a 2-D image representing a slice of the system being studied. By replacing the slice selection gradient with a second phase encoding gradient, it is possible to acquire *k*-space data in three dimensions and thus obtain 3-D images of the system.

1.9.2. CHESS imaging sequence

CHESS (CHEmical Shift Selective) imaging was briefly introduced in Section 1.8.3.3 as a means of obtaining image contrast in systems with multiple resonance frequencies. A frequency selective excitation pulse allows images to be produced in which only nuclei in a particular chemical environment contribute to the signal intensity. This is particularly advantageous when the nuclei of interest represent a small proportion of the total spin density, and the signal intensity would otherwise be dominated by contributions from the unwanted signal. This is the case with the BZ-AOT system, where the pseudo-aqueous phase, in which the majority of the chemistry takes place, accounts for a relatively small percentage (less than 20% by volume) of the

system. A CHESS imaging sequence allows the selective excitation of just the water proton resonance and destroys the signal contribution from the AOT and octane resonances.

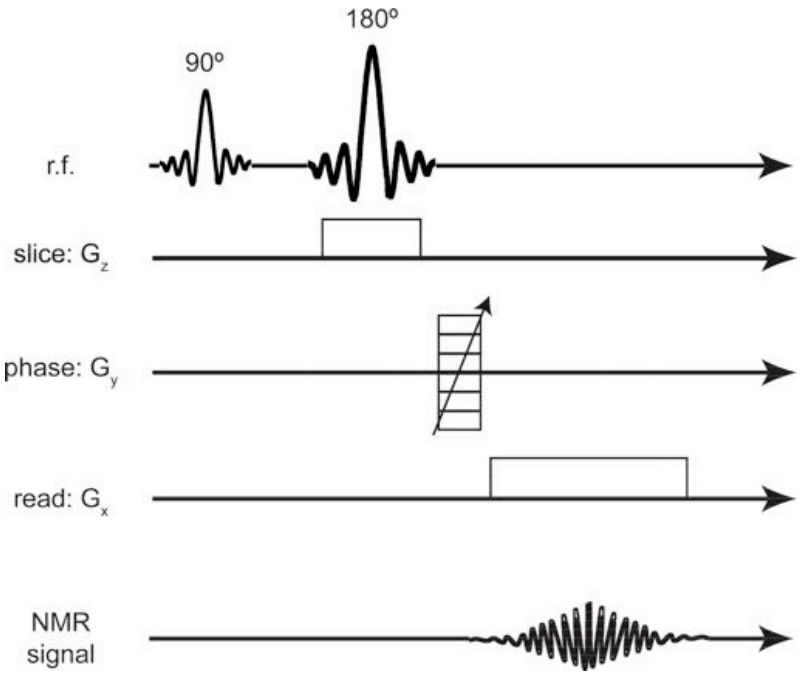

Figure 1.29 Schematic diagram of a 2-D CHESS imaging pulse sequence.

A simplified schematic diagram of the Paravision[115] M_CHESS pulse sequence is shown in Figure 1.29. The pulse-sequence is similar to the spin-echo imaging sequence discussed in Section 1.9.1, however, both the 90º and 180º pulses are frequency selective soft pulses. The 90º pulse is applied in the absence of any gradients and excites only a narrow range of chemical shifts. The pulse can, therefore, be used to excite only nuclei with a specific chemical shift. The pulse bandwidth can be set very narrow to excite only a narrow range of chemical shifts or wider to excite a group of chemical shifts. A narrow bandwidth, however, requires an r.f. pulse with a well-defined frequency, which requires a longer pulse. This results in a longer minimum

echo time T_E. The central frequency of the 90º pulse can also be varied in order to selectively excite a particular resonance. The 180º refocusing pulse is also frequency selective, but is applied during the application of the slice selection gradient. Therefore, only spins in the defined slice of the system are refocused and contribute to the spin-echo. *k*-space data is acquired in two-dimensions by using frequency and phase encoding gradients as with the spin-echo imaging sequence.

1.10. Dynamic Light Scattering (DLS)

1.10.1. Theory of DLS particle sizing experiment

DLS (sometimes referred to as Photon Correlation Spectroscopy or PCS) is a technique used to obtain the hydrodynamic radius of particles suspended in a solution. DLS is a commonly used method for obtaining the droplet size of micelles in microemulsion systems[116]. Samples are irradiated with monochromatic light from a laser beam. Droplets in the sample will cause the incident light to be scattered. The intensity of the scattered light is a function of the wavelength of the light source, the droplet diameter, *d*, and the difference between the refractive indices of the scattering matter and the solvent[117], with the scattering intensity, I, proportional to d^6. This relationship means that scattered light from larger particles can dominate that produced by smaller particles. DLS is, therefore, not suited for analysis of samples in which there is a large distribution of particle sizes. Provided the droplets are small with respect to the wavelength of the light source, the intensity is independent of the scattering angle.

In a DLS particle sizing experiment, the Brownian motion of droplets is measured by observing the signal intensity of scattered light as a function of time[118]. The signal intensity is then fitted to an auto-correlation function. For slowly diffusing droplets, there is a strong correlation between the initial signal intensity and the signal intensity a short time, *∂t*, later, for faster diffusing droplets, the correlation decays more rapidly. Equation 1.33 gives the auto-correlation function for Brownian motion of mono-disperse droplets. *A* and *B* are constants relating to the baseline and intercept of the correlation function respectively. The parameter Γ is proportional to the diffusion co-efficient of the droplets, *D*.

$$G_2(t) = A + B\exp(-2\Gamma t) \qquad \textbf{(1.33)}$$

The diffusion co-efficient can then be related to the hydrodynamic diameter of the droplets, *d(H)*, by the Stokes-Einstein equation, Equation 1.34.

$$d(H) = \frac{k_b T}{3\pi\eta D} \qquad \textbf{(1.34)}$$

k_b is Boltzmann's constant, *T* is absolute temperature and η is the viscosity of the solvent. The particle sizing obtained from the DLS method is based on a correlation function and is, therefore, statistical in nature.

1.11. References

(1) Ball, P. *The Self-Made Tapestry, Pattern formation in nature*; Oxford University Press: New York, 1999.

(2) Tyson, J. J.; Keener, J. P. *Physica D* **1988**, *32*, 327.

(3) Hauser, M. Picture Gallery, Department of Biophysics, Otto-von-Guericke University Magdeburg, 2009.

(4) Scott, S. K. *Oscillations, Waves, and Chaos in Chemical Kinetics*; Oxford University Press: New York, 1994.

(5) Turing, A. M. *Philosophical Transactions Of The Royal Society Of London Series B-Biological Sciences* **1952**, *237*, 37.

(6) Winfree, A. T. *Journal of Chemical Education* **1984**, *61*, 661.

(7) Belousov, B. P. *Sbornik Referatov po Radiatsionni Meditsine* **1958**, *145*.

(8) Atkins, P.; De Paula, J. *Atkins' Physical Chemistry*; Oxford University Press: Oxford, 2006.

(9) Zhabotinsky, A. M. *Nature* **1970**, *225*, 535.

(10) Demas, H. N.; Diemente, D. *Journal of Chemical Education* **1973**, *50*, 357.

(11) Zhabotinsky, A. M. *Chaos: An Interdisciplinary Journal of Nonlinear Science* **1991**, *1*, 379.

(12) Thompson, R. C. *Journal Of The American Chemical Society* **2002**, *93*, 7315.

(13) Degn, H. *Nature* **1967**, *213*, 589.

(14) Wood, P. M.; Ross, J. *Journal Of Chemical Physics* **1985**, *82*, 1924.

(15) Noyes, R. M.; Field, R. J.; Koros, E. *Journal Of The American Chemical Society* **1972**, *94*, 1394.

(16) Hansen, E. W.; Ruoff, P. *The Journal of Physical Chemistry* **1989**, *93*, 264.

(17) Körös, E.; Murger, M.; Friedrich, V.; Ladányi, L.; Nagy, Z.; Orbán, M. *Faraday Symp. Chem. Soc.* **1974**, *9*, 10.

(18) Burger, M.; Koros, E. *The Journal of Physical Chemistry* **1980**, *84*, 496.

(19) Field, R. J.; Burger, M. *Oscillations and Traveling Waves in Chemical Systems*; Wiley: New York, 1985.

(20) Taylor, A. F. *Progress In Reaction Kinetics And Mechanism* **2002**, *27*, 247.

(21) Pojman, J. A.; Dedeaux, H.; Fortenberry, D. *Journal Of Physical Chemistry* **1992**, *96*, 7331.

(22) Ruoff, P. *Chemical Physics Letters* **1982**, *90*, 76.

(23) Sevcik, P.; AdamcÌkov, I. *Chemical Physics Letters* **1988**, *146*, 419.

(24) SevcÌkov·, H.; Marek, M. *Physica D: Nonlinear Phenomena* **1983**, *9*, 140.

(25) Field, R. J.; Noyes, R. M. *Journal Of The American Chemical Society* **1974**, *96*, 2001.

(26) Maselko, J.; Reckley, J. S.; Showalter, K. *The Journal of Physical Chemistry* **1989**, *93*, 2774.

(27) Winfree, A. T. *Science* **1973**, *181*, 937.

(28) Tyson, J. J.; Glass, L. *Journal of Theoretical Biology* **2004**, *230*, 433.
(29) Winfree, A. T.; Strogatz, S. H. *Physica D* **1984**, *13*, 221.
(30) Winfree, A. T.; Strogatz, S. H. *Physica D* **1983**, *9*, 333.
(31) Winfree, A. T.; Strogatz, S. H. *Physica D* **1983**, *9*, 65.
(32) Winfree, A. T.; Strogatz, S. H. *Physica D* **1983**, *8*, 35.
(33) Winfree, A. T. *Faraday Symp. Chem. Soc.* **1974**, *9*, 38.
(34) Welsh, B. J.; Gomatam, J. *Phys. D* **1990**, *43*, 304.
(35) Winfree, A. T.; Caudle, S.; Chen, G.; McGuire, P.; Szilagyi, Z. *Chaos* **1996**, *6*, 617.
(36) Cross, A. L.; Armstrong, R. L.; Gobrecht, C.; Paton, M.; Ware, C. *Magnetic Resonance Imaging* **1997**, *15*, 719.
(37) Field, R. J.; Noyes, R. M.; Koros, E. *Journal Of The American Chemical Society* **1972**, *94*, 8649.
(38) Landolt, H. *Berichte der deutschen chemischen Gesellschaft* **1886**, *19*, 1317.
(39) Yatsimirskii, K. B.; Tikhonova, L. P. *Coordination Chemistry Reviews* **1985**, *63*, 241.
(40) Brandt, W. W.; Dwyer, F. P.; Gyarfas, E. D. *Chemical Reviews* **1959**, *54*, 959.
(41) Gao, Y.; Cross, A. R.; Armstrong, R. L. *Journal Of Physical Chemistry* **1996**, *100*, 10159.
(42) Housecroft, C.; Sharpe, A. G. *Inorganic Chemistry*; Prentice Hall: London, 2004.
(43) Kadar, S.; Amemiya, T.; Showalter, K. *The Journal of Physical Chemistry A* **1997**, *101*, 8200.
(44) Fruhbeis, H.; Roder, A. *Angewandte Chemie-International Edition* **1971**, *10*, 192.
(45) Koros, E. *Nature* **1974**, *251*, 703.
(46) Latimer, W. M. *Oxidation Potentials. Second Edition*; Prentice-Hall: New York, 1952.
(47) Kuhnert, L.; Pehl, K. W. *Chemical Physics Letters* **1981**, *84*, 155.
(48) Kuhnert, L.; Pehl, K. W. *Chemical Physics Letters* **1981**, *84*, 159.
(49) Bray, W. C. *Journal Of The American Chemical Society* **1921**, *43*, 1262.
(50) Epstein, I. R.; Pojman, J. A. *An Introduction to Nonlinear Chemical Dynamics: Oscillations, Waves, Patterns, and Chaos* Oxford University Press: New York, 1998.
(51) Treindl, L.; Noyes, R. M. *Journal Of Physical Chemistry* **1993**, *97*, 11354.
(52) Farage, V. J.; Janjic, D. *Chemical Physics Letters* **1982**, *93*, 621.
(53) Orban, M.; Koros, E.; Noyes, R. M. *Journal Of Physical Chemistry* **1979**, *83*, 3056.
(54) Qi, O. Y.; Tam, W. Y.; Dekepper, P.; McCormick, W. D.; Noszticzius, Z.; Swinney, H. L. *Journal Of Physical Chemistry* **1987**, *91*, 2181.
(55) Castets, V.; Dulos, E.; Boissonade, J.; De Kepper, P. *Physical Review Letters* **1990**, *64*, 2953.

(56) Berenstein, I.; Dolnik, M.; Zhabotinsky, A. M.; Epstein, I. R. *The Journal of Physical Chemistry A* **2003**, *107*, 4428.

(57) Hoar, T. P.; Schulman, J. H. *Nature* **1943**, *152*, 102.

(58) Bourrel, M.; Schechter, R. S. *Microemulsions and Related Systems - Formulation, Solvency, and Physical Properties*; Marcel Dekker, Inc.: New York, 1988; Vol. 30.

(59) De, T. K.; Maitra, A. *Advances In Colloid And Interface Science* **1995**, *59*, 95.

(60) Schwartz, L. J.; DeCiantis, C. L.; Chapman, S.; Kelley, B. K.; Hornak, J. P. *Langmuir* **1999**, *15*, 5461.

(61) Vanag, V. K. *Physics-Uspekhi* **2004**, *47*, 923.

(62) Tai, C. Y.; Hsiao, B. Y.; Chiu, H. Y. *Colloids And Surfaces A-Physicochemical And Engineering Aspects* **2004**, *237*, 105.

(63) Fedotov, V. D.; Zuev, Y. F.; Archipov, V. P.; Idiyatullin, Z. S.; Garti, N. *Colloids And Surfaces A-Physicochemical And Engineering Aspects* **1997**, *128*, 39.

(64) Valero, M.; Sanchez, F.; Gomez-Herrera, C.; Lopez-Cornejo, P. *Chemical Physics* **2008**, *345*, 65.

(65) MacDonald, H.; Bedwell, B.; Gulari, E. *Langmuir* **2002**, *2*, 704.

(66) Majhi, P. R.; Moulik, S. P. *The Journal of Physical Chemistry B* **1999**, *103*, 5977.

(67) Riter, R. E.; Willard, D. M.; Levinger, N. E. *The Journal of Physical Chemistry B* **1998**, *102*, 2705.

(68) Baruah, B.; Roden, J. M.; Sedgwick, M.; Correa, N. M.; Crans, D. C.; Levinger, N. E. *Journal Of The American Chemical Society* **2006**, *128*, 12758.

(69) Wong, M.; Thomas, J. K.; Nowak, T. *Journal Of The American Chemical Society* **2002**, *99*, 4730.

(70) Crans, D. C.; Rithner, C. D.; Baruah, B.; Gourley, B. L.; Levinger, N. E. *Journal Of The American Chemical Society* **2006**, *128*, 4437.

(71) Rack, J. J.; McCleskey, T. M.; Birnbaum, E. R. *The Journal of Physical Chemistry B* **2001**, *106*, 632.

(72) Feldman, Y.; Kozlovich, N.; Nir, I.; Garti, N.; Archipov, V.; Idiyatullin, Z.; Zuev, Y.; Fedotov, V. *Journal Of Physical Chemistry* **1996**, *100*, 3745.

(73) Hamilton, R. T.; Billman, J. F.; Kaler, E. W. *Langmuir* **1990**, *6*, 1696.

(74) Lagues, M. *Journal De Physique Lettres* **1979**, *40*, L331.

(75) Koper, G. J. M.; Sager, W. F. C.; Smeets, J.; Bedeaux, D. *The Journal of Physical Chemistry* **2002**, *99*, 13291.

(76) Lindman, B.; Olsson, U. “Structure of microemulsions studied by NMR”; Discussion Meeting of the Deutsche-Bunsen-Gesellschaft-fur-Physikalische-Chemie on Microemulsions, 1995, Gottingen, Germany.

(77) Paul, B. K.; Moulik, S. P. *Current Science* **2001**, *80*, 990.

(78) Prince, L. M. *Microemulsions : theory and practice*; Academic Press: New York, 1977.

(79) Fendler, J. H.; Fendler, E. J. *Catalysis in micellar and macromolecular systems*; Academic Press: New York, 1975.

(80) Clint, J. H. *Surfactant Aggregation*; Blackie: London, 1992.

(81) Backlund, S.; Eriksson, F.; Kanerva, L. T.; Rantala, M. *Colloids and Surfaces B: Biointerfaces* **1995**, *4*, 121.

(82) Fendler, J. H. *The Journal of Physical Chemistry* **1980**, *84*, 1485.

(83) Uskokovic, V.; Drofenik, M. *Surface Review and Letters* **2005**, *12*, 239.

(84) Boutonnet, M.; Kizling, J.; Stenius, P.; Maire, G. *Colloids and Surfaces* **1982**, *5*, 209.

(85) Balasubramanian, D.; Rodley, G. A. *The Journal of Physical Chemistry* **1988**, *92*, 5995.

(86) Vanag, V. K.; Epstein, I. R. *Physical Review Letters* **2001**, *87*.

(87) Eicke, H. F.; Shepherd, J. C. W.; Steinemann, A. *Journal Of Colloid And Interface Science* **1976**, *56*, 168.

(88) Vanag, V. K.; Epstein, I. R. *Physical Review Letters* **2004**, *92*, 128301.

(89) Epstein, I. R.; Vanag, V. K. “Complex patterns in reactive microemulsions: Self-organized nanostructures?”; Workshop on Self-Organization-Initiative Nano-Engineering (SINE), 2005, Wako, JAPAN.

(90) Vanag, V. K.; Epstein, I. R. *Int J Dev Biol* **2009**, *53*, 673.

(91) Epstein, I. R.; Berenstein, I. B.; Dolnik, M.; Vanag, V. K.; Yang, L. F.; Zhabotinsky, A. M. “Coupled and forced patterns in reaction-diffusion systems”; 9th Experimental Chaos Conference, 2006, San Jose dos Campos, BRAZIL.

(92) Vanag, V. K.; Epstein, I. R. *Physical Review Letters* **2003**, *90*.

(93) Vanag, V. K.; Epstein, I. R. *Proceedings Of The National Academy Of Sciences Of The United States Of America* **2003**, *100*, 14635.

(94) Carballido-Landeira, J.; Berenstein, I.; Taboada, P.; Mosquera, V.; Vanag, V. K.; Epstein, I. R.; Perez-Villara, V.; Munuzuri, A. P. *Physical Chemistry Chemical Physics* **2008**, *10*, 1094.

(95) Vanag, V. K.; Epstein, I. R. *Science* **2001**, *294*, 835.

(96) Kaminaga, A.; Vanag, V. K.; Epstein, I. R. *Journal Of Chemical Physics* **2005**, *122*.

(97) McIlwaine, R.; Vanag, V. K.; Epstein, I. R. *Physical Chemistry Chemical Physics* **2009**, *11*, 1581.

(98) Cherkashin, A. A.; Vanag, V. K.; Epstein, I. R. *The Journal of Chemical Physics* **2008**, *128*, 204508.

(99) Levitt, M. H. *Spin Dynamics: Basics of Nuclear Magnetic Resonance*; Wiley & Sons: New York, 2008.

(100) Freeman, R. *Magnetic Resonance in Chemistry and Medicine*; Oxford University Press: New York, 2003.

(101) Hore, P. J. *Nuclear Magnetic Resonance*; Oxford University Press: New York, 1995.

(102) Callaghan, P. T. *Principles of Nuclear Magnetic Resonance Microscopy*; Oxford University Press: New York, 1991.

(103) Haacke, M.; Brown, R.; Thompson, M.; Venkatesan, R. *Magnetic Resonance Imaging: Physical Principles and Sequence Design*; Wiley-Liss: New York, 1999.

(104) TIP, M. R. MR Technology Information Portal, 2009.

(105) Hornak, J. P. *The Basics of MRI - http://www.cis.rit.edu/htbooks/mri/index.html*, 1996-2006.

(106) Strang, G. *Linear algebra and its applications*, 3rd ed.; Harcourt Brace: London, 1988.

(107) Hahn, E. L. *Physical Review* **1950**, *80*, 580.

(108) Neuhaus, D.; Williamson, M. *The Nuclear Overhauser Effect in Structural and Conformational Analysis, 2nd Edition*; Wiley-VCH: New York, 2000.

(109) Lauffer, R. B. *Chemical Reviews* **1987**, *87*, 901.

(110) Bottrill, M.; Nicholas, L. K.; Long, N. J. *Chemical Society Reviews* **2006**, *35*, 557.

(111) Caravan, P.; Ellison, J. J.; McMurry, T. J.; Lauffer, R. B. *Chemical Reviews* **1999**, *99*, 2293.

(112) Bloembergen, N. *Journal Of Chemical Physics* **1957**, *27*, 572.

(113) Cross, A. R.; Armstrong, R. L.; Reid, A.; Su, S. Y.; Menzinger, M. *Journal Of Physical Chemistry* **1995**, *99*, 16616.

(114) Cross, A. The development of three-dimensional magnetic resonance imaging of the Belousov-Zhabotinsky reaction, The University of New Brunswick (Canada), 1999.

(115) Bruker. Paravision; 2.1.1 ed., 1996.

(116) Salabat, A.; Eastoe, J.; Mutch, K. J.; Tabor, R. F. *Journal Of Colloid And Interface Science* **2008**, *318*, 244.

(117) Finsy, R. *Advances In Colloid And Interface Science* **1994**, *52*, 79.

(118) Berne, B.; Pecora, R. *Dynamic Light Scattering: With Applications to Chemistry, Biology, and Physics*; {Dover Publications}: New York, 2000.

Chapter 2. Optical investigation of pattern formation in the BZ reaction

2.1. Introduction

One of the first objectives of this work was to identify suitable catalyst/indicator systems to enable pattern formation in the BZ-AOT system to be visualised using both optical and MR techniques. It would be preferable that the chosen catalyst possesses those properties that allow it to act as an MR contrast agent, allowing the oxidised and reduced states of the BZ-AOT reaction to be distinguished. This aspect of catalyst choice is discussed elsewhere in this thesis in Chapters 3 and 4. It is of equal importance that the chosen catalyst/indicator system catalyses the BZ reaction and promotes the formation of chemical waves and patterns. A third consideration for any potential catalyst is that the catalyst should also allow optical visualisation of pattern formation. Although not essential for the visualisation of patterns using MRI, the ability to visualise patterns using optical methods would be advantageous. It would allow the characterisation of the chemistry of the chosen catalyst system to be performed using optical visualisation methods that are already well established[1]. MR imaging experiments could then be performed on the characterised systems, with the confidence that the systems exhibit pattern formation. If patterns were not observed using MRI, then it

would be indicative that the MR imaging sequence required modification, and not the chemistry of the system. Imaging sequences could be optimised to observe the particular pattern type seen using optical methods and comparison may be made between those images obtained using optical methods, and those images obtained using MRI.

In summary, a suitable MR indicator for the BZ-AOT reaction will:

i) Catalyse the BZ reaction and promote the formation of a variety of pattern types.

ii) Provide suitable MR contrast to be able to distinguish the reduced and oxidised states of the BZ-AOT system.

iii) Preferably allow the visualisation of chemical patterns and waves using optical methods *i.e.* have different colours in the reduced and oxidised states.

As mentioned, the suitability of various metal ion catalysts as MR contrast agents is discussed in Chapters 3 and 4. The results and discussion presented in this chapter aim to deal with points i) and iii) from the above list. A number of different catalyst systems in the BZ-AOT system are investigated and their chemistry manipulated so as to reproduce the types of chemical patterns that are of interest. Catalyst/indicator systems are also investigated that would potentially allow patterns to be visualised using both optical and MR imaging techniques.

2.2. Experimental

2.2.1. Preparation of the BZ reaction in water-in-octane reverse micelles

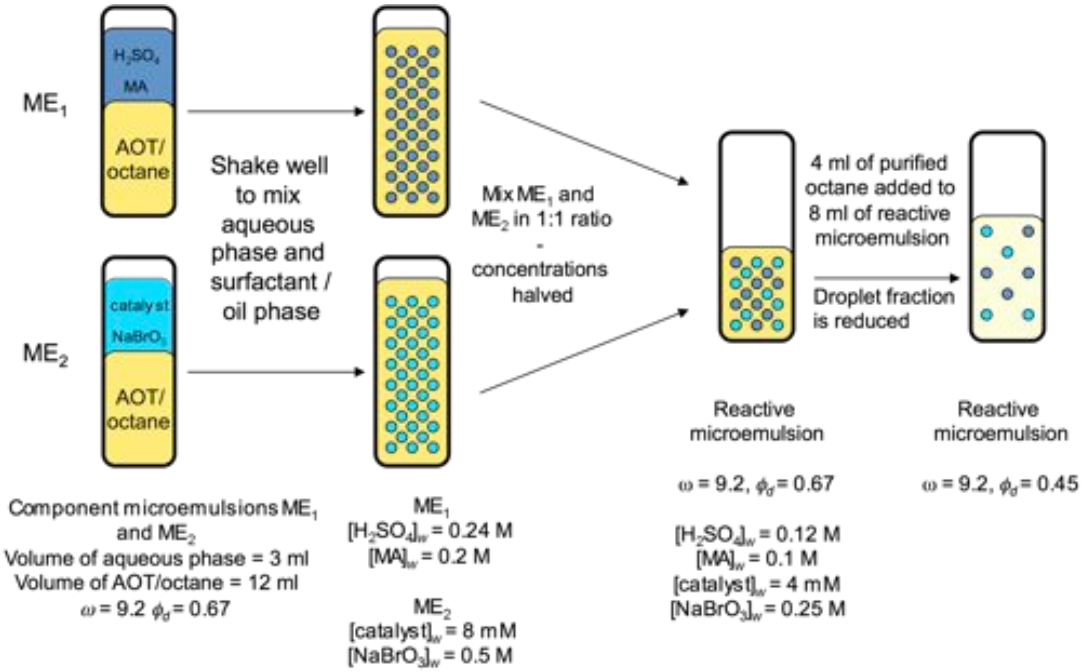

Figure 2.1 Schematic diagram showing the method for preparing a BZ reaction in an AOT/octane microemulsion. The example above shows a microemulsion prepared at a water-to-surfactant ratio ω = 9.2, and droplet fraction ϕ_d = 0.45. ω can be changed by altering the relative amounts of aqueous phase reagents and AOT/octane solution. ϕ_d is controlled by the amount of purified octane added.

Figure 2.1 shows a schematic representation of the method used to prepare the BZ reaction in the AOT/octane microemulsion system. A 1.5 mol dm^{-3} solution of AOT (Sodium bis(2-ethylhexyl) sulfosuccinate, (Fluka)) is prepared by dissolving 111.14 g of AOT in 70 ml of n-octane (Acros). The octane is first purified, by stirring over concentrated sulphuric acid for several days. This process acts to remove any double bonds in the octane that would otherwise react with Br_2 by way of an electrophillic addition mechanism. Stock solutions of 2.0 mol dm^{-3} malonic acid (Sigma) 1.5 mol dm^{-3} sodium bromate

(Sigma) and 5.0 mol dm^{-3} sulphuric acid (Fisher) were all prepared using nanopure water from a Millipak Millipore purification unit.

Two stock microemulsions, ME_1 and ME_2, were then prepared, one containing sulphuric acid, malonic acid (MA) and AOT/octane solution, and the other containing the chosen catalyst, sodium bromate and AOT/octane. The partitioning of the reactants between two stock microemulsions ensured that the BZ reaction did not begin until they were mixed together. Both stock microemulsions were prepared at the same water-to-surfactant ratio, ω, and droplet fraction, ϕ_d, where ω = $[H_2O]/[AOT]$. The required volumes of aqueous phase reagents and 1.5 mol dm^{-3} AOT surfactant solution were calculated using the desired value of ω as the starting point *e.g.* to obtain a stock microemulsion with ω = 9.2, a total of 3 ml of water ($[H_2O] \approx 55$ mol dm^{-3}) was added to 12 ml of a 1.5 mol dm^{-3} solution of AOT in octane. The volume fraction of water, ϕ_w, of this stock microemulsion was 0.2, which equates to a droplet fraction of 0.67, given the relationship[2] between ϕ_d, ϕ_w and ω, (see Equation 1.6). The pseudo-aqueous phase concentration of each of the BZ reactants was twice that required in the final reactive microemulsion. Equal volumes of each stock microemulsion were then mixed together and enough additional octane was added to give the desired droplet fraction, ϕ_d. At this point, the pseudo-aqueous phase concentration of each of the BZ reactants was half that of their concentration in the stock microemulsions *i.e.* the desired concentration for the reaction. The reacting microemulsion was then mixed for a short period of time – approximately 2 – 3 minutes – until the resulting mixture became transparent. The transparency of the mixture

indicates that the droplet size is sufficiently small so as not to significantly scatter light, and that a microemulsion has been formed[3].

2.2.2. Preparation of BZ catalyst/indicators

2.2.2.1. Preparation of the ferroin-catalysed BZ-AOT reaction

A 0.025 mol dm^{-3} ($[Fe(phen)_3]^{2+}$) stock solution was prepared by dissolving iron (II) sulphate heptahydrate (Sigma) and 1,10-phenanthroline (Sigma) in a 1:3 molar ratio in water. The scheme outlined in Section 2.2.1 was then followed to prepare the reactive microemulsion system.

2.2.2.2. Preparation of the bathoferroin-catalysed BZ-AOT reaction

The procedure for preparing the bathoferroin-catalysed BZ-AOT system is slightly different to that outlined for the ferroin catalyst, due to the insolubility of the bathophenanthroline ligand in both octane and water. The method outlined by Vanag and Epstein[2] was followed. Bathophenanthroline (4,7-diphenyl-1,10-phenanthroline) (Sigma) was dissolved in a solution of 1.5 mol dm^{-3} AOT in octane, to give a 12.3 mM solution of bathophenanthroline. The stock microemulsion containing sulphuric acid and malonic acid (ME_1) was prepared as before. ME_2 was prepared by adding aqueous solutions of iron (II) sulfate heptahydrate (Sigma) and sodium bromate to the bathophenanthroline/AOT/octane solution. The concentration of $FeSO_4$ was such that [bathophenanthroline]/[$FeSO_4$] = 3. Both stock microemulsions were prepared at the same droplet fraction and water-to-surfactant ratio. The reactive microemulsion was prepared, as before, by mixing ME_1 and ME_2 in a

1:1 ratio and adding enough additional purified octane to obtain the required droplet fraction.

2.2.2.3. Preparation of the $Ru(bpy)_3$-catalysed BZ-AOT reaction

The $Ru(bpy)_3$-catalysed BZ-AOT system was prepared in much the same way as the ferroin equivalent. $[Ru(II)(bpy)_3]SO_4$ was firstly prepared from the dichloride hexahydrate salt ($[Ru(II)(bpy)_3]Cl_2 6H_2O$ (Aldrich)) following the procedure outlined by Gao and Försterling[4]. The chloride salt is not used as chloride ions inhibit the BZ reaction. The chloride salt was dissolved in the minimum amount of water and the sulfato salt was precipitated by dropwise addition of a 5 M solution of sulphuric acid. The sulfato salt was collected via filtration and left to dry in a desiccator for several days. The dried product was then used to prepare a stock solution of $[Ru(II)(bpy)_3]SO_4$. Stock solutions of $Ru(II)(bpy)_3$ were kept in foil wrapped volumetric flasks and used within a few days of preparation. Stock solutions of the other BZ reactants were prepared as before using nanopure water. The procedure for preparing the BZ reaction in an AOT/octane microemulsion, as outlined above in Section 2.2.1, was followed, segregating malonic acid and sulphuric acid in ME_1 and $Ru(II)(bpy)_3$ and sodium bromate in ME_2.

2.2.2.4. Preparation of $Ru(bpy)_3$/diphenylamine systems

A stock solution of 0.02 mol dm^{-3} diphenylamine sulphonic acid (DPA) was prepared by dissolving diphenylamine sulphonic acid sodium salt (Sigma) in nanopure water. $Ru(bpy)_3$/DPA catalysed BZ-AOT reactions were prepared in the same way as for the $Ru(bpy)_3$ catalysed reaction described in Section 2.2.2.3, with DPA included in ME_2.

2.2.2.5. Preparation of the manganese/ferroin dual catalyst BZ-AOT reaction

A manganese/ferroin-catalysed BZ-AOT reaction stabilised with ortho-phosphoric acid was prepared as follows. Aqueous stock solutions of ferroin, manganese (II) sulfate, sodium bromate, malonic acid, sulphuric acid and phosphoric acid (H_3PO_4, Fisher) were used to prepare an aqueous phase BZ reaction. Ferroin and manganese were the last reagents added to the reaction mixture and after a brief period of mixing, an aliquot of the aqueous phase BZ reaction was added to a 1.5 mol dm^{-3} solution of AOT in octane. The AOT/octane solution had already been pre-diluted with additional octane so that upon addition of the reactive aqueous phase, the microemulsion had the desired water-to-surfactant ratio and droplet fraction. The pseudo-aqueous phase concentration of each of the reactants in the microemulsion was equivalent to the bulk concentration in the aqueous reaction.

2.2.3. Optical imaging of chemical patterns and waves in the BZ-AOT reaction

Once a reactive microemulsion had been prepared, a small droplet of the reactive mixture was then transferred to the reactor using a Pasteur pipette. The reactor (schematic diagram shown in Figure 2.2) consists of two flat round optical windows (UV Fused Silica Windows 50 mm × 4 mm, Edmund Optics Ltd.) with a thin (~ 80 μm) Teflon gasket (inside diameter ~ 25 mm) in between them.

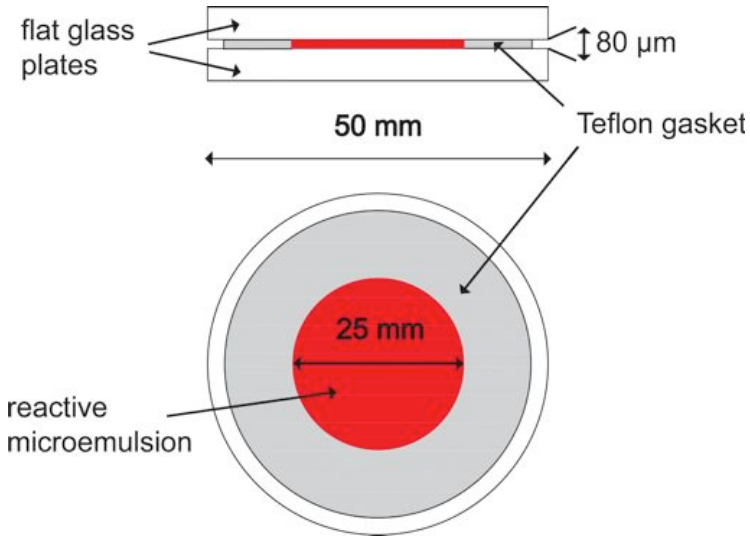

Figure 2.2 Elevation view (top) and plan view (bottom) of the reactor used to observe patterns in the BZ-AOT reaction. A thin layer of the reactive microemulsion (shown here in red) is sandwiched between two flat glass plates, separated by a Teflon gasket (grey). Note that the gap between the plates is exaggerated in the diagram.

The droplet was then sandwiched in between the two optical windows in the space created by the gasket, taking care not to trap any air bubbles in between the two windows. The circumference of the reactor was sealed with Teflon tape, and the reactor placed into a holder. The reactor was illuminated from beneath using a halogen lamp source (Dolan-Jenner Model PL-800, Edmund Optics Ltd.) fitted with a fibre optic light guide and a collimator (Edmund Optics Ltd.). The light source and collimator allowed the intensity of the illumination to be adjusted to obtain optimum contrast. Patterns were visualised using a DIN microscope objective (4× magnification) attached to a black and white Hitachi KP-M2OP CCD video camera via a C-Mount adaptor tube. The field-of-view using this configuration of camera and microscope objective is 1.6 × 1.2 mm. An interference filter - with a transmission frequency appropriate for the metal ion catalyst being used – is placed in the light path between the objective lens and the CCD camera. For visualisation

of ferroin, and also the dual catalyst manganese/ferroin system, a 510 nm interference filter (24.15 mm diameter, Edmund Optics Ltd.) was used. A 532 nm filter was used for visualisation of the bathoferroin-catalysed system and a 450 nm filter was used for visualisation of $Ru(bpy)_3$. In each case the interference filter is chosen to correspond to the wavelength of the maximum absorbance of the catalyst in its reduced form. Thus, regions where the indicator is in the oxidised state appear brighter than regions where the catalyst is in the reduced state. The holder was mounted via a series of adjustable sliding clamps that allowed the reactor to be moved in the *x, y* and *z* directions, enabling the whole plane of the reactor to be brought into the field-of-view of the microscope and focussed correctly. A schematic of the apparatus is shown in Figure 2.3.

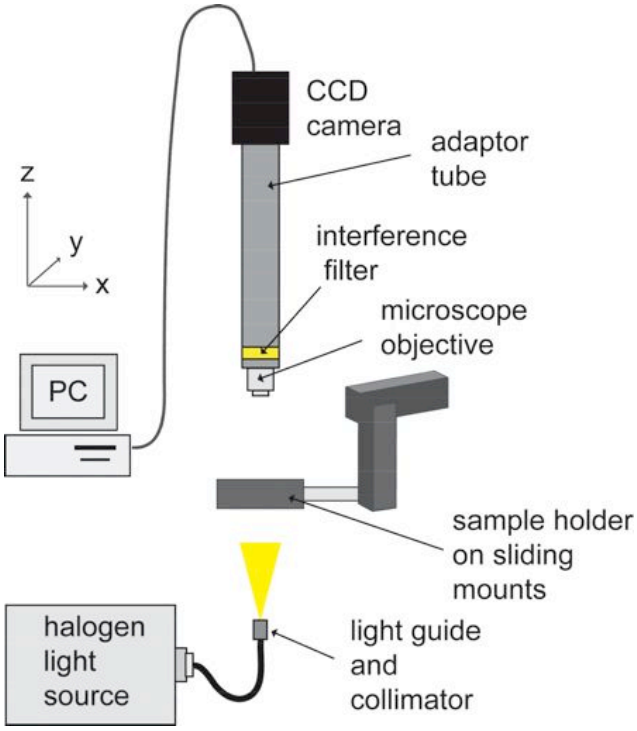

Figure 2.3 Schematic representation of the apparatus used to optically image patterns in the BZ-AOT reaction. The reactor (shown in Figure 2.2) is placed in the sample holder, which is mounted on adjustable sliding mounts allowing it to be moved in the *x, y* and *z* directions. The wavelength of the interference filter is selected to suit the catalyst / indicator being studied and it is located within the C-Mount adaptor tube.

The CCD camera was interfaced to a PC via the S-Video connection of an Osprey-100 PCI video capture card[5], allowing a variety of software packages to be used to record and process the acquired images. StopMotionmaker Plus[6] was the primary piece of software used to acquire images. The software allowed images to be acquired either continuously (video capture) or at specific time intervals. Typically, the microscope apparatus was focussed on a particular area of the reactor and the software was programmed to capture images every 10 - 15 seconds. This resulted in a series of bitmap (bmp) image files that were then combined into a movie file (avi) using StopMotionmaker Plus. The videos were compressed using Quicktime Pro[7]. A

selection of these movie files is included on an attached DVD, (refer to Appendix A).

2.2.3.1. Image processing and analysis

Individual frames from the movies were processed and analysed using a combination of Adobe Photoshop and Adobe Illustrator. To measure the dimensions of the features in the observed patterns, single frames taken from the movie files were analysed using Adobe Illustrator. The frames were first processed using Adobe Photoshop to improve the contrast between areas of the reduced and oxidised states of the catalyst. This was usually achieved by simple adjustment of the brightness, contrast and colour level controls. In extreme cases *e.g.* in cases where the images were very noisy, a smart blur filter (Overlay Edge mode with a high threshold and low radius) was applied to better define the boundaries between oxidised and reduced areas of the system. The processed images were then analysed using the rulers in Illustrator. A single frame was transferred in to Illustrator and a Scale transformation was applied so that the frame measured 1.6 × 1.2 mm, corresponding to the field-of-view of the imaging apparatus. Features (patterns, wave fronts *etc)* in the image were defined by drawing guide-lines. These were then measured to give the dimensions of the feature in question.

2.2.4. Contrast enhancement in the aqueous manganese-catalysed, phosphate-stabilised, BZ reaction

Stock solutions of the BZ reactants were prepared as before and a stock 0.25 mol dm^{-3} solution of sodium tripolyphosphate ($Na_5P_3O_{10}$) (Fluka) was also

prepared. A stirred BZ reaction was prepared by mixing the aqueous phase reagents together in a beaker. Oscillations in the oxidation state of the manganese catalyst were monitored using a platinum combination electrode (Ag/AgCl reference) (Thermo Orion). The reacting solution was observed to see if there was a noticeable colour change during the oscillation period.

A series of experiments was performed where the ratio $[Na_5P_3O_{10}]/[MnSO_4]$ was varied in an attempt to find the optimum contrast. This was done for two different concentrations of $MnSO_4$, i) $[MnSO_4]$ = 0.5 mM, ii) $[MnSO_4]$ = 1.0 mM. The ratio $[Na_5P_3O_{10}]/[MnSO_4]$ was varied from 2 to 40. The concentration of the other BZ reactants were: $[NaBrO_3]$ = 0.22 M, [MA] = 0.18 M, $[H_2SO_4]$ = 0.5 M. Another set of experiments was performed where the concentration of malonic acid was varied and its effect on the observed contrast was assessed. [MA] was varied from 0.05 M to 0.25 M. $[NaBrO_3]$ = 0.25 M $[H_2SO_4]$ = 0.5 M and $[Na_5P_3O_{10}]$ = 4 mM. This experiment was repeated for a variety of concentrations of $MnSO_4$ ranging from 0.1mM to 1.5 mM. Experiments were also performed on manganese-catalysed BZ reactions without phosphate stabilisation.

2.2.5. Observation of oscillations in the manganese catalysed BZ-AOT using UV/vis spectroscopy

Stock solutions of the BZ reactants were prepared in nanopure water. Two stock microemulsions were then prepared by adding the aqueous phase reactants to a solution of 1.5 M AOT in octane in the same manner outlined in

Section 2.2.1. ME_1 contained malonic acid, H_2SO_4 and $Na_5P_3O_{10}$. ME_2 contained $MnSO_4$, $NaBrO_3$ and $Na_5P_3O_{10}$. A third stock microemulsion, ME_B was also prepared with the same composition as ME_2 but omitting the $MnSO_4$. This would be used to prepare the "blank" sample. The reactive microemulsion was prepared by mixing ME_1 and ME_2 in a one to one ratio with enough additional octane to give the required droplet fraction. The blank was prepared by mixing ME_1 and ME_B together with additional octane. The microemulsion was prepared at ω = 9.2 and ϕ_d = 0.45. $[MnSO_4]$ = 1.2 mM, $[Na_5P_3O_{10}]$ = 45 mM, $[NaBrO_3]$ = 0.25 M, [MA] = 0.15 M and $[H_2SO_4]$ = 0.17 M. The reactive microemulsion was transferred to a 1 cm quartz glass UV cuvette with a small magnetic stirring flea in place. The reaction was stirred using a Spinette cell stirrer (Starna, Optiglass Ltd.) A preliminary scan was first performed, measuring the absorbance of the reactive microemulsion from 190 nm to 600 nm. The absorbance was then measured over time at λ = 265 nm corresponding to the wavelength of maximum absorbance. The experiment was repeated and this time, the absorbance at λ = 334 nm was measured over time. This wavelength corresponds to a point on the "shoulder" of the peak with maximum absorbance is at 265 nm.

2.3. Results and Discussion

2.3.1. Investigation of pattern selection in the BZ-AOT system

By incorporating the BZ reaction into the AOT water-in-oil reverse micelle system, the behaviour of what is already an extremely controllable system is now subject to another set of controllable variables. As well as the

concentrations of the BZ reagents and the choice of catalyst, the physical structure of the microemulsion medium in which they are dispersed can now be manipulated by controlling the size of the micelles (droplet size) and the micellar concentration (droplet fraction). The “tunability” of the BZ-AOT system has been exploited to produce and observe a diverse range of chemical patterns and waves[8]. Among these are a number of pattern types previously unseen in aqueous chemical systems including segmented spirals[2], dash waves[9] and inwardly rotating spirals[10]. Importantly, the BZ-AOT system is also able to support the formation of stationary Turing patterns[11] and is only the second chemical system in which this phenomenon has been observed.

One of the preliminary objectives of this project was to explore the range of patterns that could be produced in the BZ-AOT system and reliably reproduce them. Of particular importance was the ability to be able to observe Turing patterns. The study of the formation of Turing patterns is of chemical interest due to their proposed involvement in the mechanism of morphogenesis[12] - the biological process of cell growth and differentiation. From an imaging point of view, stationary type Turing patterns are appealing to study as they should be easier to image than travelling waves; the patterns formed in the BZ-AOT system have features that measure from fifty to several hundred microns (μm). To resolve these features using MRI will require that the pixel resolution of the imaging experiment performed is sufficiently small to elucidate the structure of the patterns. To obtain a satisfactory signal-to-noise ratio with smaller pixel sizes, multiple signal acquisitions are required, as the signal

intensity from each pixel will be reduced. As a result, the total experiment time will be lengthened. Thus, Turing patterns are particularly attractive to study using MRI as they are stationary in time for extended periods and therefore their form should not change drastically over the course of a long imaging experiment.

2.3.2. Investigation of pattern formation in the ferroin-catalysed BZ-AOT reaction

The ferroin ($[Fe(phen)_3]^{2+}$) catalysed BZ reaction is now the most studied and classical form of the system since Zhabotinsky refined Belousov's original cerium catalysed reaction[13]. The use of ferroin as an MRI contrast agent for the BZ reaction is expected to be limited. It has been shown[14] that the relaxation times of ferroin and ferriin in acidic solution are dominated by the presence of ferrous (Fe^{2+}) and ferric (Fe^{3+}) ions. The ferrous/ferric ions are produced by the dissociation of the ferroin and ferriin complexes, which are unstable in acidic solution[15]. However, the ferroin-catalysed BZ-AOT reaction makes a particularly good starting point with which to begin investigating pattern formation using optical imaging techniques, due to the marked visual contrast between the reduced (red) and oxidised (blue) forms of the catalyst. Along with $Ru(bpy)_3$, ferroin is also the most studied catalyst system in the BZ-AOT reaction. The ferroin-catalysed BZ-AOT systems as reported by Vanag and Epstein[11] were used as a starting point for investigations into pattern formation. The majority of experiments were conducted at droplet fractions below the droplet percolation threshold *i.e.* $\phi_d < 0.5$, as this is the region where Turing patterns have been observed[16].

2.3.2.1. Observation of chemical patterns in the ferroin-catalysed BZ-AOT reaction

Typically, chemical waves were observable in the reactor almost immediately. Initially, the waves observed took the form of fast moving (wave velocity = 1–2 mm min^{-1}) bulk oscillations. A distinction is made here between bulk oscillations and travelling waves. Bulk oscillations have a higher wave velocity, approximately 1 – 2 mm min^{-1}, and much broader wave fronts, > 0.2 mm, than travelling waves, which move more slowly, < 0.5 mm min^{-1} and have a more defined oxidation front, approximately 20-50 μm across. After approximately 10 – 20 minutes, periodic trigger waves were observed, often emanating from the edge of the reactor *i.e.* from the Teflon gasket, which acts as a "pacemaker" for the production of these trigger waves. Dust particles present in the reaction mixture also act as pacemaker sites for the production of trigger waves. Patterns begin to develop and evolve at this point and generally persist for 2–3 hours. After this time contrast in the ferroin system fades as the catalyst degrades in the acidic reaction conditions.

A number of different pattern types were reproduced in the ferroin-catalysed BZ-AOT reaction. Figure 2.4 shows the evolution of travelling dash waves observed in a freshly prepared microemulsion with ω = 18.3, ϕ_d = 0.48, [MA] = 0.2, [H_2SO_4] = 0.175 M, [$NaBrO_3$] = 0.15 M and [ferroin] = 4.0 mM. These were observed near the centre of the reactor approximately 40 minutes after the reaction was initiated. They travelled with a velocity of approximately 40 μm min^{-1}. The distance between successive wave fronts was approximately 230 μm and the distance between dashes in the same wave was around 60

μm. Dash waves have been observed by Vanag and Epstein[9], although they observe them at different parameters: ω = 15, ϕ_d = 0.55, [MA] = 0.3, [H_2SO_4] = 0.2 M, [$NaBrO_3$] = 0.23 M and [ferroin] = 4 mM.

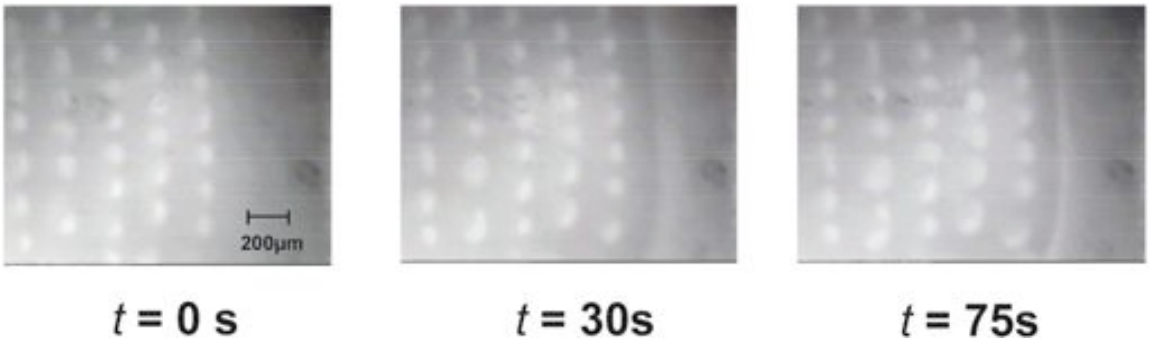

Figure 2.4 Travelling dash waves in the ferroin-catalysed BZ-AOT system. The sequence shows the progression of bands of segmented dash waves travelling from left to right. The second and third images in the sequence show the approach of a non-segmented travelling wave approaching from the right that annihilates as it approaches the segmented waves. [ferroin] = 4.0 mM, [MA] = 0.2 M, [$NaBrO_3$] = 0.15 M, [H_2SO_4] = 0.175 M, ϕd = 0.48, ω = 18.3.

Figure 2.5 and Figure 2.6 both show stationary type Turing patterns observed in the same ferroin-catalysed BZ-AOT reaction; [ferroin] = 4.2 mM, [MA] = 0.2 M, [$NaBrO_3$] = 0.15 M, [H_2SO_4] = 0.175 M, ϕ_d = 0.48, ω = 18.5. The image in Figure 2.5 was taken towards the edge of the reactor and shows labyrinth type Turing patterns. The spacing in between the stationary bands was approximately 200 μm. The image sequence shown in Figure 2.6 was captured toward the centre of the reactor approximately 45 minutes after the start of the reaction and shows stationary striped Turing patterns that gradually evolved into stationary spotted Turing patterns, over the course approximately 15 minutes. The Turing wavelength of the striped patterns is around 200 μm, but the spacing decreases, as the stripes evolve into spots,

to approximately 150 μm. The fact that all these patterns were observed in the same reaction, at different points in the reactor and at different times, shows that the same initial experimental parameters can give rise to different types of patterns.

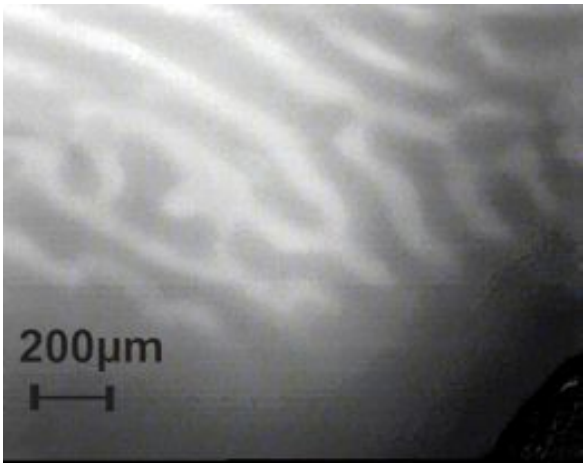

Figure 2.5 Stationary labyrinth type patterns in the ferroin-catalysed BZ-AOT system. The dark area at the bottom right of the image is the edge of the Teflon gasket that separates the two flat glass plates of the reactor. [ferroin] = 4.2 mM, [MA] = 0.2 M, [$NaBrO_3$] = 0.15 M, [H_2SO_4] = 0.175 M, ϕ_d = 0.48, ω = 18.5.

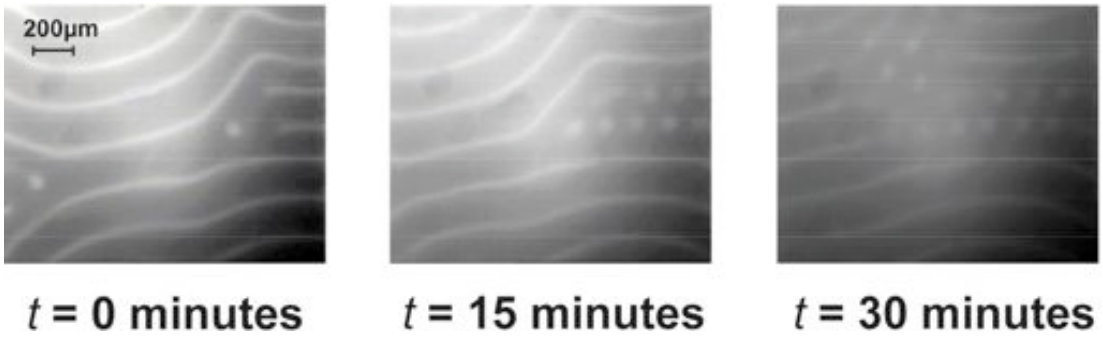

Figure 2.6 Stationary Turing patterns in the Ferroin-catalysed BZ-AOT system. The sequence shows the gradual evolution of stationary Turing striped patterns into stationary Turing spot patterns. [Ferroin] = 4.2 mM, [MA] = 0.2 M, [$NaBrO_3$] = 0.15 M, [H_2SO_4] = 0.175 M, ϕ_d = 0.48, ω = 18.5.

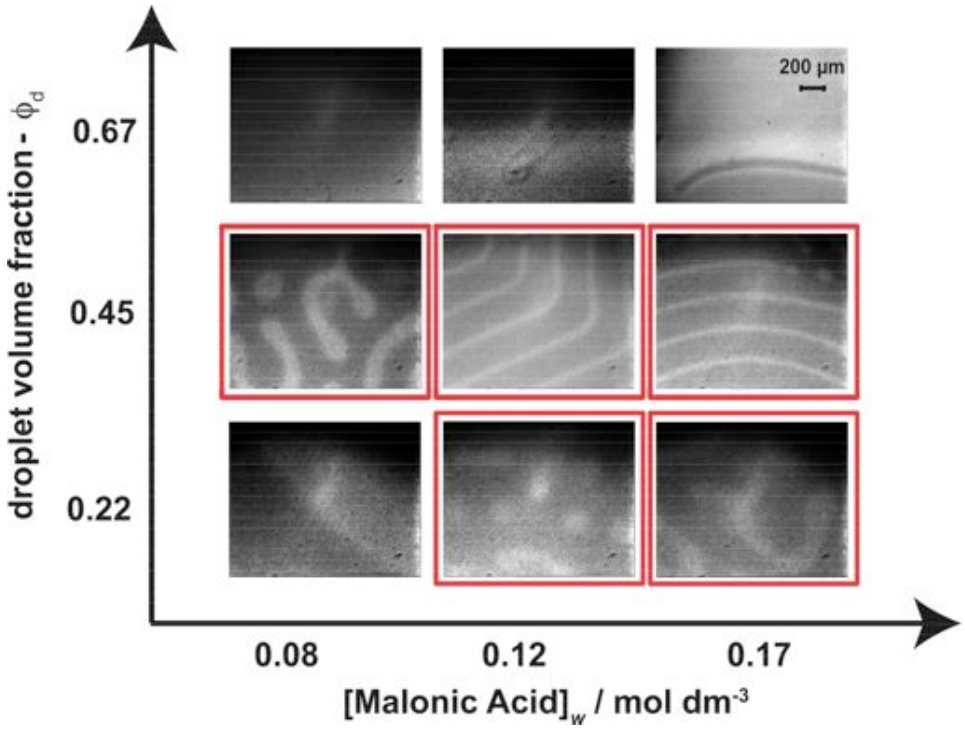

Figure 2.7 Phase diagram showing the variation of pattern types for a small area of the parameter space defined by the aqueous phase concentration of malonic acid and the droplet fraction, ϕ_d, in the ferroin-catalysed BZ-AOT reaction. Patterns that are stationary in time are signified by a red border in the diagram. In all cases [ferroin] = 3.75 mM, [$NaBrO_3$] = 0.25 M, [H_2SO_4] = 0.12 M and ω = 9.2. [MA] = i) 0.08 M, ii) 0.12 M, iii) 0.17 M. ϕ_d = i) 0.22, ii) 0.45, iii) 0.67.

Figure 2.7 shows the variation in the observed pattern type as the concentration of malonic acid and the droplet volume fraction are changed. The other experimental parameters were held constant: [ferroin] = 3.75 mM, [$NaBrO_3$] = 0.25 M, [H_2SO_4] = 0.12 M and ω = 9.2. Stationary patterns are indicated in the diagram by a red border. For reactions performed at ϕ_d = 0.67 and when [MA] = 0.08 M and [MA] = 0.12 M travelling waves and bulk oscillations were observed. In the reaction performed at [MA] = 0.17 M and ϕ_d = 0.67, accelerating waves were observed, where two separate wave fronts accelerate as they approach each other (Figure 2.8).

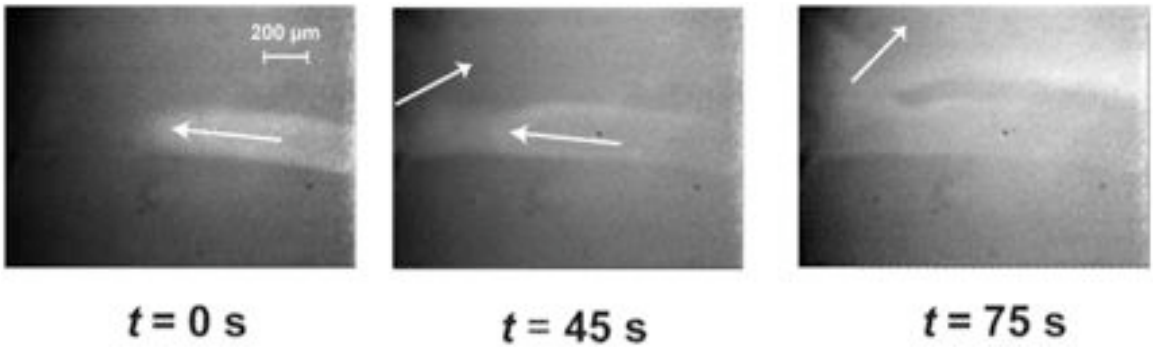

Figure 2.8 Image sequence showing accelerating wave fronts in the ferroin-catalysed BZ-AOT system. In the first image, a narrow wave front approaches from the right of the image. In the second image a "bridge" is formed between this wave front and another wave front approaching from the left of the image. In the third image, the two wave fronts have merged and continue to propagate in a different direction to each of the initial fronts, indicated by the arrows. [ferroin] = 3.75 mM, [$NaBrO_3$] = 0.25 M, [H_2SO_4] = 0.12 M, [MA] = 0.17 M, ϕ_d = 0.67 and ω = 9.2.

A variety of striped and spotted stationary Turing patterns were observed in reactions performed at ϕ_d = 0.45 and ϕ_d = 0.22. By changing [MA] it was possible to control the spacing between the stationary structures. This is discussed further in Section 2.3.3. Stationary patterns were only ever observed when the droplet fraction, ϕ_d, was below the percolation threshold ($\phi_d < 0.5$). Below the percolation threshold, the diffusion rates of polar species residing within the droplet are determined by the diffusion rate of droplet as a whole. Non-polar species such as Br_2 and the BrO_2• radical reside within the continuous oil phase and diffuse much more rapidly. Turing patterns may only arise when there is a significant difference between the diffusion rates of two chemical species within the reaction, namely the activator and the inhibitor[12]. Above the percolation threshold, individual droplets aggregate to form bicontinuous structures. Diffusion rates of polar and non-polar species are now comparable[17] and the formation of Turing patterns is precluded.

2.3.2.2. Patterns in the $Ru(bpy)_3$ BZ-AOT system

The $Ru(bpy)_3$-catalysed BZ-AOT reaction is potentially the most suitable variant of the reaction with which to study pattern formation in the BZ-AOT system using MRI. The $Ru(bpy)_3$ catalyst has been extensively studied in the aqueous BZ reaction[18-20] and more recently in the BZ-AOT system[21,22]. Its role as a catalyst and a redox indicator of the reaction is, therefore, well established and understood. In its reduced form, the catalyst is orange in aqueous solution. In its oxidised form, $[Ru(bpy)_3]^{3+}$, the catalyst is green. The catalyst is thus able to provide sufficient optical contrast with which to visualise chemical patterns and waves[18]. It has also been shown that $Ru(bpy)_3$ is able to act as an MRI contrast agent in the aqueous BZ reaction[14]. In the BZ-AOT reaction, use of the catalyst has given rise to an extended range of patterns including stationary Turing type patterns and other types of spatial patterns previously unseen in the BZ system. It would appear then, that the $Ru(bpy)_3$ catalyst is able to fulfil all three requirements for a suitable catalyst/indicator outlined at the beginning of this chapter. As with the ferroin-catalysed system, the intention of the work done in this study was, firstly, to be able to reproduce a variety of the pattern types observed in the $Ru(bpy)_3$ system, in particular, the stationary type patterns. The second objective was to be able to use the tunability of the system to control the wavelength of the patterns produced, so as to produce patterns with sufficiently large dimensions to be observable using MRI. The system described by Vanag *et al*[21] was used as the starting point for investigation into the $Ru(bpy)_3$-catalysed BZ-AOT system.

In general, patterns were observed in the $Ru(bpy)_3$-catalysed system after a brief induction period, during which bulk oscillations were observed. After this, trigger waves were observed, as with the ferroin-catalysed system, originating from the edge of the reactor. Typically, the contrast between the reduced and oxidised states of the $Ru(bpy)_3$-catalysed reaction was not as distinct as with the ferroin catalyst and deteriorated further during the course of the reaction. Patterns were observable for approximately 1-2 hours.

A number of travelling wave patterns were observed in the $Ru(bpy)_3$-catalysed system. Figure 2.9 shows travelling target waves propagating outwards from a pacemaker site. The spacing between the waves is approximately 220 μm and they propagate at around 235 μm min^{-1}.

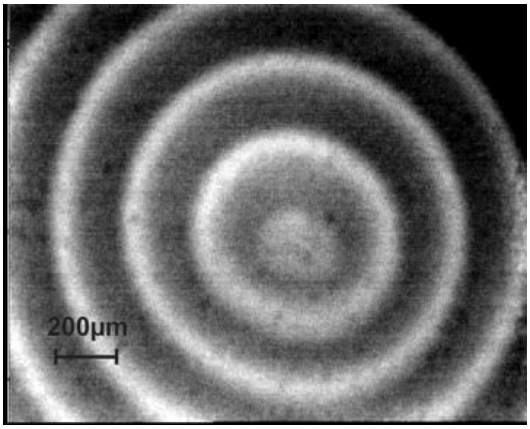

Figure 2.9 Travelling target waves in the $Ru(bpy)_3$-catalysed BZ-AOT reaction. The waves in this image are propagating outwards from the central pacemaker. [$Ru(bpy)_3$] = 3.75 mM, [MA] = 0.25 M, [$NaBrO_3$] = 0.25 M, [H_2SO_4] = 0.4 M, ϕ_d = 0.67, ω=9.2.

Conversely, Figure 2.10 shows target waves that propagate inwardly. The spacing between bands is slightly larger, approximately 280 μm and propagate more slowly, around 186 μm min^{-1}.

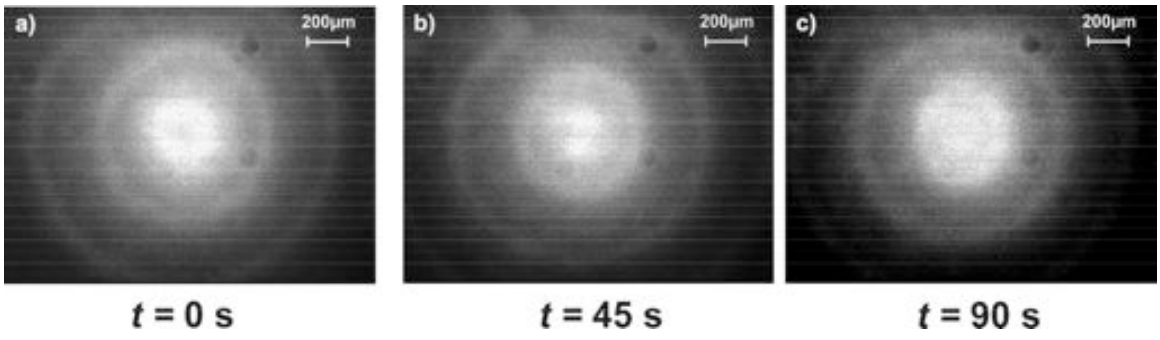

Figure 2.10. Inwardly propagating target waves in the $Ru(bpy)_3$/DPA (diphenylamine 4-sulfonic acid) catalysed BZ-AOT reaction. Waves propagate inwards toward the antipacemaker site at the centre of the "target". $[Ru(bpy)_3]$ = 4.0 mM, [DPA] = 0.25 mM [MA] = 0.2 M, $[NaBrO_3]$ = 0.3 M, $[H_2SO_4]$ = 0.32 M, ϕ_d = 0.35, ω = 9.2

One of the more striking pattern types observed in the $Ru(bpy)_3$ system were rotating spiral waves. Figure 2.11 shows an example of a spiral wave. In this example, the spiral completes about 2.3 rotations per minute with a distance of about 260 μm between each band of the spiral. Outwardly rotating spirals were observed frequently in our $Ru(bpy)_3$-catalysed reactions. Inwardly rotating spirals have been reported[10] in $Ru(bpy)_3$-catalysed reactions performed at droplet fractions above the percolation threshold, however this behaviour was not observed here.

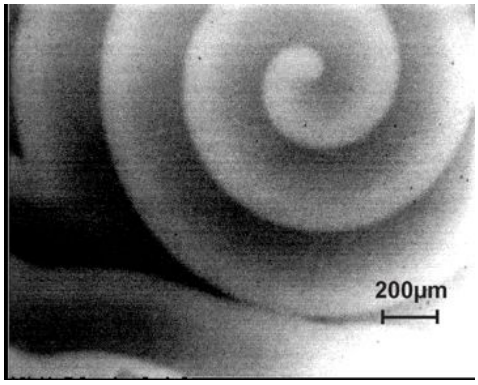

Figure 2.11 Rotating spiral waves in the $Ru(bpy)_3$-catalysed BZ-AOT reaction. The spiral above rotates in a clockwise direction. $[Ru(bpy)_3]$ = 3.75 mM, $[H_2SO_4]$ = 0.6 M, $[NaBrO_3]$ = 0.25 M, [MA] = 0.25 M, ϕ_d = 0.45, ω = 9.2.

Stationary Turing patterns were also observed in the $Ru(bpy)_3$-catalysed system. Figure 2.12 shows an example of stationary spot Turing patterns that evolve from stationary bands over time. The Turing wavelength in this case is approximately 160 μm. Figure 2.13 shows an example of stationary labyrinth type Turing patterns with a Turing wavelength of around 200 μm. Figure 2.14 shows an example of stationary Turing patterns with a larger Turing wavelength, around 350 μm. As with the ferroin-catalysed BZ-AOT system, it was possible to control the Turing wavelength by changing the concentration of malonic acid (refer to Section 2.3.3).

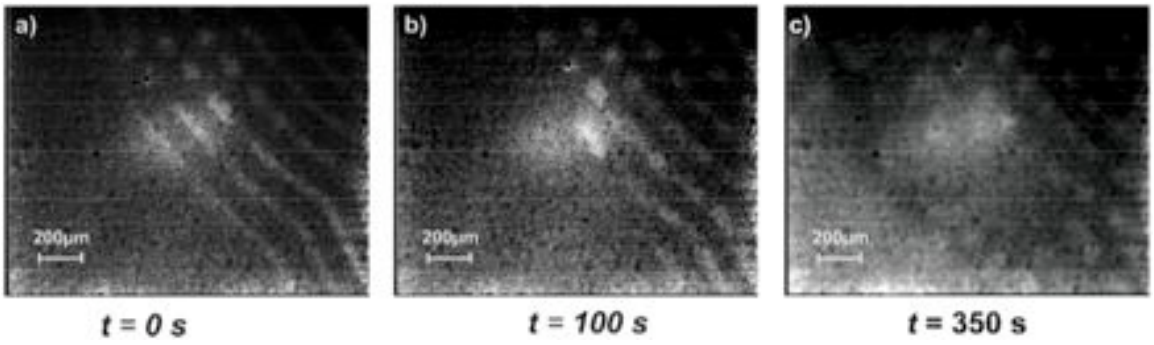

Figure 2.12 Evolution of stationary stripe patterns into stationary spots in the $Ru(bpy)_3$-catalysed BZ-AOT system. In a) a travelling wave front has approached the existing stationary waves. The travelling wave decelerates and becomes stationary. Each subsequent travelling wave settles at a periodic distance (the Turing wavelength) away from the previous wave front. The stripes are unstable and over time they evolve and segment into stationary spots as seen in b) and c). $[Ru(bpy)_3]$ = 3.75 mM, $[H_2SO_4]$ = 0.12 M, $[NaBrO_3]$ = 0.25 M, [MA] = 0.25 M, ϕ_d = 0.35, ω = 9.2

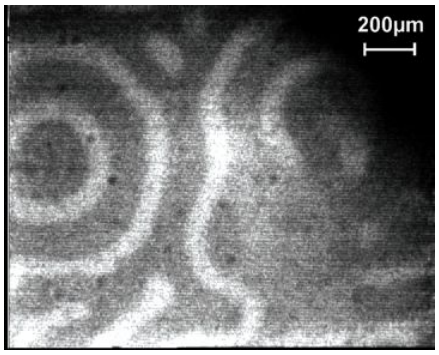

Figure 2.13 Stationary labyrinth patterns in the $Ru(bpy)_3$-catalysed BZ-AOT system. $[Ru(bpy)_3]$ = 3.75 mM, $[H_2SO_4]$ = 0.12 M, $[NaBrO_3]$ = 0.25 M, [MA] = 0.17 M, ϕ_d = 0.45, ω = 9.2

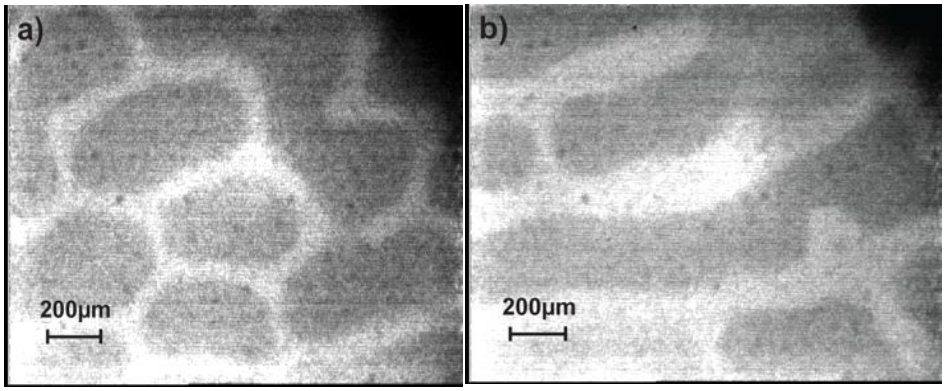

Figure 2.14 Examples of stationary labyrinth type patterns in the $Ru(bpy)_3$-catalysed BZ-AOT reaction. In this experiment the concentration of malonic acid was minimized to produce patterns with larger scale features. Both a) and b) are images taken of the same reaction at different locations in the reactor. [$Ru(bpy)_3$] = 3.75 mM, [H_2SO_4] = 0.12 M, [$NaBrO_3$] = 0.25 M, [MA] = 0.08 M, ϕ_d = 0.45, ω = 9.2.

A phase diagram of the variation in patterns as the parameters [MA] and ϕ_d were varied is shown in Figure 2.15. For these experiments, [$Ru(bpy)_3$] = 3.75 mM, [$NaBrO_3$] = 0.25 M, [H_2SO_4] = 0.12 M and ω = 9.2. Stationary patterns are indicated in the diagram by a red border. As with the ferroin-catalysed system, stationary patterns were not observed above the droplet percolation threshold. For the observation of Turing patterns, the concentration of sulphuric acid had to be reduced with respect to the value published by Vanag and Epstein[21]; [H_2SO_4] = 0.12 M in our results compared to [H_2SO_4] = 0.32 M. However, this is in qualitative agreement with a table published by Vanag[8], where Turing patterns are observed when the value of the ratio ([H_2SO_4][$NaBrO_3$])/[MA] is low. At higher values of this parameter, other non-stationary type patterns were observed.

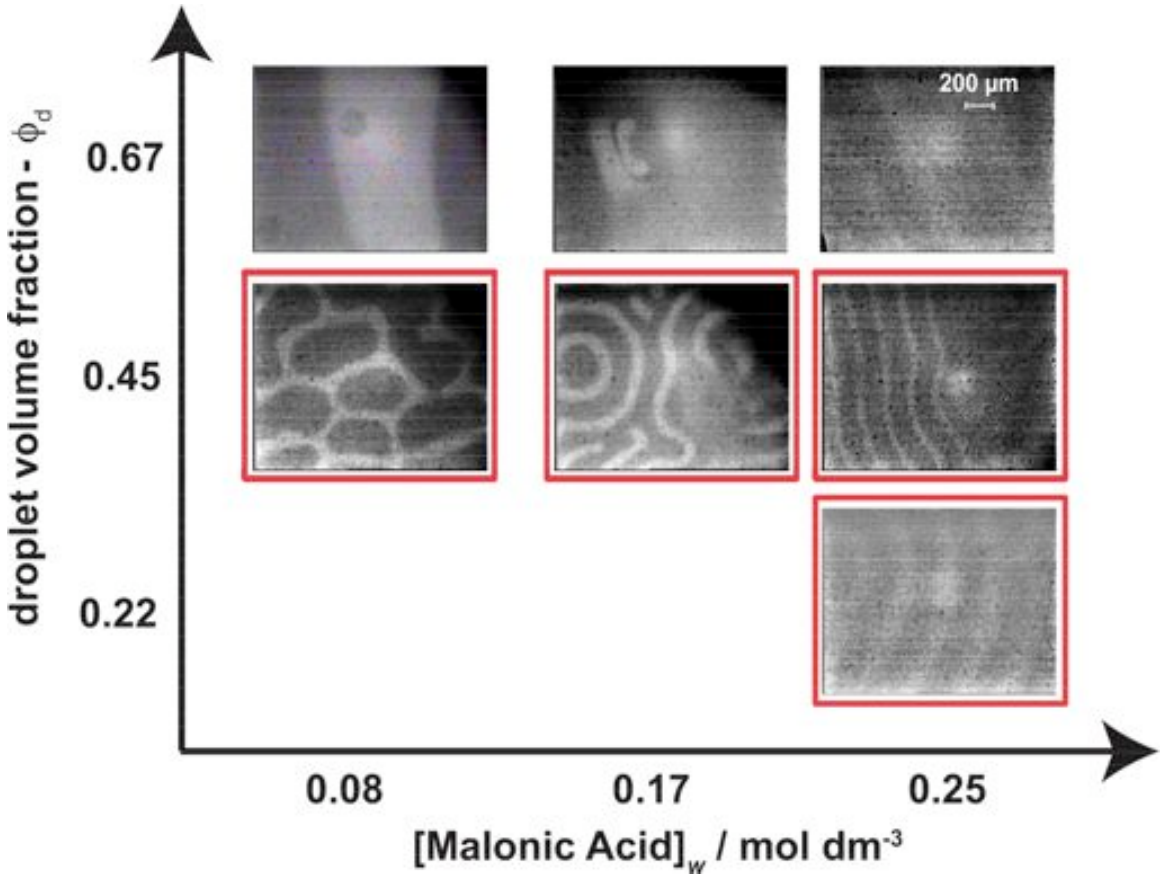

Figure 2.15 Phase diagram showing the variation of pattern types for a small area of the parameter space defined by the aqueous phase concentration of malonic acid and the droplet fraction, ϕ_d, in the Ru(bpy)$_3$-catalysed BZ-AOT reaction. Stationary patterns are denoted by a red border in the diagram. In all cases [Ru(bpy)$_3$] = 3.75 mM, [NaBrO$_3$] = 0.25 M, [H$_2$SO$_4$] = 0.12 M and ω = 9.2. [MA] = i) 0.08 M, ii) 0.17 M, iii) 0.25 M. ϕ_d = i) 0.22, ii) 0.45, iii) 0.67.

2.3.2.3. Patterns in the bathoferroin-catalysed BZ-AOT system

The bathoferroin-catalysed BZ-AOT system has played host to a number of striking and unique pattern types including dash waves[9] segmented spirals[2] and discontinuously propagating type waves[16]. However there have been no observations of stationary Turing patterns in this system, though it has been proposed that dash waves and segmented spiral waves are a form of propagating Turing structure[2]. Figure 2.16 shows an example of propagating dash waves and meandering spiral waves observed as part of this study.

[bathoferroin] = 4.2 mM, [MA] = 0.2 M, [$NaBrO_3$] = 0.15 M, [H_2SO_4] = 0.175 M, ϕ_d = 0.48, ω = 18.5. Unlike the spiral patterns observed in the $Ru(bpy)_3$-catalysed system, the centre point of the spirals observed here are not fixed in space, they move or meander as the spiral rotates.

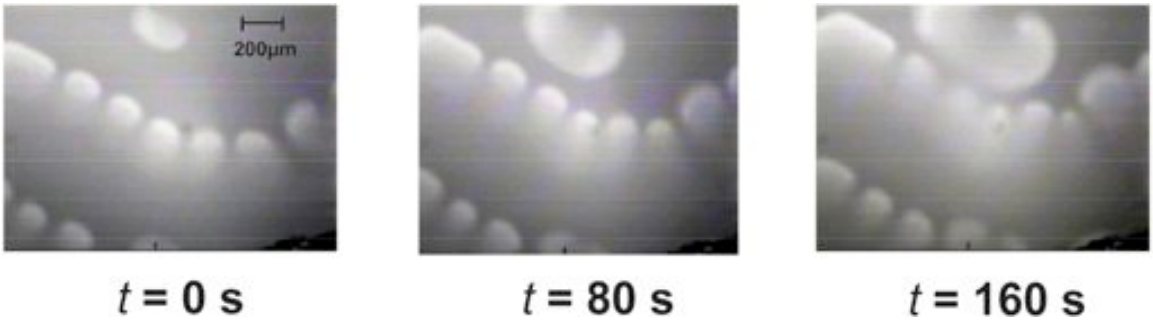

Figure 2.16 Image sequence shows the propagation of a spiral wave (top centre) and a front of dash waves in the bathoferroin-catalysed BZ-AOT system.. As the spiral front and dash wave fronts meet they annihilate. [bathoferroin] = 4.2 mM, [MA] = 0.2 M, [$NaBrO_3$] = 0.15 M, [H_2SO_4] = 0.175 M, ϕ_d = 0.48, ω=18.5.

Standing waves were also observed in the bathoferroin system. [bathoferroin] = 5 mM, [H_2SO_4] = 0.21 M, [$NaBrO_3$] = 0.18 M, [MA] = 0.25 M, ϕ_d = 0.47 and ω = 15. Figure 2.17 shows an example of this phenomenon. At first the motion of the spots appears to be random, however their position is periodic, as can be seen by comparing images a) and c) in Figure 2.17. The spacing between the spots was around 250 μm and the time period for this system was approximately 5 minutes.

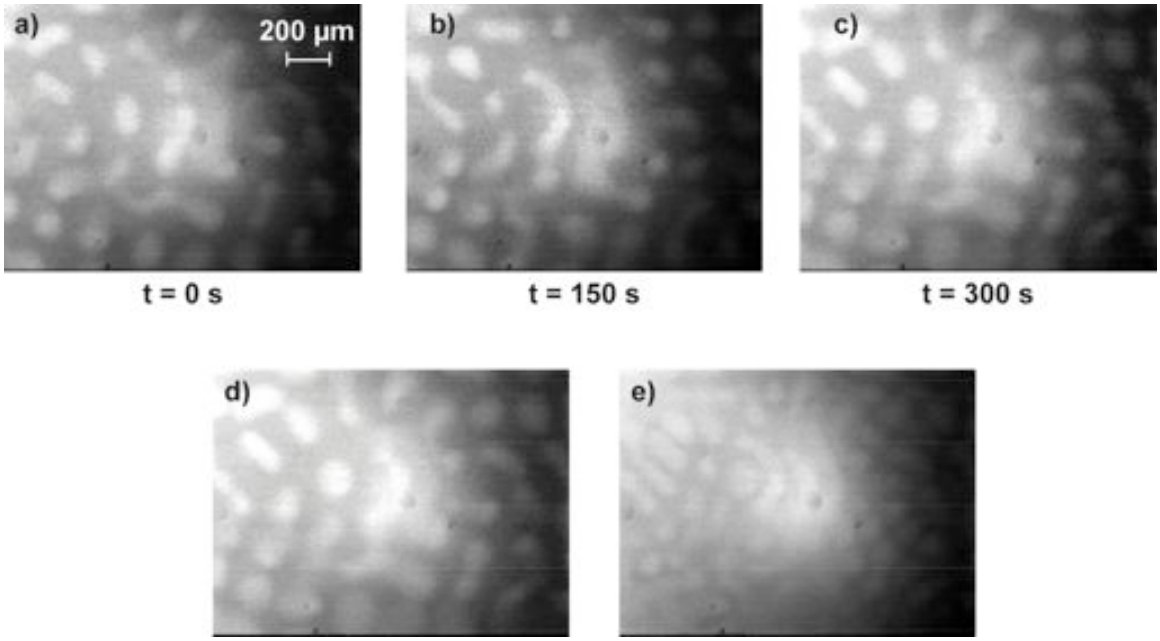

Figure 2.17 Standing waves observed in the bathoferroin-catalysed BZ-AOT system. Image a) shows the state of the system at t = 0. Images b) and c) show the system after t = T/2 and t = T, respectively, where T is the period of the standing wave. Image d) shows the summation of images a) and c), showing the system appears unchanged after a period T. Image e) shows the summation of images a) and c) and shows how the spots in image b) appear in the gaps of image a). [bathoferroin] = 5 mM, [H_2SO_4] = 0.21 M, [$NaBrO_3$] = 0.18 M, [MA] = 0.25 M, ϕ_d = 0.47 and ω = 15.

Figure 2.18 shows a phase diagram constructed for the bathoferroin-catalysed system in similar fashion to those for the ferroin and $Ru(bpy)_3$ systems. A variety of travelling waves and bulk oscillations were observed for all areas of the parameter space. Travelling waves typically moved at velocities of 50-100 µm min^{-1} and bulk oscillations at around 1000 µm min^{-1}.

For the reaction performed at [MA] = 0.17 and ϕ_d = 0.45, a localised oscillon was observed. This is a structure that is stationary in space and oscillatory in time. The period of its oscillation was around 25 minutes. Oscillons are thought to arise from the presence of microscopic dust particles that cause a localised perturbation of the system[23]. As a general observation, the observed

contrast in reactions performed using the bathoferroin-catalysed system was perhaps the best of all the catalyst systems studied and patterns were observable for up to 3 hours.

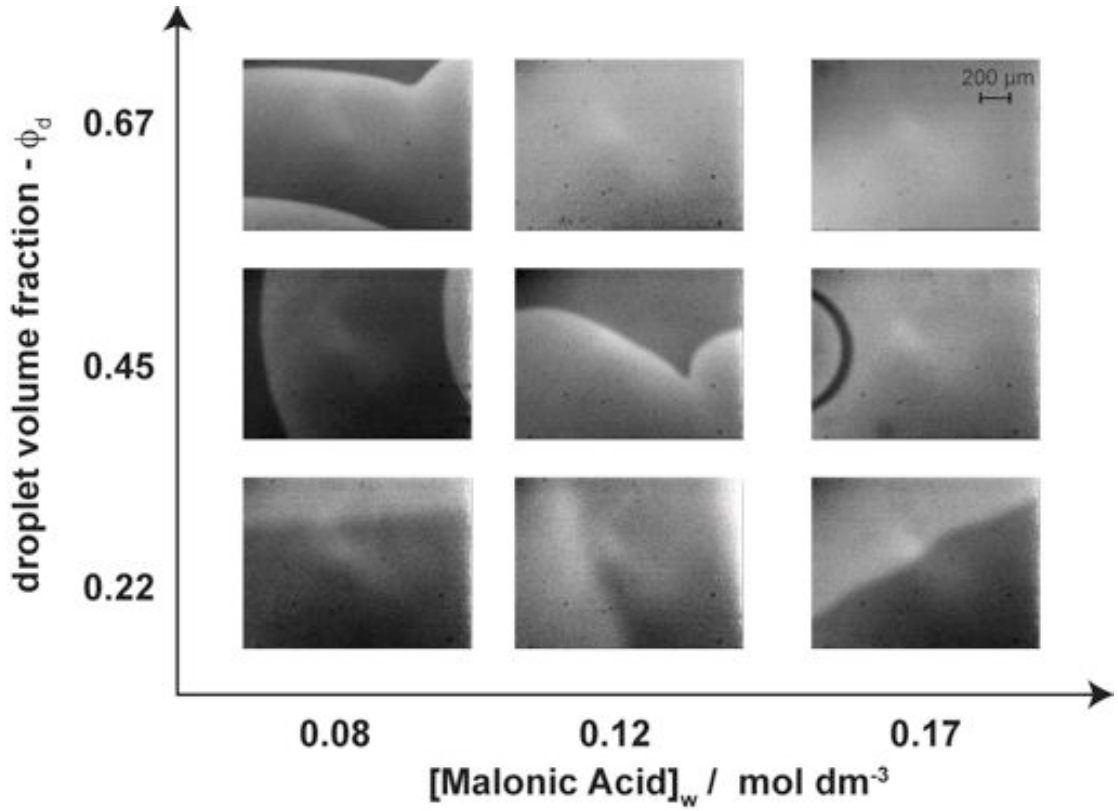

Figure 2.18 Phase diagram showing the variation of pattern types for a small area of the parameter space defined by the aqueous phase concentration of malonic acid and the droplet fraction, ϕ_d, in the bathoferroin-catalysed BZ-AOT reaction. In all cases [bathoferroin] = 3.75 mM, [$NaBrO_3$] = 0.25 M, [H_2SO_4] = 0.12 M and ω = 9.2. [MA] = i) 0.08 M, ii) 0.12 M, iii) 0.17 M. ϕ_d = i) 0.22, ii) 0.45, iii) 0.67.

2.3.2.4. Patterns in the manganese/ferroin dual catalyst BZ-AOT system

The manganese-catalysed BZ reaction has received less attention than the ferroin and $Ru(bpy)_3$-catalysed reactions, particularly with respect to optical imaging of chemical patterns and waves. Clearly, the main reason for this is the lack of significant visual contrast between the reduced and oxidised forms

of the manganese ion; aqueous solutions of Mn^{2+} are colourless and Mn^{3+} solutions are pink/purple in colour. However, at the catalyst concentrations typically employed in the BZ reaction, the observable difference between the reduced and oxidised forms is insufficient to observe patterns. By adding a small amount of ferroin indicator to the manganese-catalysed, phosphoric acid stabilised BZ-AOT reaction it was possible to observe chemical waves. However as the concentration of ferroin was relatively low (0.4 mM) the contrast between the reduced and oxidised states of the reaction was still relatively poor. Figure 2.19 shows an example of travelling waves observed in this system. [$MnSO_4$] = 1.2 mM, [$NaBrO_3$] = 0.1 M, [H_2SO_4] = 0.3 M, [H_3PO_4] = 0.2 M, [MA] = 0.1 M, ϕ_d = 0.45 and ω = 9.2. As can be seen the degree of contrast is poor as the concentration of ferroin was low. The wave velocity in this example is around 400 μm min^{-1}. No other pattern types were observed in this system, although this may be due, in part, to the lack of visual contrast available.

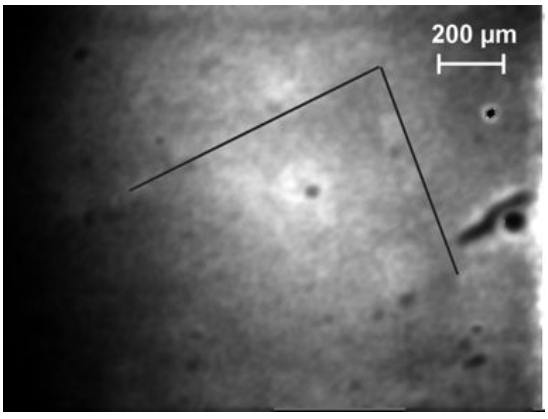

Figure 2.19 Travelling waves observed in the manganese/ferroin dual catalysed BZ-AOT reaction. The solid black lines indicate the position of the travelling wave fronts. [$MnSO_4$] = 1.2 mM, [$NaBrO_3$] = 0.1 M, [H_2SO_4] = 0.3 M, [H_3PO_4] = 0.2 M, [MA] = 0.1 M, ϕ_d = 0.45 and ω = 9.2.

2.3.2.5. Theoretical interpretation of patterns in the BZ-AOT system

Much of the pattern forming behaviour of the BZ-AOT system has been simulated using a simple model that combines the positive and negative feedback mechanisms of the BZ reaction kinetics with the compartmentalisation of key reaction intermediates between the aqueous and oil phases[24]. The variables of the Oregonator model[25], used to model the aqueous reaction, are extended to account for transfer of species between aqueous and oil phases, and the greater diffusion coefficients of species soluble in the oil phase, namely BrO_2 and Br_2. The resultant six-variable model has been able to reproduce the pattern-forming phenomena, such as dash-waves, packet waves, localised oscillons, spirals and anti-spirals, that have been observed experimentally.

2.3.2.6. Comparison with the aqueous BZ reaction

Travelling waves and target patterns are readily observed in a Petri dish containing a thin layer of the BZ reaction[26]. Travelling spiral waves can be observed if a system containing target patterns is perturbed for example by tilting the reaction or dragging a needle through the reaction solution[24]. Interaction between multiple fronts of travelling waves can lead to some relatively complex formations of patterns, Figure 2.20. However, beyond these pattern types, none of the rich variety of patterns observable in the BZ-AOT reaction is observed in the aqueous BZ reaction. The diversity and increased complexity of patterns observed in the AOT system arises due to the partitioning of polar and non-polar species between the aqueous droplet phase and the continuous organic phase respectively[11].

Figure 2.20 Target patterns observed in a Petri dish filled with a thin layer of the aqueous BZ reaction. Interaction between wave fronts emanating from multiple excitation points results in the formation of relatively complex looking structures. [ferroin] = 4 mM, [MA] = 0.25 M, [$NaBrO_3$] = 0.15 M, [H_2SO_4] = 0.5 M. The diameter of the Petri dish is approximately 8 cm.

2.3.3. Control of pattern wavelength

It was of particular interest to determine how reliably the dimensions (*e.g.* wavelength, width of oxidation fronts, spacing between pattern features *etc.*) of the observed chemical patterns and waves could be manipulated. Ideally, patterns and waves with features measuring in excess of 100 microns would need to be produced in order to image them using a typical MR imaging experiment. It has been reported that the wavelength of Turing patterns observed in the BZ-AOT system is dependent on the bulk concentration of malonic acid ($[MA]_B$) in the system[21], where $[MA]_B$ is equal to the product of the pseudo aqueous phase concentration of the substrate, $[MA]_w$, and the droplet fraction, ϕ_d. Thus, the wavelength of Turing patterns can be decreased if either of $[MA]_w$ or ϕ_d are increased. A series of experiments was performed

where ferroin and $Ru(bpy)_3$-catalysed BZ-AOT microemulsion systems were prepared and ϕ_d and $[MA]_w$ were varied in turn. The concentrations of the other BZ reactants were held constant at values that were known to produce Turing patterns. [catalyst] = 3.75 mM, where catalyst = ferroin or $Ru(bpy)_3$, $[NaBrO_3]$ = 0.25 M, $[H_2SO_4]$ = 0.12 M, ω = 9.2. The characteristic wavelength of any Turing patterns observed was measured. Phase diagrams of the observed patterns are shown in the previous section; Figure 2.7 and Figure 2.15 for ferroin and $Ru(bpy)_3$-catalysed systems respectively. Plots of the Turing wavelength versus the bulk concentration of malonic acid, $[MA]_{bulk}$, are shown in Figure 2.21. As can be seen, for both ferroin and $Ru(bpy)_3$-catalysed systems, an increase in the bulk concentration of malonic acid resulted in a reduction in the Turing wavelength of the patterns.

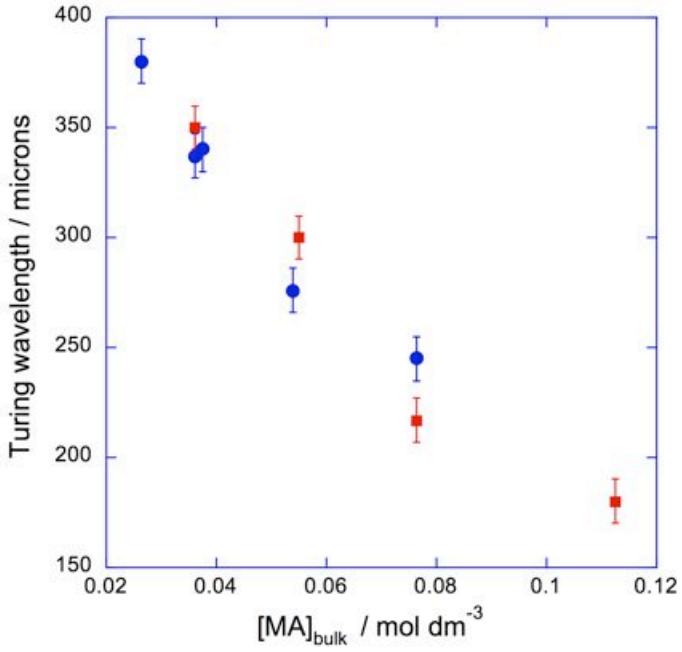

Figure 2.21 Variation in Turing wavelength of stationary patterns with bulk concentration of malonic acid in ferroin- (blue circles) and $Ru(bpy)_3$- (red squares) catalysed BZ-AOT reactions. In all cases [catalyst] = 3.75 mM, [$NaBrO_3$] = 0.25 M, [H_2SO_4] = 0.12 M and ω = 9.2.

2.3.3.1. Wave-front velocity

For imaging of stationary patterns using MRI, control of the pattern wavelength is important as outlined in the previous section. For imaging of transient patterns the wave velocity, *c*, is also an important factor. Table 2.1 shows the measured average wave velocities for some of the transient patterns observed in the BZ-AOT systems studied along with initial concentrations of BrO_3^- and H^+ that determine the autocatalytic reaction rate.

	$[BrO_3^-]$ / mol dm^{-3}	$[H^+]$ / mol dm^{-3}	c / μm min^{-1}
Ferroin (dash waves)	0.15	0.175	40
Bathoferroin (travelling waves)	0.25	0.12	50-100
$Ru(bpy)_3$ (target patterns)	0.25	0.4	235
$Ru(bpy)_3$ (inward target patterns)	0.3	0.32	186
Mn/ferroin (travelling waves)	0.1	0.5	400

Table 2.1 Showing the average wave velocity, *c,* of various transient patterns observed in the BZ-AOT systems studied.

In general, travelling waves in the BZ-AOT system move much more slowly than in the aqueous reaction, and this is because of the smaller diffusion coefficients associated with species contained within the reverse micelles (see Equation 1.2). No attempt was made as part of this study to control the wave velocities of the various systems, however, this may be important to consider for imaging of fast moving transient patterns using MRI.

2.3.4. Enhancement of contrast in the manganese-catalysed BZ reaction using phosphates

The use of a dual catalyst/indicator system such as the manganese/ferroin system, discussed in Section 2.3.2.4 is not entirely satisfactory; it raises the question as to whether the patterns and oscillations observed are catalysed by one or both catalysts, and would different behaviour be observed if either catalyst were present in the system on its own? A more satisfying solution

would be to somehow enhance the intrinsic contrast of the manganese-catalysed system, so that the reduced and oxidised forms are more easily distinguishable from each other. The manganese-catalysed BZ reactions investigated by Cross *et al*[27] use phosphates to stabilise the Mn^{3+} ion via the formation of metal-phosphate complexes, Figure 2.22.

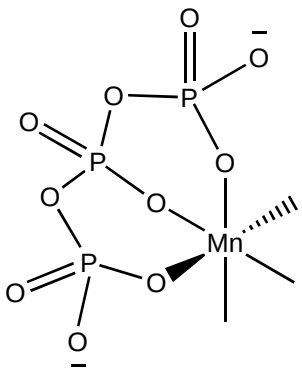

Figure 2.22 Chelate formation between Mn^{3+} ion and the metaphosphate ion $P_3O_{10}^{5-}$. The phosphate ion is able to stabilise the manganese (III) ion with respect to disproportionation.

This stabilisation effects a greater degree of conversion of Mn^{2+} to Mn^{3+} upon oxidation. They exploit this effect to enhance the NMR relaxation time contrast observable in the manganese-catalysed BZ reaction. However, it may also be possible to exploit this effect to enhance the *visual* contrast in an analogous fashion *i.e.* upon oxidation there is a greater conversion of the colourless Mn^{2+} to the pink/purple Mn^{3+}.

Initial investigations into the phosphate-stabilised, manganese-catalysed, BZ reaction centred on the stirred, oscillatory, aqueous system. Oscillations in

redox potential (Figure 2.23) were observed in manganese-catalysed BZ reactions *not* stabilised with phosphate, however there was no discernible visual contrast between the reduced and oxidised states.

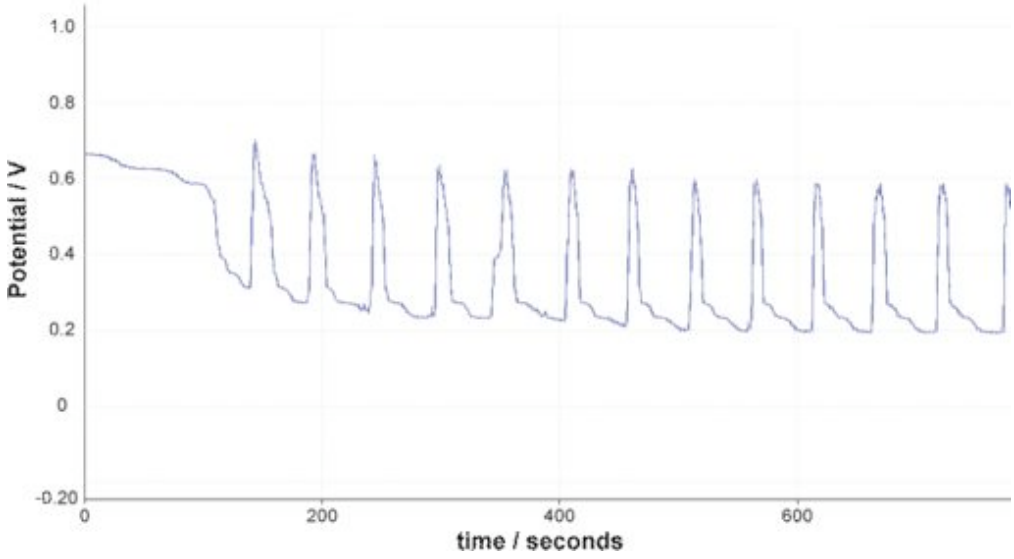

Figure 2.23 Oscillations in redox potential of a stirred, aqueous, manganese-catalysed BZ reaction as measured by a platinum combination electrode. The oscillation period in this case is approximately 50 seconds. [$MnSO_4$] = 1.0 mM, [$NaBrO_3$] = 0.25 M, [MA] = 0.25 M and [H_2SO_4] = 0.12 M.

For each phosphate-stabilised reaction, an attempt was made to quantify the degree of contrast between the reduced and oxidised states of the reaction, as perceived with the naked eye. A four-point scale was used:

i) *No contrast* – the difference between reduced and oxidised states was imperceptible.

ii) *Poor contrast* – there was only a very slight perceptible difference between the reduced and oxidised states.

iii) *Fair contrast* – there was a reasonable difference between reduced and oxidised states.

iv) *Good contrast* – the reduced and oxidised states were clearly distinguishable from each other.

Figure 2.24 shows an example of the level of contrast observed in a manganese-catalysed BZ reaction. In this case the level of contrast was deemed to be fair. Clearly this scale is based on subjective opinion, however, this is not entirely inappropriate, as the ability to visualise chemical patterns and waves using optical methods depends upon the observer's perception of differences between the reduced and oxidised states. Therefore, if oscillations are not observable as an obvious colour change in the stirred system, it is likely that the colour contrast will be insufficient to observe chemical patterns and waves in the unstirred system with the unaided eye. However, by using appropriate optics (interference filters, sensitive CCD cameras) it may be possible to detect even small changes in colour and thus image pattern formation in the manganese-catalysed BZ and BZ-AOT reactions. With this in mind, a more quantitative approach than the four-point scale used above could be employed to measure the observable colour change during the oscillatory reaction. Given more time, this could easily have been achieved using UV/visible spectrophotometry to measure the absorbance of the reaction solution at a given wavelength during the course of the reaction.

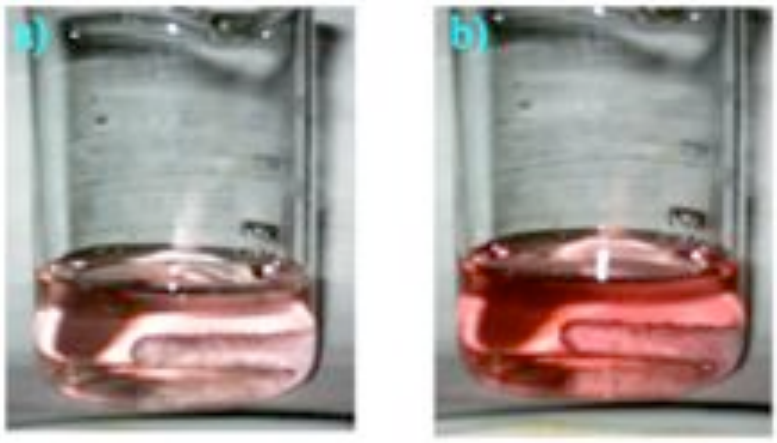

Figure 2.24 Example of the contrast between the reduced a) and oxidised b) states of the aqueous manganese-catalysed BZ system. [$MnSO_4$] = 1.0 mM, [MA] = 0.25 M, [$NaBrO_3$] = 0.25 M, [$Na_5P_3O_{10}$] = 4 mM and [H_2SO_4] = 0.5 M. The above example would be an example of fair contrast between states. Note however, that a degree of colour remains in the reduced state, indicating incomplete reduction of Mn^{3+} to Mn^{2+}.

The effect of increasing the concentration of malonic acid at a given concentration of $MnSO_4$ is summarised in the phase diagram in Figure 2.25. At each concentration of $MnSO_4$, increasing the malonic acid concentration improved the visual contrast between the two oxidative states. At low concentrations of malonic acid, the pink colour of the Mn^{3+} dominated and these solutions retained a degree of colour throughout the oscillation period. At the highest concentration of $MnSO_4$ used, low concentrations of malonic acid resulted in solutions where the pink colour dominated. This suggests that the malonic acid concentration needs to be high enough to effect complete conversion of Mn^{3+} to Mn^{2+} in order to obtain good visual contrast.

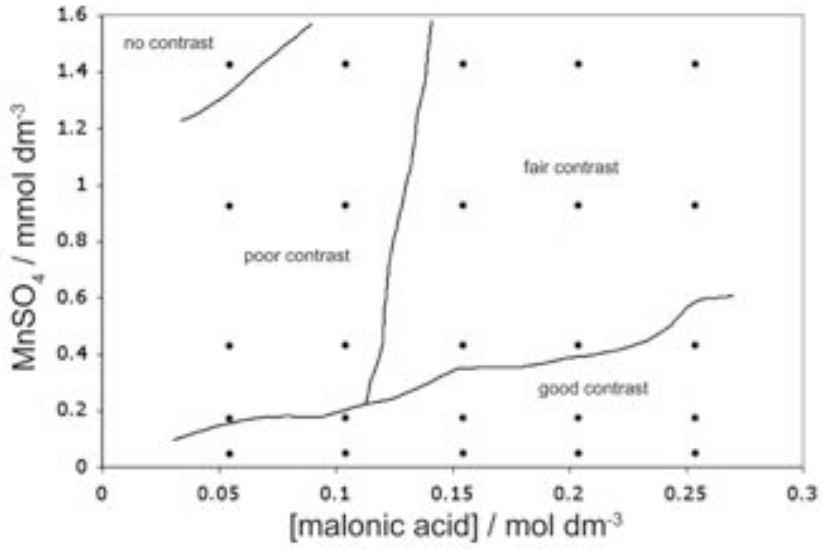

Figure 2.25 Phase diagram showing the degree of colour contrast observed in stirred aqueous BZ reactions catalysed by $MnSO_4$, as the concentrations of malonic acid and $MnSO_4$ were varied. [H_2SO_4] = 0.5 M, [$NaBrO_3$] = 0.25 M and [$Na_5P_3O_{10}$] = 4 mM; [MA] = i) 0.05 M, ii) 0.1 M, iii) 0.15 M, iv) 0.2M, v) 0.25 M; [$MnSO_4$] = (1) 0.1 mM, (2) 0.25 mM, (3) 0.5 mM, (4) 1.0 mM, (5) 1.5 mM. Individual data points (•) are shown on the diagram.

Increasing the concentration of $Na_5P_3O_{10}$ for a given concentration of $MnSO_4$, resulted in a more intense pink colour in the oxidised state. At higher ratios of $Na_5P_3O_{10}$ to $MnSO_4$ the oxidised and reduced states were indistinguishable, with both oxidised and reduced states of the reaction having the same deep pink colour. This suggests that there may be incomplete conversion of Mn^{3+} back to Mn^{2+}, as the phosphate increasingly stabilises Mn^{3+} relative to Mn^{2+}. Figure 2.26 shows the dependence of contrast on the ratio of phosphate to $MnSO_4$ for two different concentrations of $MnSO_4$.

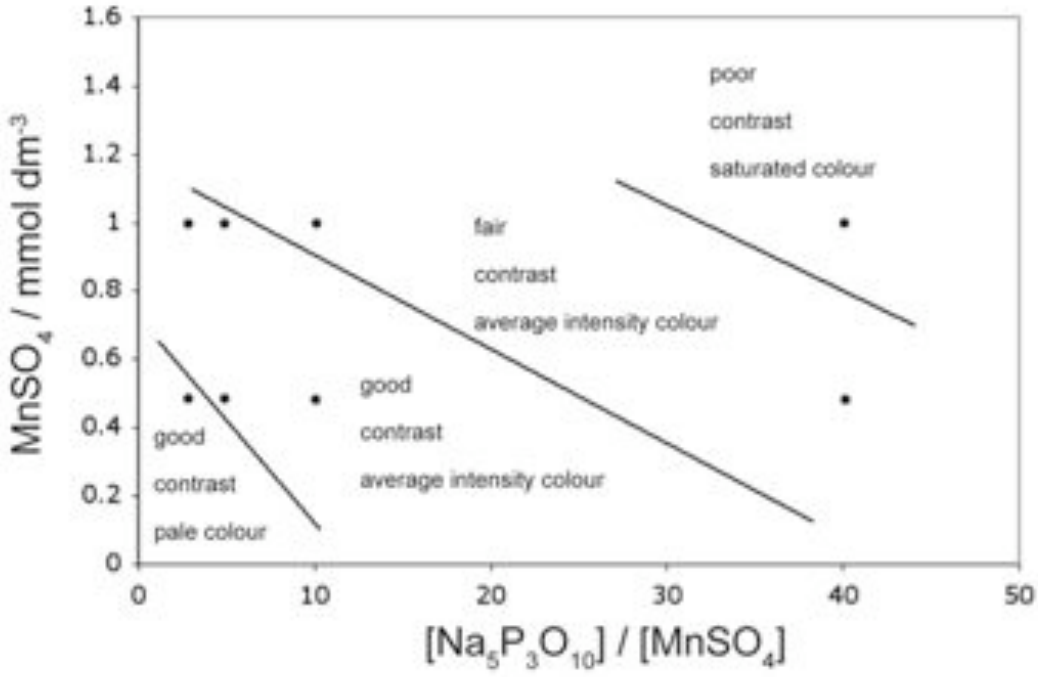

Figure 2.26 Phase diagram showing the degree of colour contrast observed in stirred aqueous manganese-catalysed phosphate stabilised BZ reaction as the ratio of $[Na_5P_3O_{10}]$:$[MnSO_4]$ was changed. Two subjective observations are made in each case; firstly the degree of colouration is assessed *i.e.* the intensity of the pink colour; secondly, the degree of contrast between the reduced and oxidised states is judged. $[NaBrO_3]$ = 0.22 M, [MA] = 0.18 M, $[H_2SO_4]$ = 0.5 M; $[Na_5P_3O_{10}]$ / $[MnSO_4]$ = i) 2, ii) 4, iii) 10, iv) 40; $[MnSO_4]$= (1) 0.5 mM, (2) 1.0 mM. Individual data points (•) are shown on the diagram.

Although it was possible to increase the degree of contrast by adding $Na_5P_3O_{10}$, there was still insufficient contrast available to observe two-dimensional patterns in a Petri dish containing the manganese-catalysed aqueous BZ reaction.

2.3.5. Observation of oscillations in the manganese-catalysed BZ-AOT reaction using UV/vis spectroscopy

When the manganese-catalysed BZ reaction is performed in the AOT microemulsion system the bulk concentration of the manganese catalyst is reduced, (recalling that the bulk concentration is equal to the product of the pseudo-aqueous phase concentration and the droplet fraction, $[MnSO_4]_B = \phi_d[MnSO_4]_w$). Thus, the ability to observe oscillations in the oxidation state of manganese, as a colour change, is further diminished with respect to the aqueous system. Oscillations can, however, be monitored by following the absorbance at a particular wavelength using UV/vis spectrophotometry.

Figure 2.27 shows the UV/vis absorption spectra recorded for a manganese-catalysed phosphate-stabilised BZ-AOT reaction in its reduced and oxidised states. $[MnSO_4]$ = 1.2 mM, [MA] = 0.15 M, $[NaBrO_3]$ = 0.10 M, $[Na_5P_3O_{10}]$ = 45 mM and $[H_2SO_4]$ = 0.17 M ϕ_d = 0.45, ω = 9.2. Figure 2.28 a) shows temporal oscillations in the oxidation state of the manganese catalyst at λ = 265nm. The period of the oscillations is long at around 17 minutes. This may be due to the inefficiency of the stirring; a small magnetic “flea” was required to fit into the sample cuvette and the microemulsion is quite viscous. The absorbance maximum is at 265 nm, however, this wavelength corresponds to the near UV region and is outside the detection limits of both the human eye and the CCD camera used for optical imaging experiments. As can be seen from Figure 2.27 however, the absorption is broad and there is still a difference in the absorbance at 334 nm. Figure 2.28 b) shows temporal oscillations in the absorbance measured at 334 nm. This wavelength corresponds to the

shortest wavelength narrow bandpass interference filter available from Edmund Optics Ltd, compatible with the optical imaging apparatus described previously. It may therefore be possible to image patterns in the manganese-catalysed BZ-AOT system by using a CCD camera that has sensitivity in this region of the electromagnetic spectrum.

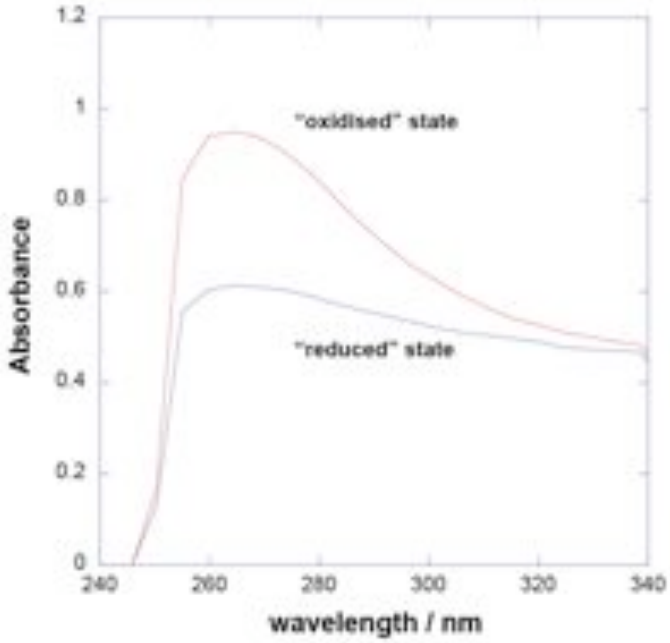

Figure 2.27 UV/vis absorption spectra of a stirred $MnSO_4$ catalysed, phosphate-stabilised, BZ-AOT reaction taken at different points during the oscillation period. The "oxidised" state spectrum was acquired when the absorbance at λ = 265 nm had reached its maximum value. The "reduced" state spectrum was acquired at the minimum value of absorbance at 265 nm. [$MnSO_4$] = 1.2 mM, [MA] = 0.15 M, [$NaBrO_3$] = 0.10 M, [$Na_5P_3O_{10}$] = 45 mM and [H_2SO_4] = 0.17 M ϕ_d = 0.45, ω = 9.2.

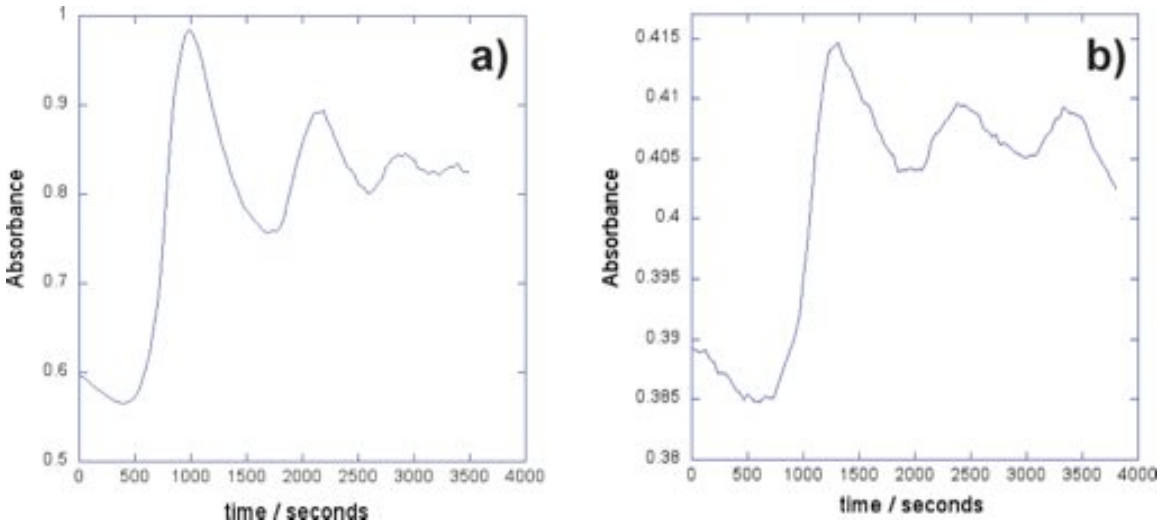

Figure 2.28 Temporal oscillations in the UV/vis absorbance, at a) λ = 265 nm and b) 334 nm, of a stirred $MnSO_4$ catalysed, phosphate-stabilised, BZ-AOT reaction. [$MnSO_4$] = 1.2 mM, [MA] = 0.15 M, [$NaBrO_3$] = 0.10 M, [$Na_5P_3O_{10}$] = 45 mM and [H_2SO_4] = 0.17 M. ϕ_d = 0.45, ω = 9.2.

2.4. Conclusions

The formation of chemical patterns and waves has been investigated in the BZ-AOT system using established optical imaging techniques. A variety of pattern types have been reproduced across a number of different catalyst/indicator systems. The "tunability" of the AOT microemulsion, *i.e.* the ability to control the concentration and size of the water droplets in the microemulsion, has been used to control the types of patterns that are formed. Stationary Turing patterns have been observed in the ferroin- and $Ru(bpy)_3$-catalysed reactions, and the Turing wavelength of these patterns has been manipulated by variation of the bulk concentration of malonic acid in the reaction.

The manganese-catalysed BZ-AOT system has been studied for the first time. The enhancement of visual contrast using phosphoric acid and phosphate has been investigated. It has been shown that colour contrast in the manganese-catalysed BZ reaction can be enhanced through the addition of metaphosphate and that it may be possible to optically image patterns in such a system.

2.5. References

(1) Epstein, I. R.; Vanag, V. K. “Complex patterns in reactive microemulsions: Self-organized nanostructures?”; Workshop on Self-Organization-Initiative Nano-Engineering (SINE), 2005, Wako, JAPAN.

(2) Vanag, V. K.; Epstein, I. R. *Proceedings Of The National Academy Of Sciences Of The United States Of America* **2003**, *100*, 14635.

(3) Torchilin, V. P. *Nano Today* **2007**, *2*, 54.

(4) Gao, Y.; Forsterling, H. D. *Journal Of Physical Chemistry* **1995**, *99*, 8638.

(5) http://www.viewcast.com/products/osprey-100

(6) Stopmotion Maker; 1.09 ed.; Stopmotion Maker.com.

(7) Quicktime Pro; 7.6 ed.; Apple.

(8) Vanag, V. K. *Physics-Uspekhi* **2004**, *47*, 923.

(9) Vanag, V. K.; Epstein, I. R. *Physical Review Letters* **2003**, *90*.

(10) Vanag, V. K.; Epstein, I. R. *Science* **2001**, *294*, 835.

(11) Vanag, V. K.; Epstein, I. R. *Physical Review Letters* **2001**, *87*.

(12) Turing, A. M. *Philosophical Transactions Of The Royal Society Of London Series B-Biological Sciences* **1952**, *237*, 37.

(13) Zhabotinsky, A. M. *Nature* **1970**, *225*, 535.

(14) Gao, Y.; Cross, A. R.; Armstrong, R. L. *Journal Of Physical Chemistry* **1996**, *100*, 10159.

(15) Brandt, W. W.; Dwyer, F. P.; Gyarfas, E. D. *Chemical Reviews* **1959**, *54*, 959.

(16) Cherkashin, A. A.; Vanag, V. K.; Epstein, I. R. *The Journal of Chemical Physics* **2008**, *128*, 204508.

(17) Schwartz, L. J.; DeCiantis, C. L.; Chapman, S.; Kelley, B. K.; Hornak, J. P. *Langmuir* **1999**, *15*, 5461.

(18) Bolletta, F.; Prodi, L.; Zaccheroni, N. *Inorganica Chimica Acta* **1995**, *233*, 21.

(19) Yatsimirskii, K. B.; Tikhonova, L. P. *Coordination Chemistry Reviews* **1985**, *63*, 241.

(20) Demas, H. N.; Diemente, D. *Journal of Chemical Education* **1973**, *50*, 357.

(21) Kaminaga, A.; Vanag, V. K.; Epstein, I. R. *Journal Of Chemical Physics* **2005**, *122*.

(22) McIlwaine, R.; Vanag, V. K.; Epstein, I. R. *Physical Chemistry Chemical Physics* **2009**, *11*, 1581.

(23) Vanag, V. K.; Epstein, I. R. *Physical Review Letters* **2004**, *92*, 128301.

(24) Epstein, I. R.; Vanag, V. K. *Chaos: An Interdisciplinary Journal of Nonlinear Science* **2005**, *15*, 047510.

(25) Field, R. J.; Noyes, R. M. *The Journal of Chemical Physics* **1974**, *60*, 1877.

(26) Epstein, I. R.; Pojman, J. A. *An Introduction to Nonlinear Chemical Dynamics: Oscillations, Waves, Patterns, and Chaos* Oxford University Press: New York, 1998.

(27) Cross, A. R.; Armstrong, R. L.; Reid, A.; Su, S. Y.; Menzinger, M. *Journal Of Physical Chemistry* **1995**, *99*, 16616.

Chapter 3. Nuclear Magnetic Resonance studies of the $Ru(bpy)_3$ catalysed BZ-AOT microemulsion system

3.1. Introduction

Image contrast in MRI is often obtained by exploiting differences in the relaxation times of solvent water molecules in different environments[1]. Differences in the spin-lattice (T_1) and spin-spin (T_2) relaxation times can be used to provide T_1- and T_2-weighted images respectively. Both T_1 and T_2 are sensitive to the presence of paramagnetic species present in the system. Thus, relaxation measurements can be used to detect changes in oxidative states of paramagnetic ions provided the degree of paramagnetism is different in each oxidation state.

$Ru(bpy)_3$ has previously been used as an MRI contrast indicator in aqueous BZ reactions[2] by Gao *et al*. They were able to demonstrate that image contrast should be obtainable using either T_1- or T_2-weighting methods, by measuring the T_1 and T_2 relaxivities of $Ru(bpy)_3$ in its reduced and oxidised states. They were subsequently able to obtain both one- and two-dimensional T_1-weighted images of travelling waves, utilising the relaxivity measurements to set the imaging parameters for optimal contrast.

In this chapter, the feasibility of using the $Ru(bpy)_3$ catalyst as an indicator/catalyst for the BZ-AOT system is assessed. The catalyst complex is

first characterised in terms of its NMR relaxivity in both its reduced and oxidised states and also in aqueous and AOT microemulsion media. Results are then presented that show that the AOT microemulsion medium has a detrimental effect on the ability of the $Ru(bpy)_3$ complex to act as an MR active contrast indicator for the BZ-AOT reaction. In an effort to elucidate the origin of this effect, 2-D NMR-NOESY spectroscopy and DLS measurements are used in conjunction with the relaxivity measurements performed, to probe the physical structure of the microemulsion system and investigate the interaction between the reverse micelles and the $Ru(bpy)_3$ complex. The implications of these results are discussed with respect to the use of the complex as an MR contrast indicator and also how the choice of catalyst and the tunability of the microemulsion structure affect pattern formation in the BZ-AOT system.

3.2. Experimental

3.2.1. Relaxivity measurements of the aqueous $Ru(bpy)_3$ system

3.2.1.1. Preparation of aqueous samples of $[Ru(II)(bpy)_3]SO_4$

In the present study, the relaxivity of $[Ru(II)(bpy)_3]$ was first measured in aqueous solution. Aqueous samples of $[Ru(II)(bpy)_3]SO_4$ were prepared by dilution of a stock solution of 0.020 mol dm^{-3} $[Ru(II)(bpy)_3]SO_4$. The sulfato salt was prepared from the chloride salt of the complex ($[Ru(II)(bpy)_3]Cl_2$ (Aldrich)) using the method outlined by Gao and Försterling[3]. The chloride salt was dissolved in the minimum amount of water and the sulfato salt was precipitated by dropwise addition of a 5 M solution of sulphuric acid. The

sulphate salt was collected via filtration and left to dry in a desiccator for several days. The stock solution was kept in a foil wrapped volumetric flask out of direct sunlight and was used within a few days of its initial preparation. Oxidised forms of $Ru(bpy)_3$ *i.e.* $[Ru(bpy)_3]^{3+}$ were prepared by addition of solid PbO_2 (Aldrich) to the reduced form samples. Excess solid was removed by filtration and samples were used immediately.

3.2.1.2. Preparation of aqueous samples of $[Ru(II)(bpy)_3]Cl_2$

Aqueous samples of $[Ru(II)(bpy)_3]Cl_2$ in its reduced state were also prepared. The chloride salt of the $Ru(bpy)_3$ catalyst is ordinarily converted to the sulfato salt for use in the BZ reaction. The removal of chloride ions is necessary as they inhibit the BZ reaction[3]. However, for the purpose of measuring the relaxivity of the complex, the chloride salt was deemed suitable for use. It was also preferable to use the chloride salt as it was commercially available and required no further purification. As such, measurements performed on the chloride salt should be more reliable. A 0.015 mol dm^{-3} stock solution of $[Ru(II)(bpy)_3]Cl_2$ was prepared using the chloride salt as received from the supplier. Samples were prepared at a range of $Ru(bpy)_3$ concentrations by dilution of this stock solution. All solutions were prepared using nanopure water from a Millipak purification unit. The relaxivity of the solvent water was measured for a range of concentrations of $Ru(bpy)_3$ from 0.001 mol dm^{-3} to 0.020 mol dm^{-3}.

3.2.2. Relaxivity measurements of the $Ru(bpy)_3$ catalyst in AOT microemulsions

A series of water-in-oil microemulsion samples containing $[Ru(II)(bpy)_3]Cl_2$ were also prepared and the T_1 and T_2 relaxation times of these samples were measured. A stock solution of 1.5 mol dm^{-3} AOT (Fluka) was prepared by dissolving 111.14g of AOT in 70 ml of octane. The octane was first purified by stirring over concentrated sulphuric acid for several days. Sufficient volumes of a 0.010 mol dm^{-3} stock solution of $[Ru(II)(bpy)_3]Cl_2$ and of nanopure water were added to the AOT/octane solution, to give the required aqueous phase concentration of $Ru(bpy)_3$ and required water to surfactant molar ratio, ω. Additional octane was then added to dilute the microemulsion samples to the desired droplet fraction, ϕ_d. Refer to Section 2.2 and Figure 2.1 for details on the preparation of water-in-oil microemulsions. All samples were prepared at ω = 9.2 and ϕ_d = 0.45. The aqueous phase concentration of $Ru(bpy)_3$ was varied from 0.001 mol dm^{-3} to 0.010 mol dm^{-3}.

3.2.3. Measuring the relaxivity of $Ru(bpy)_3$ in the oxidised state - $[Ru(bpy)_3]^{3+}$

Attempts were also made to determine the relaxivity of the $Ru(bpy)_3$ catalyst in its oxidised state *i.e.* $[Ru(bpy)_3]^{3+}$ of the AOT system. The oxidised state of $Ru(bpy)_3$ has previously been accessed by addition of an excess of bromate in acidic conditions[2]. It has also been accessed by addition of solid lead (IV) oxide[4] to a solution of $[Ru(bpy)_3]^{2+}$; residual solid is subsequently removed by filtration, leaving a green solution of $[Ru(bpy)_3]^{3+}$. Both of these methods were utilised to measure the relaxivity of $Ru(bpy)_3$ in its oxidised form in the AOT microemulsion system.

3.2.3.1. Preparation of $[Ru(bpy)_3]^{3+}$ using bromate in acidic conditions

A stock solution of 0.015 mol dm^{-3} $[Ru(II)(bpy)_3]SO_4$ was prepared. The sulfato salt of the $Ru(bpy)_3$ complex was prepared from the chloride salt as outlined in Section 3.2.1. Aqueous solutions of sulphuric acid (1.0 mol dm^{-3}) and sodium bromate (1.0 mol dm^{-3}) were also prepared using nanopure water as before. Samples were prepared by adding the aqueous phase reagents to a solution of 1.5 mol dm^{-3} AOT in octane. Samples were prepared at a range of $Ru(bpy)_3$ concentrations, for both reduced and oxidised forms of the catalyst. "Reduced" catalyst solutions ($[Ru(bpy)_3]^{2+}$) contained sulphuric acid (0.12 mol dm^{-3}); "oxidised" catalyst solutions ($[Ru(bpy)_3]^{3+}$) contained sulphuric acid (0.12 mol dm^{-3}) and sodium bromate (0.25 mol dm^{-3}). In all cases the water-to-surfactant ratio, ω, was 9.2 and the droplet fraction, ϕ_d, was 0.45. The concentration of $Ru(bpy)_3$ was varied from zero to 0.005 mol dm^{-3}.

3.2.3.2. Preparation of $[Ru(bpy)_3]^{3+}$ using PbO_2

A 0.015 mol dm^{-3} stock solution of $[Ru(II)(bpy)_3]SO_4$ was prepared as before. Aqueous samples were prepared for a range of concentrations of $Ru(bpy)_3$ and acidified by adding sulphuric acid (0.12 mol dm^{-3}). The orange coloured solutions were then oxidised by adding solid PbO_2 (Sigma). Any remaining solid was removed by filtration, leaving green solutions of $[Ru(bpy)_3]^{3+}$. Aliquots of the oxidised solution were then added to a solution of 1.5 mol dm^{-3} AOT in octane to give a microemulsion with ω = 9.2 and ϕ_d = 0.45.

3.2.4. Relaxivity measurements of $Ru(bpy)_3$ microemulsion samples prepared at a high water to surfactant ratio

Microemulsion samples containing $Ru(bpy)_3$ were prepared at a high water to surfactant ratio. A stock solution of $[Ru(II)(bpy)_3]Cl_2$ was prepared, this was added to a 1.5 mol dm^{-3} solution of AOT in octane, to give the required concentration of $Ru(bpy)_3$. All samples were prepared at a water to surfactant ratio, ω = 64.7 and a droplet fraction, ϕ_d = 0.45. The concentration of $Ru(bpy)_3$ was varied from zero to 0.01 mol dm^{-3}.

3.2.5. Combined relaxation time measurements and DLS particle sizing experiments

T_1 and T_2 relaxation measurements and DLS particle sizing were performed on a variety of water-in-oil AOT microemulsion samples, to further characterise and probe the structure of these systems.

3.2.5.1. Preparation of microemulsion samples at various water-to-surfactant ratios

AOT/octane water-in-oil microemulsion samples were prepared for a range of values of ω, by adding an appropriate volume of water to a 1.5 mol dm^{-3} solution of AOT in octane. Values of ω ranged from 5.1 to 64.7. Additional octane was added to obtain the desired droplet fraction, ϕ_d, which was 0.45 for all samples.

3.2.5.2. Preparation of microemulsion samples containing $Ru(bpy)_3$ at different water to surfactant ratios

Microemulsion samples containing $[Ru(II)(bpy)_3]Cl_2$ were prepared by addition of the appropriate volume of a stock solution of $[Ru(II)(bpy)_3]Cl_2$ to 1.5 mol dm^{-3} AOT in octane solution. All samples were prepared at ϕ_d = 0.45 and values of ω ranged from 5.1 to 64.7. Samples were prepared with $[Ru(bpy)_3]^{2+}$ = 0.010 mol dm^{-3}.

3.2.6. Measurement of the NMR relaxation times

Once a sample had been prepared, a small amount was transferred to a 5 mm o.d. NMR tube that was then placed inside the probe in the bore of the magnetic resonance spectrometer and allowed to equilibrate to a bore temperature of 17° C. The spectrometer used was a Bruker DMX–300, comprising a 7.0 Tesla superconducting magnet operating at a proton frequency of 300 MHz. Measurements were performed using a single transmit/receive 10 mm saddle r.f. coil. The spectrometer was controlled via a Silicon Graphics workstation running XWIN-NMR software[5].

An inversion recovery pulse sequence[6] was used to measure T_1. A variable delay list was used with τ values that were exponentially spaced between 5 μs and 15 s. Four signal averages were acquired for each τ value in the variable delay list with a repetition time T_R of 15 s between each scan. T_2 values were measured using a CPMG pulse sequence[6]. A variable count list was used with values ranging from 0 to 220. Again, four scans were accumulated for each value in the list with a repetition time of 15 s between

each scan with τ = 10 ms. The spectral width was 10 kHz for both inversion recovery and CPMG experiments with 16k complex data points acquired. The 180° r.f. pulse was 28 μs at 0.0 dB attenuation and the 90° pulse was 14 μs. Both pulse sequences produced two-dimensional data sets, with spectral data acquired for each point in the variable delay list (inversion recovery) or variable counter list (CPMG). Once acquired, the two-dimensional data sets were processed and analysed using a combination of KaliedaGraph[7] and Prospa[8] software, to obtain the T_1 and T_2 relaxation time constants for the samples. For a more detailed description of this analysis, refer to Section 1.7.

3.2.7. DLS methodology

DLS particles sizing was used to measure the size of reverse micelles in various microemulsion samples. A description of the DLS technique is given in Section 1.10. Samples were allowed to equilibrate to the ambient laboratory temperature and then left for a further 5 minutes once placed inside the sample holder of the High Performance Particle Sizer (HPPS) instrument (Malvern Instruments model HPP5001) at 20 °C. The viscosity of octane[9] was taken as 0.542 cP at 20 °C and the refractive index was taken as 1.391. For each sample, the software was set to analyse the sample three separate times. The HPPS software uses the cumulants method of analysis to fit the intensity of the scattered light to a correlation function. It also provides a report on the reliability of the fit. For each sample, this report was examined to ensure the acquired data was of sufficient quality.

3.2.8. Investigation of $Ru(bpy)_3$ – micelle interactions using 2D NOESY NMR

The nuclear Overhauser effect (NOE) can be exploited to obtain the spatial arrangements of nuclei in close proximity[10]. A study was envisaged, whereby the location of the $Ru(bpy)_3$ complex in an AOT/octane reverse micelle system would be probed using a two-dimensional NOESY (Nuclear Overhauser Effect SpectroscopY) NMR experiment.

3.2.8.1. Preparation of $Ru(bpy)_3$ microemulsion for NOESY experiment

A 0.01 mol dm^{-3} solution of $[Ru(II)(bpy)_3]Cl_2$ was prepared in deuterium oxide (Goss Scientific, >99.9% D). This was then added to a solution of 1.5 mol dm^{-3} AOT in per-deuterated n-octane (Cambridge Isotope Laboratories Inc., 99% D), to give a microemulsion with ϕ_d = 0.67, ω = 9.2 and $[Ru(bpy)_3]$ = 0.01 mol dm^{-3}. Deuterated solvents were used to maximise the signal to noise ratio, so that NOEs between $Ru(bpy)_3$ and AOT could be observed over the noise in the acquired data. A sample was also prepared at ϕ_d = 0.79, ω = 34.9 and $[Ru(bpy)_3]$ = 0.01 mol dm^{-3}.

^1H-^1H NOESY NMR experiments were performed using a Bruker DRX-500 spectrometer, operating at a proton frequency of 500 MHz, fitted with a 5 mm radio frequency coil. The supplied Bruker gradient selection TPPI NOESY pulse sequence was used. Spectrometer control and analysis were done using the Topspin software package (Windows XP version 1.3). The spectral width was 4664 Hz with a repetition time of 2.1 s between transients. 512 data points were collected in F1 (512 transients) and 2k data points in F2. The NOESY mixing time was varied from 17 ms to 1.0 s. The 90° r.f. pulse was 11 μsec and the 180° pulse was 12 μsec at –3.6 dB attenuation. The spectral

resolution was 2.3 Hz per point in F2 and 9.1 Hz per point in F1. NOESY experiments and subsequent analysis were performed with the assistance and guidance of Dr Neil Spencer.

3.3. Results and Discussion

3.3.1. Relaxivity measurements of aqueous $Ru(bpy)_3$

Figure 3.1 shows the T_1 and T_2 relaxation rates plotted versus concentration of the $[Ru(II)(bpy)_3]SO_4$ complex in aqueous solution. A linear regression procedure is used to fit the data. The gradient calculated using this regression gives the T_1 and T_2 relaxivities for the species. The calculated relaxivities are collated in Table 3.1. Figure 3.2 shows T_1 and T_2 relaxivity plots obtained for the reduced form of $[Ru(II)(bpy)_3]Cl_2$. The T_1 and T_2 relaxivities for the reduced state of the sulfato and chloride salts are compared in Table 3.2. The error bars shown on each plot are an estimate of the total experimental error expressed as a percentage (between 5 – 10%). For consistency, only one data set is plotted in each case, however, the error bars reflect variance observed across several repeats of the same experiments. The most significant source of error is likely to be temperature fluctuations in the laboratory, though there may be smaller contributions from variation in the sample preparation process (sample ageing, error in reagent concentrations *etc.).*

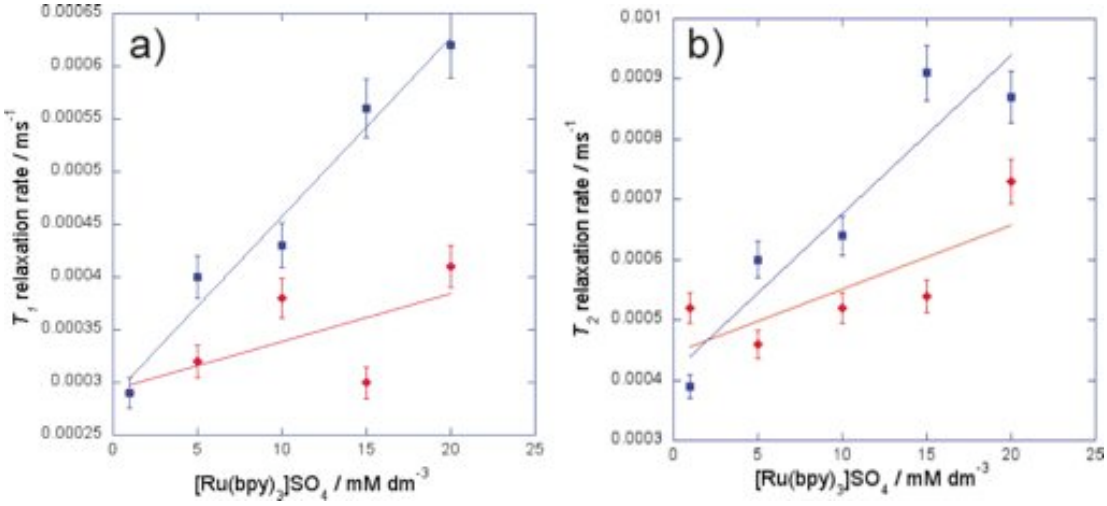

Figure 3.1 a) T_1 and b) T_2 relaxivity plots for the reduced (red diamonds) and oxidised (blue squares) forms of aqueous solutions of [Ru(bpy)$_3$]SO$_4$.

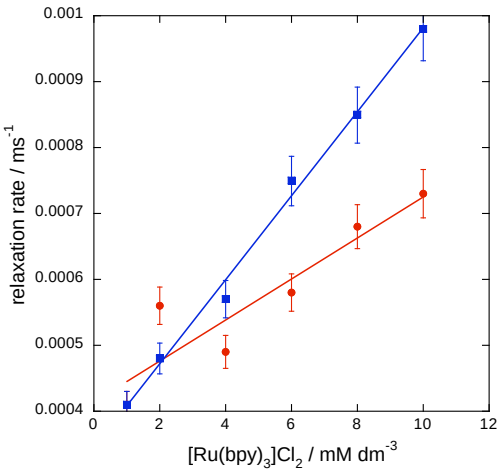

Figure 3.2 T_1 (red circles) and T_2 (blue squares) relaxivity plots for aqueous solutions of [Ru(II)(bpy)$_3$]Cl$_2$. The relaxivities calculated from the linear fitting procedure were 3.1×10^{-2} mM^{-1} s^{-1} for T_1 and 6.4×10^{-2} mM^{-1} s^{-1} for T_2.

	T_1 relaxivity / mM^{-1} s^{-1}	T_2 relaxivity / mM^{-1} s^{-1}
Reduced form	4.5×10^{-3}	1.1×10^{-2}
Oxidised form	1.7×10^{-2}	2.6×10^{-2}

Table 3.1 T_1 and T_2 relaxivity values for the reduced and oxidised forms of the [Ru(bpy)$_3$]SO$_4$ complex.

	T_1 relaxivity / $mM^{-1} s^{-1}$	T_2 relaxivity / $mM^{-1} s^{-1}$
$[Ru(bpy)_3]SO_4$	4.5×10^{-3}	1.1×10^{-2}
$[Ru(bpy)_3]Cl_2$	3.1×10^{-4}	6.4×10^{-2}

Table 3.2 Comparison of measured T_1 and T_2 relaxivities for the reduced forms of $[Ru(bpy)_3]SO_4$ and $[Ru(bpy)_3]Cl_2$.

The plots show that for the sulfato salt, both T_1 and T_2 are higher for the oxidised form of the catalyst. This is in qualitative agreement with measurements presented by Gao *et al*[2]. $[Ru(bpy)_3]^{3+}$ is a low spin d^5 octahedral complex and therefore has one unpaired electron compared to $[Ru(bpy)_3]^{2+}$, which is low spin d^6 and has no unpaired electrons. The relaxation times of solvent water molecules surrounding the more paramagnetic oxidised form are therefore expected to be lower than those surrounding the reduced form. While this was the expected result, it should be noted that in general, acquired data for the oxidised forms of $Ru(bpy)_3$ samples were of poor quality. This was the case for aqueous samples and microemulsion samples, and for both methods of oxidation used; oxidation with acidified bromate and oxidation with solid PbO_2. One possible cause of this is the stability of the oxidised form with respect to reduction back to $[Ru(bpy)_3]^{2+}$. $[Ru(bpy)_3]^{3+}$ is reduced to $[Ru(bpy)_3]^{2+}$ in the presence of water, producing oxygen and hydroxide ions[11]. The half-life of the oxidised form is 1.4 hours[12], which is significant on the time scale of the NMR relaxation measurements performed here. The consequence of this is that the ratio of

$[Ru(bpy)_3]^{2+}$ to $[Ru(bpy)_3]^{3+}$ is changing during the course of the relaxation time measurement. Reducing the experiment time is difficult; the most significant factor in determining the experiment time is the repetition time T_R, which is long due to the large values of T_1 being measured. This is most problematic when using the PbO_2 method of oxidation as the oxidant is removed from the system prior to the measurement being performed. An accurate measurement is therefore dependent upon the stability of the oxidised form over the course of the experiment. Oxidation using acidified bromate circumvents this problem, as the oxidising conditions are present throughout the measurement.

The instability of $[Ru(bpy)_3]^{3+}$ was particularly noticeable when trying to prepare samples of the oxidised form of the catalyst in microemulsion systems. Upon addition of the aqueous oxidised $[Ru(bpy)_3]^{3+}$ solution to the AOT/octane solution, the mixture immediately turned from green to orange, indicative of the reduction of $[Ru(bpy)_3]^{3+}$ to $[Ru(bpy)_3]^{2+}$. Exactly why the microemulsion medium promotes the reduction of $[Ru(bpy)_3]^{3+}$ is unclear. One possible explanation is that upon addition of the $[Ru(bpy)_3]^{3+}$ solution to the microemulsion, partitioning of the complex between the water pool and the micelle interface occurs, and that the exchange between the two environments is a dynamic equilibrium process that favours the reduced form of the metal complex or the neutral salt. Given the immediacy of the reduction of $[Ru(bpy)_3]^{3+}$ to $[Ru(bpy)_3]^{2+}$ upon its addition to the microemulsion, it seems more likely that this is a thermodynamic effect, with the reduced oxidation state energetically favoured. However, properties of the water pool in reverse micellar solutions of AOT including the micropolarity, microviscosity and pH

can affect reaction kinetics and dynamics[13]. The mechanism proposed for the reduction of $[Ru(bpy)_3]^{3+}$ by water by Ghosh *et al*[14] involves nucleophilic addition of water to a carbon atom on the bpy ligands. It is, therefore, not unfeasible that the kinetics of this reaction could be affected by the microemulsion structure, although the individual case would need to be investigated.

Another consideration is that the $Ru(bpy)_3$ complex may be susceptible to dissociation in the reverse micelle medium. The dissociation of $[Fe(bpy)_3]^{2+}$ in a Triton X-100/hexanol/cycholhexane reverse micelle system has been investigated by Sarkar *et al*[15]. They show that the dissociation of the complex in the reverse micelle system obeys first order kinetics, and that the equivalent reaction in the aqueous system is immeasurably slow. They rationalise this by considering the increased nucleophilicity of the water in the micellar environment[16]. The reaction rate also increases with an increase in the surface area of the micellar interface, indicative that the reaction occurs at the interface. If the $Ru(bpy)_3$ complex does dissociate in the reverse micelle system via a similar mechanism, then the measured relaxation times will be affected. The ruthenium could potentially exist as either oxidised or reduced and also as complexed and uncomplexed ruthenium, all of which would have different relaxivities. However, a disappearance of the orange colour that would be indicative of the dissociation of the $[Ru(bpy)_3]^{2+}$ complex was not observed for the samples studied as part of this study, and so this explanation seems less likely.

3.3.1.1. Evolution of oxygen during reduction of $[Ru(bpy)_3]^{3+}$

Another consequence of the reduction of $[Ru(bpy)_3]^{3+}$ by hydroxide is the production of molecular oxygen which is itself a paramagnetic species and could therefore affect the relaxation times measured. The reaction, however, yields only small amounts[14] of O_2. The non-polarity of dioxygen is also likely to mean it will be sequestered within the continuous oil phase.

3.3.1.2. Comparison of the relaxivities of $[Ru(bpy)_3]Cl_2$ and $[Ru(bpy)_3]SO_4$

T_1 and T_2 relaxivity plots for the $[Ru(II)(bpy)_3]Cl_2$ complex in aqueous solution are shown in Figure 3.2. As can be seen, the measured relaxation rate increases with the concentration of $Ru(bpy)_3$ for both T_1 and T_2. Table 3.2 shows the comparison between the measured relaxivities for the reduced form of the chloride and sulfato salts of the $Ru(bpy)_3$ complex. It is apparent that the measured T_1 and T_2 relaxivities are higher for the chloride salt than the sulfato salt. It is unlikely that the counter-ions themselves would have a drastic effect upon the relaxivity of the solvent water molecules, as they are both diamagnetic, and should therefore contribute very little to relaxation processes. It is possible, however, that the different counter ions affect the ability of the $Ru(bpy)_3$ complex to coordinate water molecules and therefore have an indirect influence upon the relaxivity. A possible source of error is in the determination of the concentration of the sulfato salt samples. The concentration of the stock solution of $[Ru(II)(bpy)_3]SO_4$ prepared was calculated assuming a completely pure product was obtained from the conversion process. Any impurities would obviously affect the validity of this assumption. It is possible that the conversion of the chloride salt to the sulfato salt was not complete and this may account for an impure product.

Complex (metal ion / ligand)	T_1 relaxivity / mM^{-1} s^{-1}	Field strength / MHz	Temperature / °C	Ref.
Mn(II) / aquo	44	0.02	35	[17]
Mn(III) / TPPS	7.8	0.02	35	[17]
Gd(III) / aquo	22	0.02	35	[17]
Ru(II) / $(bpy)_3$	4.5×10^{-3}	300	17	This study
Ru(III) / $(bpy)_3$	1.7×10^{-2}	300	17	This study
Fe(III) / aquo	17	0.02	35	[17]

Table 3.3 T_1 (longitudinal) relaxivities of some common metal ion complexes including those measured for the reduced and oxidised forms of $[Ru(bpy)_3]SO_4$ as part of this study. The field strength in MHz and temperature at which the measurements were performed are also shown. Other values are taken from a table published by Lauffer[17].

Table 3.3 shows the relaxivities of some common paramagnetic contrast agents. It should be noted that T_1 and, therefore, T_1 relaxivity, vary with field strength. Direct comparison of the measurements taken in this study (performed at 300 MHz) with those reported by Lauffer[17] (performed at 0.02 MHz) is, therefore, difficult. However, it can be seen from the table that the

relaxivity of $Ru(bpy)_3$ in both of its oxidation states is several orders of magnitude lower than other paramagnetic species such as Mn^{2+}. This is partially due to the number of unpaired electrons; $[Ru(bpy)_3]^{2+}$ has no unpaired electrons and $[Ru(bpy)_3]^{3+}$ has only one, compared to five unpaired electrons in the Mn^{2+} aquo complex. Another contributing factor is the ability of each complex to coordinate solvent water molecules into its relaxation sphere. In the Mn^{2+} ion, six solvent water molecules are coordinated in the inner coordination sphere[17], whereas the ruthenium complex has three bulky chelating bidentate bipyridine ligands, which prevent the coordination of water into the inner sphere. As such, outer sphere processes will account for the majority of the relaxation. In such cases, where outer sphere processes dominate, the residence time of coordinated water molecules is a significant factor in determining the overall relaxivity. Thus, in slowly tumbling, low mobility systems, residence times are increased and outer sphere relaxation processes are enhanced. So while the $Ru(bpy)_3$ complex may not be as strong a contrast agent as highly paramagnetic ions such as Mn^{2+} that are able to coordinate water molecules in the inner relaxation sphere, it is still able to influence the relaxation times of surrounding water molecules through outer sphere processes.

3.3.2. Relaxivity of $Ru(bpy)_3$ in the AOT/octane microemulsion system

Figure 3.3 shows the T_1 and T_2 relaxivity data for the water proton resonance in the $[Ru(II)(bpy)_3]Cl_2$ – AOT/octane microemulsion system. It can be seen from the plots that there is effectively no change in the relaxation rate with increasing concentration of $Ru(bpy)_3$.

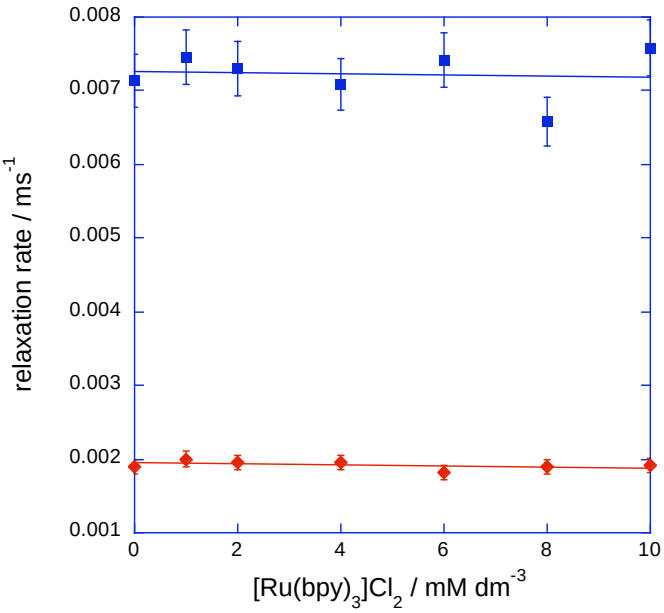

Figure 3.3 T_1 (red circles) and T_2 (blue squares) relaxivity plots for the water proton signal of AOT microemulsion samples containing $[Ru(II)(bpy)_3]Cl_2$ at various concentrations. All samples were prepared with a water to surfactant molar ratio, ω = 9.2 and a droplet fraction ϕ_d = 0.45.

The relaxation times measured for all concentrations of $Ru(bpy)_3$ complex were the same as those measured for the samples with no $Ru(bpy)_3$ complex. Essentially, $Ru(bpy)_3$ is not affecting the relaxation times of the water molecules at all. Compare this to the data for the aqueous system, (Figure 3.2) where the gradient of the plot shows that the relaxation rate is dependent upon the concentration of $Ru(bpy)_3$. The reason for this may be that the $[Ru(bpy)_3]^{2+}$ does not reside within the water droplet and is instead located in either the micellar interface or in the continuous oil phase. In either of these cases, the $Ru(bpy)_3$ complex would not be in a favourable position to coordinate water molecules from within the water droplet, and hence the

water molecules will not feel the influence of the unpaired electron. As such, the relaxation times of the water molecules in the reverse micelle would be unaffected and a plot of their relaxation rate versus concentration of $Ru(bpy)_3$ would show no concentration dependence.

3.3.3. Probing the location of $Ru(bpy)_3$ within the AOT reverse micelle system

A number of researchers have investigated the location of probe molecules in AOT microemulsions. Rack *et al*[18] have even used $Ru(bpy)_3$ as a probe for the intramicellar medium of AOT microemulsions. Using time resolved emission studies of the $Ru(bpy)_3$ complex in AOT reverse micelles, they have shown that for small droplet sizes, ($\omega \leq 15$), the $Ru(bpy)_3$ molecule is located at the surfactant-water interface. Similarly, Crans *et al* have used NMR correlation spectroscopy to determine the location of a small oxovanadium complex in an AOT/iso-octane reverse micelle system[19]. They have exploited the nuclear Overhauser effect (NOE) to determine the spatial proximity of protons associated with the oxovanadium complex to protons associated with the AOT surfactant molecule. Their results suggest that their vanadium complex resides within the micellar interface and not, as previously thought, within the aqueous water droplet core.

The ability of paramagnetic contrast agents to affect the relaxation times of surrounding solvent water molecules is dependent upon the water molecules approaching close enough to the contrast agent to feel the influence of its localised magnetic field[17]. The location of $Ru(bpy)_3$ within the structure of the AOT reverse micelles will, therefore, affect its ability to act as an MRI contrast

indicator. A series of NOESY and NMR relaxation time measurements were performed to determine the location of the $Ru(bpy)_3$ complex in a series of reverse micelle systems of varying droplet size.

3.3.3.1. T_1 relaxation rates of AOT protons

As the $Ru(bpy)_3$ complex does not have an effect on the relaxation times of the water, it is then plausible to assume the complex resides in the micellar interface. If this is the case, it is possible that the complex may affect the relaxation times of protons associated with the AOT surfactant molecule.

Figure 3.4 shows the structure of the AOT surfactant molecule and the 2,2'-bipyridyl ligand along with a table showing the ^{1}H-NMR peak assignments for both AOT and bipyridyl. A one-dimensional ^{1}H-NMR spectrum of the AOT/octane microemulsion system is also shown. AOT has been characterised previously by NMR spectroscopy[19,20], and peak assignments for the $Ru(bpy)_3$ complex were determined using a previous characterisation of the $Ru(bpy)_3$ complex[21]. The peak positions of the multi component system are similar to those of its constituent parts. However, the peaks at 1.3 and 1.7 ppm associated with protons on the tail section of the AOT molecule are masked by the octane resonances at similar chemical shift. The position of the water peak is also dependent upon the water content of the system[22], with the peak moving downfield as the water content is increased.

a)

Ru(bpy) complex	δ / ppm
H_a	8.2
H_b	7.8
H_c	8.5
H_d	9.1
AOT molecule	
H8, H8', H10, H10'	1.30
H5, H5', H6, H6', H7, H7', H9, H9'	1.71
H4, H4'	2.03
H1'	3.55
H1, H3, H3'	4.56

b)

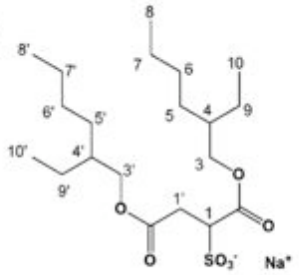

c)

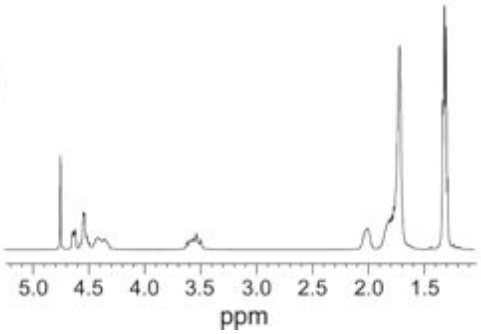

d)

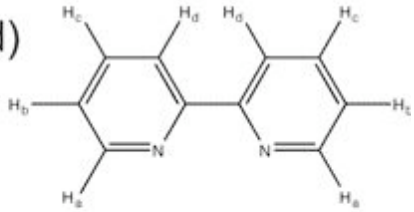

Figure 3.4 a) Table showing ^{1}H-NMR peak assignments for the AOT molecule and Ru(bpy)$_3$ complex b) Structure of AOT showing the numbering system used to make the assignments in a). c) ^{1}H-NMR spectrum of an AOT/octane microemulsion sample. d) Structure of 2,2'-bipyridine showing the proton assignments made in a).

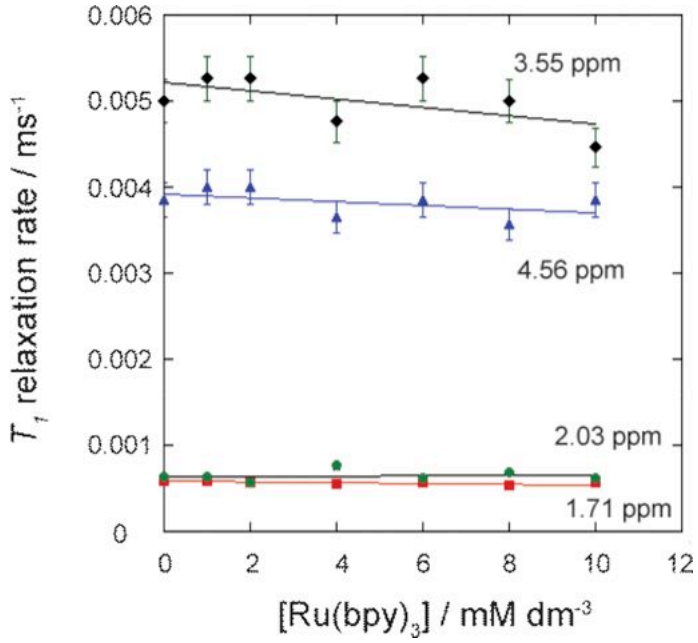

Figure 3.5 T_1 relaxivity plots for the AOT proton resonances assigned in Figure 3.4. ω = 9.2, ϕ = 0.45.

Figure 3.5 shows the T_1 relaxivity plots for the AOT proton resonances assigned in Figure 3.4. Two of the resonances are associated with protons located in the hydrophobic tail group of the surfactant molecule. Protons from the octane continuous phase also contribute to these signals. The two other resonances are associated with protons closer to the hydrophilic head group of the surfactant molecule.

As can be seen, the T_1 relaxation times of all four resonances investigated appear unaffected by the concentration of $Ru(bpy)_3$. Assuming that the $Ru(bpy)_3$ complex is actually located within the micellar interface, it is perhaps unsurprising that the complex does not appear to affect the relaxation times of the surfactant protons. As has been observed with the aqueous system, the $Ru(bpy)_3$ complex is only a very weak paramagnetic contrast agent, therefore its effect on the relaxation times of solvent molecules is expected to be small. Any detrimental changes in the parameters that affect the relaxivity will only serve to decrease the observed effect. Perhaps the most important consideration is the ability of the paramagnetic centre of the complex to approach close enough to the AOT molecules to influence their relaxation times. Clearly AOT is a much larger molecule than water and so this will limit how closely AOT can approach to the paramagnetic centre and therefore to what extent the $Ru(bpy)_3$ can influence relaxation processes. Given the size and shape of the AOT molecule compared to water molecules, and the presence of three large bipyridine ligands, it seems unlikely that AOT could be considered to be coordinated to the $Ru(bpy)_3$ complex in the same way as

water molecules. If the $Ru(bpy)_3$ complex is immobilised within the micellar interface, then exchange of AOT molecules that are close enough to feel its influence with un-associated AOT will be limited. There are also only a small number of $Ru(bpy)_3$ molecules per droplet (approximately three molecules per droplet). The effect of this will be that only very small percentage of the AOT molecules in the surfactant interface will actually be in close enough proximity of a metal ion centre to feel the effect of its local magnetic field.

3.3.3.2. Variation in droplet size and T_1 relaxation time with water-to-surfactant ratio

Figure 3.6 shows the water proton T_1 relaxation times (note that it is the relaxation *time* plotted in this case and not relaxation *rate*) plotted against the water to surfactant ratio ω, for microemulsion samples containing $Ru(bpy)_3$ ($[c]_w$ = 0.01 mol dm^{-3}). The relaxation times are also shown for "blank" microemulsion samples containing no metal ion catalyst. DLS particle sizing measurements were also performed in order to investigate the effect of $Ru(bpy)_3$ on the size of reverse micelles in the AOT microemulsion system. Figure 3.7 shows the particle size measured for microemulsion samples containing $Ru(bpy)_3$ and samples prepared without $Ru(bpy)_3$. As can be seen, the droplet size appears unaffected by the inclusion of $Ru(bpy)_3$, and there is a linear relationship with the water-to-surfactant ratio. From Figure 3.7 it can be seen that at the low values of ω (and hence, smaller droplet sizes), the measured T_1 relaxation times are unaffected by the presence of the $[Ru(bpy)_3]^{2+}$ complex. At higher values of ω, (larger droplets), however, the T_1 relaxation times for microemulsions containing $Ru(bpy)_3$ are lower than those measured for the samples containing no $Ru(bpy)_3$ complex. It would appear,

then, that in larger droplets, $Ru(bpy)_3$ is able to reduce the relaxation times of solvent water molecules. This suggests the complex spends some time in the droplet and hence the complex is able to influence the relaxation times of water molecules inside the water droplet core. The T_2 relaxation times shown in Figure 3.6 b) do not appear to be affected by the presence of $Ru(bpy)_3$ at any value of the water-to-surfactant ratio. This may be because the effect on the T_2 relaxation time is much smaller and so the difference is not observable.

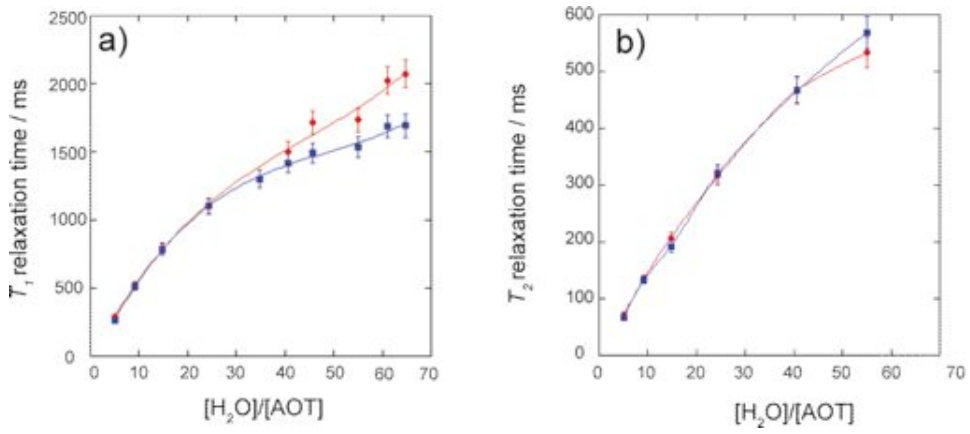

Figure 3.6 a) Water proton T_1 relaxation times of AOT/octane microemulsion systems at various water to surfactant ratios. Data are shown for microemulsions containing no metal ion catalyst (red diamonds) and for microemulsions containing 10 mM dm^{-3} $[Ru(II)(bpy)_3]Cl_2$ (blue squares). All samples were prepared at ϕ_d = 0.45.

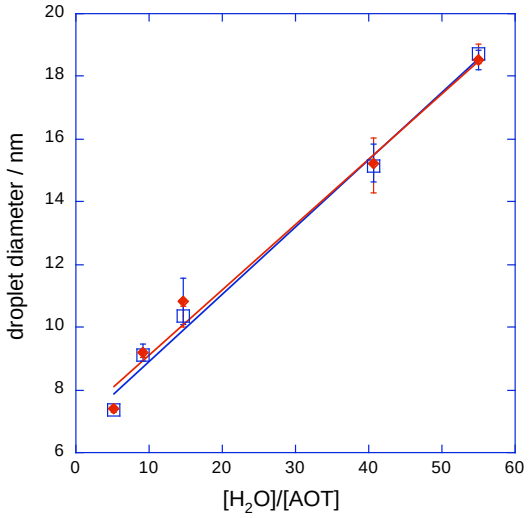

Figure 3.7 Variation in hydrodynamic diameter with water to surfactant ratio of AOT/octane microemulsion samples. The red diamonds show the variation for samples containing $[Ru(II)(bpy)_3]Cl_2$ ($[c]_w$ = 0.010 mol dm^{-3}). The open blue squares show the variation for microemulsion samples with no $Ru(bpy)_3$ present. All samples were prepared at ϕ_d = 0.45.

Figure 3.8 shows the water proton T_1 and T_2 relaxation times for microemulsion samples containing $Ru(bpy)_3$ prepared at high water-to-surfactant ratio, ω = 64.7. As can be seen, both T_1 and T_2 are reduced with increasing concentration of $Ru(bpy)_3$, which further supports the hypothesis that the complex spends more time in the water droplet than at smaller droplet sizes. This would seem to suggest that for larger droplet sizes $Ru(bpy)_3$ is not immobilised within the water-surfactant interface, but is able to coordinate water molecules from within the water droplet core.

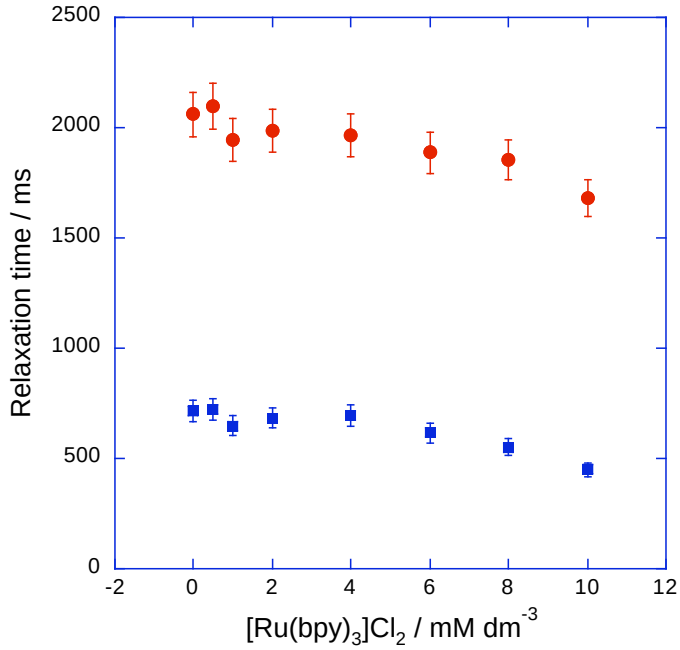

Figure 3.8 Water proton T_1 (red circles) and T_2 (blue squares) relaxation times of AOT/octane microemulsion samples at various concentrations of Ru(bpy)$_3$ prepared at a high water to surfactant ratio. All samples were prepared at ϕ_d = 0.45 and ω = 64.7.

3.3.3.3. Probing the location of Ru(bpy)$_3$ within the reverse micelle system using the Nuclear Overhauser effect

In order to investigate the location of the complex and the effect of droplet size on the ability of Ru(bpy)$_3$ to influence the relaxation times of water further, NOE correlation spectroscopy was performed on microemulsion samples containing Ru(bpy)$_3$ for two different values of ω. The first value of ω chosen was where Ru(bpy)$_3$ was found to have had no influence on the water proton T_1 relaxation time, ω = 9.2. The second value was chosen with a value where the relaxation times were sensitive to the presence of Ru(bpy)$_3$, ω = 34.9. NOE enhancements were measured for a range of mixing times, and an

example of the 2-D NOESY spectra obtained is shown in Figure 3.9. The structure of 2,2'-bipyridine with proton assignments is shown in Figure 3.4. The negative NOE intensities for proton H_a on the bipyridine ligand at ω = 9.2 and ω = 34.9 are presented in Table 3.4 and Table 3.5 respectively. The complete set of NOESY spectra and NOE enhancements for all the bipyridine protons are included in Appendix B.

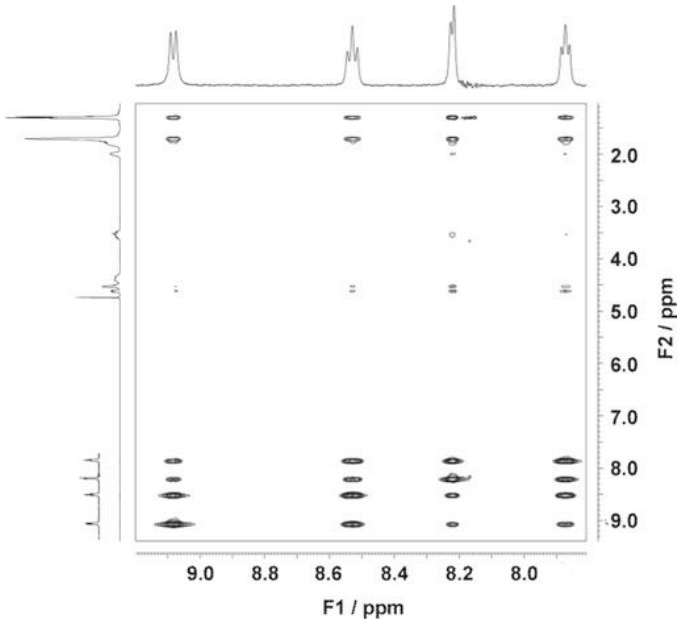

Figure 3.9 Example of a 2-D NOESY spectrum showing negative NOE enhancements observed between protons on the $Ru(bpy)_3$ complex and protons on the AOT surfactant molecule. The scale of F1 has been expanded to show only bipyridine ligand protons.

mixing time / ms	1.3 ppm (tail group)	1.7 ppm (tail group)	2.0 ppm (head group)	3.5 ppm (head group)	4.6 ppm (head group)
17	0.000	0.000	0.000	0.000	0.000
65	0.002	0.000	0.000	0.000	0.000
100	0.005	0.000	0.000	0.000	0.000
150	0.006	0.006	0.000	0.000	0.000
400	0.030	0.041	0.003	0.007	0.007
650	0.061	0.084	0.007	0.016	0.012
1000	0.110	0.143	0.015	0.025	0.055

Table 3.4 Negative NOE intensities observed between proton H_a on the bipyridine ligand and different AOT protons at varying mixing times for microemulsion samples prepared at ω = 9.2.

mixing time/ ms	1.3 ppm (tail group)	1.7 ppm (tail group)	2.0 ppm (head group)	3.5 ppm (head group	4.6 ppm (head group)
17	0.000	0.000	0.000	0.000	0.000
65	0.000	0.000	0.000	0.000	0.000
100	0.000	0.000	0.000	0.000	0.000
150	0.000	0.001	0.000	0.000	0.000
300	0.005	0.007	0.000	0.000	0.000
400	0.008	0.011	0.000	0.000	0.002
650	0.015	0.021	0.001	0.000	0.004
1000	0.013	0.019	0.002	0.001	0.004

Table 3.5 Negative NOE intensities observed between proton H_a on the bipyridine ligand and different AOT protons at varying mixing times for microemulsion samples prepared at ω = 34.9.

Strong negative NOE enhancements are observed between all bipyridine protons and the AOT proton resonances at 1.3 ppm and 1.7 ppm. These

chemical shifts correspond to protons associated with the long alkyl tails of the AOT surfactant molecule. This then suggests that the bipyridine protons and the surfactant tails are in close proximity, and that the $Ru(bpy)_3$ complex is located within the surfactant interface, between the surfactant tails, and not at the water-surfactant interface. If the complex were located at the water-surfactant interface, stronger NOE enhancements would be expected between the bipyridine protons and AOT protons close to the head group, *i.e.* the AOT resonances at 2.0 ppm, 3.5 ppm and 4.6 ppm. NOE enhancements are observed between bipyridine and protons associated with the head group of AOT, however, they are much lower intensity enhancements particularly at shorter mixing times. The intensities of these enhancements are expected to be lower because there are fewer protons contributing to the peak intensities *i.e.* there are sixteen protons contributing to the tail group peak at 1.71 ppm, but there are only two head group protons that contribute to the peak observed at 2.03 ppm. The lower enhancement intensity, however, may also suggest that these enhancements are due to a longer-range proximity effect, or that they arise from spin diffusion *i.e.* an indirect NOE enhancement.

At the higher water-to-surfactant ratio, the negative NOE enhancements observed between bipyridine protons and the AOT protons are less intense. This suggests that for larger droplet size the $Ru(bpy)_3$ spends less time immobilised within the surfactant interface and that it may be able to penetrate the water droplet core. The $Ru(bpy)_3$ is, therefore, in exchange between the two environments, and the intensities of the NOE enhancements observed between bipyridine and AOT are lower as a result. For both values of ω, all

intermolecular NOE enhancements observed between bipyridine protons and AOT protons were negative. Intramolecular NOE enhancements were also negative. This is indicative of a long rotational correlation time, $\tau_{c,}$ for the AOT molecule and the bipyridine ligand[10] *i.e.* $\omega_0\tau_c >> 1$, (ω_0 in this case refers to the Larmor frequency, not the water-to-surfactant ratio). For the larger droplet, the rotational correlation time should be longer than for the smaller droplet. As a result, the intensities of the negative NOE enhancements between bipyridine and AOT should be greater (more negative). However, the opposite is observed, and NOE enhancements for the larger droplet are less intense (more positive). This is also supportive of the conclusion that in the larger droplet $Ru(bpy)_3$ is more mobile, and provides more evidence that $Ru(bpy)_3$ is able to penetrate into the water droplet core.

3.3.3.4. Implications of the location of $Ru(bpy)_3$ in the surfactant interface

The location of the $Ru(bpy)_3$ within the surfactant interface has a number of implications regarding its use as a catalyst in the BZ-AOT reaction. As the $Ru(bpy)_3$ complex is unable to influence the relaxation times of water molecules in the droplet core, $Ru(bpy)_3$ is not suitable for use as an MRI relaxation time contrast indicator at the low water-to-surfactant ratios typically employed in the BZ-AOT reaction. The observation that $Ru(bpy)_3$ is immobilised in the surfactant interface at low water-to-surfactant ratios also has implications with respect to pattern formation in the BZ-AOT reaction. The location of metal-complexes such as the $Ru(bpy)_3$ and ferroin catalysts within the reverse micelle structure may be a significant factor in determining the types of patterns that are formed. A number of pattern types observed in the $Ru(bpy)_3$-, ferroin- and bathoferroin- catalysed BZ-AOT reactions are only

seen when a particular catalyst is used. Additionally, some pattern types are only observed at a particular water-to-surfactant ratio[23], or when there is a bimodal distribution of droplet sizes[24]. Previously this has been attributed to the change in the droplet diffusivity with droplet size, however, the effect of droplet size upon the location of the catalyst within the micelle may also be a contributing factor. The location of the catalyst also raises the question as to how the BZ reaction, which consists predominantly of polar species that reside within the aqueous droplet, is catalysed if the metal-ion catalyst is immobilised within the surfactant interface.

3.4. Conclusions

The T_1 and T_2 relaxivities of $Ru(bpy)_3$ were measured in aqueous solution for both the reduced and oxidised forms of the catalyst. It was found that the relaxation times of solvent water molecules surrounding the oxidised form of the catalyst were shorter than those surrounding the reduced form. The magnitude of the effect, however, was small compared with values reported for other paramagnetic contrast agents such as manganese. This was attributed to the low number of unpaired electrons in the low spin $Ru(bpy)_3$ complex and also to the inability of $Ru(bpy)_3$ to coordinate water molecules into its inner sphere. These results are in agreement with those published by Gao *et al*[2].

The T_1 and T_2 relaxivities of the $Ru(bpy)_3$ catalyst were also measured in the AOT microemulsion system. At low water-to-surfactant ratios, and hence small droplet sizes, the relaxation times of solvent water molecules were not

reduced by the presence of the $Ru(bpy)_3$ complex. However, at higher water-to-surfactant ratios, a decrease in the water proton relaxation times was observed. This observation was rationalised by the immobilisation of the $Ru(bpy)_3$ catalyst in the surfactant interface at low water-to-surfactant ratios. At higher water-to-surfactant ratios, the $Ru(bpy)_3$ complex is able to exchange between the surfactant interface and the water droplet core, thus, allowing it to influence the relaxation times of water molecules in the droplet core. NOE correlation spectroscopy supported this conclusion, with NOE enhancements observed between bipyridine ligand protons and AOT protons associated with the surfactant tails. At higher water-to-surfactant ratio, the intensities of these enhancements are reduced. This was explained by the increased mobility of the $Ru(bpy)_3$ complex in larger droplets and its ability to enter the water droplet core. These results support the conclusion that the behaviour of probe molecules, such as the $Ru(bpy)_3$ complex, can be used to infer information about the physical structure of the microemulsion system through changes in the properties of the probe molecule upon inclusion in the microemulsion. These findings also show that $Ru(bpy)_3$ cannot act as an MRI contrast indicator for the BZ-AOT reaction performed at low water-to-surfactant ratios, as it is unable to provide the necessary relaxation time contrast between the reduced and oxidised states of the reaction. There are also implications of the location of the catalyst within the micelle with respect to pattern formation in the BZ-AOT reaction. These implications are not limited to the $Ru(bpy)_3$ catalyst, and may also apply to other catalyst systems such as ferroin and bathoferroin.

3.5. References

(1) Haacke, M.; Brown, R.; Thompson, M.; Venkatesan, R. *Magnetic Resonance Imaging: Physical Principles and Sequence Design*; Wiley-Liss: New York, 1999.

(2) Gao, Y.; Cross, A. R.; Armstrong, R. L. *Journal Of Physical Chemistry* **1996**, *100*, 10159.

(3) Gao, Y.; Forsterling, H. D. *Journal Of Physical Chemistry* **1995**, *99*, 8638.

(4) Szalai, I.; Kurin-Csorgei, K.; Epstein, I. R.; Orban, M. *Journal Of Physical Chemistry A* **2003**, *107*, 10074.

(5) XWIN-NMR; 2.6 ed.; Bruker.

(6) Callaghan, P. T. *Principles of Nuclear Magnetic Resonance Microscopy*; Oxford University Press: New York, 1991.

(7) Kaleidagraph; 4.03 ed.; Synergy Software.

(8) Prospa; 2.1 ed.; Magritek.

(9) Lide, D. *CRC Handbook of Chemistry and Physics, 88th Edition (Crc Handbook of Chemistry and Physics)*; CRC: New York, 2007.

(10) Neuhaus, D.; Williamson, M. *The Nuclear Overhauser Effect in Structural and Conformational Analysis, 2nd Edition*; Wiley-VCH: New York, 2000.

(11) Creutz, C.; Sutin, N. *Proceedings Of The National Academy Of Sciences Of The United States Of America* **1975**, *72*, 2858.

(12) Matsuura, K.; Kevan, L. *Journal of the Chemical Society-Faraday Transactions* **1997**, *93*, 1763.

(13) Fendler, J. H.; Fendler, E. J. *Catalysis in micellar and macromolecular systems*; Academic Press: New York, 1975.

(14) Ghosh, P. K.; Brunschwig, B. S.; Chou, M.; Creutz, C.; Sutin, N. *Journal Of The American Chemical Society* **1984**, *106*, 4772.

(15) Sarkar, D.; Subbarao, P. V.; Begum, G.; Ramakrishna, K. *Journal Of Colloid And Interface Science* **2005**, *288*, 591.

(16) Kondo, H.; Fujiki, K.; Sunamoto, J. *The Journal of Organic Chemistry* **2002**, *43*, 3584.

(17) Lauffer, R. B. *Chemical Reviews* **1987**, *87*, 901.

(18) Rack, J. J.; McCleskey, T. M.; Birnbaum, E. R. *The Journal of Physical Chemistry B* **2001**, *106*, 632.

(19) Crans, D. C.; Rithner, C. D.; Baruah, B.; Gourley, B. L.; Levinger, N. E. *Journal Of The American Chemical Society* **2006**, *128*, 4437.

(20) Ueno, M.; Kishimoto, H.; Kyogoku, Y. *Journal Of Colloid And Interface Science* **1978**, *63*, 113.

(21) Cang, L.; Sun, H.; Hoffman, M. Z. *Journal of Photochemistry and Photobiology A: Chemistry* **1997**, *108*, 129.

(22) Zhou, N.; Li, Q.; Wu, J.; Chen, J.; Weng, S.; Xu, G. *Langmuir* **2001**, *17*, 4505.

(23) Kaminaga, A.; Vanag, V. K.; Epstein, I. R. *Journal Of Chemical Physics* **2005**, *122*.

(24) Vanag, V. K.; Epstein, I. R. *Physical Review Letters* **2003**, *90*.

Chapter 4. NMR measurements of the manganese-catalysed BZ-AOT reaction

4.1. Introduction

The manganese-catalysed BZ-AOT reaction is potentially the strongest candidate for visualisation of chemical patterns and waves using MRI, and represents an opportunity to image, for the first time, three-dimensional Turing patterns in a chemical system. It is known that the Mn^{2+}/Mn^{3+} pair is a suitable one-electron redox couple, able to catalyse temporal oscillations in the BZ reaction[1-3]. It has also been shown that spatial patterns and waves, in both two- and three-dimensions, can be imaged in the liquid phase BZ reaction, using the manganese catalyst as an MRI indicator[4-9]. This was achieved by exploiting differences in the paramagnetism of the reduced and oxidised forms of the catalyst to obtain image contrast.

To date, the manganese-catalysed BZ-AOT system has received no attention, mainly due to a lack of significant visual contrast between the two oxidative states of the catalyst. Measurements would need to be performed on the oscillatory system to ensure the reaction is still catalysed by manganese in the AOT microemulsion. The system could then be characterised in terms of its NMR relaxation times in order to find appropriate experiment parameters with which to observe oscillatory behaviour using NMR. This characterisation

process will also assist in developing and optimising the parameters for MRI pulse sequences, so that pattern formation in the BZ-AOT system may subsequently be investigated using MRI.

This chapter deals firstly with the process of characterising the reduced and oxidised states of the manganese-catalysed BZ-AOT system in terms of their NMR relaxivity. The stabilising effect of phosphates is also investigated, particularly with respect to enhancement of the relaxation time contrast. Secondly, results are presented that show it is possible to monitor the oscillatory behaviour of a variety of manganese-catalysed BZ-AOT reactions, through observation of the differences in the NMR relaxation times of solvent water molecules surrounding the reduced and oxidised forms of the manganese catalyst.

4.2. Experimental

4.2.1. Relaxivity measurements of the manganese-catalysed BZ-AOT system

4.2.1.1. Preparation of microemulsion samples containing Mn^{2+}

A 0.015 mol dm^{-3} stock solution of manganese (II) was prepared by dissolving $MnSO_4 \bullet 4H_2O$ (BDH Ltd.) in a 5.0 mol dm^{-3} solution of H_2SO_4 (Fisher). A 1.5 mol dm^{-3} stock solution of AOT (sodium (bis-2-ethyl-hexyl) sulfosuccinate (Fluka)) in n-octane (Acros) was also prepared. The octane was purified, by stirring over concentrated sulphuric acid for several days. Microemulsion samples were prepared by adding a sufficient volume of the stock $MnSO_4$ solution to the AOT/octane solution to give the required concentration of

$MnSO_4$. Additionally a stock solution of sulphuric acid was added to maintain $[H_2SO_4]$ = 3.3 mol dm^{-3} for all samples. The volume of aqueous phase reagents and AOT-in-octane solution was such that it gave the required water-to-surfactant ratio, ω = 9.2. Additional octane was added to give the required droplet fraction, ϕ_d = 0.45. Samples were prepared for a range of manganese concentrations between 0.001 mol dm^{-3} and 0.01 mol dm^{-3}. More details on the preparation of microemulsions can be found in Section 2.2.1.

4.2.1.2. Preparation of microemulsion samples containing Mn^{3+}

A 0.015 mol dm^{-3} stock solution of manganese (III) was prepared by dissolving $Mn(AcO)_3 \bullet 2H_2O$ (Sigma) in a 5.0 mol dm^{-3} solution of sulphuric acid. Microemulsion samples were prepared as in Section 4.2.1.1, to give samples with ω = 9.2, ϕ_d = 0.45 and $[H_2SO_4]$ = 3.3 mol dm^{-3}. The concentration of manganese was varied between 0.001 mol dm^{-3} and 0.01 mol dm^{-3}.

4.2.1.3. Oxidation of Mn^{2+} by acidified bromate

Microemulsion samples containing manganese in its oxidised form were also prepared by oxidation of the reduced form using acidified bromate. Stock solutions of 0.015 mol dm^{-3} of $MnSO_4$ were prepared in i) 5.0 mol dm^{-3} sulphuric acid and ii) 1.0 mol dm^{-3} sulphuric acid. A stock solution of 0.25 mol dm^{-3} sodium bromate was also prepared. Microemulsion samples were prepared as before with ω = 9.2, ϕ_d = 0.45 and $[H_2SO_4]$ = i) 3.3 mol dm^{-3} or ii) 0.67 mol dm^{-3}. Oxidised samples were prepared by adding sodium bromate solution to give $[NaBrO_3]$ = 0.36 mol dm^{-3}. This is a slightly higher

concentration than would be used in a typical BZ reaction, ([$NaBrO_3$] = 0.1-0.25 mol dm^{-3}) but represents the intent to fully oxidise the system.

4.2.1.4. Preparation of microemulsion samples containing manganese and sodium metaphosphate

0.015 mol dm^{-3} stock solutions of $MnSO_4 \bullet 4H_2O$ and $Mn(AcO)_3 \bullet 2H_2O$ were prepared in 1.0 mol dm^{-3} sulphuric acid. $Na_5P_3O_{10}$ (Fluka) was also present in these solutions at a concentration of 0.045 mol dm^{-3}. Microemulsion samples were prepared using these stock solutions at ω = 9.2 and ϕ_d = 0.45 and [H_2SO_4] = 0.67 mol dm^{-3}. The concentration of manganese was varied between 0.001 mol dm^{-3} and 0.01 mol dm^{-3} and the concentration of $Na_5P_3O_{10}$ was three times that of the concentration of manganese. Microemulsion samples containing the oxidised form of the catalyst were also prepared by adding sodium bromate to oxidise the $MnSO_4$: ω = 9.2 and ϕ_d = 0.45, [$NaBrO_3$] = 0.25 mol dm^{-3} and [H_2SO_4] = 0.67 mol dm^{-3}. The concentration of $MnSO_4$ was varied between 0.001 mol dm^{-3} and 0.01 mol dm^{-3}. Again, the concentration of $Na_5P_3O_{10}$ was always three times that of the concentration of manganese.

4.2.1.5. Preparation of microemulsion samples containing manganese and ortho-phosphoric acid

A stock solution of 0.42 mol dm^{-3} sulphuric acid and 0.28 mol dm^{-3} phosphoric acid was prepared. A second identical stock solution was prepared and solid sodium bromate added to give [$NaBrO_3$] = 0.28 mol dm^{-3}. Reduced catalyst microemulsions were prepared by adding the sulphuric/phosphoric acid stock solution and sufficient volume of a 0.015 mol

dm^{-3} stock solution of $MnSO_4$ to a 1.5 mol dm^{-3} solution of AOT in octane. Oxidised catalyst microemulsions were prepared in the same way using the sulphuric/phosphoric/sodium bromate stock solution. All samples were prepared at ω = 9.2, ϕ_d = 0.45, $[H_2SO_4]$ = 0.3 mol dm^{-3} and $[H_3PO_4]$ = 0.2 mol dm^{-3}. For oxidised samples, $[NaBrO_3]$ = 0.2 mol dm^{-3}.

4.2.1.6. NMR methodology

After preparation, the samples were transferred to a 5 mm o.d. NMR tube that was then placed inside the probe in the bore of the magnetic resonance spectrometer and allowed to equilibrate to a bore temperature of 17° C. The spectrometer used was a Bruker DMX–300, comprising a 7.0 Tesla superconducting magnet operating at a proton frequency of 300 MHz. Measurements were performed using a single transmit/receive 10 mm saddle r.f. coil. The spectrometer was controlled via a Silicon Graphics workstation running XWIN-NMR[10].

T_1 relaxation times of the samples were measured using an inversion recovery pulse sequence. A variable delay list with values ranging from 1 μs to 100 ms was used and the repetition time, T_R, was 7 seconds. The spectral width was 50 kHz and 16k data points were acquired, with four signal averages. T_2 relaxation times were measured using a 2-D Hahn echo pulse sequence. A variable delay list with 30 values ranging from 100 μs to 500 ms was used. The repetition time was 5 seconds. The spectral width was 40 kHz and 16k data points were acquired in the spectral dimension. Four signal averages were acquired. For both types of experiment the 180° r.f. pulse was

28 μs at 0 dB attenuation and the 90° pulse was 14 μs. For more details refer to Section 1.7.

Once the data sets were acquired, they were analysed using Prospa[11], to extract exponential recovery (T_1) and exponential decay (T_2) curves. KaleidaGraph[12] was then used to fit these curves to Equations 1.16 and 1.13 to obtain the T_1 and T_2 relaxation times respectively. The relaxivity for each system was found by plotting the relaxation rate versus the concentration of manganese, and fitting the data using a linear regression procedure.

4.2.2. NMR detection of oscillations in the oxidation state of manganese in the BZ reaction

A number of oscillatory manganese-catalysed BZ reactions were investigated, using NMR measurements to observe oscillations in the oxidation state of the manganese. Reactions were performed in the aqueous system and also in the AOT/octane microemulsion system.

4.2.2.1. Preparation of aqueous BZ reactions

Stock solutions of 0.010 mol dm^{-3} $MnSO_4 \bullet 4H_2O$, 1.5 mol dm^{-3} sodium bromate, 5.0 mol dm^{-3} sulphuric acid and 2.0 mol dm^{-3} malonic acid, were all prepared using nanopure water from a Millipak Millipore purification unit. Phosphoric acid (85%, 15 mol dm^{-3}) was used as received from the supplier. Aqueous manganese-catalysed BZ reactions were prepared by mixing the aqueous reagents in a beaker stirred using a magnetic flea. Typically, the reaction composition was $[MnSO_4]$ = 1.0 mmol dm^{-3}, $[NaBrO_3]$ = 0.1 mol dm^{-3},

[MA] = 0.15 mol dm^{-3} and [H_2SO_4] = 0.3 mol dm^{-3}. Aqueous, phosphoric acid-stabilised, manganese-catalysed reactions were also prepared with the typical reaction composition [$MnSO_4$] = 1.0 mmol dm^{-3}, [$NaBrO_3$] = 0.1 mol dm^{-3}, [MA] = 0.15 mol dm^{-3} and [H_2SO_4] = 0.3 mol dm^{-3} and [H_3PO_4] = 0.2 mol dm^{-3}.

4.2.2.2. Preparation of manganese-catalysed BZ-AOT reactions

Stock solutions of the BZ reactants were prepared as in Section 4.2.2.1. A stock solution of 1.5 mol dm^{-3} AOT in octane was also prepared. These were used to prepare two stock microemulsions, ME_1 and ME_2. ME_1 contained sulphuric acid, malonic acid and AOT-in-octane solution. ME_2 contained manganese sulphate, sodium bromate and AOT-in-octane. Both stock microemulsions were prepared at the same water-to-surfactant ratio, ω, and droplet fraction, ϕ_d. ME_1 and ME_2 were then mixed in a one-to-one ratio, and enough additional octane was added to give the required droplet fraction. Refer to Section 2.2.1 for more details on the preparation of microemulsions. Typical initial reactant concentrations were: [$MnSO_4$] = 1.0 mmol dm^{-3}, [$NaBrO_3$] = 0.18 mol dm^{-3}, [MA] = 0.22 mol dm^{-3} and [H_2SO_4] = 0.29 mol dm^{-3}, with ω = 9.2 and ϕ_d = 0.45.

4.2.2.3. Preparation of phosphoric acid stabilised manganese-catalysed BZ-AOT reactions

Stock solutions of the BZ reactants and phosphoric acid were used to prepare an aqueous BZ reaction. After a brief period (approximately 1 minute) of mixing, an aliquot of this aqueous reaction was taken and added to a solution of 1.5 mol dm^{-3} AOT in octane. The AOT solution had been pre-diluted with

sufficient additional octane so that upon addition of the aqueous aliquot, the resultant microemulsion had the required water-to-surfactant ratio and droplet fraction. Typical reagent concentrations were: [$MnSO_4$] = 1.2 mmol dm^{-3}, [$NaBrO_3$] = 0.1 mol dm^{-3}, [MA] = 0.15 mol dm^{-3}, [H_2SO_4] = 0.3 mol dm^{-3} and [H_3PO_4] = 0.2 mol dm^{-3}, with ω = 9.2 and ϕ_d = 0.45. A dual catalyst manganese/ferroin BZ-AOT reaction was also prepared in the same way with [$MnSO_4$] = 1.2 mmol dm^{-3}, [$NaBrO_3$] = 0.1 mol dm^{-3}, [MA] = 0.15 mol dm^{-3}, [H_2SO_4] = 0.3 mol dm^{-3} and [H_3PO_4] = 0.2 mol dm^{-3}, [ferroin] = 0.33 mmol dm^{-3}, ω = 9.2 and ϕ_d = 0.45.

4.2.2.4. Monitoring oscillations in the BZ reaction using NMR

Hansen and Ruoff[13] were able to monitor oscillations in a manganese-catalysed BZ reaction using NMR. Their experiment involved stirring a small reaction volume inside the bore of the magnet. The BZ-AOT system is more viscous and requires much more vigorous stirring. Attempts were made to perform the BZ-AOT reaction inside the bore of the magnet, using a compressed air driven stirrer made of polyetheretherketone (PEEK). However, it was found that the reactor was not efficiently mixed using this method. Therefore, an experiment was designed where a stirred BZ-AOT reaction was performed outside the magnet. A stirred reaction vessel of approximately 50 ml volume was filled with the reacting BZ system. The stirring rate was controlled to ensure sufficient mixing whilst avoiding the formation of air bubbles in the vessel, as these would have an extremely detrimental effect on the quality of the NMR spectra obtained. A four channel peristaltic pump (Ismatec) was used to pump the reaction mixture out of the reaction vessel, through the bore of the magnetic resonance spectrometer

and back into the reaction vessel. Clear Tygon tubing (Cole Parmer, inner diameter = 1.6 mm) was used to connect the pump to the reaction vessel. Two glass capillaries (5 cm × 1 mm i.d.) connected with a loop of tubing made up the “sample section” inside the r.f. coil of the spectrometer. The cartridges that control the pumping flow rate were fitted with clear Tygon tubing (Cole Parmer, inner diameter = 2.79 mm). The tubing was fixed together using appropriate plastic connectors. The smaller diameter tubing was used wherever possible to minimise the time taken for the reaction mixture to travel the entire loop of the system. Larger diameter tubing was used for the pumping section to maximise the flow rate, again minimising the circuit time. A schematic diagram of the apparatus is shown in Figure 4.1. The total volume of the system was approximately 58 ml, with the connecting tubing and sample section accounting for ~ 8 ml of this total volume. For aqueous systems, the flow rate obtained using the pump at maximum capacity was found to be ~ 0.77 ml s^{-1}. Given the volume of the system inside the r.f. coil is approximately 0.06 ml, the time between reaction mixture entering the region surrounded by the r.f. coil and exiting it is ~ 80 ms. When pumping the more viscous AOT system, the flow rate was found to be ~ 0.38 ml s^{-1}, which equates to a residence time within the r.f. coil of ~160 ms. There was a compromise between having a high flow rate so that the reaction spent as short a time as possible outside of the stirred reaction vessel, and having a low enough flow rate so that the residence time inside the r.f. coil was long enough to obtain an NMR spectrum *i.e.* that it experienced the full pulse sequence. The second of these considerations was more important when running the inversion recovery pulse sequence (refer to Section 4.2.2.4). This

pulse sequence consists of two r.f. pulses separated by a delay, therefore, the residence time had to be long enough so that a significant proportion of the volume of reaction in the sample section experienced both the 180° pulse and the 90° pulse.

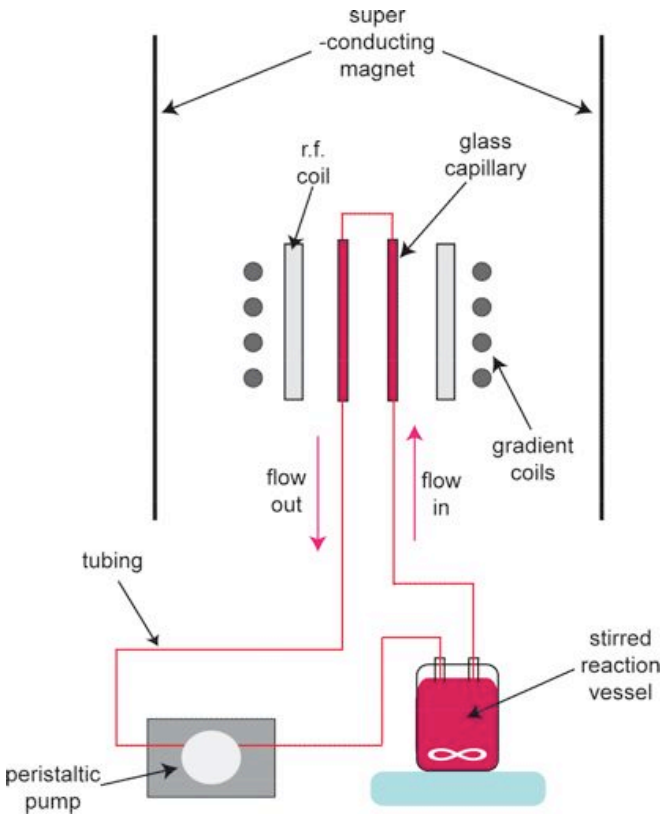

Figure 4.1 Schematic representation of the apparatus used to monitor oscillations in the BZ reaction using NMR measurements.

Pumping was switched on to fill the sample section and then switched off. Tuning and shimming was performed on the system in this static state, which took approximately 5 minutes. Pumping was then resumed. Oscillations in the T_2^* relaxation time of the water signal were observed via oscillations in the NMR linewidth, using a 2-dimensional pulse-acquire pulse sequence. This pulse sequence consists simply of a 90° r.f. excitation pulse followed by acquisition of the FID. This pulse sequence was repeated multiple times to

collect a series of time resolved NMR spectra. Depending on the duration of the reaction, approximately 3000 spectra were collected. The time between each spectrum is equal to the product of the repetition time, T_R, and the number of signal averages. Typically only one signal average was acquired to keep the time between each spectrum to a minimum. The disadvantage of this is that there is no phase cycling, which helps to remove unwanted signal and artefacts from the NMR signal. The repetition time was also kept as short as possible, typically T_R = 2 s. Oscillations in the T_1 relaxation time of the water signal were observed using a one-dimensional inversion recovery pulse sequence with a user-defined delay between the inverting 180° pulse and the 90° recovery pulse. The pulse sequence was first performed in setup (GS) mode, where the user-defined delay was adjusted to obtain the minimum amount of signal. This corresponded to the τ_{null} of the reduced state of the system, (refer to Section 1.7.1.2 and Equation 1.15). The oxidised state of the system has a different τ_{null} and therefore more signal was observed when the system was in its oxidised state. With the τ_{null} set to 23 ms, the inversion recovery experiment was then performed in full. The repetition time was kept short, T_R = 2 s, and only one signal average was acquired. This gave an acquisition time between successive spectra of approximately 2 s.

A small portion of the reaction mixture was kept aside and oscillations in the redox potential were measured using a platinum combination redox electrode (Thermo Orion) (Ag/AgCl internal reference). In some cases, a bromide combination ion-selective electrode (Jencons) was also used to monitor oscillations in [Br^-].

4.3. Results and Discussion

4.3.1. Comparison of the relaxivity of AOT microemulsions containing manganese

	$[H_2SO_4]$ / mol dm^{-3}	R_1 / mM^{-1} s^{-1}	R_2 / mM^{-1} s^{-1}
$MnSO_4$	0.67	33	280
$MnSO_4$	3.3	35	220
$Mn(AcO)_3$	3.3	23	170
$MnSO_4 + BrO_3^-$	0.67	34	230
$MnSO_4 + BrO_3^-$	3.3	15	120
$MnSO_4 + Na_5P_3O_{10}$	0.67	31	180
$Mn(AcO)_3 + Na_5P_3O_{10}$	0.67	19	120
$MnSO_4 + H_3PO_4$	0.3	26	360
$MnSO_4 + H_3PO_4 + BrO_3^-$	0.3	8	150
$^{14}Mn^{2+}$ - aquo ion	-	44	-
$^{15}Mn^{3+}$ - TPPS	-	7.8	-

Table 4.1 Compilation of water proton T_1 and T_2 relaxivities, R_1 and R_2, for the various manganese microemulsion systems studied in this work. The last two entries in the table show the relaxivities of Mn^{2+} and Mn^{3+} in aqueous systems, for comparison purposes. Entries in red text correspond to reduced oxidation state samples; blue text signifies oxidised state samples.

Table 4.1 collates the relaxivity data for all the manganese microemulsions systems studied. The high relaxivity of manganese in general arises from a large number of unpaired electrons – Mn^{2+} and Mn^{3+} have five and four unpaired electrons respectively, and have magnetic moments close to the value given by the spin only formula, 5.92 BM and 4.90 BM respectively[16]. The effect is compounded by the ability of Mn^{2+} and Mn^{3+} to coordinate large numbers of solvent water molecules; Mn^{2+} is able to coordinate 6 water molecules in its inner sphere[14]. Coordinated water molecules are able to exchange rapidly with the bulk solvent water, which further facilitates the relaxation of solvent nuclei[17]. Paramagnetic ions are thus able to greatly

reduce the relaxation times of surrounding solvent water molecules. The magnitude of this effect will be greater for more paramagnetic ions. The relaxivity of Mn^{2+} is, therefore, expected to be higher than that of Mn^{3+}, as Mn^{2+} has a high spin d^5 electronic configuration, possessing a total of 5 unpaired electrons. Mn^{3+} is d^4 and has fewer unpaired electrons, and as such is less paramagnetic[16].

The relaxivity of Mn^{2+} and Mn^{3+} has previously been measured in the liquid phase. These values appear as the last two entries in Table 4.1. The T_1 relaxivities of Mn^{2+} and Mn^{3+} reported are from two separate studies[14,15]. Here, the manganese(II) species was the Mn^{2+} hexa-aquo ion, and the manganese(III) species was a complex of Mn^{3+} with TPPS4, a large macro-cyclic molecule. Formally, six water molecules are directly coordinated to the Mn^{2+}, compared to only two water molecules for the Mn^{3+} complex. The rotational correlation time of the large Mn^{3+} macro-cycle complex will also be longer, which will affect the measured relaxivity. It is therefore difficult to directly compare the relaxivities measured, however, it can be seen that the relaxivities measured in the liquid phase and in the microemulsion systems are of the same order of magnitude. This suggests that manganese ions have a similar effect on the water contained within reverse micelles as they do in the pure liquid phase.

Unlike the $Ru(bpy)_3$-AOT microemulsion systems investigated (refer to Chapter 3 for more details), the ability of the manganese ions to increase the relaxivity of the water pool does not appear to be inhibited by their location in

the reverse micelle system. In all cases there is a clear dependence of the measured relaxation time upon the concentration of manganese. With the $Ru(bpy)_3$ system, the complex resides predominantly within the micellar interface. As such, the relaxation times of the water pool are dominated by the tumbling rate of the reverse micelle system as a whole, and the presence of the weakly paramagnetic $Ru(bpy)_3$ complex has no influence in smaller droplets. With the manganese system it would seem much more likely that the manganese ions reside almost exclusively within the water droplet core, and are able to exert their strong paramagnetic influence upon the relaxation times of the water molecules. This conclusion is supported by ESR measurements[18], which show that manganese ions are solubilised within the water droplet core of reverse micelles in a CTAB-chloroform-water microemulsion system.

4.3.1.1. Relaxivity of manganese in its reduced and oxidised states in the AOT/octane microemulsion

To characterise the manganese-catalysed BZ-AOT system in terms of NMR relaxation times, the relaxivity of the system was measured for both the reduced and oxidised form of the manganese catalyst. Reduced oxidation state (Mn^{2+}) microemulsions were prepared using $MnSO_4$, oxidised state (Mn^{3+}) microemulsions were prepared using $Mn(acetate)_3$. It was assumed that these "phantom" samples would be representative of the manganese-catalysed BZ-AOT reaction in its reduced and oxidised states, and assist in choosing appropriate MRI parameters. Figure 4.2 shows the water proton T_1 and T_2 relaxivity plots for these samples. The T_1 relaxivity (R_1) for the reduced and oxidised forms was 35 mM^{-1} s^{-1} and 23 mM^{-1} s^{-1} respectively. T_2

relaxivities (R_2) for the reduced and oxidised states were calculated as 220 mM^{-1} s^{-1} and 170 mM s^{-1} respectively. As expected the relaxivity of the oxidised form is lower than that of the reduced form due to fewer unpaired electrons in the oxidised state.

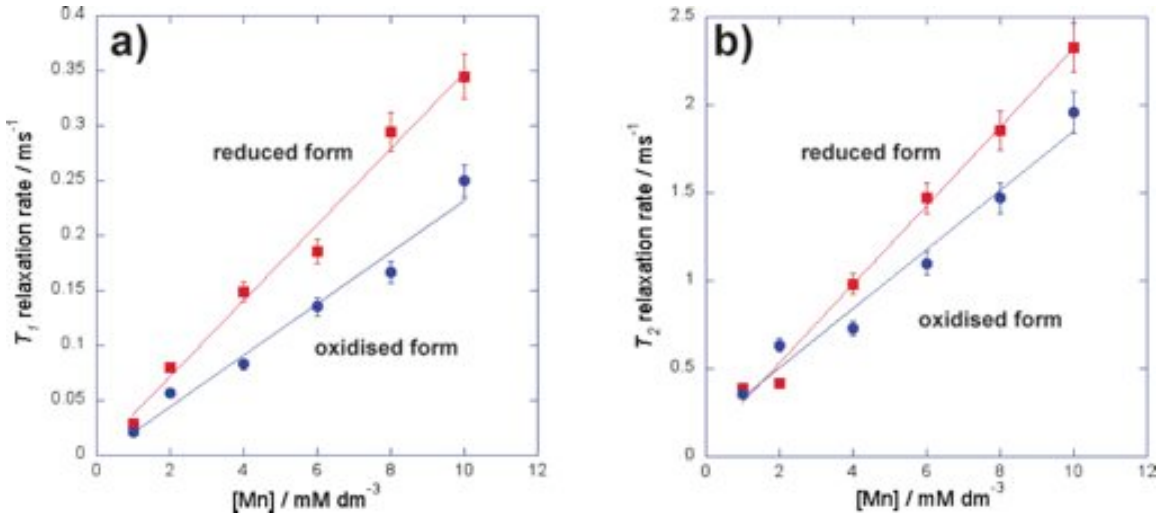

Figure 4.2 Water proton T_1, a), and T_2, b), relaxivity plots of AOT/octane microemulsion samples containing manganese in its reduced (red squares) and oxidised (blue circles) states. Reduced oxidation state microemulsions were made with $MnSO_4$, oxidised state microemulsions were made with $Mn(Acetate)_3$. All samples were prepared at ω = 9.2, ϕ_d = 0.45 and $[H_2SO_4]$ = 3.3 M.

The oxidised state of the manganese catalyst was also accessed by oxidation of $MnSO_4$ using acidified bromate. The relaxivity of this system was measured for two different concentrations of sulphuric acid, i) 3.3 mol dm^{-3} and ii) 0.67 mol dm^{-3}, with sodium bromate added for oxidised microemulsion samples, $[NaBrO_3]$ = 0.36 mol dm^{-3}. Figure 4.3 shows the results of these measurements. As can be seen, similar relaxivities were measured for reduced catalyst microemulsions at both high and low sulphuric acid concentrations, R_1 = 35 mM^{-1} s^{-1} and 33 mM^{-1} s^{-1} respectively. R_2 = 220 mM^{-}

^{1} s^{-1} and 280 mM^{-1} s^{-1}. For the oxidised catalyst microemulsions, it was only at the higher concentration of sulphuric acid, $[H_2SO_4]$ = 3.3 mol dm^{-3}, that the relaxivity was affected. R_1 for the low acid concentration system was 34 mM^{-1} s^{-1} and R_2 = 230 mM^{-1} s^{-1}. For the high acid concentration R_1 and R_2 were significantly less, 15 mM^{-1} s^{-1} and 120 mM^{-1} s^{-1} respectively.

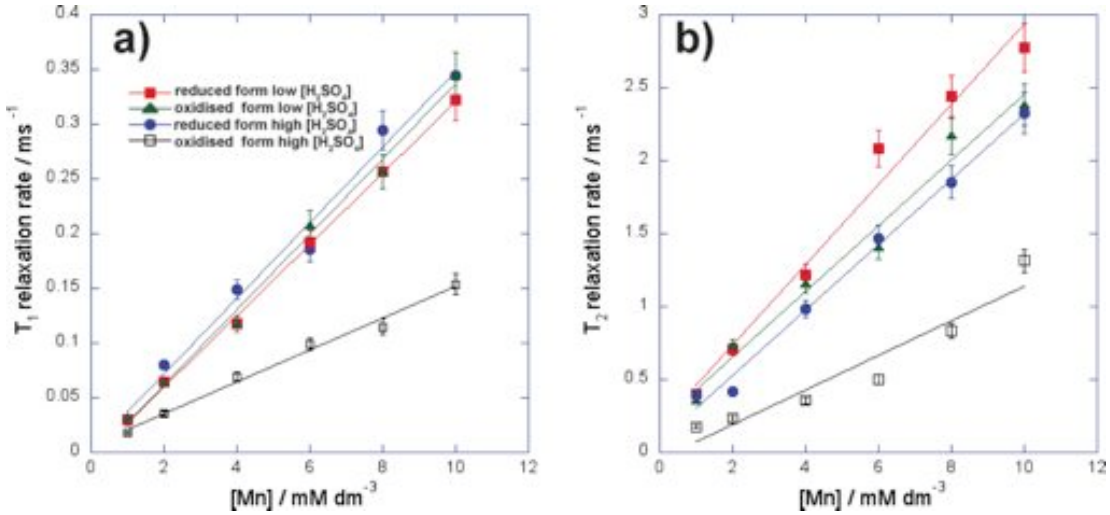

Figure 4.3 Water proton T_1, a) and T_2, b), relaxivity plots for AOT/octane microemulsion samples containing "reduced" (red squares and blue circles) and "oxidised" (green triangles and open squares) states of $MnSO_4$ at different concentrations of H_2SO_4. All microemulsions were prepared at ω = 9.2 and ϕ_d = 0.45. "Low" acid concentration microemulsions (red squares and green triangles) were prepared at $[H_2SO_4]$ = 0.67 M. "High" acid concentration samples (blue circles and open squares) were prepared at $[H_2SO_4]$ = 3.3 M. Reduced catalyst microemulsions were prepared with $MnSO_4$. Oxidised catalyst microemulsions were prepared with $MnSO_4$ and sodium bromate, $[NaBrO_3]$ = 0.36 M.

It has been reported[19] that acidified bromate does not completely oxidise Mn^{2+} to Mn^{3+}, instead an equilibrium exists between the reduced and oxidised forms.

$$Mn^{2+} + BrO_2\bullet + H^+ \rightleftarrows Mn^{3+} + HBrO_2 \qquad \textbf{(4.1)}$$

By increasing the acid concentration, the position of the equilibrium is shifted, and greater conversion of Mn^{2+} to Mn^{3+} is effected. Hence, longer relaxation times and lower relaxivity are observed at the higher concentration of sulphuric acid when sodium bromate is present. It is possible that the AOT reverse micelle environment contributes to this effect. It has been reported[20] that sulfonate groups present on the head group of the AOT molecule have a buffer-like action on the water contained within the reverse micelles. The microemulsion medium may therefore be able to regulate the acidity of the water droplet, leading to less conversion of Mn^{2+} to Mn^{3+} at a given acid concentration.

4.3.2. Improving relaxation time contrast using phosphate

Image contrast in MR imaging is dependent on a number of factors. The signal intensity of a given region in an image will be governed by the spin density of the nuclei within that region and the relaxation times, T_1 and T_2 of those nuclei[21]. By manipulating pulse sequences and setting the parameters of the pulse sequence *e.g.* the repetition time, T_R, and echo time, T_e, contrast in the image can be made to be more, or less dependent (or *weighted)* on the above factors. By having a long repetition time ($T_R >> T_1$) and short echo time ($T_e << T_2$), images are produced where spin density is the major factor in determining image contrast. Parameter-weighted contrast can be introduced into MR images by shortening T_R (T_1-weighted contrast) and by lengthening the echo time (T_2-weighted contrast)[22].

By increasing the difference in relaxation times of the reduced and oxidised forms of the manganese catalyst, greater image contrast can be obtained through T_1 and T_2 weighting[17]. Imaging sequences can then be optimised to perform, for example, faster experiments or to obtain higher resolution images, whilst maintaining a sufficient degree of image contrast. Improving the relaxation time contrast between reduced and oxidised forms of the manganese catalyst has previously been achieved by using various phosphates[5]. Na_3PO_4, $Na_4P_2O_7$ and $Na_5P_3O_{10}$ have all been shown to enhance the relaxation time contrast available using a manganese catalyst. The Mn^{3+} ion is unstable in solution and disproportionates [23] to form Mn^{2+} and Mn^{4+}.

$$2Mn^{3+} + 2H_2O \rightleftarrows Mn^{2+} + MnO_2 + 4H^+ \qquad \textbf{(4.2)}$$

Phosphates (as well as sulphates) are able to stabilise the Mn^{3+} ion[24] and effect a greater degree of conversion from the reduced form of the catalyst to the oxidised form, resulting in a greater difference in the observed signal intensities in MR images. Cross *et al*[5] have shown that $Na_5P_3O_{10}$ is particularly suited to enhancing relaxation time contrast when using manganese as the catalyst of the BZ reaction. The metaphosphate ion $P_3O_{10}^{5-}$ is able to stabilise the Mn^{3+} ion, through the formation of a manganese-phosphate chelate, shown in Figure 4.4.

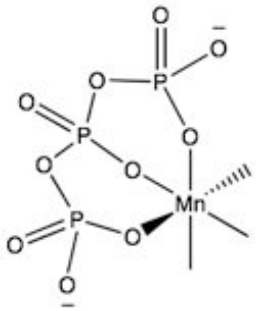

Figure 4.4 Formation of stabilising chelate between manganese (III) ion and metaphosphate ion ($P_3O_{10}^{5-}$).

4.3.2.1. Relaxation time contrast enhancement using $Na_5P_3O_{10}$

The relaxivity of microemulsions containing the reduced and oxidised states of the manganese catalyst in the presence of sodium tripolyphosphate ($Na_5P_3O_{10}$) was measured. Figure 4.5 shows the comparison between the water proton T_1 relaxivities measured for reduced catalyst microemulsions and oxidised catalyst microemulsions with and without the presence of phosphate. The T_1 relaxivities calculated from these plots are summarised in Table 4.2. As the figure demonstrates, the relaxivity of the oxidised microemulsion system containing phosphate is lower than that for the oxidised microemulsion system without phosphate. The phosphate is able to stabilise the Mn^{3+} population, effectively increasing the conversion of Mn^{2+} to Mn^{3+} in the prevailing oxidising conditions, which decreases the relaxivity of the stabilised system with respect to the non-stabilised system. The formation of the Mn^{3+}–phosphate chelate is also likely to limit the co-ordination of water molecules, which will further reduce the relaxivity of the phosphate-stabilised system. Another factor is the lower reduction potential of chelated manganese

complexes[25], which would also favour the Mn^{3+} oxidation state, thereby reducing the measured relaxivity.

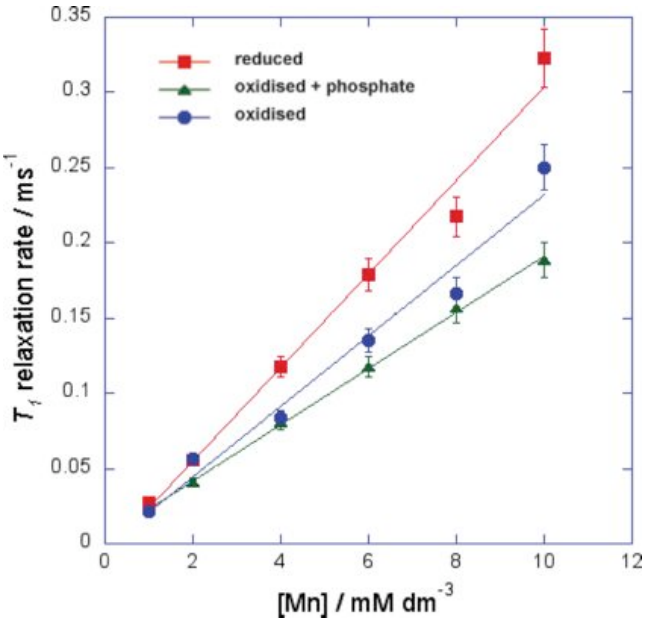

Figure 4.5 Comparison of water proton T_1 relaxivities for reduced catalyst (red squares) microemulsions and oxidised catalyst microemulsions with (green triangles) and without (blue circles) the presence of $Na_5P_3O_{10}$. All samples were prepared at ω = 9.2 and ϕ_d = 0.45. Reduced catalyst samples were prepared using $MnSO_4$. Oxidised samples were prepared using $Mn(acetate)_3$. For samples containing $Na_5P_3O_{10}$, the phosphate was present in a 3:1 ratio of $[Na_5P_3O_{10}]$:[Mn].

	T_1 relaxivity / mM^{-1} s^{-1}
$MnSO_4$ + phosphate	31
$Mn(acetate)_3$	23
$Mn(acetate)_3$ + phosphate	19

Table 4.2 Comparison of water proton T_1 relaxivities obtained from the relaxivity plots shown in Figure 4.5.

4.3.2.2. Relaxivity of phosphoric acid-stabilised manganese microemulsions

Phosphoric acid is also able to stabilise the Mn^{3+} ion via the formation of manganese-phosphate complexes[5]. As can be seen from Equation 4.2,

increased acidity also affects the hydrolysis equilibrium, favouring the Mn^{3+} oxidation state. However, the stabilising effect of chelate formation is not as profound as with the metaphosphate compound discussed in Section 4.3.2.1. Whereas, the metaphosphate only needs to be present in relatively small amounts (approximately 50 mM), the concentration of phosphoric acid required is much greater (in excess of 1 M)[5,26]. This increased acidity is restricting with respect to preparation of the BZ reaction. Ideally, the acidity of the reaction is regulated by the concentration of sulphuric acid present. With the inclusion of phosphoric acid the acidity of the reaction is now dependent upon the concentration of both phosphoric and sulphuric acid. Given that some phosphoric acid must be present to stabilise the manganese, this reduces the range over which the concentration of sulphuric acid can be varied. It is particularly restricting with respect to the formation of stationary patterns, as these patterns are typically only seen at lower acid concentrations[27]. It was also necessary to reduce the phosphoric acid concentration in order to prepare stable microemulsions. The relaxivity of phosphoric acid stabilised manganese microemulsions was measured for the reduced and oxidised states of the catalyst. Reduced catalyst samples were prepared using $MnSO_4$, and oxidised catalyst samples were prepared by oxidising $MnSO_4$ using acidified bromate. Figure 4.6 shows the T_1 relaxivity plots obtained for these microemulsions. The calculated relaxivities were 26 mM^{-1} s^{-1} and 8.2 mM^{-1} s^{-1} for the reduced and oxidised forms respectively. The stabilising effect of ortho-phosphoric acid is apparent in the low relaxivity value measured for the oxidised state. From Figure 4.6, it can be seen that the data for the oxidised form deviates from the straight line fit. It has been

reported that complex formation between the orthophosphate ion PO_4^{3-} and Mn^{3+} is a relatively slow process[5]. At higher concentrations of Mn^{3+} it is plausible that this complexation rate is increased, and hence a greater population of phosphate-stabilised Mn^{3+} is established more quickly, leading to a reduction in relaxivity. The measured relaxation times are still significantly longer for the oxidised state than the reduced state, as would be expected due to its lower paramagnetism.

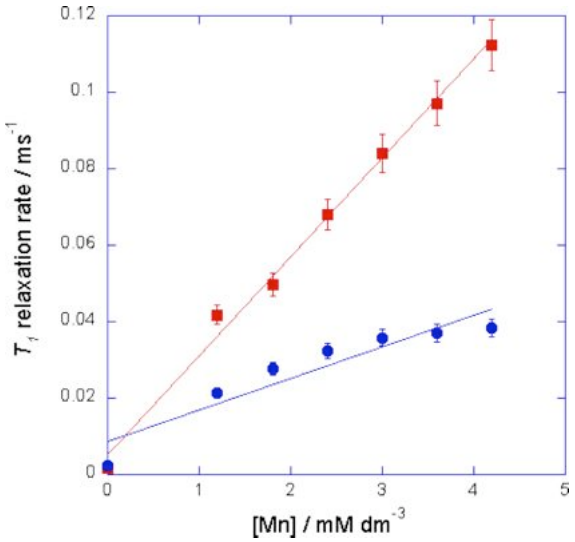

Figure 4.6 Water proton T_1 relaxivity plots for microemulsions containing phosphoric acid stabilised manganese in its reduced (red square) and oxidised (blue circle) states. All samples were prepared at ω = 9.2, ϕ_d = 0.45, [H_2SO_4] = 0.3 M and [H_3PO_4] = 0.2 M. Oxidised microemulsions were prepared with [$NaBrO_3$] = 0.2 M.

4.3.3. Observation of oscillations in the BZ-AOT system using NMR

To observe oscillatory behaviour in the BZ reaction using NMR requires that the reduced and oxidised states of the system are distinguishable from one another. As has been shown in the previous sections, the reduced and oxidised forms of the manganese catalyst are characterised by different T_1

and T_2 relaxivities. This is the case in both the aqueous system and the AOT/octane microemulsion system. Hansen and Ruoff[13] have shown that oscillations in the manganese-catalysed BZ reaction can be observed by measuring the line width of the water solvent peak over time. The line width of a peak in an NMR spectrum is determined by the transverse relaxation time, T_2, of the spin system giving rise to that particular peak [28.] The line width at full width half maximum, $\Delta_{\nu_{1/2}}$, in units of Hertz is given by Equation 4.3.

$$\Delta_{\nu_{1/2}} = \frac{1}{\pi T_2} \qquad \textbf{(4.3)}$$

Oscillations in the manganese-catalysed BZ reaction are thus observable as a change in the NMR line width as the catalyst oscillates between its reduced and oxidised states.

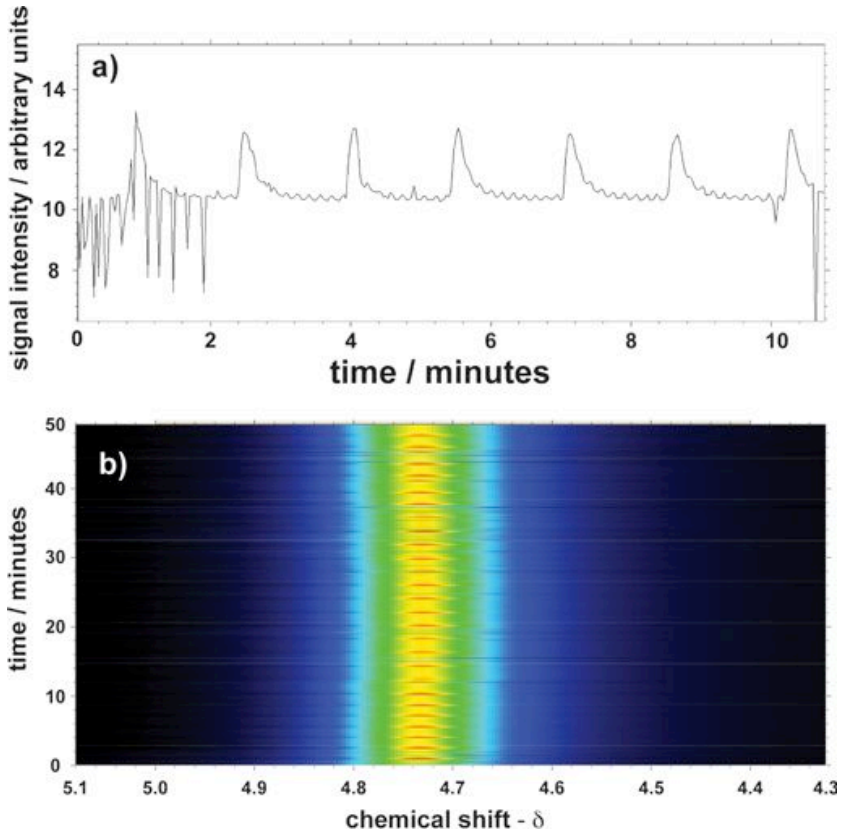

Figure 4.7 a) Oscillations observed in the water proton NMR signal intensity in the aqueous manganese-catalysed BZ reaction. b) Two-dimensional data set showing NMR spectra as a function of time for the aqueous manganese-catalysed BZ reaction. The colour scale ranges from low signal intensity (black) to high signal intensity (red). The oscillation period is approximately 115 seconds. [$MnSO_4$] = 1.0 mM, [$NaBrO_3$] = 0.18 M, [MA] = 0.22 M, [H_2SO_4] = 0.29 M. The noise present in the spectra arises from bubbles present in the reaction.

A two-dimensional pulse-acquire sequence was used to observe oscillations in the signal intensity of the water proton NMR signal in the aqueous manganese-catalysed BZ reaction, (Figure 4.7). Figure 4.7 b) shows the two-dimensional data set acquired using the pulse-acquire sequence, comprising a series of NMR spectra acquired at timed intervals during the course of the reaction. Note that there is no chemical shift reference for the spectra presented in this chapter; rather, the frequency axis of the two-dimensional data sets was calibrated to give a relative chemical shift scale, with the water

proton resonance assigned at around 4.7 ppm. Figure 4.7 a) shows the signal intensity of the water proton resonance plotted versus time. The period of the oscillations was approximately 115 seconds and they lasted in excess of 90 minutes. Oscillations in the signal intensity are associated with oscillations in the line width; the line width in the oxidised state is narrower due to the longer T_2^* of the system. As the area of the peak must stay the same, the intensity must increase to compensate. Hence, in the reduced state, broader, lower intensity lines are observed, and narrower, higher intensity lines are observed in the oxidised state, (Figure 4.8). Figure 4.9 shows oscillations in the same aqueous manganese-catalysed BZ reaction observed using a bromide combination electrode. The oscillation period in this case is longer at approximately 160 seconds. This discrepancy could arise from the temperature difference; the laboratory temperature for the NMR experiment was 20°C (the bore temperature was cooler at 17°C, but the reaction mixture spends the majority of the time outside of the bore), whereas the electrode measurement was performed at 19°C, and it is known that an increase in temperature leads to a shortening of the oscillatory period[29]. It is also possible that the periods are sensitive to the presence of oxygen, which is known to affect the oscillation period[30]. It is possible that the pumping apparatus and vigorous stirring used for the NMR experiment introduced more oxygen into the system than in the electrode measurement.

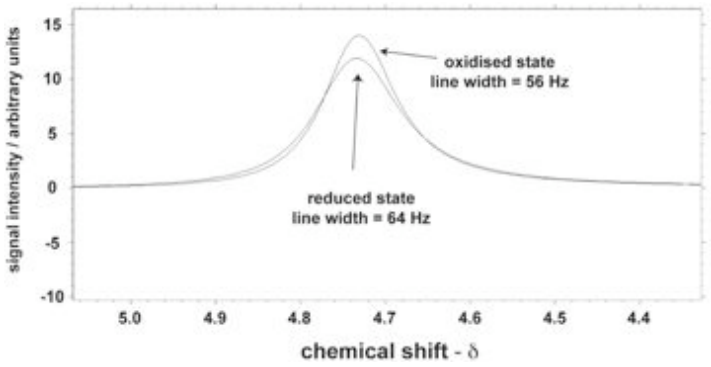

Figure 4.8 Comparison of FWHM line widths of the water proton NMR signal of the reduced and oxidised states of the aqueous manganese-catalysed BZ reaction performed in Figure 4.7. [$MnSO_4$] = 1.0 mM, [$NaBrO_3$] = 0.18 M, [MA] = 0.22 M, [H_2SO_4] = 0.29 M.

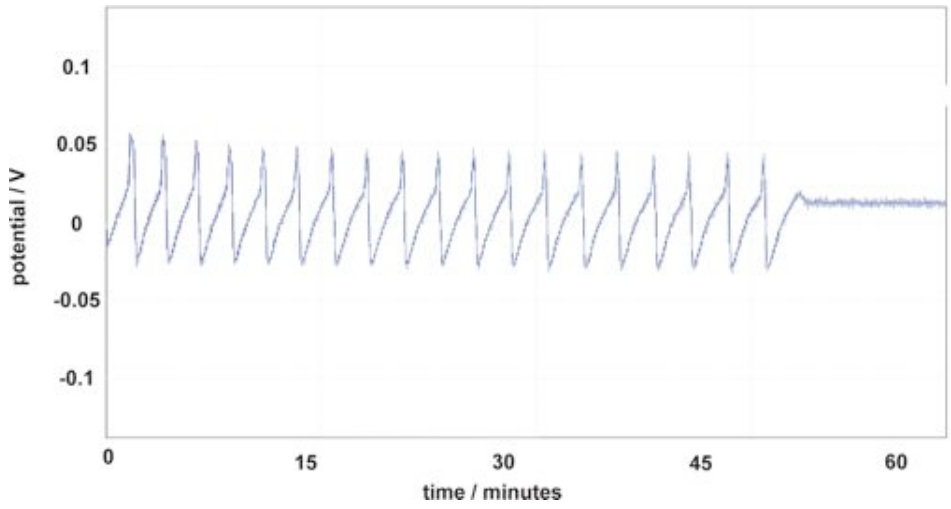

Figure 4.9 Oscillations in electrode potential observed in the aqueous manganese-catalysed BZ reaction using a bromide combination electrode. The oscillation period is approximately 160 seconds. [$MnSO_4$] = 1.0 mM, [$NaBrO_3$] = 0.18 M, [MA] = 0.22 M, [H_2SO_4] = 0.29 M.

NMR spectra of the manganese-catalysed BZ-AOT reaction were acquired at timed intervals, using a two-dimensional pulse-acquire sequence. Figure 4.10 b) shows the two-dimensional data set that was acquired, focussing on the region of the spectrum containing the water proton resonance. Figure 4.10 a) shows the signal intensity at the centre of the water proton resonance plotted

versus time. Oscillations can be observed after approximately 32 minutes with a time period of around 110 seconds.

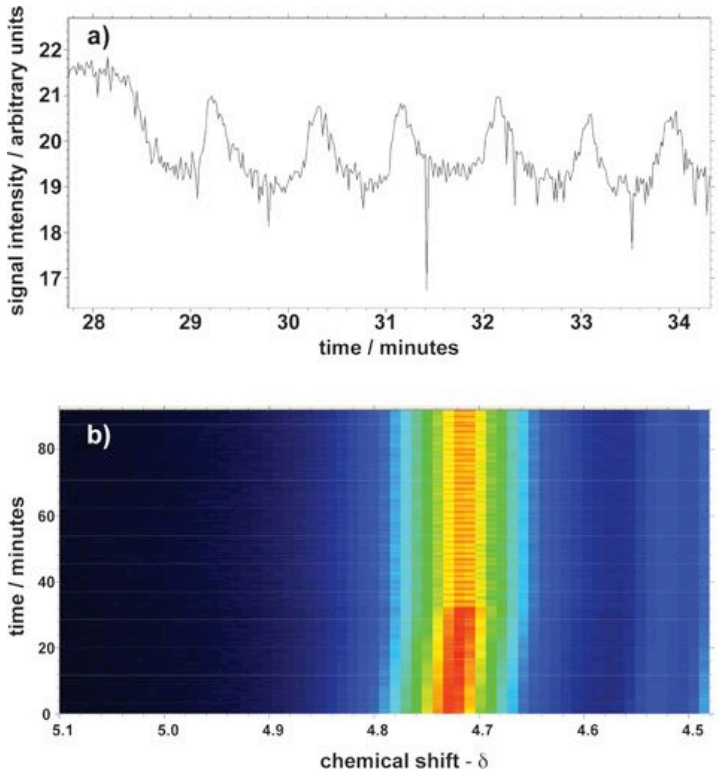

Figure 4.10 a) Oscillations in the signal intensity of the solvent water proton peak in the manganese-catalysed BZ-AOT reaction. b) ^{1}H-NMR spectra as a function of time for the same manganese-catalysed BZ-AOT reaction as in a). The colour scale ranges from low signal intensity (black) to high signal intensity (red). The induction period of the reaction lasts approximately 32 minutes, after which oscillations are observed with a period of around 110 seconds. [$MnSO_4$] = 1.0 mM, [$NaBrO_3$] = 0.18 M, [MA] = 0. 22 M, [H_2SO_4] = 0.29 M, ω = 9.2 and ϕ_d = 0.45. The time between acquisitions of successive spectra is approximately 2 seconds.

It was also possible to observe oscillations in the oxidation state of the manganese catalyst via a change in the T_1 relaxation time of the solvent water molecules. By setting the inter-pulse delay, τ, to the τ_{null} of the water solvent peak in the reduced state of the system, (in this case τ_{null} = 23 ms, corresponding to a reduced state T_1 of 33 ms) the 90° recovery pulse was

applied as the longitudinal magnetisation vector goes through its null point *i.e.* there is no net magnetisation vector. Therefore when the 90° pulse was applied whilst the system was in its reduced state, no signal was observed from the water solvent peak. The T_1 relaxation time of the water solvent peak in the oxidised form is different and as such the 90° pulse was applied when there was an overall net magnetisation vector *i.e.* $\tau \neq \tau_{null}$. Therefore, more signal was observed from the solvent water peak when the system was in its oxidised state. Figure 4.11 shows oscillations observed in the signal intensity of the water proton peak using a one-dimensional inversion recovery pulse sequence. Oscillations were observed with a time period of 110 seconds, as was the case with the two-dimensional pulse-acquire performed on the same reaction in Figure 4.10. As can be seen, the data acquired using the pulse-acquire sequence was less noisy. This is because the pulse-acquire sequence consists of only one r.f. pulse, whereas the inversion-recovery sequence requires two r.f. pulses separated by a delay. Therefore, in the inversion-recovery experiment, not all of the sample in the r.f. coil's observable region, had experienced both r.f. pulses. The net result of this is that sample section contains a mixture of spin systems, some of which have undergone inversion and some that have not, resulting in somewhat noisy spectra. As such, the two-dimensional pulse-acquire sequence represents a better method with which to observe oscillations, provided there is a difference in T_2^* between the reduced and oxidised states of the reaction.

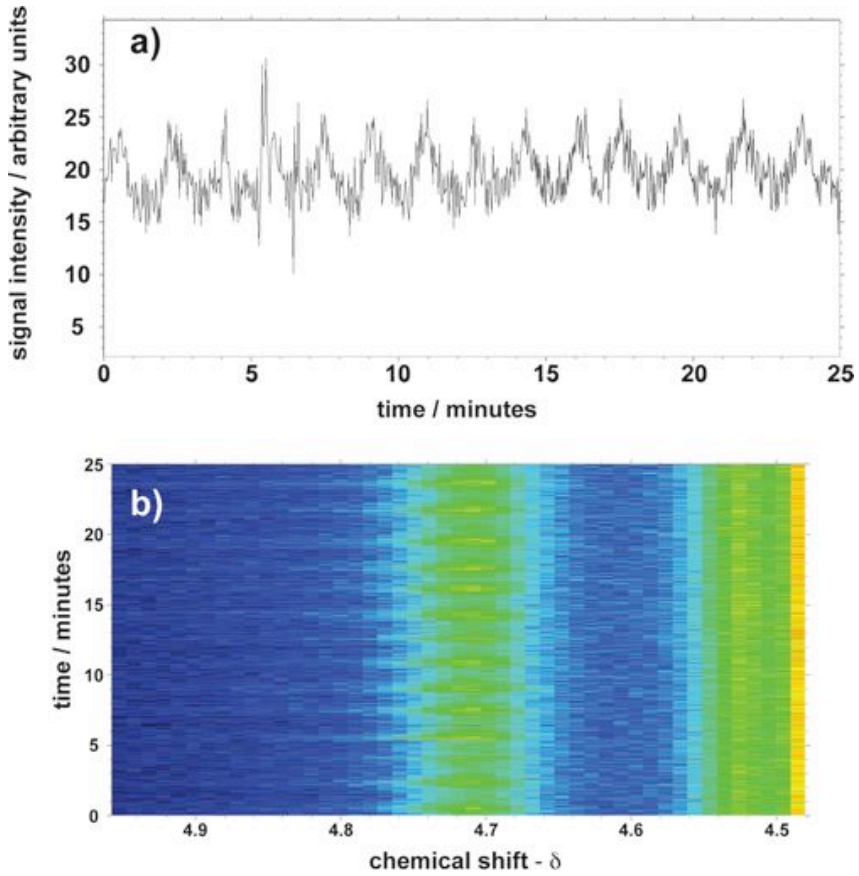

Figure 4.11 a) Oscillations observed in the signal intensity of the water proton peak of a manganese-catalysed BZ-AOT reaction. b) Two-dimensional data set acquired using an inversion-recovery pulse sequence. The colour scale ranges from low signal intensity (blue) to high signal intensity (yellow/orange). The reaction is the same as that in Figure 4.10 and the time period is approximately 110 seconds. [$MnSO_4$] = 1.0 mM, [$NaBrO_3$] = 0.18 M, [MA] = 0. 22 M, [H_2SO_4] = 0.29 M, ω = 9.2 and ϕ_d = 0.45.

4.3.3.1. Observation of oscillations and travelling waves in a dual catalysed BZ-AOT reaction

The two-dimensional pulse-acquire sequence was also used to monitor oscillations in a phosphoric acid-stabilised, manganese-catalysed BZ-AOT reaction; the results are shown in Figure 4.12. It was also possible to observe the oscillations in this system as a colour change. In the reduced state the microemulsion was colourless. Upon oxidation, the microemulsion took on a

very pale pink colour. Whether this colour change was sufficient to provide the necessary contrast to observe patterns in an unstirred system would have to be assessed using the optical imaging techniques described in Chapter 2.

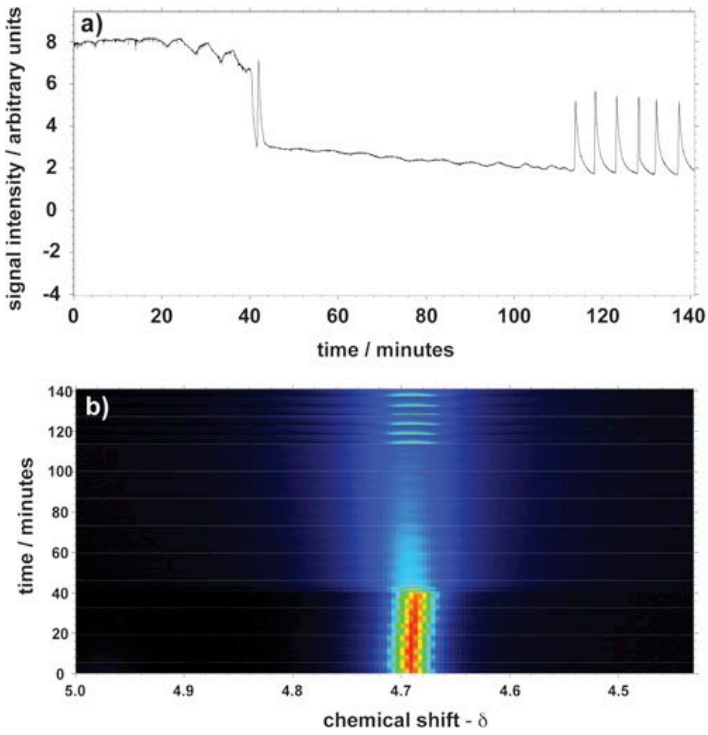

Figure 4.12 a) Oscillations observed in the signal intensity of the water proton peak of a phosphoric acid-stabilised, manganese-catalysed BZ-AOT reaction. b) Two-dimensional data set acquired using an inversion recovery pulse sequence. The colour scale ranges from low signal intensity (black) to high signal intensity (red). After an induction period of around 115 minutes, oscillations were observed with a time period of approximately 280 seconds. [$MnSO_4$] = 1.2 mM, [$NaBrO_3$] = 0.1 M, [MA] = 0.15 M, [H_2SO_4] = 0.3 M, [H_3PO_4] = 1.4 M, ω = 9.2 and ϕ_d = 0.45.

The phosphoric acid-stabilised system was characterised by much greater contrast between its reduced and oxidised states. This can be seen clearly in a comparison of the NMR line widths. Figure 4.13 a) shows the line widths in the reduced and oxidised states for the manganese-catalysed BZ-AOT reaction, and Figure 4.13 b) shows the line widths for the phosphoric acid-

stabilised reaction. The difference in the line widths for the non-stabilised reaction is minimal, Δ = 4 Hz. In the stabilised reaction, the difference is much greater, Δ = 37 Hz. Given the inverse relationship between line width and T_2^* (Equation 4.3), this equates to a difference of only 0.4 ms between T_2^* for the non-stabilised system. For the stabilised system the difference is 9.0 ms. It is expected that a similar result would be obtained with the metaphosphate-stabilised manganese-catalysed BZ-AOT reaction, however, time constraints prevented the acquisition of this data.

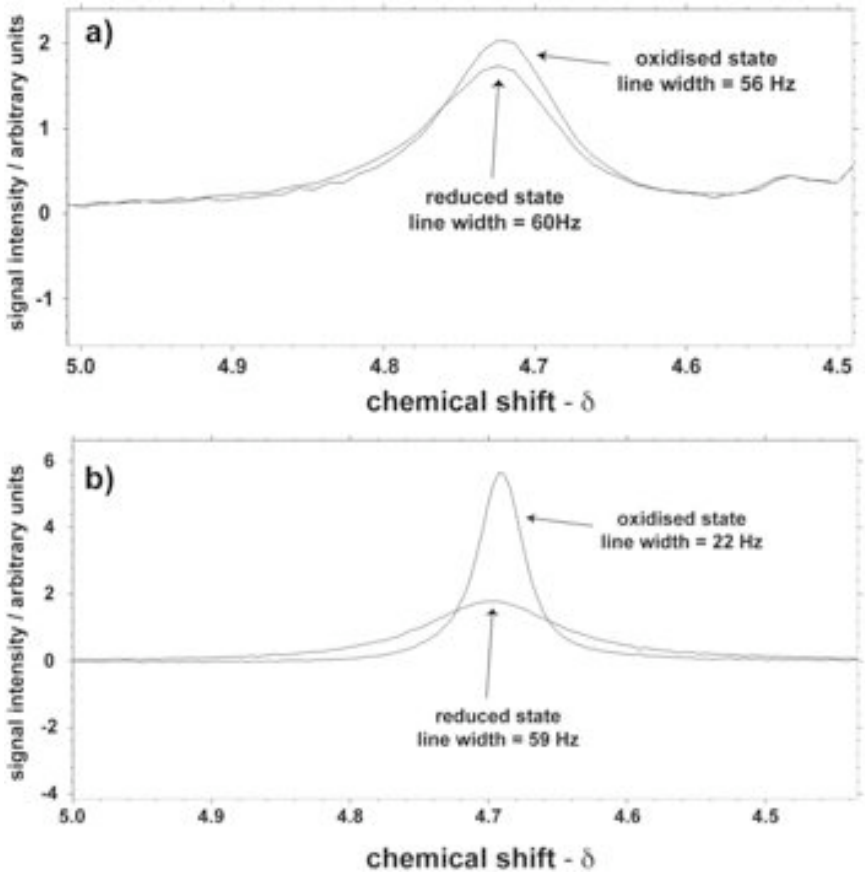

Figure 4.13 Comparison between FWHM line widths for the reduced and oxidised states of a) a manganese-catalysed BZ-AOT reaction and b) a phosphoric acid-stabilised manganese-catalysed BZ-AOT reaction. Experiment parameters for a) are [$MnSO_4$] = 1.0 mM, [$NaBrO_3$] = 0.18 M, [MA] = 0. 22 M, [H_2SO_4] = 0.29 M, ω = 9.2 and ϕ_d = 0.45. Experiment parameters for b) are [$MnSO_4$] = 1.2 mM, [$NaBrO_3$] = 0.1 M, [MA] = 0.15 M, [H_2SO_4] = 0.3 M, [H_3PO_4] = 1.4 M, ω = 9.2 and ϕ_d = 0.45.

It was also possible to observe oscillations in the ferroin/manganese dual catalysed BZ-AOT system. Oscillations were seen in the signal intensity/line width of the water proton NMR signal, indicative of oscillations in the oxidation state of the manganese catalyst, Figure 4.14. Again, the presence of phosphoric acid in this system improved the T_2* contrast. Travelling waves were also observed in this system via differences in the oxidation state of the ferroin catalyst/indicator, Figure 4.15.

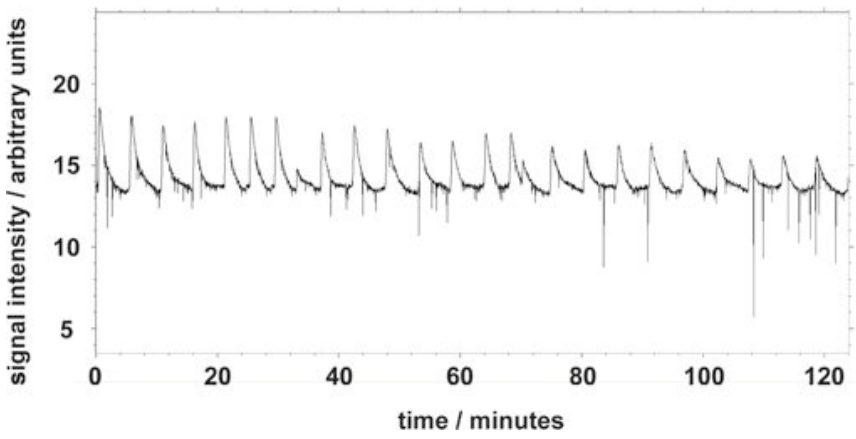

Figure 4.14 Oscillations observed in the signal intensity of the water proton peak of a phosphoric acid-stabilised, ferroin/manganese dual-catalysed BZ-AOT reaction. [$MnSO_4$] = 1.2 mM, [ferroin] = 0.33 mM, [$NaBrO_3$] = 0.1 M, [MA] = 0.15 M, [H_2SO_4] = 0.3 M, [H_3PO_4] = 0.2 M, ω = 9.2 and ϕ_d = 0.45.

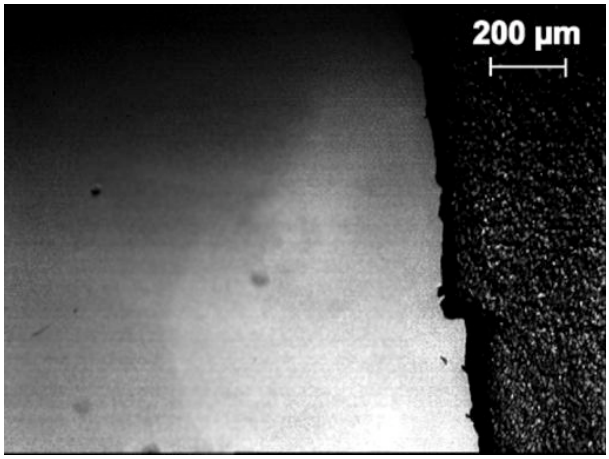

Figure 4.15 Travelling waves observed in the same dual-catalysed BZ-AOT reaction shown in Figure 4.14. [$MnSO_4$] = 1.2 mM, [ferroin] = 0.33 mM, [$NaBrO_3$] = 0.1 M, [MA] = 0.15 M, [H_2SO_4] = 0.3 M, [H_3PO_4] = 0.2 M, ω = 9.2 and ϕ_d = 0.45.

Optical imaging of the dual catalyst ferroin/manganese system is discussed in more detail in Chapter 2. The result obtained here is significant; the dual catalyst system potentially represents a catalyst system in which patterns in the BZ-AOT system can be observed both optically, and also using MRI. Results of optical imaging and MR imaging experiments could then be compared to see if patterns and waves observed utilising the colour contrast of the ferroin catalyst are similar to those observed using the relaxation time contrast available with the manganese catalyst.

4.4. Conclusions

The T_1 and T_2 relaxivities of manganese have been measured in the AOT/octane microemulsion system in both its reduced (Mn^{2+}) and oxidised (Mn^{3+}) states. In all cases, manganese was found to reduce the relaxation times of the water pool contained within the reverse micelles. For the majority of systems investigated the relaxivities for the higher oxidation state were

lower than in the reduced state, as would be expected due to the lower paramagnetism of the Mn^{3+} ion. The conversion of Mn^{2+} to Mn^{3+} brought about by acidified bromate was found to be incomplete as has been previously reported[8,19]. At higher acidity, a greater degree of conversion of Mn^{2+} to Mn^{3+} was effected.

It has also been shown that phosphates (both orthophosphate (PO_4^{3-}) and metaphosphate ($P_3O_{10}^{5-}$) were able to stabilise the oxidised form of the manganese catalyst in the AOT microemulsions system. This stabilisation effected a greater conversion between Mn^{2+} and Mn^{3+} enhancing the NMR relaxation time contrast. Of the two phosphate-stabilised systems investigated, the sodium tripolyphosphate (metaphosphate) was preferred for investigations of the BZ-AOT reaction. It does not affect the preparation of stable microemulsion samples, and it does not restrict the range of parameter space that can be observed.

The T_1 and T_2 relaxation time contrast available in the manganese-catalysed BZ-AOT reaction has been exploited to observe temporal oscillations during the reaction through oscillations in the line-width and signal intensity of the water proton resonance. Again, the stabilising effect of phosphoric acid was observed. The relaxation time contrast was greatly enhanced in the stabilised system. A manganese/ferroin dual-catalysed BZ-AOT reaction was also investigated. The NMR relaxation time contrast available in this system due to the presence of manganese was exploited to observe temporal oscillations in a stirred BZ-AOT reaction, whilst the visual contrast offered by the ferroin

catalyst/indicator was utilised to observe chemical waves in a two-dimensional reactor containing the same reaction.

The reduced and oxidised states of a number of manganese-catalysed BZ-AOT reactions have been characterised in terms of their NMR relaxation times, and it has been shown possible to distinguish between the two states using NMR. These results then form the basis for work presented in the next chapter, namely the imaging of patterns and waves in the BZ-AOT reaction using MRI.

4.5. References

(1) Fruhbeis, H.; Roder, A. *Angewandte Chemie-International Edition* **1971**, *10*, 192.

(2) Thompson, R. C. *Journal Of The American Chemical Society* **1971**, *93*, 7315.

(3) Koros, E. *Nature* **1974**, *251*, 703.

(4) Gao, Y.; Cross, A. R.; Armstrong, R. L. *Journal Of Physical Chemistry* **1996**, *100*, 10159.

(5) Cross, A. R.; Armstrong, R. L.; Reid, A.; Su, S. Y.; Menzinger, M. *Journal Of Physical Chemistry* **1995**, *99*, 16616.

(6) Cross, A. L.; Armstrong, R. L.; Gobrecht, C.; Paton, M.; Ware, C. *Magnetic Resonance Imaging* **1997**, *15*, 719.

(7) Tzalmona, A.; Armstrong, R. L.; Menzinger, M.; Cross, A.; Lemaire, C. *Chemical Physics Letters* **1990**, *174*, 199.

(8) Britton, M. M. *Journal Of Physical Chemistry A* **2006**, *110*, 13209.

(9) Britton, M. M. *Journal Of Physical Chemistry A* **2006**, *110*, 2579.

(10) XWIN-NMR; 2.6 ed.; Bruker.

(11) Prospa; 2.1 ed.; Magritek.

(12) Kaleidagraph; 4.03 ed.; Synergy Software.

(13) Hansen, E. W.; Ruoff, P. *The Journal of Physical Chemistry* **1989**, *93*, 264.

(14) Chen, C.-w.; Cohen, J. S.; Myers, C. E.; Sohn, M. *FEBS Letters* **1984**, *168*, 70.

(15) Koenig, S. H.; Brown, R. D.; Spiller, M. *Magnetic Resonance in Medicine* **1987**, *4*, 252.

(16) Earnshaw, A.; Greenwood, N. *Chemistry of the Elements, Second Edition*; Butterworth-Heinemann: Oxford, 1997.

(17) Lauffer, R. B. *Chemical Reviews* **1987**, *87*, 901.

(18) Seno, M.; Sawada, K.; Araki, K.; Kise, H.; Iwamoto, K. *Journal Name: Bull. Chem. Soc. Jpn.; (Japan); Journal Volume: 53:7* **1980**, Medium: X; Size: Pages: 2083.

(19) Szalai, I.; Kurin-Csorgei, K.; Epstein, I. R.; Orban, M. *Journal Of Physical Chemistry A* **2003**, *107*, 10074.

(20) Hasegawa, M. *Langmuir* **2001**, *17*, 1426.

(21) Haacke, M.; Brown, R.; Thompson, M.; Venkatesan, R. *Magnetic Resonance Imaging: Physical Principles and Sequence Design*; Wiley-Liss: New York, 1999.

(22) Callaghan, P. T. *Principles of Nuclear Magnetic Resonance Microscopy*; Oxford University Press: New York, 1991.

(23) Housecroft, C.; Sharpe, A. G. *Inorganic Chemistry*; Prentice Hall: London, 2004.

(24) Cotton, A.; Murillo, C.; Bochmann, M. *Advanced Inorganic Chemistry, 6th Edition*; Wiley-Interscience: New York, 1999.

(25) Gorbacheva, M.; Morozova, O.; Shumakovich, G.; Streltsov, A.; Shleev, S.; Yaropolov, A. *Bioorganic Chemistry* **2009**, *37*, 1.

(26) Britton, M. M.; Sederman, A. J.; Taylor, A. F.; Scott, S. K.; Gladden, L. F. *Journal Of Physical Chemistry A* **2005**, *109*, 8306.

(27) Vanag, V. K. *Physics-Uspekhi* **2004**, *47*, 923.

(28) Levitt, M. H. *Spin Dynamics: Basics of Nuclear Magnetic Resonance*; Wiley & Sons: New York, 2008.
(29) Nagy, G.; Kˆrˆs, E.; Oftedal, N.; Tjelflaat, K.; Ruoff, P. *Chemical Physics Letters* **1996**, *250*, 255.
(30) Field, R. J.; Burger, M. *Oscillations and Traveling Waves in Chemical Systems*; Wiley: New York, 1985.

Chapter 5. MR Imaging of chemical patterns and waves in the BZ-AOT reaction

5.1. Introduction

The BZ-AOT reaction has been shown to exhibit a diverse range of non-equilibrium patterns, including Turing patterns[1-3]. However, to date, the investigation of pattern formation in the system has been confined to two-dimensional studies due to limitations and restrictions imposed by conventional optical imaging techniques. Yet, the closed reaction conditions employed in the BZ-AOT reaction allow for the formation of patterns in three dimensions. The BZ-AOT reaction thus presents an opportunity to observe, for the first time, three-dimensional Turing patterns in a chemical system. MRI is an ideal technique with which to directly observe 3-D patterns, as it is able to penetrate the entire volume of the reaction. Indeed, MRI has been used successfully to image three-dimensional travelling wave patterns in the liquid phase BZ reaction[4]. However, imaging of the BZ reaction in the AOT microemulsion system presents a further challenge in that the dimensions of patterns in the microemulsion system can be less than 100 μm, which is several orders of magnitude smaller than in the liquid phase. Imaging parameters will therefore need to be optimised in order to obtain sufficient resolution in the images to resolve pattern features.

Image contrast in the BZ reaction is available inherently due to the presence of transition metal-ions that catalyse the reaction and oscillate between two

oxidation states during the reaction. The relaxation times of solvent water molecules are sensitive to these changes in oxidation state and it is this relaxation time difference that is exploited to obtain image contrast. To image the BZ-AOT system, it will be necessary to isolate the NMR signal of the water phase by eliminating signal from the AOT and octane phases, as it is expected that relaxation time differences will only be observed for the water phase. A number of catalyst/indicator systems have been shown to provide the necessary image contrast in the liquid phase reaction, namely $Ru(bpy)_3$ and manganese[5]. The feasibility of using the $Ru(bpy)_3$ and manganese catalysts as MR indicators in the BZ-AOT reaction has been explored as part of this work in Chapter 3 and Chapter 4 respectively. As has been shown, the $Ru(bpy)_3$ catalyst has proved incompatible with MR imaging in the AOT microemulsion as it provides little or no contrast between the reduced and oxidised states. The manganese catalyst, however, has been shown to provide the relaxation time contrast required to distinguish between the reduced and oxidised states of the BZ-AOT system. The relaxation time contrast has been exploited to observe temporal changes in oxidation state of the manganese catalyst in the stirred oscillatory reaction.

Having identified a suitable MR active catalyst/indicator system for the BZ-AOT reaction, the aims of this chapter are to identify an MR imaging sequence that can exploit the available relaxation time contrast in order to visualise pattern formation in the system. Imaging parameters are first optimised to obtain satisfactory image contrast and resolution using a phantom system *i.e.* a non-reactive version of the system containing two

separate microemulsions; one representative of the reduced state of the reaction and another representative of the oxidised state. Once this objective is achieved, attempts can be made to image pattern formation in the working reaction using the optimised parameters. Successful completion of these aims will constitute a proof of concept, and will allow the first MR images of pattern formation in the BZ-AOT reaction to be obtained.

5.2. Experimental

5.2.1. Sample preparation

5.2.1.1. Preparation of phantom microemulsions

Phantom microemulsion samples representing the reduced and oxidised states of the manganese catalyst BZ-AOT reaction were prepared. Stock solutions of 5.0 mol dm^{-3} sulphuric acid, 1.5 mol dm^{-3} sodium bromate, 2.0 mol dm^{-3} malonic acid (MA) and 0.01 mol dm^{-3} manganese sulphate were prepared using nanopure water from a Millipak Millipore purification unit. A stock solution of 1.5 mol dm^{-3} of AOT in n-octane was also prepared, by dissolving 111.14 g of AOT in 70 ml of n-octane. A "reduced" state aqueous phase was prepared with $[MnSO_4]$ = 1.2 mmol dm^{-3}, $[H_2SO_4]$ = 0.3 mol dm^{-3} and $[H_3PO_4]$ = 0.2 mol dm^{-3}. A 3 ml aliquot of this aqueous phase was added to 12 ml of the AOT/octane stock solution. This microemulsion was further diluted with 7.5 ml of n-octane to give a reduced state phantom microemulsion with ω = 9.2, ϕ_d = 0.45, $[MnSO_4]$ = 1.2 mmol dm^{-3}, $[H_2SO_4]$ = 0.3 mol dm^{-3} and $[H_3PO_4]$ = 0.2 mol dm^{-3}. An "oxidised" state phantom microemulsion was

similarly prepared with ω = 9.2, ϕ_d = 0.45, [$MnSO_4$] = 1.2 mmol dm^{-3}, [H_2SO_4] = 0.3 mol dm^{-3}, [H_3PO_4] = 0.2 mol dm^{-3} and [$NaBrO_3$] = 0.2 mol dm^{-3}.

5.2.1.2. Preparation of manganese-catalysed, phosphoric acid-stabilised BZ-AOT reaction

An aqueous BZ reaction was prepared containing $MnSO_4$, H_2SO_4, H_3PO_4, $NaBrO_3$ and malonic acid. After a brief period of mixing (approximately 1 minute) a 3 ml aliquot of the reaction was added to 12 ml of 1.5 mol dm^{-3} AOT in octane. This microemulsion was diluted with 7.5 ml of n-octane to give a reactive microemulsion with ω = 9.2 and ϕ_d = 0.45. Typical concentrations of the BZ reactants were: [$MnSO_4$] = 1.2 mmol dm^{-3}, [H_2SO_4] = 0.3 mol dm^{-3}, [H_3PO_4] = 0.2 mol dm^{-3}, [$NaBrO_3$] = 0.2 mol dm^{-3} and [MA] = 0.15 mol dm^{-3}.

5.2.1.3. Preparation of manganese-catalysed, metaphosphate-stabilised BZ-AOT reaction

Stock solutions of the BZ reactants were prepared as in Section 5.2.1.1. A stock solution of 0.1 mol dm^{-3} $Na_5P_3O_{10}$ was also prepared. Two stock microemulsions were prepared by adding aqueous reagents to a 1.5 mol dm^{-3} AOT/octane solution. ME_1 contained H_2SO_4 and malonic acid, ME_2 contained $MnSO_4$, $NaBrO_3$ and $Na_5P_3O_{10}$. Both stock microemulsions were prepared at ω = 9.2 and ϕ_d = 0.67. Equal volumes of ME_1, ME_2 and additional n-octane were mixed to give a reactive microemulsion with ω = 9.2 and ϕ_d = 0.45. Refer to Section 2.2.1 for general details on the preparation of microemulsions. Typical BZ reactant concentrations were: [$MnSO_4$] = 1.2 mmol dm^{-3}, [H_2SO_4] = 0.17 mol dm^{-3}, [$Na_5P_3O_{10}$] = 0.045 mol dm^{-3}, [$NaBrO_3$] = 0.1 mol dm^{-3} and [MA] = 0.15 mol dm^{-3}.

5.2.2. MR imaging of the manganese-catalysed BZ-AOT reaction

5.2.2.1. MR imaging of phosphoric acid-stabilised manganese phantom microemulsions

A 10 mm o.d. NMR tube was filled with the reduced state phantom microemulsion. A 5 mm o.d. NMR tube filled with the oxidised state phantom was then placed inside the 10 mm tube, using a Teflon spacer to align the 5 mm tube centrally in the 10 mm tube, Figure 5.1.

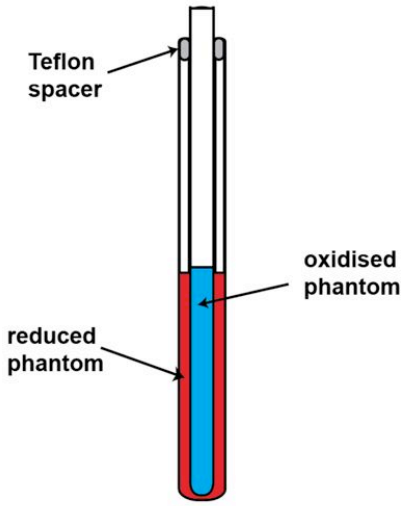

Figure 5.1 Schematic diagram showing the arrangement of a 5 mm NMR tube filled with oxidised state phantom microemulsion, within a 10 mm NMR tube filled with reduced state phantom microemulsion.

The tubes were then placed inside the probe, in the bore of the magnetic resonance spectrometer. The Bruker DMX-300 spectrometer comprises a 7.0 Tesla superconducting magnet operating at a proton frequency of 300 MHz. Imaging experiments were performed using a 25 mm bird-cage resonator r.f. coil. The r.f. coil was surrounded by a three-axis water cooled gradient

system, with a maximum gradient strength of 100 G cm^{-1} in all three directions. The spectrometer was controlled via a Silicon Graphics Workstation using a combination of XWIN-NMR and Paravision software. Refer to Section 1.8 and the references contained therein, for an introduction to the MRI technique. The phantoms were allowed to equilibrate to the bore temperature (17°C), the r.f. coil was tuned and matched and the sample was shimmed. The spectrometer was set on resonance for the water proton signal. Images of the phantoms were acquired using the Paravision M_CHESS pulse sequence; refer to Section 1.9 for more details. The M_CHESS sequence selectively excites only a particular signal. In this case the water proton signal was selectively excited. Two-dimensional images were acquired with a slice-selection gradient used to excite a slice of the system. Typically, the slice thickness was set at 1 mm. The geometry of the slice was varied in order to image the phantom system in a variety of orientations. A horizontal slice, *i.e.* a 1 mm horizontal cross-section of the tubes, and a longitudinal slice, *i.e.* a 1 mm cross-section spanning the length of the tubes, were acquired, Figure 5.2.

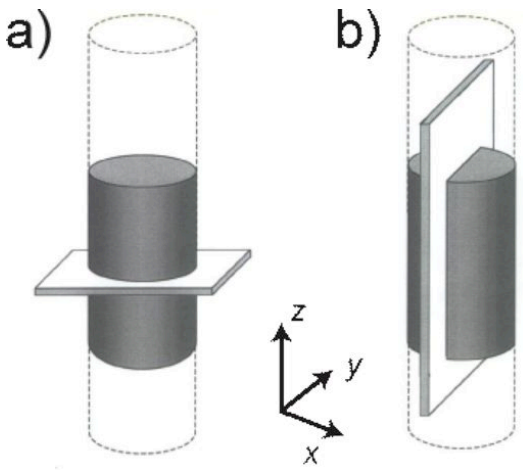

Figure 5.2 Schematic representations of the geometry of a horizontal slice, a) and a longitudinal slice b).

The pulse sequence parameters (T_R, T_E, r.f. pulse lengths, excitation pulse bandwidth, number of signal averages, pixel size, FOV and slice thickness) were first optimised to obtain image contrast between the reduced and oxidised phantoms. The bandwidth of the chemical shift selective pulse was varied to excite only the water proton resonance; the bandwidth was set narrow enough that only the water peak was excited, but sufficiently wide so as to keep the minimum echo time, T_E, within the desired range. The repetition time, T_R, and the echo time were then set to obtain optimum contrast. Typically, the excitation pulse bandwidth was set to 1500 Hz and the echo time and repetition time to 7.6 ms and 150 ms respectively. The spectral width was 100 kHz. The field-of-view and pixel dimensions were adjusted to obtain the best compromise between signal-to-noise ratio, image resolution and the time required to acquire the image. Once suitable parameters had been found to obtain contrast between the reduced and oxidised phantoms, the 5 mm NMR tube containing the oxidised phantom was removed and replaced with a 5 mm NMR tube containing the BZ-AOT reaction. A longitudinal slice of the tube containing the BZ-AOT reaction was then imaged repeatedly. The field-of-view was 40 mm × 20 mm with a 1 mm slice thickness. The image measured 128 pixels in both read and phase encoding directions. Two signal averages were acquired for each image. A single image therefore required approximately 38 s to acquire. The imaging sequence was repeated multiple times to acquire a time series of images, each separated by approximately 38 s.

5.2.2.2. MR imaging of the manganese-catalysed metaphosphate-stabilised BZ-AOT reaction

A 10 mm o.d. NMR tube was filled with the reaction mixture and placed into the bore of the spectrometer. The reaction was imaged using the same CHESS imaging sequence outlined in Section 5.2.2.1. In this case the excitation pulse bandwidth was set to 1600 Hz, centred on the water proton resonance. The spectral width was 100 kHz, the repetition time was 150 ms and the echo time was 9.0 ms. Four signal averages were acquired per image. The image slice was positioned so that each image represents a longitudinal cross section of the reaction tube. Each image was 128 × 64 pixels with a field of view of 20 mm × 10 mm and a 1 mm slice thickness. The total acquisition time for one image was approximately 38 seconds. Again the image sequence was repeated multiple times to obtain a time sequence of images.

5.3. Results and Discussion

5.3.1. MR images of the manganese-catalysed, phosphoric acid-stabilised BZ-AOT reaction

5.3.1.1. Imaging of BZ-AOT phantom system

In order to optimise imaging parameters to provide suitable image contrast between the reduced and oxidised states of the manganese-catalysed BZ-AOT reaction, imaging experiments were first performed on a phantom system. An outer tube was filled with the reduced oxidation state phantom, and a tube containing the oxidised state phantom was placed inside. It was

assumed that these phantoms would be representative of the reduced and oxidised states of the actual working reaction.

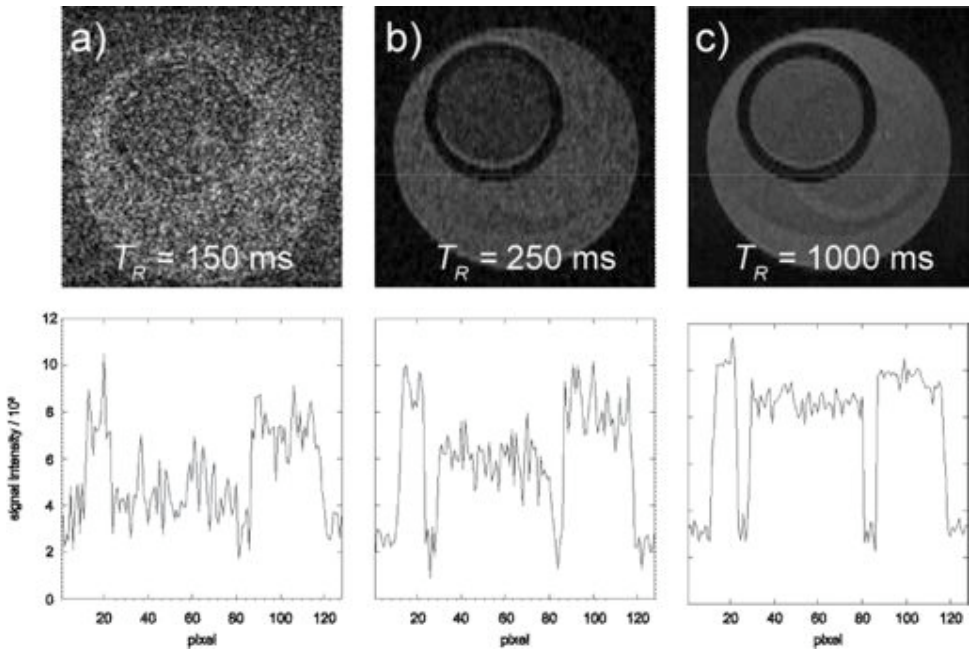

Figure 5.3 M_CHESS images showing a 1 mm horizontal slice of reduced (outer tube) and oxidised (inner tube) phantom systems for various repetition times. In all cases, T_E = 7.6 ms, the FOV is 10 mm × 10 mm, the matrix size is 128 × 128 pixels and four signal averages were acquired. [$MnSO_4$] = 1.2 mM, [H_2SO_4] = 0.3 M, [H_3PO_4] = 0.2 M, ω = 9.2 and ϕ_d = 0.45. The oxidised phantom also contains sodium bromate; [$NaBrO_3$] = 0.2 M. Average signal intensity profiles for the four rows of pixels passing through the centre of the inner tube are also shown for each image. Darker regions in the images correspond to the oxidised state of the catalyst, brighter regions correspond to the reduced state.

Repetition time / ms	Reduced	Oxidised	Reduced/Oxidised ratio	Total experiment time / s
150	4000 ± 500	1000 ± 600	4	77
250	6000 ± 250	3000 ± 250	2	128
1000	7000 ± 100	6000 ± 150	1.2	512

Table 5.1 Table showing the measured signal intensity of oxidised and reduced state phantoms imaged in Figure 5.3. The ratio of reduced signal intensity to oxidised signal intensity is also shown *i.e.* the level of image contrast, as well as the total time required to acquire each image.

Figure 5.3 shows a series of horizontal cross sections acquired using the M_CHESS imaging sequence with varying repetition times, T_R. Signal intensity profiles for the four rows of pixels passing through the centre of the inner tube are also shown for each image. In each case there is contrast between the reduced and oxidised state phantoms, with the signal intensity from the reduced state phantom being greater. At longer repetition times, the image contrast declines. Conversely, the overall signal-to-noise ratio increases for longer repetition times, as progressively more magnetisation is recovered between successive excitation pulses. For each image, the average signal intensity of the reduced and oxidised phantoms was found. The average background noise value was then deducted to obtain the normalised signal intensity. In each case the reduced/oxidised signal intensity ratio was also found. This data is collated in Table 5.1. As can be seen, the image contrast is greatest for the lower repetition time, T_R = 150 ms, though ideally, the contrast could be increased further. The total experiment time is also proportionally shorter, which is clearly advantageous for the visualisation of travelling waves. However, the overall signal-to-noise ratio suffers as a result of the short repetition time. Figure 5.4 shows an image acquired of the phantom system using the same imaging parameters as Figure 5.3 a), with the slice orientation and FOV adjusted to obtain a longitudinal cross section of the phantoms. Again, the contrast between reduced and oxidised phantoms can be seen, with the signal intensity of the oxidised state phantom being lower than for the reduced state. The distortion at the top and bottom of the image, where the tubes appear to narrow, is caused by inhomogeneities in

the r.f. and magnetic gradient fields. The horizontal dark bands at the top and bottom of the image are artefacts, most likely caused by slight imperfections in the durations of the r.f. pulses.

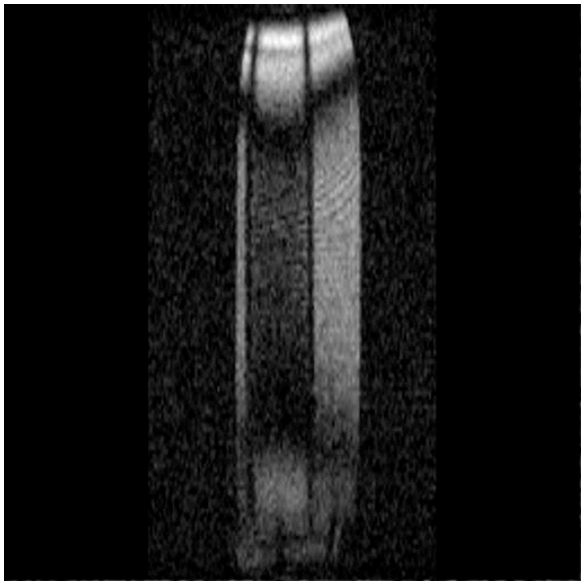

Figure 5.4 CHESS image showing a longitudinal cross-section of two tubes containing reduced and oxidised phantoms of the manganese-catalysed BZ-AOT reaction. The outer tube contains the reduced oxidation state phantom; the inner tube contains the oxidised state phantom. T_R = 150 ms and T_E = 7.6 ms. The FOV is 40 mm × 20 mm and the matrix size is 128 × 128 pixels (the pixels, in this case, are not square). The slice thickness is 1 mm. Two signal averages were acquired. [$MnSO_4$] = 1.2 mM, [H_2SO_4] = 0.3 M, [H_3PO_4] = 0.2 M ω = 9.2 and ϕ_d = 0.45. The oxidised phantom also contains sodium bromate; [$NaBrO_3$] = 0.2 M. Dark regions in the image correspond to the oxidised state of the catalyst, bright regions correspond to the reduced state.

5.3.1.2. Imaging of the reacting system

Figure 5.5 shows a time series of images of the reacting manganese-catalysed phosphoric-acid stabilised BZ-AOT system obtained using the CHESS imaging sequence. The repetition and echo times, T_R and T_E, were the same as those used to acquire images of the phantom system. This

image sequence was taken approximately 30 minutes after the beginning of the reaction. Several successive oxidation fronts were observed with a period of approximately 17 minutes between fronts. The periodic behaviour suggests that the observed travelling fronts may simply be the manifestation of bulk temporal oscillations in an unstirred reactor. However, the front also propagates in a concerted manner and successive fronts propagate in the same direction from the same origin. This suggests the periodic nature of the fronts may arise from a pacemaker site *e.g.* the wall of the NMR tube. As with the phantom system, the signal-to-noise ratio suffers because of the short repetition time. The degree of contrast is also similar to that observed in the phantom system.

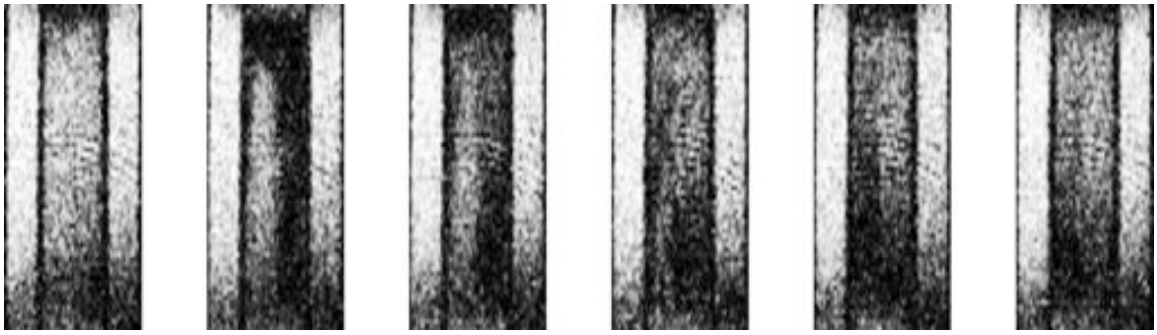

Figure 5.5 CHESS images showing a travelling oxidation front in the manganese-catalysed phosphoric acid-stabilised BZ-AOT reaction. [$MnSO_4$] = 1.2mM, [H_2SO_4] = 0.1 M, [H_3PO_4] = 0.2 M, [MA] = 0.15 M, [$NaBrO_3$] = 0.1 M, ω = 9.2 and ϕ = 0.45. T_R = 150 ms, T_E = 7.6 ms and two signal averages were acquired per image. The matrix size was 128 × 128, the FOV is 40 mm × 20 mm and the slice thickness is 1 mm. The images have been cropped here to show a region measuring approximately 24 mm × 10 mm. The time between images was approximately 38 s. Dark regions correspond to the oxidised state of the catalyst, bright regions correspond to the reduced state.

5.3.2. MR images of the manganese-catalysed, metaphosphate-stabilised BZ-AOT reaction

The acidity of the phosphoric acid-stabilised BZ-AOT reaction is determined in part by the presence of phosphoric acid in they system. The stabilisation of manganese using metaphosphate is preferable, as the metaphosphate ion does not contribute to the overall acidity of the reaction. Increased acid concentrations also have an effect on the structure and stability of the microemulsion. At higher acid concentrations microemulsion samples prepared were unstable and separated into two phases. The metaphosphate-stabilised reaction is, therefore, less restrictive as it allows the reaction to be performed at lower acid concentrations than the phosphoric acid stabilised system allows. This is an important factor, given that pattern selection is sensitive to the concentration of H_2SO_4, and also the physical properties of the microemulsion.

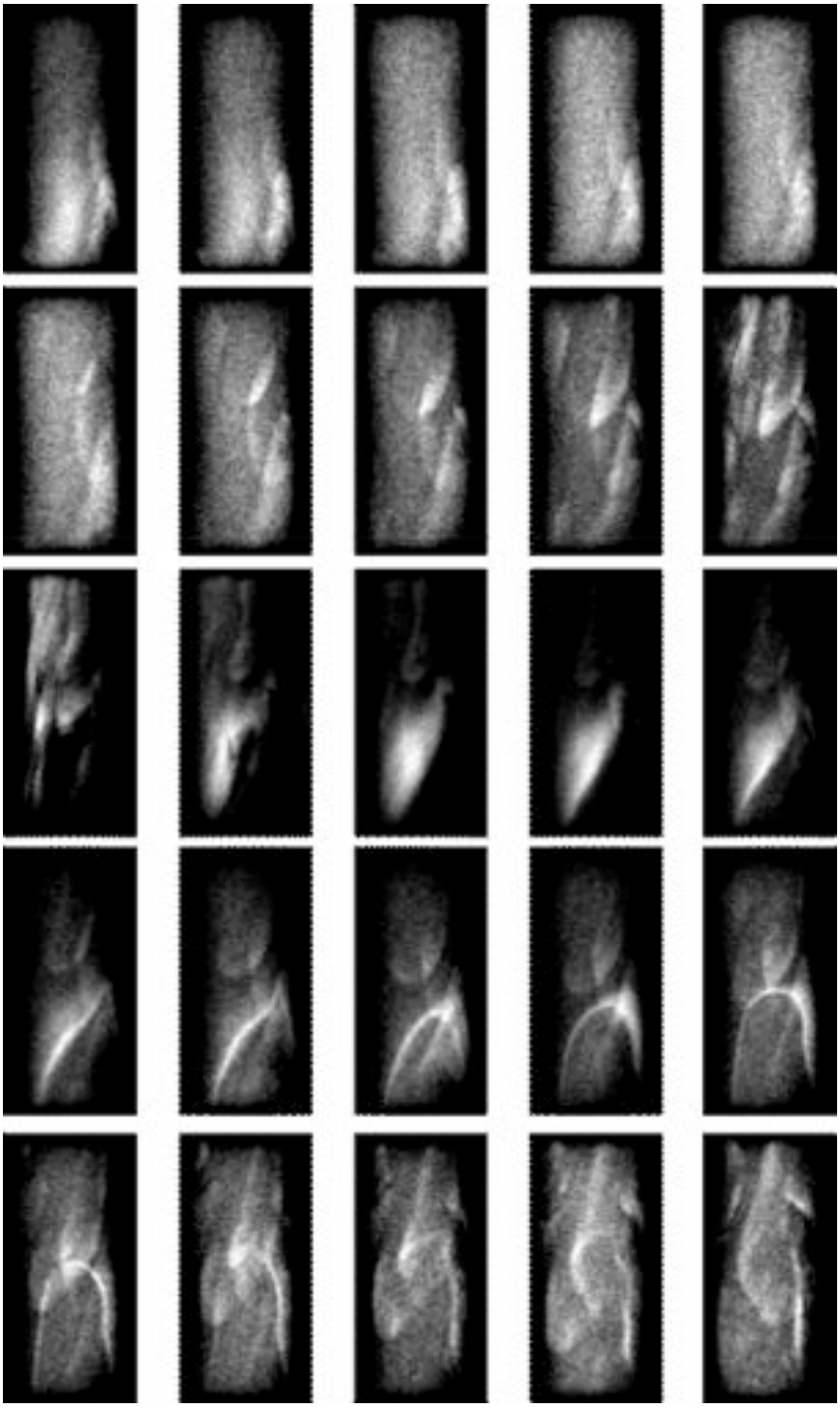

Figure 5.6 MR images of the manganese-catalysed BZ-AOT reaction stabilised by metaphosphate. There is approximately 5 minutes elapsed between each image. Each frame measures approximately 10 mm × 20 mm. [$MnSO_4$] = 1.2 mM, [$Na_5P_3O_{10}$] = 45 mM, [H_2SO_4] = 0.17 M, [MA] = 0.15 M, [$NaBrO_3$] = 0.1 M, ω = 9.2 and ϕ_d = 0.45. Dark regions correspond to the reduced state of the catalyst, bright regions correspond to the oxidised state.

Figure 5.6 shows a time series of images of travelling waves observed in the manganese-catalysed metaphosphate-stabilised BZ-AOT reaction. A movie file of the image sequence is also presented on the attached DVD, (refer to Appendix C). The pixel resolution in both the frequency- and phase-encoded directions is 0.156 mm/pixel, corresponding to a 20 mm × 10 mm FOV with a 128 × 64 pixel array. As the chemical selective excitation pulse was centred about the water proton resonance, contribution to the signal from protons associated with AOT and octane is minimal. As such, image contrast is produced through spin density and the relaxation time differences of the water molecules surrounding the manganese catalyst in its different oxidation states. In this case, the oxidised state of the reaction appears as bright regions in the image. In contrast to the oscillatory behaviour observed in the phosphoric acid-stabilised system, the images here clearly show the formation of distinct travelling waves. The latter half of the sequences then shows the formation of a prominent travelling wave that propagates from the lower right of the image towards the top. The width of the oxidation fronts is approximately 500 μm and they travel at approximately 200 μm min^{-1}, which equates to the fronts travelling approximately 130 μm during the acquisition of one image. As the images are only 2-D projections of a 3-D system, and the waves are moving - albeit slowly - during the acquisition of each image, accurate measurement of the dimensions and velocities of the waves is difficult. It is also difficult to determine the direction in which they travel, particularly in the direction perpendicular to the plane of the image.

Another consequence of the limited dimensionality of the images is that a relatively large volume of the reaction space is condensed into the image. In the two-dimensional systems studied in Chapter 2, a 1 mm square section of the reactor could contain at least 5-6 successive wave fronts. This also appears to be the case in the 3-D reactor, which complicates interpretation of the 2-D images further. Extending the imaging sequence to a third dimension would help to resolve the structure and formation of the patterns. This would, however, require an additional phase encoding gradient to access the third-dimension. To maintain the same pixel size, 64 phase encoding steps would be required, increasing the experiment time to nearly 41 minutes per image, which is clearly insufficient for visualisation of travelling waves.

5.3.2.1. Spatial and temporal resolution

As mentioned, the pixel size in this experiment was 0.156 mm/pixel. Clearly, this is enough to resolve image features that measure much greater than 150 μm, however, to image smaller features this pixel size is inadequate. There is, then, the possibility that patterns and waves with smaller dimensions exist in this system, but the spatial resolution is insufficient to resolve them. Similarly, the temporal resolution, *i.e.* the number of images acquired per unit time, is one image every 38 s. A wave travelling at 200 μm min^{-1}, therefore, travels 130 μm during the acquisition of one image. The appearance of the wave front in the image may then be blurred due to truncation of signal during image acquisition. In order to accurately image such waves, the temporal resolution would need to be improved. Increasing the pixel resolution could be achieved by increasing the number of pixels in the frequency and/or phase encoding directions. However, in the frequency encoding direction this

requires the FID to be sampled for longer which can result in signal degradation due to dephasing. In the phase encoding direction, each extra pixel would require a further excitation, and thus the experiment time is increased proportionally. Additionally, in both cases the reduced pixel size (*i.e.* 0.156 mm^2 pixels reduced to 0.078 mm^2) results in the signal being reduced by a factor of four, as there are less spins contributing to the signal in each pixel. Increasing the number of signal averages would rectify this, but this would result in an increased experiment time. It is evident, then, that there is a compromise between maintaining sufficient spatial resolution and image quality to resolve smaller features, whilst maintaining sufficient temporal resolution to be able to resolve transient features. Clearly, for the visualisation of stationary patterns, spatial resolution and signal-to-noise ratio can be increased at the expense of some temporal resolution. However, for visualisation of transient patterns faster imaging sequences may be required. Extending the imaging sequence into three-dimensions presents a similar challenge. A second phase encoding gradient is required to image the third-dimension. The experiment time is thus increased by a factor equal to the number of pixels in the second phase-encoded direction.

5.4. Conclusions

Having identified the manganese catalyst as a suitable catalyst/indicator system to observe oscillations in the stirred BZ-AOT reaction, MR imaging sequences suitable for visualising pattern formation in the spatially extended system have been identified and optimised in order to achieve satisfactory image contrast. A CHESS imaging sequence has been used to selectively

excite only the water proton resonance of the microemulsion system. Using this sequence, it has been possible to distinguish between two phantom microemulsion systems representing the reduced and oxidised states of the manganese-catalysed, phosphoric acid-stabilised BZ-AOT reaction. It was subsequently possible to visualise oxidation fronts in a 5 mm NMR tube containing the reacting system. Image contrast in the system, was available due to relaxation time differences in the solvent water molecules surrounding the reduced and oxidised form of the manganese catalyst. The manganese-catalysed, metaphosphate-stabilised BZ-AOT reaction was also visualised using the CHESS imaging sequence and, in this case, it was possible to observe the formation and propagation of travelling waves.

The results presented in this chapter represent the first MR images of chemical patterns and waves in the BZ-AOT reaction. Having shown that MRI is a suitable technique for the visualisation of patterns in the system, the opportunity now exists to further develop and optimise imaging sequences and investigate the system in more detail. In particular, the visualisation of three-dimensional Turing patterns can be envisaged. Having identified manganese as a suitable contrast indicator, the tunability of the microemulsion system will need to be exploited in order to produce Turing patterns in the manganese-catalysed system.

5.5. References

(1) Vanag, V. K. *Physics-Uspekhi* **2004**, *47*, 923.

(2) Epstein, I. R.; Vanag, V. K. *Chaos: An Interdisciplinary Journal of Nonlinear Science* **2005**, *15*, 047510.

(3) Vanag, V. K.; Epstein, I. R. *Int J Dev Biol* **2009**, *53*, 673.

(4) Cross, A. L.; Armstrong, R. L.; Gobrecht, C.; Paton, M.; Ware, C. *Magnetic Resonance Imaging* **1997**, *15*, 719.

(5) Gao, Y.; Cross, A. R.; Armstrong, R. L. *Journal Of Physical Chemistry* **1996**, *100*, 10159.

Chapter 6. Concluding Remarks

6.1. Conclusions

In this research, the BZ-AOT reaction has been investigated using magnetic resonance techniques with a view to visualising pattern formation and probing the structure of the microemulsion medium. Pattern formation in the ferroin-, bathoferroin-, and $Ru(bpy)_3$-catalysed reactions has been investigated in order to understand the factors controlling the types of patterns that are formed. The BZ-AOT reaction catalysed by manganese has been investigated for the first time. Optical visualisation of pattern formation in the manganese-catalysed reaction proved difficult due to the poor visual contrast between the reduced and oxidised states of the manganese catalyst. Visual contrast, however, could be improved through stabilisation of the oxidised state of the catalyst using either phosphoric acid or metaphosphate. It was found that contrast could be increased to the extent where oscillations were observed through a colour change, but visualisation of pattern formation was not possible. Pattern formation was, however, optically visible in the manganese/ferroin dual-catalysed BZ-AOT reaction relying on the visual contrast offered by the ferroin indicator.

Manganese and $Ru(bpy)_3$ catalyst systems have previously been used as MRI contrast indicators for the BZ reaction in aqueous and gel media. Their application as MRI contrast indicators in an AOT microemulsion was investigated as part of this research. It was found that the $Ru(bpy)_3$ catalyst resided within the micellar interface and was thus unable to act as an

indicator, as it did not influence the relaxation times of solvent water molecules in the aqueous droplet. The manganese catalyst was shown to provide the necessary NMR relaxation time contrast between the reduced and oxidised states of the system. Oscillations in the manganese-catalysed BZ-AOT reaction were then observed through changes in the T_1 and T_2 relaxation times of solvent water molecules surrounding the manganese catalyst. MRI has been used to observe the propagation of travelling waves in both the phosphoric acid-stabilised, manganese-catalysed BZ-AOT reaction and the metaphosphate-stabilised, manganese-catalysed BZ-AOT reactions. This was the first time the BZ-AOT reaction has been visualised using MRI.

6.2. Further work

Now that the existence of patterns in the manganese-catalysed BZ-AOT system has been shown, there is a need to develop an understanding of the behaviour of the reaction. The chemistry of the reaction and the physical structure of the microemulsion medium will need to be varied, as has been done for the ferroin-, bathoferroin-, and $Ru(bpy)_3$- catalysed reactions, in order to explore and visualise the range of patterns that may be formed. To achieve this, it may be necessary to explore the use of faster imaging sequences. This will be of importance for three-dimensional imaging and also for the visualisation of fast moving or transient patterns. It will be of particular interest to see if the manganese catalyst is able to support the formation of Turing patterns. This would, then, represent an opportunity to observe 3-D Turing structures for the first time. There is also the potential of observing patterns in the manganese-catalysed system that are not observed using other catalysts.

In short, through the optimisation of the MR imaging technique, more complex chemical patterns and waves may be visualised, and in greater detail. As confidence is developed in the technique and its capabilities the variety of patterns that can be visualised will be limited only by the ability to produce them by varying the chemistry and structure of the system.

It may also be possible to further the understanding of the BZ-AOT system in general using combined magnetic resonance and optical imaging techniques. The improved optical contrast offered by the phosphate-stabilised variant of the reaction may allow pattern formation to be visualised using established optical techniques. Although, the degree of contrast is not as high as with the ferroin, bathoferroin and $Ru(bpy)_3$ catalysts, none of these catalyst systems offer the MRI contrast that the manganese catalyst does. It may therefore be possible to visualise pattern formation using both optical methods and MRI. Investigation of pattern formation using a combination of these methods may have synergistic advantages, where one technique may compensate for limitations of the other.

The use of NMR/MRI is not limited solely to the visualisation of patterns; it is also possible to probe the structure and transport properties of the microemulsion system. As the structure of the microemulsion plays such a key role in the formation of Turing patterns in the BZ-AOT system, magnetic resonance measurements could potentially be used to investigate how pattern formation is affected by the structure of the reaction medium. The diversity of pattern formation in the BZ-AOT system is brought about by differences in the

diffusivity of reactants in the aqueous and organic phases. Measurement of the diffusion coefficients of the water droplets and oil phase using NMR may allow this relationship to be probed further. Another aspect for further investigation is the location of different catalysts within the reverse micelle. The location of the ferroin and bathoferroin complexes could be probed using NOE as was done for the $Ru(bpy)_3$ complex. Their location within the reverse micelle may have implications for the types of patterns that are formed for different catalyst systems.

Appendix A. Optical images

A selection of movie files is included on an attached DVD. Movies are grouped into directories based on the catalyst/indicator used for the reaction. For each movie, the file name as it appears on the DVD is listed here, followed by the reaction conditions.

Ferroin-catalysed BZ-AOT reactions

BZ_Fer_002.avi

[MA] = 0.25 M

[H_2SO_4] = 0.175 M

[ferroin] = 4.2 mM

[$NaBrO_3$] = 0.15 M

ω = 18.5, ϕ = 0.48

frame rate = 4 frames per minute

BZFer_280306_002.avi

[MA] = 0.1 M

[H_2SO_4] = 0.175 M

[ferroin] = 4.2 mM

[$NaBrO_3$] = 0.15 M

ω = 18.5, ϕ = 0.48

frame rate = 4 frames per minute

BZFer_070206_03.avi

[MA] = 0.2 M

$[H_2SO_4]$ = 0.175 M

[ferroin] = 4.2 mM

$[NaBrO_3]$ = 0.15 M

ω = 18.5, ϕ = 0.33

frame rate = 4 frames per minute

BZFer_090206_01.avi

[MA] = 0.2 M

$[H_2SO_4]$ = 0.175 M

[ferroin] = 4.2 mM

$[NaBrO_3]$ = 0.15 M

ω = 18.5, ϕ = 0.58

frame rate = 4 frames per minute

Bathoferroin-catalysed BZ-AOT reactions

BZ_BFer_030406_002.avi

[MA] = 0.25 M

$[H_2SO_4]$ = 0.21 M

[bathoferroin] = 5 mM

$[NaBrO_3]$ = 0.18 M

ω = 15, ϕ = 0.36

frame rate = 6 frames per minute

BZ_BFer_040406_001.avi

[MA] = 0.25 M

$[H_2SO_4]$ = 0.21 M

[bathoferroin] = 5 mM

[$NaBrO_3$] = 0.18 M

ω = 15, ϕ = 0.47

frame rate = 6 frames per minute

BZ_BFer_040406_002.avi

[MA] = 0.25 M

[H_2SO_4] = 0.21 M

[bathoferroin] = 5 mM

[$NaBrO_3$] = 0.18 M

ω = 15, ϕ = 0.47

frame rate = 6 frames per minute

BZ_BFer_110406_001.avi

[MA] = 0.3 M

[H_2SO_4] = 0.2 M

[bathoferroin] = 5 mM

[$NaBrO_3$] = 0.18 M

ω = 15, ϕ = 0.36

frame rate = 6 frames per minute

$Ru(bpy)_3$-catalysed BZ-AOT reactions

BZ_Ru_240107_004.avi

[MA] = 0.1 M

[H_2SO_4] = 0.1 M

[$Ru(bpy)_3$] = 4 mM

[$NaBrO_3$] = 0.27 M

ω = 9.2, ϕ = 0.39

frame rate = 6 frames per minute

BZ_Ru_260107_002.avi

[MA] = 0.17 M

[H_2SO_4] = 0.12 M

[$Ru(bpy)_3$] = 3.75 mM

[$NaBrO_3$] = 0.25 M

ω = 9.2, ϕ = 0.45

frame rate = 6 frames per minute

BZ_Ru_191206_001.avi

[MA] = 0.17 M

[H_2SO_4] = 0.12 M

[$Ru(bpy)_3$] = 4 mM

[$NaBrO_3$] = 0.27 M

ω = 9.2, ϕ = 0.45

frame rate = 6 frames per minute

BZ_Ru_260107_001.avi

[MA] = 0.08 M

[H_2SO_4] = 0.12 M

[$Ru(bpy)_3$] = 3.75 mM

[$NaBrO_3$] = 0.25 M

ω = 9.2, ϕ = 0.45

frame rate = 6 frames per minute

BZ_Ru_081206_002.avi

[MA] = 0.25 M

[H_2SO_4] = 0.2 M

[$Ru(bpy)_3$] = 3.75 mM

[$NaBrO_3$] = 0.25 M

ω = 9.2, ϕ = 0.45

frame rate = 6 frames per minute

BZ_Ru_111206_002.avi

[MA] = 0.25 M

[H_2SO_4] = 0.4 M

[$Ru(bpy)_3$] = 3.75 mM

[$NaBrO_3$] = 0.25 M

ω = 9.2, ϕ = 0.45

frame rate = 6 frames per minute

BZ_Ru_111205_005.avi

[MA] = 0.25 M

[H_2SO_4] = 0.4 M

[$Ru(bpy)_3$] = 3.75 mM

[$NaBrO_3$] = 0.25 M

ω = 9.2, ϕ = 0.67

frame rate = 6 frames per minute

BZ_Ru_181206_003.avi

[MA] = 0.08 M

[H_2SO_4] = 0.12 M

[$Ru(bpy)_3$] = 3.75 mM

[$NaBrO_3$] = 0.25 M

ω = 9.2, ϕ = 0.45

frame rate = 6 frames per minute

BZ_Ru_100806_001.avi

[MA] = 0.1 M

[H_2SO_4] = 0.32 M

[$Ru(bpy)_3$] = 4 mM

[$NaBrO_3$] = 0.18 M

ω = 9.2, ϕ = 0.39

frame rate = 6 frames per minute

BZ_Ru_220906_003.avi

[MA] = 0.2 M

[H_2SO_4] = 0.32 M

[$Ru(bpy)_3$] = 4 mM

[DPA] = 0.25 mM

[$NaBrO_3$] = 0.3 M

ω = 9.2, ϕ = 0.335

frame rate = 6 frames per minute

Manganese/ferroin-catalysed BZ-AOT reaction

mnfepmp_171108_1.avi

[MA] = 0.15 M

[H_2SO_4] = 0.3 M

[H_3PO_4] =0.2

[$MnSO_4$] = 1.2 mM

[ferroin] = 0.33 mM

[$NaBrO_3$] = 0.1 M

ω = 9.2, ϕ = 0.45

frame rate = 4 frames per minute

Appendix B. NOESY data

The NOESY build up data are presented here in the form of an excel spreadsheet, (NOE_BUILDUPS.xls) contained on the attached DVD. The first worksheet contains the data for small droplets ω = 9.2. The second worksheet contains the data for ω = 34.9. The third worksheet contains the data for intramolecular NOE enhancements between bipyridine protons. Also included are the complete set of 2-D NOESY spectra, in the form of pdf files, for both water-to-surfactant ratios at each value of the mixing time. Spectra for ω = 9.2 are contained in the W_9_2 directory, and spectra for ω = 34.9 are contained in the W_34_9 directory. The file name for each spectrum corresponds to the mixing time.

Appendix C. MR images

The MR images shown in Chapter 5 are presented in the form of movie files on the attached DVD. For each movie, the file name as it appears on the DVD is listed here, followed by the reaction conditions.

Phosphoric acid-stabilised manganese catalysed BZ-AOT reactions

1602_34.avi

[MA] = 0.15 M

[H_2SO_4] = 0.3 M

[H_3PO_4] = 0.2

[$MnSO_4$] = 1.2 mM

[$NaBrO_3$] = 0.1 M

ω = 9.2, ϕ = 0.45

T_R = 150 ms, T_E = 7.637 ms, FOV = 40 mm × 20 mm, slice thickness = 1mm, matrix size = 128 × 128, signal acquisitions = 2, image acquisition time = 38 s

2402_02.avi

[MA] = 0.15 M

[H_2SO_4] = 0.1 M

[H_3PO_4] = 0.2

[$MnSO_4$] = 1.2 mM

[$NaBrO_3$] = 0.1 M

ω = 9.2, ϕ = 0.45

T_R = 150 ms, T_E = 7.637 ms, FOV = 40 mm × 20 mm, slice thickness = 1mm, matrix size = 128 × 128, signal acquisitions = 2, image acquisition time = 38 s

Metaphosphate-stabilised manganese catalysed BZ-AOT reaction

2904_13.avi

[MA] = 0.15 M

[H_2SO_4] = 0.17 M

[$Na_5P_3O_{10}$] = 0.2

[$MnSO_4$] = 45 mM

[$NaBrO_3$] = 0.1 M

ω = 9.2, ϕ = 0.45

T_R = 150 ms, T_E = 9.0 ms, FOV = 20 mm × 10 mm, slice thickness = 1mm, matrix size = 128 × 64, signal acquisitions = 4, image acquisition time = 38 s